# AN EXPERIMENTAL INVESTIGATION OF THE EFFECT OF FUEL DROPLET SIZE ON THE VAPORIZATION PROCESS IN A TURBULENT ENVIRONMENT AT ELEVATED TEMPERATURE AND PRESSURE

by

Cameron Mark Verwey

A Thesis submitted to the Faculty of Graduate Studies of

The University of Manitoba

in partial fulfilment of the requirements of the degree of

MASTER OF SCIENCE

Department of Mechanical Engineering

University of Manitoba

Winnipeg

# ABSTRACT

The performance of liquid-fuelled spray combustion systems has a massive impact on the efficiency of energy production in many sectors across the globe. Realistic combustors generate sub 100-μm droplets and operate under high pressure and temperature in strong turbulence. Investigations into droplet evaporation and combustion provide fundamental knowledge and validation data regarding the behaviour of sprays, and although single droplet approaches have been a staple of energy research for many decades, there is little information regarding the effect of turbulence and initial diameter, especially micro-sized, on droplet evaporation rates. The present experimental study develops, interprets, and correlates the results of almost 500 tests performed on isolated heptane and decane droplets. Droplets in the range of 110 – 770 μm (initial diameter) were generated and suspended on small intersecting micro-fibers in a spherical fan-driven chamber and exposed to quasi-zero mean turbulence of intensity up to 1.5 m/s, temperatures ranging from 25 – 100°C, and pressures between 1 and 10 bar. The results indicate that droplet size has a major influence on evaporation rate, as measured by the temporal reduction in droplet surface area, when the environment is turbulent. Evaporation rates increased with both initial diameter and turbulence intensity at all test conditions. The effectiveness of turbulence, defined as the ability of turbulence to improve the evaporation rate over the rate of a stagnant droplet at identical ambient conditions, increased with pressure but decreased with temperature. Both the ratio of Kolmogorov length scale to droplet diameter and the theoretical molar concentration gradient of fuel at the droplet surface are found to be excellent predictors of turbulence effectiveness. Correlation approaches utilizing a turbulent Reynolds number or a vaporization Damköhler number are suggested to predict the evaporation rate of a single droplet exposed to a purely turbulent flow field.

# ACKNOWLEDGEMENTS

I primarily wish to acknowledge the support, guidance, and knowledge of my advisor Dr. Madjid Birouk. Furthermore, I must express my gratitude to the many other excellent professors and instructors, some of whom I was fortunate to TA for, at the University of Manitoba. Additional thanks go to the members of the examining committee who took the time to read this (lengthy) thesis and provide valuable feedback. I am especially grateful for the financial assistance provided by, at various stages, the University of Manitoba, the Province of Manitoba, and the Natural Sciences and Engineering Research Council of Canada (NSERC). The dedication and helpfulness of the laboratory technical staff and fellow graduate students, past and present, has not gone unnoticed. For their assistance in the lab, thanks go to Sviatoslaw Karnaoukh, Abu Mahmud Iqbal Chowdhury, Meghdad Saediamiri, Mahmoud Moussa Abdel Azim, and Ahmad Ayache. Finally, I extend my sincere appreciation to my supportive friends and family; in particular my parents, Mark and Elaine, and my girlfriend, Claudia.

# TABLE OF CONTENTS

# LIST OF FIGURES

# LIST OF TABLES

# NOMENCLATURE

*Symbols:*

| | |
|---|---|
| $B$ | mass transfer number [-] |
| $C$ | empirical constant [-] |
| $d$ | diameter [µm] |
| $D_{AB}$ | mass diffusion coefficient of species *A* into *B* [$m^2/s$] |
| $Da_v$ | vaporization Damköhler number [-] |
| $f(r)$ | longitudinal correlation coefficient [-] |
| $f\#$ | camera f-number [-] |
| $G$ | group combustion number [-] |
| $Gr$ | Grashof number [-] |
| $h_{fg}$ | enthalpy of vaporization [J/mol] |
| $K$ | evaporation rate constant [$mm^2/s$] |
| $L$ | turbulence integral length scale [mm] |
| $\dot{m}$ | mass evaporation or burning rate [kg/s] |
| $MW$ | molecular weight [g/mol] |
| $N$ | fan speed [RPM] |
| $Nu$ | Nusselt number [-] |
| $P$ | pressure [bar] |
| $Pr$ | Prandtl number [-] |
| $q$ | turbulence kinetic energy [$m^2/s^2$] |

| | |
|---|---|
| $q^{0.5}$ | turbulence intensity [m/s] |
| $R$ | universal gas constant [J/mol·K] |
| $r$ | radius [µm] |
| $Re$ | Reynolds number [-] |
| $Sh$ | Sherwood number [-] |
| $Sc$ | Schmidt number [-] |
| $T$ | temperature [K or °C] |
| $T.I.$ | turbulence intensity [%] |
| $t$ | time [s] |
| $\overline{U}$ | mean velocity [m/s] |
| $u$ | fluctuating velocity component [m/s] |
| $\nu$ | kinematic viscosity [$m^2/s$] |
| $X$ | molar fraction [-] |
| $Y$ | mass fraction [-] |
| $\lambda$ | turbulence Taylor microscale [µm] |
| $\eta$ | turbulence Kolmogorov length scale [µm] |
| $\rho$ | mass density [$kg/m^3$] |
| $\delta$ | vapor layer thickness [µm] |

*Subscripts:*

| | |
|---|---|
| $avg$ | average |
| $b$ | boiling point |

| | |
|---|---|
| $c$ | critical value |
| $d$ | diameter, droplet |
| $dev$ | deviation |
| $e$ | extinction |
| $f$ | fiber, film, flame |
| $F$ | fuel |
| $g$ | gas |
| $i$ | interface |
| $l$ | laminar, liquid |
| $M$ | modified |
| $n$ | nodule |
| $r$ | reduced value, reference value |
| $rms$ | root mean square average |
| $s$ | droplet surface |
| $sat$ | saturation |
| $t$ | turbulent |
| $v$ | vapor |
| $x$ | horizontal direction |
| $y$ | vertical direction |
| 0 | initial, stagnant, origin |
| $r$ | radial |
| $\infty$ | ambient value |

*Acronyms:*

| | |
|---|---|
| $fps$ | frames per second |
| $PIV$ | particle image velocimetry |
| $psia$ | absolute pressure in pounds per square inch |
| $RMS$ | root mean square average |
| $RPM$ | revolutions per minute |
| $SiC$ | silicon carbide |
| $SMD$ | Sauter mean diameter |

# CHAPTER 1
# INTRODUCTION

Throughout the world, no energy source is as important as liquid fuels. Overall, liquid fuel accounts for 33% of the world's total energy consumption with a projected minor decline of 3% by 2040 due primarily to the growth of renewable energy sources and natural gas [1]. The transportation sector, in particular, is dominated by the consumption of gasoline, diesel, and jet fuel. Currently, liquid fuels maintain a 96% share of all energy related to the movement of people and goods; this is expected to decrease only slightly to 88% by 2040 [1]. There are several reasons for the sustained reliance on liquid fuels, both economic and technical. At the time of writing this thesis, inexpensive crude oil combined with continued high production rates provide little short-term economic incentive to invest in revolutionary alternate energy sources. From an engineering perspective, petroleum fuels offer impressively high energy densities of over 40 MJ per kilogram of fuel [2]. The internal combustion engine has been developed, studied, and refined for well over one hundred years, leading to excellent reliability and relatively low cost. In the aerospace industry, the result of even a single failure in a propulsion system could be disastrous, which all but ensures that a paradigm shift in gas turbine fuelling techniques is unlikely [3]. Conversely, the drawbacks associated with conventional liquid-fuelled transportation and industrial processes are numerous and well known, including poor efficiency (for example, ~12% of the fuel energy in a typical spark ignition engine is used to drive the wheels of a vehicle [2]), serious pollution concerns, and the fact that fossil fuel reserves will eventually (and inevitably) run out. Air pollution has been estimated to cause 6.5 million deaths worldwide on yearly basis, and inefficient combustion combined with weak regulation is the single most important source [4]. Although the ultimate solution may be a complete shift away from petroleum-based fuel sources, the above data

suggests this is not achievable in the short term. Furthermore, it is unclear exactly which green technology will emerge as the successor to fossil fuels, as different approaches have, with the passage of time and investment of research, fallen in and out of favor [5]. In any case, there are compelling reasons to continue investigating methods to enhance the efficiency of liquid-fuelled combustion: the almost certain widespread usage of liquid fuels well into the future, and the room for enhancement in current technologies. Even small, incremental improvements in emissions and fuel consumption (typical of spark ignition engines [6], for example) can have major positive impacts.

A key function of any liquid combustion system is the preparation of the liquid to be burned. In general, this is achieved by either heating and vaporizing the fuel to form a gaseous combustible mixture or by pressurizing and injecting the liquid fuel into a combustion chamber. The latter technique, commonly called spray combustion, is by far the most common in engineering applications. Spray combustion operates on the principle of maximizing surface area as the liquid jet rapidly breaks down into dispersed droplets (e.g., [7]). These droplets will either burn individually or vaporize to form a flammable mixture depending upon several environmental conditions (e.g., [8]). The evaporation characteristics of fuel droplets is crucial in assessing pollutant emissions, ignition delays, and the efficiency of a combustor (e.g., [9]). Expensive and time-consuming experimental tests mostly drive the design decisions for practical devices [10] which indicates that the development of such experiments should carefully consider all of the individual processes involved. By the 1960's, the annular combustor design, which is difficult to test experimentally at lab scale, was firmly entrenched as the automatic choice for aircraft gas turbine engines [11]. In these types of situations, where experiment is difficult or prohibitive, numerical models become increasingly important. Such codes are heavily reliant upon accurate

knowledge of single droplet evaporation processes (e.g., [12]). Indeed, a persistent belief encountered in fuel vaporization studies is that a single, isolated droplet can adequately predict certain fundamental characteristics of atomized liquid emanating from a spray, as droplets tend to act independently of one another after the swift breakup of liquid-fuel jets (e.g., [7,13,14]). Although ultimately an idealization, the basic physics of single droplet evaporation apply throughout a range of realistic spray combustion modes from single droplet combustion, where heat and mass transfer may take precedence over kinetics, to large group diffusion flames which rely on the vaporization of the dispersed constituent droplets to sustain a flammable mixture (e.g., [15]).

Wu et al. [16] denotes the three most important factors affecting combustion efficiency as temperature, ambient turbulence, and residence time. Droplet size is interrelated to all three parameters. Considering that the residence time in a modern aircraft gas turbine combustor is only 1 – 3 ms [17], it is imperative that the injected fuel is rapidly mixed and burned. Unconsumed fuel represents a source of pollution and lost engine efficiency. A comprehensive understanding of the lifetime of fuel droplets, which depends profoundly upon temperature, turbulence, size, and pressure, is thus of prime importance.

Researchers typically measure the lifetime of a droplet by tracking the evolution of volume, surface area, or diameter with the passage of time. Surface area, which is proportional to the droplet diameter squared, $d^2$, is undoubtedly the most common lifetime measurement approach due to the important finding that droplet surface area decreases linearly with time under many different conditions (e.g., [18,19]). A droplet with a linear temporal variation of $d^2$ is said to follow the $d^2$ law. Fig. 1.1 illustrates classic $d^2$ behaviour for a suspended alkane droplet in a quiescent atmosphere. The evaporation rate, $K$, which is a measure of phase change from liquid to vapor, is

calculated by determining the slope of the linear portion of $d^2$ vs. $t$. In the case of Fig. 1.1, linearity remains intact throughout the entire droplet lifetime. In other situations, linearity may begin or end after a certain amount of time has elapsed, or the profile may be transient throughout. Droplet studies are often interested in assessing the degree of linearity and the magnitude of $K$ for various fuels and environmental conditions. There are, however, substantial gaps in the knowledge base surrounding the turbulent evaporation of small, single droplets despite the decades of direct and related research.

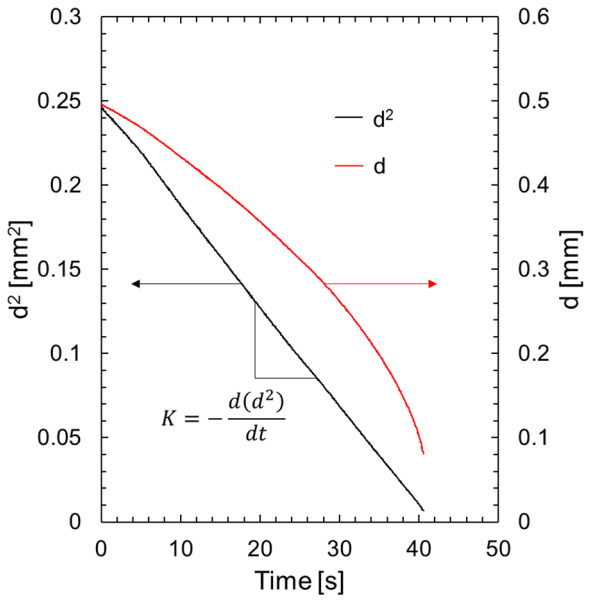


**Fig. 1.1.** Temporal plot of heptane droplet diameter and the diameter squared.

Numerous studies have investigated the effect of pressure and temperature on droplet evaporation (e.g., [20–24], [25] and the references cited therein), whereas investigations into the effect of droplet size (e.g., [26,27]) and turbulence (e.g., [16,28–31]) have been less abundant, especially when evaluated simultaneously (e.g., [32,33]). With an emphasis on predicting the mass burning rate, the consequences of varying droplet size in combustion scenarios have largely been attributed to soot formation and heat loss by radiation (e.g., [34–36]), yet at a more fundamental

level, the reasons for the effect of droplet size in pure evaporation conditions remain undetermined. Evaporation is often considered the rate-limiting precursor to combustion (e.g., [13,37]). Thus, the effect of droplet size on the evaporation rate, coupled with the interrelated parameters of ambient pressure, temperature, and turbulence, remains a topic of considerable interest.

The present study seeks to address several of the above issues. The objectives of this thesis are summarized as follows:

1) Utilize the cross-fiber suspension technique to generate a range of initial droplet sizes for fuel evaporation analysis under turbulent conditions. Emphasis is placed on the evaluation of droplets in the sub 400-μm range as this size range is both realistic and under-represented in the current literature. Droplets with initial diameters approaching 100 μm are ideal.
2) Determine the relationship between droplet size, turbulence intensity, and fuel type at room conditions to establish a baseline of understanding.
3) Expand the turbulent results to include high temperature and pressure. This extension serves to increase the validity of the data, as actual combustion systems operate at elevated conditions and, more importantly, alter the turbulence characteristics.
4) Modify and expand existing predictive correlations, such as turbulent Reynolds number and vaporization Damköhler number techniques, for droplets evaporating in turbulent flow to include the effects of droplet size.
5) Identify areas of potential future research through experimental observation and literature review.

This thesis is structured into five chapters. Chapter 1, which contains the preceding discussion, introduced the topics of spray combustion and single droplet evaporation, and outlined several thesis goals. Chapter 2 explores the broad literature base devoted to the numerous aspects of droplet vaporization. Each of the seven main sections in Chapter 2 (Section 2.2 to 2.8) focuses on a relevant topic, such as the effect of turbulence on droplet evaporation rate. Chapter 3 outlines the experimental equipment and techniques employed in this study. Chapter 4 presents the results and is split into two major parts: Section 4.1 discusses the findings at room conditions while the results at elevated pressure and temperature are located in Section 4.2. A significant portion of Chapter 4 is dedicated to interpreting and correlating the gathered data. Chapter 5 concludes the thesis and suggests detailed recommendations for future work. A comprehensive appendix follows the list of references and includes raw data tables, code listings, error analysis, experimental techniques, and tabulated summaries of equipment.

# CHAPTER 2
# LITERATURE REVIEW

## 2.1 Overview

The depth of knowledge related to the evaporation and burning of liquid-fuel droplets is expansive. Research in this area involves many different engineering disciplines including thermodynamics, heat and mass transfer, aerodynamics, turbulent fluid dynamics, and chemistry. The evaporation of isolated and suspended fuel droplets under a variety of experimental conditions is the focus of the present investigation. Thus, the literature review presented in this section emphasizes experimental data in the absence of combustion, although the discussion includes findings which fall outside of this scope where applicable.

From a practical standpoint, the widespread usage of spray combustion systems necessitates the study of droplets. Thus, Section 2.2 provides a brief overview of the mechanisms which affect liquid sprays. Section 2.3 discusses the legitimacy of applying the knowledge gathered in isolated droplet studies, along with the challenges that arise because of single droplet suspension techniques. Section 2.4 describes some of the key differences between evaporation and combustion studies and establishes that the evaporative characteristics of droplets are of fundamental importance in the field of spray combustion. Modern studies are often concerned with comparing results to classic theories or relaxing the restrictive assumptions built into older models and in Section 2.5, the most important early theoretical and experimental findings, including the famous $d^2$ law, are presented and explained. Later sections expand upon some of these concepts when appropriate. The effect of temperature and pressure on droplet evaporation has been well studied, and Section 2.6 contains the main results. The primary novelty of the present experiment

lies in the generation of a range of droplet sizes and the subsequent exposure of the individual droplets to a turbulent convective flow. Therefore, the present state of knowledge regarding convective evaporation (turbulence in particular) and the effect of initial droplet size are thoroughly detailed in Sections 2.7 and 2.8. Section 2.9 summarizes the results of the literature review as they pertain to the current work.

## 2.2 Importance and general characteristics of spray combustion

Spray combustion is exceedingly important to modern industry and transportation. Spark-ignition and compression-ignition engines, as well as most gas turbine engines and industrial burners, utilize some form of spray distribution to generate a fine mist of atomized fuel droplets prior to ignition and burning. Of primary importance is the maximizing of surface area of the fuel which promotes two fundamental phenomena; convective heat transfer from the hot gases to the typically cool droplets and the mass transfer of oxidizer and fuel vapor to the flame interface. Increasing the droplet's temperature is necessary to promote rapid evaporation, which is a precursor to combustion, and both vapor and oxidizer must be available in proper proportions to maintain the mixture within its flammability limit for a stable and strong flame. Efficient and clean combustion thus begins with the seemingly simple injection of fuel in a manner which will generate tiny liquid droplets. However, the number of parameters which influence overall spray characteristics are substantial [38], which makes spray combustion an active area of study.

The fuel injector is tasked with introducing the liquid fuel into the combustor (or chamber, in the case of reciprocating engines). This environment is typically hot, pressurized, and very turbulent. Advanced gas turbine engines, for example, can expect to see overall pressure ratios on

the order of 45:1 and turbine inlet temperatures approaching 1800 K [39]. In most instances, the combustion environment easily exceeds the critical point of the fuel, although whether the spray itself becomes supercritical depends on the precise conditions as well as the residence time [25,40]. Injectors are designed to operate over a wide range of fuel inlet pressures and are required to atomize fuel at various spray angles depending on the current engine demand [41]. Further details on injector types and the fuel injection process for general spray atomization, as well as for gas turbine and diesel engines, can be found in [11,41–43].

An in-depth review by Faeth [7] outlines some of the more complex fundamentals of spray combustion and indicates many areas where important data is lacking. To briefly summarize, injection begins with a dense spray region where a liquid core progressively breaks apart along its radial edges until a dispersed multiphase flow exists downstream of the injector. High ambient pressure helps to reduce the distance from the jet exit at which rapid reduction in liquid volume fraction occurs, while increasing fuel injection pressure will reduce the occurrence of larger droplets appearing in the overall distribution [11]. Even in near-injector regions where the liquid core remains prominent, the mixing layer is surprisingly dilute. This primary breakup of the liquid phase is strongly dependent on the jet exit conditions and the degree of shear instability and wave formation along the liquid surface [44]. At this point, the irregularly-shaped droplets and ligaments are still relatively large. Now fully exposed to the high-pressure environment typical of many applications, a reduction in surface tension ensues and deformation readily occurs as the droplets approach the critical point; secondary breakup has begun. The exact mode of this breakup is complex, and depends on the dimensionless Weber number, among others. In general, a progressive reduction in droplet size will continue until the surface tension force exceeds that of the aerodynamic distortion force (e.g., drag). To generate small droplets, it is therefore critical that

the relative velocity between the liquid and gas phase remains large. After secondary breakup, the droplets are stable and generally spherical in shape. For the purposes of the current discussion, the important aspect is that secondary breakup yields a dilute region where the effect of droplet collisions is negligible. The droplets essentially become independent of one another before ignition.

Most of the spray phenomena discussed above occurs in the relatively cool region near the injector yet far from the combustion zone [7]. This feature imposes a degree of separation between the liquid jet breakup and the succeeding droplet evaporation and burning such that the two processes may be analyzed independently. Regardless of the subsequent ignition mode (individual, group, or global), evaporation of the droplets must precede the combustion event [45]. The characteristics of fuel droplet evaporation are highly influential in determining the overall efficiency of a spray combustion system [9]. Rapid heat transfer from the gaseous phase to the liquid, which can only occur in the dilute downstream region due to the high level of droplet dispersion, drives the evaporative process [15]. Indeed, the relatively long diffusion time scale as compared to that of the actual reaction kinetics suggests that evaporation is not only a precursor to combustion but may assume the role of the rate-limiting step throughout the burning process (e.g., [13]).

Although combustion provides the greatest motivation to study the evaporation of sprays, there are a significant number of other applications that require detailed knowledge of the behaviour of droplets for efficient design. For example, the distribution of water droplet size in an evaporative cooling spray for gas turbine inlet fogging (e.g., [46]) or transportation tunnel cooling (e.g., [47]) plays a major role in the overall performance of the system. In this manner, discoveries which arise in a study pertaining to one field can often be applied to another.

## 2.3 Relevance and applicability of single droplet analysis

The dilute region of a liquid spray consists of a droplet ensemble which may number in the millions [48,49]. The relevance and applicability of single droplet investigations is therefore questionable. The study of single isolated droplets is unquestionably simpler, although this fact alone would not account for the predominance of such endeavours unless the physics are also considered important and representative of actual sprays. As discussed in Section 2.2, liquid jets tend to disintegrate rapidly into dilute regions of atomized droplets. In many cases, the inter-droplet spacing is sufficient to assume that the droplets act independently from their neighbors. If, in fact, droplets in a spray do not burn individually but rather as a turbulent diffusion flame (e.g., [50–52]), such a flame requires the evaporation of the individual drops to generate a flammable mixture. In this case, vaporization of individual droplets remains fundamental and may be a more realistic scenario than the combustion of large isolated droplets. If single droplet combustion does occur, for instance, at locations sufficiently downstream of injection or for droplets which have radially escaped the flame, fuel vaporization remains the probable rate-determining step in predicting the burning rate of the envelope or wake flame surrounding the droplet. Single droplet evaporation, therefore, is at the heart of spray combustion. Section 2.4 expands upon the issue of evaporation vs. burning.

There are definite limitations to single droplet studies. Even if the droplets in a spray do not physically contact each other (shattering or coalescing in the process), droplets in proximity affect the ambient gas environment, both near and far field, as well as the diffusion characteristics surrounding each droplet [12]. Single droplets evaporated or combusted in an infinite expanse cannot be used to evaluate these types of multiphase interactions. Many studies have attempted to address this gap by analyzing droplet arrays (defined and periodic geometry), groups (necessitates

statistical description), or sprays (full coupling between liquid and gaseous phases). Such approaches are not discussed, although recent examples include [22,32,53,54], to name but a few. Even so, models designed to calculate the properties of arrays, groups, or sprays of droplets still rely upon a comprehensive understanding of individual droplet processes (e.g., [55,56]).

Mikami et al. [57] classifies droplet generation techniques into seven categories based on the precise methodology of generation and suspension (or lack thereof). To simplify the present discussion, experimental studies on individual droplets are assumed to proceed along one of two broad paths: freely floating or suspended. A free-floating droplet moves with the flow and is not constrained or influenced by any external supports. In this sense, free droplets are an excellent approximation to true spray combustion. Certain information on droplet aerodynamics and ballistics cannot be obtained using captive droplet techniques, necessitating the free droplet approach. However, free droplet studies are relatively rare when compared to their numerous suspension-based counterparts. As discussed by Liu et al. [58] and many others, the problem of a free droplet drifting out of focus is one of the greatest challenges in the field of droplet science. For combustion, ignition is also a major problem although several classic studies have overcome these issues (e.g., [35,59,60]). Many researchers have used piezoelectric generation to create a stream of droplets which, depending on the inter-droplet spacing, could be considered as a cyclic repetition of isolated droplet evaporation (e.g., [27,61–64]). The piezoelectric technique can consistently generate sub 100-μm droplets (e.g., [27,64]). These studies typically require advanced laser-based sizing techniques to avoid the shortcomings associated with digital imaging equipment, such as fixed pixel size limits and poor depth of field [27]. It would be a nearly impossible task to track a free droplet in a strong turbulent environment which is why most, if not all turbulent studies, discussed in Sections 2.7.4 and 2.7.5, utilize the suspended droplet technique.

The widespread implementation of fiber suspension techniques has naturally lead to the question of whether fibers induce effects which alter the evaporation characteristics of the droplet. Researchers have long understood that a supporting fiber or thermocouple can conduct heat to (e.g., [65]) or from (e.g., [59]) the droplet faster than the surrounding gaseous phase. Several studies have attempted to quantify such impacts and suggest mitigation strategies. Shih and Megaridis [66] recognized that the effects of support fibers on a vaporizing droplet extend beyond providing an additional conductive path, such as altering the internal liquid circulation and reducing the volume of liquid for a given droplet diameter. Both effects are due to the presence of the enlarged fiber nodule, or bead, which is necessary to anchor the droplet at the end of the fiber. In their comprehensive numerical study of a droplet exposed to hot (1250 – 1600 K) laminar flow, the authors concluded that the properties of the fiber (diameter and thermal conductivity) are less important than the fact that droplet is held stationary, and therefore behaves much differently than a free-floating drop. Although the lifetimes of all suspended droplets were roughly equivalent, comparison between the suspended droplets and those which are unconstrained demonstrated that the free droplet evaporates much slower. The weak evaporation of the free droplet is attributed to the rapid decrease in Reynolds number, and thus poor shear-induced mixing, as well as large liquid volume. It is therefore questionable as to whether large tethered droplets exposed to laminar flow can adequately predict evaporation rates for realistic, unconstrained droplets.

Yang and Wong [67,68] investigated the impact of single support fibers at more moderate temperatures (490 – 750 K) and found that inclusion of the conductive fiber effect improved the predictions of their numerical model when compared to high-pressure experimental data in microgravity. The effect of increasing fiber diameter always shortens the droplet lifetime; this is especially prevalent at lower flow temperature. However, an intermediate value of fiber diameter

may maximize the heat input from the fiber. For example, Yang and Wong [68] found that a quartz fiber of 150 μm in diameter maintained greater heat transfer rates to the droplet as compared to a fiber of 300-μm diameter. A droplet on the 300-μm fiber will still evaporate at a faster rate due to the reduced liquid volume. The authors conclude that a quartz fiber of 50-μm diameter will not affect the evaporation of a droplet. If the support fiber is to improve the evaporation rate, the effect is most likely to be witnessed later in the droplet lifetime. The experiments and numerical simulations of Han et al. [69] agree that the conductive heat rate through the fiber first increases and then decreases with increasing fiber diameter, although they conclude that the early stage of droplet evaporation can be affected by the fiber conduction. If experiments are repeated for several fiber diameters under identical conditions, it may be possible to extrapolate the evaporation rate to a fiber diameter of zero to predict the true $K$ value (e.g., [70]). However, strong non-linearities manifest as the fiber diameter approaches zero, especially at elevated ambient temperature, indicating that this approach should be used cautiously [71]. Shringi et al. [72] discovered that while the heat transfer from the gas phase to the droplet surface is initially very high, it rapidly reduces with time as the droplet surface temperature increases. Heat transfer through the fiber, on the other hand, remains relatively constant, leading to the fiber supplying a significant portion of the droplet's late stage vaporization energy. They also showed that fibers can slow down droplet vaporization by promoting thermal Marangoni flows near the fiber-droplet contact point. The circulation of the cooler interior fluid lowers the droplet surface temperature. Fiber-induced liquid convection is less important for high Reynolds environments because the droplet is already strongly mixed due to the surface shear. Several researchers have studied the effect of fibers on combustion using experimental (e.g., [58,73]) and numerical (e.g., [74]) means. Fibers used for

combustion studies can interfere with burning rate, flame and soot stand-off ratios, and extinction characteristics.

The previous discussion illustrates the complexity and number of factors involved in assessing the potential for fiber effects. Fortunately, many of the above complications can be reduced and practically eliminated by implementing a cross-fiber suspension technique (e.g., [54,57,73,75–77]). The cross-fiber technique eschews a single large support fiber in favor of two smaller fibers which are forced to intersect. The intersection point supports the droplet, which can now be made smaller and more spherical. Although ellipsoidal droplets suspended on a single fiber generally adhere to the $d^2$ law, the various methods of calculating an equivalent diameter can result in significant variation of the calculated vaporization rate [78]. The droplet sphericity promoted by the cross-fiber reduces this issue. The angle of intersection and the fiber properties, such as material and thickness, vary in the literature. Most, if not all, experimentation has been performed at atmospheric pressure. To the author's knowledge, the extent of cross-fiber validation is the experimental comparison between various single fiber arrangements and the cross-fiber technique. For instance, Mikami et al. [57] used crossed 14-μm SiC fibers to support droplets in flame spread experiments and concluded that the effects on flame shape and heat transfer were much smaller than for a 125-μm single quartz fiber. Hicks et al. [73] experimented with 10-μm SiC fibers with a 220-μm epoxy bead located at the fiber intersection. Droplets suspended on the cross-fiber featured lower burning rates than droplets on a 110-μm single quartz fiber with a 360-μm bead. Liu et al. [58] implemented a 14-μm cross-fiber system for ground-based microgravity tests and compared the results to droplets anchored by an 80-μm single fiber aboard the International Space Station. Droplets suspended on the cross-fiber exhibit very similar burning characteristics, such as the temporal $d^2$ profile and flame and soot stand-off ratios, to free-floating

drops. In contrast, the large single fiber tends to distort the soot shell near where the fiber intersects the droplet, indicating a non-symmetric gas flow field. Chauveau et al. [77] extrapolated the evaporation rates of 800-μm decane droplets suspended on several quartz filaments of varying diameters and discovered that the theoretical $K$ at a fiber diameter of zero was equal to the experimental value of the same droplet suspended on a 14-μm cross-fiber. The ambient temperature was moderately elevated (570 K), and although extrapolation to zero is controversial (e.g., [71]), this study remains the best (and perhaps only) validation of the cross-fiber method in a purely evaporative environment.

## 2.4 Droplet evaporation versus burning

The previous section addressed the issue of applying knowledge gained from single droplet studies to combustion applications that use sprays. A similar question arises when studying droplet evaporation instead of combustion. Although droplets and sprays certainly have utility beyond combustion (e.g., [46,47]), it is useful to consider the similarities between an evaporating droplet and one which is burning. Indeed, the topic of droplet evaporation is undeniably popular (see, for example, the narrow in scope but incredibly detailed reviews by Sazhin [79,80] regarding droplet heating and evaporation). If the overarching goal is to understand and model spray combustion, then droplet evaporation, similar to how non-evaporating sprays represent a reasonable first step in the analysis of combusting sprays [7], represents a reasonable first step in understanding droplet combustion. Matlosz et al. [81] expressed a similar sentiment in perusing experimental data on high-pressure single droplet evaporation which, although representative of a major departure from actual rocket engine conditions, remains a logical first indicator of expected behaviour.

As discussed by Williams [14], the basic assumption of proportionality between the droplet mass vaporization rate and droplet diameter applies to both low-temperature evaporation and high-temperature combustion [82]. Thus, from the quasi-steady $d^2$ framework, evaporation and combustion are expected to behave similarly. The partial equivalence of the two modes is perhaps best understood by considering the following interrelated theories: the thin flame front acts as a source of heat at some stand-off distance from the droplet, and diffusion is the rate-limiting precursor to combustion. Taken together, these two concepts imply that single droplet combustion is roughly equivalent to evaporation in a high-temperature ambience. Law [83] suggests that the similarity between evaporation and combustion of droplets is so great that droplet burning in a cold environment can simulate high-temperature evaporation. Combustion-specific anomalies include the presence of oxidation product near the droplet surface, which will affect heat and mass transfer properties, and a non-uniform temperature field due to the localized spike at the flame. Additional complications may arise if the flame is not of the envelope type but rather a wake. This mode of flame can occur in a strong convective flow (e.g., [84]), and would result in the exposure of the droplet to a temperature field that varies circumferentially. It should be emphasized that regardless of the differences between pure evaporation and combustion, a liquid must always vaporize before burning.

Certain researchers have suggested that studying droplet combustion is irrelevant since droplet vaporization is the dominant process in determining the characteristics of spray combustion [85]. Although this may be an oversimplification, there are several practical reasons why analyzing evaporation can be preferable to combustion. Curtis and Farrell [56] discussed how flames obscure fundamental vaporization processes through soot, radiation, and transport phenomena modification. The soot shell generated by certain fuels may result in ambiguous or difficult to

obtain droplet size measurements (e.g., [86]). In assessing fluid physics, evaporation is advantageous over combustion because the surrounding environment, including the temperature, pressure, and atmospheric composition, can be well characterized and defined by the experimentalist [25]. Furthermore, the results of combustion studies at normal gravity are difficult to interpret due to the enhanced buoyancy effect [25], which is why microgravity conditions constitute a significant fraction of single droplet combustion investigations.

Another issue at work is the fact that droplets in realistic sprays almost certainly do not burn individually but rather evaporate to form a combustible mixture which burns as a gaseous diffusion flame (Section 2.3). Gökalp et al. [87] describe total droplet vaporization prior to reaching the flame zone as a possible scenario in actual spray combustion. From this perspective, the evaluation of droplet evaporation is merited without consideration of combustion analogies. As discussed by Sirignano [12], the increased use of heavy fuel distillates in combustor applications further enforces droplet vaporization as the rate-controlling factor. Therefore, investigations into novel areas of fuel droplet science, such as the evaluation of high turbulence across a range of small droplet sizes (as in the current study), should ideally begin with a thorough assessment of fuel evaporation characteristics.

## 2.5 Classic theories and developments

The establishment of the basic theory of a liquid droplet evaporating into a gas began in the late 1800's. Maxwell [88] and Stefan ([89] and later papers) laid the foundation by assuming that the vaporizing mass flux was solely the result of steady-state molecular diffusion [90]. Integration of the mass diffusion equation ([91] provides the full expression) assuming steady-state one-

dimensional radial diffusion leads to a vapor concentration profile that is inversely proportional to the radial coordinate. Furthermore, making the assumptions of constant vapor concentration values at both the surface and at infinite distance from the droplet, along with a constant molecular diffusion coefficient, $D_{AB}$, leads to a simple mathematical equation which equates the temporal reduction in the square of droplet diameter, $d(d^2)/dt$, to a group of constants. The properties which make up the group of constants depend on the method of derivation (see [90] and [14] for alternate approaches), but the overall interpretation is the same: the rate of reduction in droplet surface area is constant with time. This conclusion leads to the famous $d^2$ law, and is expressed in both standard and non-dimensionalized integrated forms below:

$$d^2 = d_0^2 - Kt \tag{2.1}$$

$$\left(\frac{d}{d_0}\right)^2 = 1 - K\left(\frac{t}{d_0^2}\right) \tag{2.2}$$

Equations (2.1) and (2.2) depict one of the most important and fundamental concepts in the field of droplet evaporation and burning. The evaporation rate constant, $K$, determines how quickly the surface area of a droplet recedes and is a function of both the liquid and gaseous properties as well as the temperature, pressure, and flow conditions. Since the analytical $d^2$ law was derived, studies have focused on tabulating $K$ values for different fuels, determining the degree of linearity of the temporal $d^2$ profile for various conditions, and reducing the assumptions built into the classic model. Some of the most common assumptions in basic droplet evaporation theory and modelling are listed below with a brief discussion on their validity and usefulness. The reviews by Law [83] and Faeth [55] provide highly detailed accounts of classic droplet theory assumptions.

*1) Spherical droplet*

The clear majority of theoretical investigations and numerical models assume a perfectly spherical droplet. As discussed in Section 2.2, spray combustion tends to favor the creation of small, spherical drops due to surface tension and, although not always the case, this approximation is largely justified. An assumption of sphericity reduces the governing transport equations to their simplified one-dimensional (radial) forms. Recent studies have investigated the heat transfer (e.g., [92]) and evaporative characteristics (e.g., [93]) of oblate and prolate spheroids, however, the results are not discussed here. Figure 2.1 illustrates a spherically symmetric droplet surrounded by a thin flame.

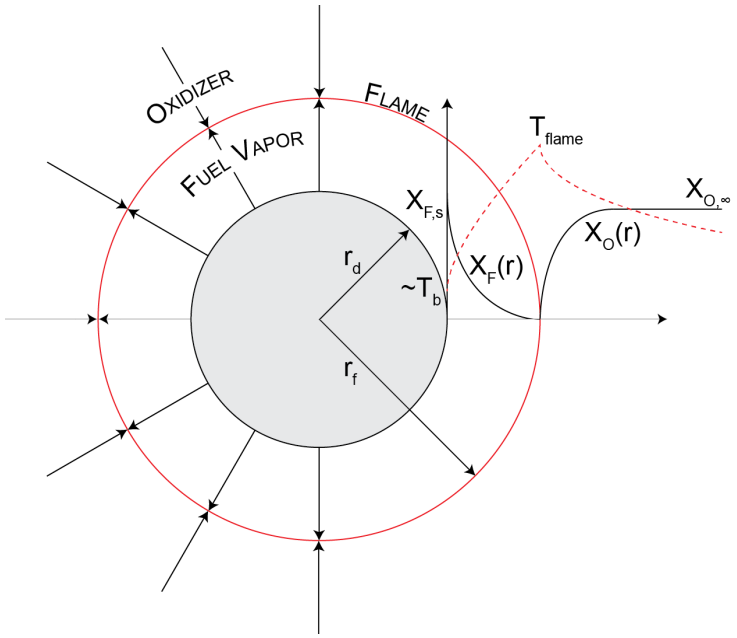


**Fig. 2.1.** Diagram of a spherical droplet burning in a stagnant environment. Classic $d^2$ theory predicts that the flame stand-off ratio, $r_f/r_d$, remains constant throughout the droplet lifetime, although this is generally not observed in actual experiments [83].

*2) Negligible buoyancy*

The classic sphero-symmetric model of droplet evaporation and combustion is purely diffusion controlled and thus does not include the effect of gravity-induced buoyancy,

which can alter heat and mass transfer rates. Failure to account for natural convection can result in significant error when attempting to match predictions to experimental results performed in normal gravity, particularly for droplet combustion (e.g., [94,95]). The high temperatures generated by combustion promote an upward convective flow which distorts the flame, resulting in axisymmetric rather than spherical burning. Due to the buoyancy effect, many researchers perform combustion studies at microgravity conditions as outlined in [96]. These investigations forgo realistic application (most combustion events take place at normal gravity) in exchange for detailed information which could not otherwise be extracted, such as soot shell formation. Experimental results at microgravity are desirable for validating numerical models, as most codes do not incorporate natural convection unless the evaluation of buoyancy-related phenomena is an explicitly stated goal (e.g., [97]). In the absence of a combustion event, free convection can affect the evaporation of droplets if the pressure and droplet size are large enough, as the Grashof number, $Gr$, varies proportional to the square and cube of those variables, respectively.

*3) Constant droplet temperature*

The assumption of constant droplet temperature is one of the most common approximations found in the literature. Calculation of the mass evaporation or burning rate requires knowledge of the surface temperature, $T_s$. The complicated process of coupling energy balances for the gas and liquid phase is immediately simplified if the droplet is assumed to maintain a steady, spatially-independent temperature. This approach can even be used at early stages of the droplet lifetime with appropriate corrective factors and forms the basis of liquid-phase heating in many computational fluid dynamics codes [79]. For a droplet

which is burning or exposed to an otherwise high-temperature ambient, the temperature is often assumed to be the droplet boiling point, $T_b$, or slightly below [42]. However, lifetime predictions for rapidly vaporizing droplets may suffer in accuracy as the transient heat-up period is generally comparable to the overall expected lifetime. Newer models may utilize different droplet temperature models which progressively increase in complexity (Sirignano [37] provides a summary of six different liquid-phase models).

*4) Quasi-steady gas phase*

Like the reduction in complexity which accompanies the approximation of a constant droplet temperature, invoking an assumption of a quasi-steady gas phase simplifies the problem dramatically. An order of magnitude comparison between the liquid and gas-phase thermal diffusivities, $\alpha$, where $\alpha_l \ll \alpha_g$, provides the justification for the quasi-steady gas phase assumption [79]. Thus, the gas-phase response to variable thermal conditions is spatially independent. The rapid reaction of the gas phase is also why a droplet with a receding boundary (i.e., evaporation) is analyzed in a conceptually similar manner to a porous sphere of fixed size supplied with fuel. If the droplet temperature is considered a constant (discussed above) or is otherwise a known function, this results in the calculation of a single reference temperature for evaluating gas-phase properties, $T_r = T_s + 1/3\,(T_\infty - T_s)$ [98,99]. Assigning the reference temperature in this manner is known as the "1/3 rule" and the replacement of $T$ with $Y$ provides a method of calculating reference mass fractions. If the surface temperature does vary, a numerical routine can use the 1/3 rule to update the reference temperature upon each iteration for recalculation of thermophysical properties [79,100]. Gas-phase unsteadiness becomes important at high pressure and temperature, and

models which incorporate transient effects can provide superior predictions when compared to quasi-steady approaches (e.g., [24]). Retaining the quasi-steady assumption while accounting for the spatial variation in temperature field near the droplet surface has also been investigated [101].

5) *Unity Lewis number*

Many early theories assumed that the Lewis number for each gas-phase species was unity, where $Le = \alpha/D_{AB}$ [102]. Assuming equivalent thermal and mass diffusivities simplifies certain aspects of the analysis and implies that second order diffusion (i.e., Soret and Dufour effects) is negligible [103]. As discussed by Faeth [55], this assumption is questionable despite the common usage in early studies. In fact, a redefinition of the Lewis number to include second order diffusion may best represent the relative importance of thermal and mass diffusion at elevated temperature [25].

6) *Negligible radiation*

Radiative exchange between droplet and surroundings is typically considered minor in comparison to convective and conductive heat transfer. The assumption of negligible radiation is evident based on the cursory treatment of radiation in many early comprehensive review papers (e.g., [14,55,104]). The small droplet size typical of most combustion sprays and incompatible radiation bands between liquid and gas help justify this simplification [55]. There are instances where radiation should be considered, such as droplets which are evaporating in a relatively cool spray region but subject to radiation from a sooty flame [104]. Tseng and Viskanta [105] outlined many of the difficulties

associated with incorporating radiative effects into spray combustion models, and investigations into the complex effect of radiation on single droplets (e.g., [102,106]) remain relatively uncommon.

Many of the above assumptions play an important role in the design, execution, and interpretation of experimental studies in addition to guiding numerical and theoretical investigations. For example, experiments should strive to generate spherical droplets for proper comparison with models, which almost universally assume a spherical shape. Natural convection and radiation can typically be relegated as minor contributors when gauging the parameters which determine the evaporation rate. The assumptions of constant droplet temperature and quasi-steady gas phase can be utilized for property evaluation when developing empirical correlations. The above examples illustrate the impact that classic theory has on the experimental aspect of droplet study.

Several landmark studies built upon the basic concepts of droplet evaporation and combustion and helped form a useful framework for understanding the important phenomena. In particular, the studies by Godsave [18] and Spalding [19] are credited with producing some of the most influential findings in the field. Although these two papers primarily discuss combustion, the results also apply to evaporation. Godsave [18] differentiated between two evaporation regimes: low temperature, in which mass diffusion chiefly controls the rate of evaporation, and high temperature, where the heat transfer from gas to liquid becomes the rate-limiting process. A corollary to this statement is that fuel volatility is important at low temperature, while enthalpy of vaporization is critical at high temperature. Furthermore, this study provided convincing experimental proof of the $d^2$ law for a variety of liquid fuels. Spalding [19] introduced the concept

of a transfer number, $B$, which represents the driving potential for mass transport. The specific form of $B$ depends on the derivation methodology (mass vs. heat balances), but for pure droplet vaporization, both approaches apply with equal validity. The primary utilization of the mass transfer number is in the purely analytical prediction of the mass evaporation or burning rate, $\dot{m}_F$ [107]:

$$\dot{m}_F = 4\pi r_l \bar{\rho}_g \bar{D}_{\mathrm{AB}} \ln(1+B) \tag{2.3}$$

A formula for predicting $K$ readily follows, with unity Lewis number often assumed (as discussed above). The chief problem with these types of equations is the uncertainty in calculating temperature- and mixture-dependent properties (such as density and mass diffusivity). The next step in model complexity involves the inclusion of variable thermophysical properties (e.g., [108]), although this, along with many other extensions to the classic theory, exceeds the scope of the present discussion.

Although early theory typically involved single droplets in a stagnant environment, researchers made important empirical discoveries regarding droplets exposed to laminar flow. In particular, the efforts of Frössling [109] and Ranz and Marshall [110,111] yielded correlations which predict laminar evaporation rate and dimensionless heat and mass transfer parameters, respectively. The Frössling correlation is expressed as follows:

$$\frac{K_l}{K_0} = 1 + C_{Fr\ddot{o}} Re_d^{\frac{1}{2}} Sc^{\frac{1}{3}} \tag{2.4}$$

Ranz-Marshall formulations feature similar dependencies on the various non-dimensional groups as Eq. (2.4). Birouk and Gökalp [13] noted that this style of correlation is still widely used and

may be modified to predict turbulent vaporization rates. The Schmidt dependence is weak, which indicates that the improvement in evaporation rate for a droplet exposed to laminar flow is relatively independent of fuel type.

This section concludes with the observation that the majority of early investigations did not attempt to quantify the effect of turbulence or initial droplet size (with some notable exceptions, e.g., [94,112]) on the evaporative behaviour of fuel droplets. Research into these areas should thus be considered relatively new.

## 2.6 The effects of temperature and pressure

Spray combustion, by its very nature, generates immense heat within a confined volume. It is therefore unsurprising that the evaporation and burning of droplets exposed to varying levels of temperature and pressure has been studied extensively via theoretical, experimental, and numerical approaches. Temperature and pressure are two of the most influential factors in determining the overall lifetime of a vaporizing droplet. This survey of the relevant literature emphasizes experimental and theoretical discoveries over numerical work. Furthermore, the presentation of evaporative findings predominates over those strictly applicable to burning. Temperature and pressure are discussed concurrently because these two parameters are highly interrelated. Additional complicating factors, such as convective flow and initial droplet size, continue to build upon the relationships discussed in this section.

The distinction between liquid and gas phases relies on the fluid remaining below its critical point. The critical point is a thermodynamic property designated by a unique pressure-temperature pair known as the critical pressure, $P_c$, and critical temperature, $T_c$. If either the

temperature or pressure exceeds their respective critical value, the fluid is said to be in a supercritical state, and the potential for the coexistence of two unique phases (liquid and gas) disappears [113]. It is therefore convenient to divide droplet studies featuring elevated temperature and pressure into either sub or supercritical regimes. The supercritical regime is of major practical interest as many modern combustion systems, including gas turbine and diesel engines, expose the injected fuel to ambiences well beyond the fuel's critical point [25]. As the critical point of the fuel is approached and exceeded, observation indicates a dramatic alteration in the evaporative droplet behaviour as compared to a droplet in a subcritical ambient. Indeed, evaporation as typically defined cannot occur in a supercritical state, since evaporation implies a directional phase change from liquid to gas, yet no such phase distinction is possible. The well-defined interface which separates liquid from gas ceases to exist. Thorough review articles by Givler and Abraham [40], Yang [114], and Bellan [25] discuss this concept along with non-ideality, gas-phase solubility, variation in thermophysical properties, and other supercritical phenomena. The temperature and pressure range in the present study ensures that the droplets remain in the subcritical regime, thus no further consideration is given to the complex issue of supercritical vaporization.

In discussing the effect of temperature, it is important to distinguish between the temperature of the gas and liquid phases. In general, the two phases will attain different values depending on the initial conditions, fuel volatility, and pressure. Although the temperature field is typically considered continuous and therefore coupled at the droplet interface, there is evidence that the temperature may be discontinuous at this point (e.g., [115–117]). Intricate details on temperature discontinuity is not important for the current discussion; however, the concept does reinforce the complexity of the physics involved with an evaporating droplet.

In most experiments, the gas-phase temperature is spatially constant and time invariant. Near an evaporating droplet, evaporative cooling reduces the temperature; some studies have directly measured this effect (e.g., [118]). If the range of ambient temperature is relatively low (below $T_b$), the evaporation rate is largely diffusion controlled. The proportionality constant which determines the rate of Fickian diffusion, $D_{AB}$, is itself proportional to $T^{3/2}$ [91]:

$$\dot{m}_f'' = -\rho D_{AB} \nabla Y_i \tag{2.5}$$

Where, for an ideal gas [119]:

$$D_{AB} = \frac{0.00266 T^{\frac{3}{2}}}{P M_{AB}^{\frac{1}{2}} \sigma_{AB}^2 \Omega_D} \tag{2.6}$$

Equations (2.5) and (2.6) indicate that increasing the ambient temperature will improve the diffusion characteristics of the gaseous phase, thereby increasing the rate of evaporation.

If the droplet(s) are at a lower initial temperature than the gas, a period of transient heat-up will occur. During this stage, the primary result of the transfer of heat from gas to liquid is the raising of the droplet sensible energy (i.e., temperature) rather than improving the vaporization at the surface [83]. Preliminary heat-up appears as an initial plateau or expansion (in the case of thermal swelling or condensation) on a temporal $d^2$ plot. Once the temperature in the droplet becomes steady, additional heat transfer serves to furnish the energy required for phase change and quasi-steady evaporation begins. For all the conditions examined in the present study, the droplet is essentially in thermal equilibrium with the gaseous phase prior to evaporation and thus no significant heat-up period is witnessed.

The steady-state surface temperature controls the mole fraction of fuel vapor available for diffusion. If thermodynamic equilibrium is assumed, the surface molar fraction, $X_{F,s}$, can be calculated via the saturation pressure of the vapor:

$$P_{sat} = X_{F,s}P = \exp\left[\frac{h_{fg}}{RT_b} - \frac{h_{fg}}{RT}\right] \tag{2.7}$$

Equation (2.7) is the Clausius-Clapeyron relation, and its derivation assumes constant enthalpy of vaporization and gas-phase ideality. Reference [119] outlines less restrictive formulations, although usage of the Clapeyron equation remains widespread. Higher surface temperatures lead to a greater mole fraction of fuel at the surface which, upon a simple conversion to mass fraction, aids the driving gradient, $\nabla Y_F$, in Eq. (2.5). If the droplet is at boiling conditions ($T_s \approx T_b$), the fraction of fuel at the surface is essentially unity. As outlined by Godsave [18], the rate-limiting process becomes the transfer of heat necessary to vaporize the liquid phase. Ghassemi et al. [20] illustrated that the evaporation rate, $K$, of a kerosene droplet increases monotonically with ambient temperatures ranging from 500 – 1000°C, regardless of pressure. As demonstrated by Chauveau et al. [77], elevated temperature helped recover $d^2$ behaviour for decane droplets evaporating in microgravity. It is important to note that the enthalpy of vaporization, $h_{fg}$, decreases as the temperature of the fuel increases; this phenomenon has important consequences for high-pressure evaporation as discussed later. As the temperature range implemented in the present study remains below the boiling point of each fuel, diffusion is considered the rate controlling mechanism.

The issue of ambient pressure as it relates to the rate of droplet evaporation or combustion is slightly more complex. Unlike temperature, which universally improves the evaporation rate, pressure can either increase or decrease the lifetime of a droplet depending on additional factors.

For low-temperature evaporation, Eq. (2.7) indicates that $X_{F,S} \propto 1/P$. Due to this relationship, high pressure can significantly reduce the vapor available for diffusion. Although $D_{AB}$ is also proportional to $1/P$, the overall term $\rho D_{AB}$ in Eq. (2.5) remains relatively constant with changes in pressure.

For high-temperature evaporation (or combustion) where $T_\infty > T_b$, the effect of pressure depends on the ambient temperature. The added complexity is a result of two competing effects which occur as the pressure rises; an increase in liquid boiling point and a decrease in enthalpy of vaporization. For a fixed ambient temperature, $T_\infty$, increasing the pressure will result in a higher attainable steady-state surface temperature, $T_s$, where $T_s \approx T_b$. If the ambient temperature is relatively low, the reduced temperature difference, $T_\infty - T_s$, is detrimental to the rate of heat transfer to the droplet and, consequently, the evaporation rate. However, if the ambient temperature is high, the reduction in temperature gradient is less consequential than the reduction in $h_{fg}$. In this case, the droplet lifetime can reduce with increasing pressure. In either scenario, the transient heat-up period as a fraction of the overall droplet lifetime will increase with pressure due to the increased fuel boiling point [120].

The temperature at which increasing pressure begins to increase the evaporation rate is obviously of significant interest. An analytical study by Chin and Lefebvre [121] placed the transition temperature between 600 and 800 K. Nomura et al. [21] discovered that the evaporation lifetime for a *n*-heptane droplet in microgravity became pressure insensitive at approximately 480 K. At higher temperatures, pressure helped reduce the droplet lifetime while temperatures below 480 K produced the opposite trend. Several numerical studies have confirmed this phenomenon and placed the transition temperature between ~600 and 1000 K depending on fuel and the degree of non-ideality and high-pressure effects (such as transient gas-phase dynamics)

incorporated into the model (e.g., [22,23,120,122]). It is important to note that the $d^2$ law is generally considered valid at elevated temperature and pressure conditions until the critical values are approached or exceeded (e.g., [20,123]), despite the extended initial heat up phase.

## 2.7 Convective flow

### 2.7.1 Outline

The majority of engineering applications for spray combustion involve some form of convective flow. For the purposes of this review, convective effects are divided into four categories: natural convection, laminar flow, forced turbulent convective flow with a strong mean component, and turbulent flow with a quasi-zero mean velocity. Most practical combustors are highly turbulent in nature, and therefore turbulence, also being the subject of this thesis, will be the focus of the following discussion. For example, an internal combustion engine produces a highly turbulent field in the cylinder due to the shear which occurs during the intake stroke and the compression/ejection of fluid in the squish band as the piston approaches the cylinder head [124]. In a gas turbine engine, the high level of radial turbulence at the compressor exit improves diffuser performance, while swirlers create strong toroidal flow reversal in the fuel injector region to recirculate the combustion products and anchor the flame [11]. However, free convection and laminar flow remain important topics for certain spray combustion applications as well as various other areas in droplet science and are thus allocated a brief assessment. Regardless, exposure to convection affects both heat and mass transfer between the droplet and the surroundings and is, therefore, a matter of great interest. This outline introduces each topic below.

Natural convection occurs because of gravity-induced buoyancy. Density variation in a gas, which commonly arises due to temperature or species gradients, will induce flow and assist in the droplet evaporation process. Although typically negligible due to the dominance of forced convection, free convection can become an important mechanism in certain situations including quiescent environments, high-pressure ambiences, and when the initial droplet size is large.

Laminar flow received much early attention by researchers due to the relative ease of investigation as compared to turbulent flow. There are, however, certain complicating factors which make laminar flow an interesting case study. For example, the thickening of the boundary layer which occurs as a result of the evaporating fuel will alter the characteristic Sherwood and Nusselt numbers of the system [125]. Additionally, there is evidence that strong mean flow can mask the effect of turbulence (e.g., [126]), indicating that laminar phenomena could significantly influence droplets which experience a large relative velocity with respect to the mean. Law [83] discussed the need to perform studies at low, intermediate, and moderately high Reynolds numbers to emulate the conditions found in actual spray systems where the droplet size and relative velocity are constantly changing due to breakup and evaporation.

The next step in flow complexity is forced convective turbulence with a significant mean velocity. Wind tunnels with inserted grids or perforated plates are most commonly used to generate this type of turbulence. The ratio of fluctuating velocity to mean velocity, $U_{rms}/\overline{U}$, is often denoted the turbulence intensity, $T.I.$, and is a standard measure of the level of turbulence in a flow. Experimental and numerical studies often feature intensities ranging up to 60%. Such studies may infer the effect of turbulence by comparing the evaporation rate with purely laminar values. This concept is questionable because it implicitly assumes that a turbulent flow with a strong mean is a superposition of purely laminar and purely turbulent flow.

From a fundamental perspective, the purest type of turbulent flow is one that is homogeneous, isotropic, and has a quasi-zero mean flow. The present study generates this type of turbulence to a close approximation. Turbulence without a strong mean flow is a desirable topic of research because it separates the effect of the chaotic and variably-sized eddies from steady convective transport effects. Many experiments have successfully generated high turbulence intensity (typically defined as the square root of turbulence kinetic energy, $q^{0.5}$, which should not be confused with the definition of intensity for turbulence with a mean flow) with low mean velocity ($\overline{U}/U_{rms} < 0.1$). Although investigations into homogeneous and isotropic turbulence with quasi-zero mean flow and its effect on droplet evaporation date back several decades (e.g., [127]), the overall body of knowledge is still relatively thin. Section 2.7.5 provides a thorough assessment of both existing zero mean flow apparatus and the results of droplet vaporization studies which utilize them.

### 2.7.2 Natural convection

In normal gravity, natural convection generates a weak to moderate buoyancy-induced flow field around a droplet. Natural convection improves heat and mass transfer rates by modifying the characteristic Nusselt or Sherwood number, respectively. In the case of heat transfer, a temperature gradient must exist near the droplet surface while a concentration gradient is necessary to promote mass transfer via natural convection. In either situation, natural convection is driven by density variation and is characterized by the Grashof number:

$$Gr = \frac{g(\rho_s - \rho_\infty)d^3}{\rho_{avg}\nu^2} \tag{2.8}$$

Gradients of both types will generally be present for any evaporating droplet, however, natural convection is far more prevalent for burning droplets. The characteristic raindrop-shaped envelope flame which surrounds a burning droplet is the result of strong natural convection and is the primary reason microgravity is an attractive option for analyzing droplet combustion (e.g., [96,128]). In the case of large porous spheres typical of early experimental efforts, the effects of natural convection may persist even with reasonably strong forced convection (e.g., [129,130]). Since the Grashof number is proportional to $d^3$, natural convection is often considered negligible for small droplets (especially when compared to the large spheres as found in [127,129]). Monaghan et al. [94] investigated the effect of natural convection on suspended droplets in the $d_0$ range of 150 – 2000 μm and determined that the burning rates of the smallest droplets are approximately 30% less than those associated with the upper range of initial size. The authors hypothesize that natural convection is dependent only upon the initial diameter and that the flame maintains a strong upward flow throughout the droplet lifetime despite the transient reduction in droplet size. The theory that burning rate depends only upon initial, and not temporal, droplet diameter is an extension of the concept developed by Isoda and Kumagai [95] who determined that the upward convective flow velocity does not change with the passage of time. Because classic theory fails to account for natural convection, Law and Williams [131] recommend including a buoyancy correction factor with empirically determined constants of the form $f_B = A_1(Gr)^{n_1}$. Improved predictions of $K$ result when calculated as $K = K_0(1 + f_B)$. Proper modification of $K_0$ for alkane fuels might require this corrective term in combination with similar groups to account for finite-rate chemistry and forced convection, depending on the flow scenario.

The Grashof number (Eq. (2.8)) is proportional to $P^2$ through the kinematic viscosity term and thus burning rates of droplets can vary markedly with pressure despite the fact that classic

theory predicts little pressure effect [14]. The lifetime of burning fuel droplets tends to drop rapidly as the critical fuel pressure is approached [132]. Natural convection may be responsible for the continued reduction of burning lifetime into the supercritical regime since results at microgravity have indicated that droplet lifetime can start to increase when $P_r$ exceeds unity (e.g., [133]). Sato et al. [86,134] reported a similar strong decrease in droplet lifetime with subcritical pressure but determined that the lifetime will start to increase after the critical pressure is exceeded, even in normal gravity. Although the development of the $d^2$ law did not include natural convection, linear $d^2$ behaviour is typically still observed at elevated pressure when natural convection contributes significantly to the droplet burning rate (e.g., [123]).

A droplet in pure evaporation does not generate the same level of density gradients as one which is surrounded by a flame. However, natural convection may still assist in the evaporation process, especially if the droplet is large or the ambient pressure is high. Although most droplet evaporation studies are performed in apparatus with large dimensions in comparison to the droplet, Langstroth et al. [65] noted that narrow cylinders retarded the development of natural convection boundary layers and consequently reduced the evaporation rate of the droplet. Matlosz et al. [81] investigated the evaporation of large droplets (720 – 1780 μm) exposed to extreme pressure (up to 102 atm) in normal gravity. The ambient temperature is also elevated, which makes it difficult to discern the effects of natural convection and heat transfer. However, a sequence of pictures of an evaporating droplet plainly shows a downward flow of vapor which, the authors postulate, is the result of density variation between the cooler evaporating fuel and the hotter ambient. Sato et al. [134] compared the evaporation constants of heptane fuel at 10 bar for micro and normal gravity throughout a range of sub and supercritical temperatures. Their results indicate no clear trend with temperature; that is, although $K$ is universally higher in normal gravity for identical conditions, it

is not obvious if increasing the ambient temperature increases or decreases the disparity in evaporation rate between normal and microgravity. From the perspective of natural convection, a droplet evaporating in a hot ambience is quite different than a droplet surrounded by a flame.

The success of predictive models can depend upon the inclusion of natural convection, which complicates the numerical codes as the problem is no longer one-dimensional. Axisymmetric (e.g., [97]) or three-dimensional (e.g., [22]) approaches are necessary when approaching the problem from first principles. Several studies (e.g., [135,136]) have concluded that natural convection is particularly important when predicting the evaporation of multicomponent droplets. Although microgravity should, in theory, represent the ideal $d^2$ law scenario, a recent experimental study by Chauveau et al. [77] determined that the lack of natural convection experienced in reduced gravity is actually detrimental to the linear temporal variation of $d^2$. The authors conclude that excessive vapor build-up can occur in the absence of buoyant forces which results in a distinct two-stage $d^2$ vs. $t$ profile. While both stages are individually linear, the second stage is much flatter than the first. The evaporating droplet recovers fully linear $d^2$ behaviour in normal gravity or microgravity of a sufficiently hot ambience (~900 K). The elevated temperature increases vapor diffusion to the point where build-up is no longer a concern.

### 2.7.3 Forced laminar convection

The effect of forced laminar convective flow on droplet evaporation and combustion is a rich topic with many variations. While natural convection (Section 2.7.2) and turbulence (Sections 2.7.4 and 2.7.5) are subjects with direct application to the present study, this brief discussion on laminar flow is provided for continuity and acts as a transition between the topics involving stagnant and

turbulent environments. Furthermore, investigations into turbulent droplet evaporation often use laminar results as a base case or reference solution.

Laminar flow over a droplet promotes the development of thermal and concentration boundary layers along the surface. The thickness, and thus effectiveness, of these boundary layers vary circumferentially, and the problem of evaporation is no longer spherically symmetric but rather axisymmetric which complicates mathematical modelling significantly (e.g., [137]). Early empirical correlations such as those developed by Frössling [109] and Ranz and Marshall [110,111] predicted normalized evaporation rates, $K_l/K_0$, or heat and mass transfer parameters, $Nu$ and $Sh$, based on $CRe^m Pr^n$ or $CRe^m Sc^n$. For droplet combustion, where heat transfer limits the overall vaporization rate, it may suffice to simplify the correction factor to $CRe^{1/2}$ (e.g., [129,131]). While laminar convection increases the evaporation rate of a fuel droplet, there exists a practical maximum Reynolds number due to the fragmentation of large droplets [83]. Thus, large droplets artificially anchored in place and exposed to highly convective fields may not be realistic from an application perspective. If the droplet is burning, the flame shape will be distorted by the flow. The extent of flame shape alteration will depend on the strength of the mean flow as illustrated in Fig. 2.2. The transition from envelope to wake flame (Fig. 2.2 b) to c)) can result in a reduced burning rate, as the droplet is no longer completely surrounded by the flame, which itself acts as the heat source for vaporization. Surprisingly, $d^2$ behaviour may remain throughout the range of flame modes (e.g., [84]). Indeed, convective flow studies often report $d^2$ evaporation (e.g., [138,139]) despite the classic empirical correlations, discussed above, predicting linear temporal variation with $d^{3/2}$ [37].

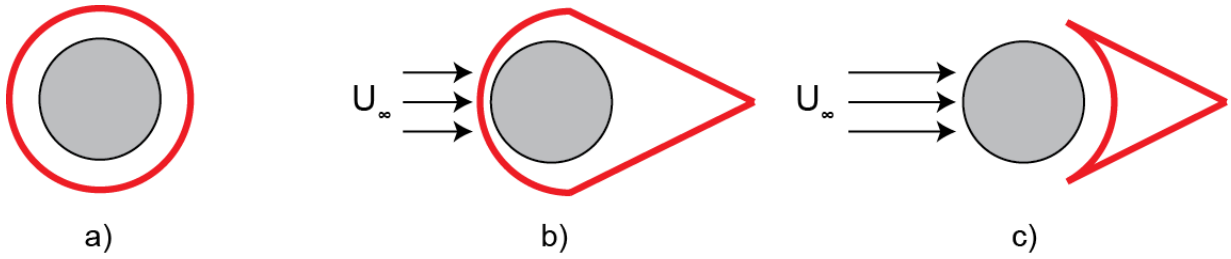


**Fig. 2.2.** The conceptual effect of laminar flow over a burning isolated droplet. The droplet burning in a) exhibits spherically symmetric burning, typical of stagnant conditions and no buoyancy. The addition of a mean horizontal flow forces the development of a tailed flame in b). If the flow is strong enough, as depicted in c), the envelope flame will transition to a wake. Further increases to the mean velocity will eventually result in the extinction of flame.

While empirical correlations continue to find uses (even beyond their original intent, as correlations developed for laminar flow have been extended to account for turbulence [13]), understanding of the complex boundary layer phenomena requires a more detailed approach. For example, the popular model by Abramzon and Sirignano [125] makes use of film theory, which models the convective resistance surrounding a droplet via a thin shell of constant thickness, to calculate accurate Sherwood and Nusselt numbers. The unique aspect of this model stems from the inclusion of the Stefan, or radial blowing, velocity which arises from the droplet evaporation. The Stefan flow thickens the laminar boundary layer and thus reduces $Nu$ and $Sh$ as compared to a non-vaporizing droplet. The Abramzon and Sirignano model [125] yields significantly improved predictions over simpler models while remaining easy to implement [140,141]. Studies which analyze free-falling droplets (e.g., [27,63]) must also consider the potential effect of laminar flow, as a relative velocity will exist between the droplet and the air. Due to drag forces and the steady reduction in droplet size, the relative velocity will remain transient throughout the droplet lifetime.

The viscous boundary layer at the surface of the droplet modifies not only the gas-phase transport properties but also liquid-phase convection. If the Reynolds number is sufficiently high, the shearing force at the surface can induce axisymmetric quasi-steady liquid circulation (e.g.,

[142,143]). Although the enhanced liquid circulation, including a pair of Hill's vortices near the upper and lower droplet surfaces, appears to endorse the concept of a uniform droplet temperature, the temperature variation in each vortex is relatively independent of the vortex strength [103]. Variation in surface tension forces can also encourage internal circulation through a phenomenon known as the Marangoni effect. This effect arises when temperature variation is present on the droplet surface, and although convective flow is not the only cause (conduction through support fibers, for example, can generate Marangoni flows [144]), a strong gaseous flow over a droplet will enhance the effect due to its inherent axisymmetric nature (e.g., [145]).

### 2.7.4 Forced convective turbulent flow

The following discussion investigates the current state of knowledge regarding the evaporation of a single droplet exposed to a turbulent flow with a significant mean component. Although droplet-turbulence interactions extend well beyond the modification of heat and mass transport rates for a single droplet (for example, the dispersion of droplets by turbulence and the modification of turbulence properties by the droplets themselves [7]), such topics are beyond the scope of the present report. The effect of turbulence on droplet arrays or sprays (e.g., [7,55,146–151]) is likewise avoided. To the author's knowledge, most studies involving convective turbulent combustion, as opposed to pure evaporation, are performed on sprays or arrays rather than single suspended droplets.

Early studies into the effect of turbulence on single droplets generally utilized a mean flow to support the turbulent structures. In many cases, a porous sphere was used in place of an evaporating droplet as discussed in [13]. Attempts to develop correlations regarding turbulent heat and mass transfer typically revolved around modifying a Frössling or Ranz-Marshall relation for

laminar flow. An example of a generic Sherwood number correlation adapted for turbulent flow is provided below along with a specific Nusselt number correlation developed by Yearling and Gould [152] for illustrative purposes. Discrepancies in the determination of the various coefficients were commonplace amongst early turbulent investigations.

$$Sh = A + BRe_d^{\frac{1}{2}} Sc^{\frac{1}{3}} (C_T)^n \tag{2.9}$$

$$Nu_f \left(1 + B_{M,f}\right)^{0.7} = 2 + 0.584 Re_M^{\frac{1}{2}} Pr_f^{\frac{1}{3}} \left[1 + 0.07 \left(\frac{U_{rms}}{\bar{U}} \times 100\right)^{0.843}\right] \tag{2.10}$$

The basic interpretation of Eq. (2.9) is that the Reynolds number accounts for the mean flow velocity while $C_T$, itself a function of $Re_d$, also contains the turbulence intensity, $T.I. = U_{rms}/\bar{U}$. Most reports agreed upon the concept that heat and mass transfer increases with intensity (e.g., [153]), and How [112] concluded that intensity, rather than integral length scale, controls the rate of gaseous phase mixing and is thus responsible for the increase in turbulent flame speed over the laminar value. Yet, as discussed by Birouk and Gökalp [13], other studies reported little influence of turbulence on evaporation rates if the integral length scale exceeded the size of the droplet. Because the integral scale is generally much larger than droplets in actual combustion systems, the issue of length scale, intensity, and their relation to droplet vaporization became a topic of great interest.

Gökalp et al. [87] recognized that turbulence, consisting of a continuous spectrum of length and time scales, may influence evaporation rates through the interaction between the smaller eddies and comparably-sized droplets regardless of the integral length scale. Their experimental study analyzed the evaporation of heptane and decane droplets at room temperature and pressure

in the presence of moderate intensity (up to 44%) isotropic turbulence. Despite the integral length scale being several times larger than the droplets, decane evaporation rates were found to increase with intensity at every mean velocity. The more volatile heptane fuel, on the other hand, was not affected by turbulence. This study is an example of one which defined an effective turbulent evaporation rate, $K_t'$, based on the observed difference in $K$ between turbulent and laminar flows at the same mean velocity.

$$K_t' = \frac{K_t - K_l}{K_0} \tag{2.11}$$

Although the ratio $L/d_0$ is noted to have a minor influence on evaporation rate, this ratio cannot account for the discrepancy in behaviour between heptane and decane. To address this issue, Gökalp et al. [87] introduced a vaporization Damköhler number, $Da_v$, which is defined as the ratio of characteristic turbulent flow time to vaporization time. The calculation of the former is based on energy cascade considerations and eddies equivalent in size to the droplet diameter, while classic quasi-steady theory determines the latter. The authors assert that only small values of $Da_v$ have corresponding increases in $K_t'$, hence the ineffectiveness of turbulence for a heptane droplet since heptane has a very rapid vaporization time scale. Furthermore, $K_t'$ will not be affected by eddies with scales greater than the droplet diameter.

Hiromitsu and Kawaguchi [154] performed a similar study for the purposes of evaluating the Damköhler method at elevated temperatures (323 – 423 K). Despite low turbulence intensities (up to 14%), the authors report that $K_t'$ increases for all materials (paraffins, water, and ethanol) with increasing intensity. The authors state that it is the action of the Kolmogorov scale eddies, which reduce in size with increasing intensity, that destroy the vapor layer around the droplet and

thus promote increased diffusion. Higher temperatures are shown to depress the gains in $K_t{}'$ at any given intensity. Finally, it is suggested that the Damköhler number as introduced by Gökalp et al. [87] is inappropriate when correlating evaporation rates at high temperature. However, the reasoning provided to support this claim, namely, that temperature variations do not alter $Da_v$, is questionable.

Eckartsberg and Kapat [155] further advanced the theory of length scale ratio by hypothesizing that the impact of turbulence on an evaporating droplet is due to the total energy content of the eddies which are smaller than the droplet. Furthermore, they state that eddies smaller than the Taylor microscale are not energetic enough to interact with the droplet or vapor boundary layer which stands in contrast to the conclusion of Hiromitsu and Kawaguchi [154]. The maximum turbulence intensity was only 14% although several other parameters were varied including free stream velocity, temperature, and droplet size.

Wu et al. [16,29] followed up these investigations with an experimental study on five paraffin fuels exposed to turbulence intensities as high as 60%. Despite similar conditions to Gökalp et al. [87] including comparable $L/d$ ratios, initial droplet size, and standard pressure and temperature, Wu et al. [16] show a clear improvement to the evaporation rate of heptane with increasing turbulence intensity. Gökalp et al. [87] found no such relationship, although both studies agree that the turbulence effect is more profound for decane. In fact, the only clear difference between the two studies is the much higher mean velocities used by Gökalp et al. [87]. The discrepancy in velocities suggests that the mean flow can perhaps mask the effects of turbulence, especially when the fluctuations are relatively weak. Wu et al. [16] conclude that, in general, the effectiveness of turbulence decreases as $L/d_0$ increases, although the authors provide counter-examples to this behaviour. They also successfully correlated the turbulent evaporation of heptane

and decane [16], as well as pentane, hexane, and octane [29] over a wide range of Reynolds number with a single Damköhler expression. Turbulence is shown to be ineffective as $Da_v$ exceeds 0.1. Because the temperature remained at room value, the success of the Damköhler correlation does not necessarily serve as a rebuttal to the work of Hiromitsu and Kawaguchi [154]. However, the vaporization time scale used to calculate $Da_v$ makes use of a modified theoretical film thickness, $\delta_M$, which, although incorporated into the highly successful Abramzon and Sirignano model for laminar evaporation [125], is not inherently applicable to turbulent flows. In fact, the very predictive success of the Damköhler correlation when defined in this manner could be used as an indictment of the entire approach of analyzing turbulence in tandem with a significant mean flow.

In perhaps the most recent experimental study of similar motivation and technique, Marti et al. [126] conclude what is evident but not necessarily emphasized in previous investigations: the mean convective flow dominates over the turbulence intensity. This study generated high Reynolds numbers due to the combination of large heptane droplets and significant mean velocities and varied the intensity at a given mean velocity via active grids. The highest mean velocity featured the lowest impact of turbulent fluctuations from the perspective of droplet evaporation. The droplets generated here exceeded 1000 μm in initial diameter, as have all the aforementioned studies.

Numerical studies offer the ability to analyze droplets approaching the small sizes that exist in a realistic spray combustion distribution, although early investigations were quite rare (e.g., [156,157]). The most relevant results include the findings from a series of papers by Abou Al-Sood and Birouk [158–163]. Aside from the ability to analyze droplets of 100-μm initial diameter, these numerical investigations also examined the impact of extreme temperature and pressure (up to 1350 K and 100 bar, respectively) and high freestream turbulence intensities (up to 60%).

However, only the findings at moderate temperature and pressure are considered pertinent to the current discussion. Calculable quantities include the temperature and vapor gradient at the surface of the droplet; precise measurements of such variables are not feasible with most experimental setups. The Damköhler correlation as developed by Gökalp et al. [87] and implemented by Wu et al. [16,29] was shown to be invalid at elevated temperatures which concurs with the conclusion of Hiromitsu and Kawaguchi [154]. In all analyzed cases, the improvement in normalized evaporation rate with turbulence is most noticeable in the lower range of intensities (0 – 20%) [158,160]. Beyond this range, $K/K_l$ will continue to increase but at a significantly reduced rate. Higher ambient temperatures weaken the effect of turbulence. While the steady-state surface temperature is a function of turbulence intensity when the ambient temperature is high, simulations at room temperature indicate that turbulence in the range of 0 – 60% intensity has essentially no impact on the steady surface temperature [159]. However, the steady state is reached quicker for higher turbulence intensities when the initial droplet temperature is significantly lower than the ambient. In a size comparison between a 100-μm and 1500-μm droplet, Abou Al-Sood and Birouk [162] demonstrated much higher evaporation rates for the initially larger droplet. The lower calculated surface temperature of the larger droplet improves the driving gradient for heat transfer, $T_\infty - T_s$, and ultimately increases the evaporation rate. However, when the ambient temperature is relatively low (~300 K), the average evaporation rate, $K$, for all conditions trends towards the same value regardless of initial size or turbulence intensity which corroborates the finding that droplet surface temperature is unaffected by turbulence in low ambient temperatures.

### 2.7.5 Turbulence without mean flow

#### *2.7.5.1 Summary of chambers designed for zero mean flow*

The study of turbulent droplet evaporation in a quasi-zero mean flow is an attractive alternative to the traditional wind tunnel experiment or numerical simulation with a strong mean velocity component. This type of flow represents the effect of pure turbulent fluctuations and is thus desirable from the perspective of fundamental understanding. Furthermore, droplets in actual combustion systems may attain the bulk flow velocity in a near-instantaneous fashion (e.g., [87]) and, if the integral length scale is significantly larger than the droplet, the smaller scale eddies become responsible for the modification of the droplet's evaporation characteristics. To the author's knowledge, study of the effect of low mean flow turbulence on droplet evaporation lies almost exclusively in the domain of experimental work. Therefore, a brief timeline of the development of such test rigs is warranted. This section prioritizes fan-stirred chambers designed to study droplet evaporation, although specialized setups in other fields are discussed if relevant. The following summary neglects vessels which use alternative methods to drive the flow such as jets, speakers, or oscillating grids (e.g., [164–168]) as they are typically not utilized for studying droplet evaporation.

The development of a specialized test apparatus capable of generating zero mean flow with high levels of turbulent fluctuations is intensive, hence the relative scarcity of such rigs as compared to wind tunnels with grid generated turbulence. An early fan-stirred device was developed by Ohta et al. [127] to study the effect of turbulence on droplet evaporation and combustion. The vertical cylindrical chamber used an interchangeable mesh liner and four fans arranged at 90° intervals around the horizontal midplane. The integral length scale, although modifiable by the mesh type (by design), was not affected by the fan speed. Later studies would

confirm this important finding. The authors state that the generated field was isotropic although no data is provided to substantiate this claim. There is no discussion of homogeneity, and such omissions of detailed flow field characteristics were typical of early efforts [13]. The absence of disclosure is understandable given the relative infancy of the work (in addition to primitive measurement equipment) and helps explain the lack of agreement amongst such investigations [13].

Recognizing the need for detailed flow field description, Fansler and Groff [169] provided isotropy and homogeneity data on their cylindrically symmetric quad-fan chamber (similar designs may be found in the works of Abdel-Gayed et al. [170], Semenov [171], and Kwon et al. [172]). They state that the chamber intensity is isotropic to within 12% and homogeneous to within 20%, although the authors did not explicitly provide precise calculation of these values. Their findings also confirm a linear relationship between fan speed and turbulence intensity, a result which various vessels and geometries have repeatedly proven and is now factually accepted. Leisenheimer and Leuckel [173] determined that the geometric influence on the integral length scale extended only to the chamber dimensions; however, a recent study illustrated that impeller geometry, including blade count and blade angle, can significantly impact the integral length scale [174].

In an effort to generate increased levels of isotropy and homogeneity, subsequent setups added additional fans to the corners of cubic chambers, such as the one developed by Birouk et al. [175] and used in several additional studies [28,176,177]. This chamber maintained isotropy and homogeneity ratios bounded by 0.9 and 1.1 for all fan speeds (up to 3000 RPM) within a spherical region of approximately 40 mm in diameter. The criteria of $\pm$ 10% anisotropy or inhomogeneity

(ratio measures $U_{rms}/V_{rms}$ and $q^{0.5}/q_{avg}^{0.5}$ bounded by 0.9 and 1.1) appears to be the de facto standard for a high-quality turbulent flow field.

Modern chambers tend to be spherical instead of cubic, as both volume and symmetry are important parameters for generating homogeneous and isotropic turbulence with large $Re_\lambda$ [178]. However, the literature reveals the continued development and usage of cubic-style chambers (e.g., [179–181]). Applications typically involve high pressure and temperature fuel droplet evaporation or combustion (e.g., [30,31,182]) and flame speed analysis (e.g., [183]). Researchers have implemented as many as 20 symmetrically mounted fans in an attempt to obtain $Re_\lambda$ values close to 400 [178]. Galmiche et al. [184] performed a study to compare the various popular methods of analyzing flow fields, including high- and low-resolution Particle Image Velocimetry (PIV), Laser Doppler Velocimetry (LDV), and time-resolved PIV. Their conclusion is that PIV can yield almost identical results to LDV in terms of single-point statistical accuracy, with the obvious inherent benefit of capturing the entire flow field in a single trial run. Of particular significance is the fact that many modern experiments are designed to vary a large number of factors including turbulence intensity, length scales, temperature, and pressure. In general, the integral length scale and turbulence intensity is independent of temperature and pressure.

*2.7.5.2 Results of zero mean flow studies*

In a 1983 review paper, Sirignano reflected on the current state of knowledge regarding the interaction between turbulent eddies and fuel droplets by designating the area as virgin territory for researchers [12]. While the investigations outlined in Section 2.7.4 have contributed significantly to the understanding of how droplets evaporate in turbulence, fundamental advances are perhaps best achieved by utilizing flows with a negligible mean component. There are two main reasons why such studies are particularly impactful. First, from a theoretical perspective,

analyzing flows with a quasi-zero mean velocity essentially segregates the effect of bulk convection from that of the turbulence. Separation represents an important first step in isolating the physics of pure turbulent fluctuations. Second, a droplet exposed to high-intensity turbulence with negligible mean flow is a scenario rooted in realistic application. Consider, for example, that an internal combustion engine can generate relative turbulence intensity ($U_{rms}/\overline{U}$) spikes over unity (e.g., [185]). Traditional grid-induced turbulence, discussed in Section 2.7.4, is typically incapable of generating this level of relative intensity. The turbulence kinetic energy of an engine can easily exceed 50 $m^2/s^2$ (e.g., [186]), and the necessary mean velocity required in a wind tunnel to realize this level of energy would surely induce droplet anchoring and imaging problems, in addition to the issue of the mean flow potentially dominating the fluctuations. Furthermore, combustor flows which feature a significant mean component may accelerate a droplet such that the drop reaches a state of zero relative velocity almost instantaneously. The majority of the droplet lifetime would then exist in a regime in which the droplet only interacts with the characteristic small-scale eddies of the flow field. It is perhaps surprising, then, that the number of studies in the literature concerning turbulent droplet evaporation in a quasi-zero mean velocity field is minimal. As discussed by Birouk and Gökalp [13], the experimental facilities required for creating such flows are difficult to develop and rather specialized. Despite the reasonable number of chambers which have, either recently or in the distant past, been developed with intent to generate high-intensity turbulence with low mean velocity (see Section 2.7.5.1), researchers have used very few of them in droplet evaporation or combustion research. A careful review of the literature reveals that until the 1975 study by Ohta et al. [127], and in the time between that study and the beginning of a series of investigations by Birouk and collaborators in 1996 [175], very little progress was made in this area. Due to the manageable number of papers in the literature, combined with the

relevance to the current work, all studies which focus on the vaporization characteristics of a droplet exposed to turbulence with a negligible mean flow are discussed, including those that analyze droplet combustion.

As discussed in Section 2.7.5.1, Ohta et al. [127] developed a cylindrical fan-stirred chamber with interchangeable mesh liners to study turbulence in the absence of a mean flow. The reported results on droplet evaporation at room temperature and standard pressure were preliminary, although the authors clearly showed that the evaporation rate of a droplet increased quasi-linearly with turbulence intensity. The integral length scale, although not explicitly provided in relation to the plotted results, was similar in magnitude to the initial droplet diameter (where $d_0$ = 1000 μm). The authors did not discuss information about $d^2$ adherence. The apparatus was also used to study the burning rates of porous fuel-fed spheres. A flame which is spherically symmetric, in a time-averaged sense, replaces the classic "tailed" flame which normally appears due to natural or forced laminar convection. The rate of combustion increased with turbulence intensity due to improved gas-phase mixing, however, if the intensity exceeded a certain threshold, the burning rate trend was reversed due to excessive heat loss. The intensity value corresponding to the burning rate maxima was therefore expected to increase with ambient temperature due to the reduced heat loss.

Birouk et al. [175] analyzed the evaporation characteristics of five different alkane fuel droplets suspended at the center of a fan-stirred cube. This design doubled the fan count featured in the Ohta et al. [127] chamber, and the authors report turbulence characterization in great detail. All tested fuels adhered to the $d^2$ law and saw significant improvement in droplet evaporation rate with turbulence intensity. Fuel volatility influences the improvement in $K$, where heavier fuels such as nonane and decane were the primary beneficiaries of increased turbulence intensity.

Furthermore, all fuels appeared to approach a plateau at the highest turbulence intensity (~1.2 m/s). The average integral length scale of 8.6 mm is substantially larger than the initial droplet size, indicating that rough equivalence of droplet size and large-scale eddies is not a requirement for turbulent evaporation enhancement.

Subsequent studies on mono and bicomponent droplet combustion [176] and evaporation [28] continued to utilize the chamber developed by Birouk et al. [175]. The combustion studies at room conditions carried out by Birouk et al. [176] largely refute the findings of Ohta et al. [127]. Birouk et al. [176] determined that the primary role of increasing turbulence intensity is to promote flame extinction rather than improve the burning rate. Extinction was found to occur at relatively low turbulence intensity values (0.3 – 0.4 m/s) for a variety of alkane fuels, and the increasing intensity prior to extinction resulted in marginal improvement to $K$. Burning bicomponent 50% heptane/50% decane droplets maintain the $d^2$ law. The least volatile component controls the burning rate while the most volatile fuel in the mixture influences the point of extinction. Evaporation of the same mixture at room conditions resulted in a distinct two-stage $d^2$ evaporation sequence [28]. The first stage is dominated by the evaporation and depletion of the highly volatile component while the second stage exhibits a $K$ almost identical to that of the less volatile fuel. The effect of turbulence clearly depends a great deal upon whether the droplet is burning or evaporating. This study also generated turbulent evaporation data on monocomponent droplets which led to the following correlation:

$$\frac{K}{K_0} = 1 + 0.02 Re_{t,d_0}^{\frac{2}{3}} Sc^2 \tag{2.12}$$

Unlike the correlations presented in Section 2.7.4, Eq. (2.12) does not attempt to modify a Frössling expression (which features $Re^{1/2}$ and $Sc^{1/3}$ functionality), nor does it contain any reference to a laminar flow evaporation rate, $K_l$. As discussed by Birouk and Gökalp [13], the physical interpretation of the 2/3 exponent of the Reynolds number is elusive although previous correlation attempts have included a similar term. The increased dependence on the Schmidt number is understandable since heavier fuels (which typically have large Schmidt numbers due to poor mass diffusivity coefficients) are strongly impacted by turbulence.

Birouk and Gökalp [13] also proposed a new Damköhler correlation based on the time scales of turbulent and molecular diffusion using previously gathered data. Although the proposed correlation successfully predicts the turbulent droplet evaporation rate of several alkane fuels, close inspection of the formulation reveals that there is no term to account for the effect of droplet size. This deficiency is not important for similarly-sized droplets. However, even the minor experimental variation in initial droplet size is visible in the plotted data. A review of the literature concerning the effect of droplet size is in Section 2.8.

Birouk and Fabbro [30,187] developed a large spherical fan-stirred chamber to enable evaporation and combustion tests at high pressure and temperature. This chamber, utilized in the present report, generates a higher integral length scale (~22 mm) and greater turbulence intensity than the previous cubic apparatus. Evaporation tests on heptane in ambiences of up to 21 bar revealed that the evaporation rate rapidly decreases with pressure until approximately 10 bar. Beyond this pressure, $K$ remains relatively constant. Plots of $K$ vs. $P$ at several turbulence intensities have the same qualitative shape with the curves at higher intensities shifted to higher $K$. The observation that the level of turbulence has no apparent effect on this behaviour is attributed to the severely reduced temperature difference, $T_\infty - T_s$, which accompanies high-pressure

evaporation. The authors theorized that turbulence is unable to overcome the poor driving gradient for heat transfer. On the other hand, the effectiveness of turbulence, $K/K_0$, increases with pressure. The eventual plateau of $K$ vs. $q^{0.5}$ (which occurs regardless of pressure) justifies the theory that turbulence can only improve the existing vapor gradient near the droplet surface. Further tests at elevated temperature [31] found that temperature has the opposite effect as pressure; specifically, while the absolute value of $K$ always increases with temperature, the effectiveness of turbulence, $K/K_0$, decreases. The addition of pressure and temperature force the expansion of Eq. (2.12) in the following manner:

$$\frac{K}{K_0} = 1 + 0.026 Re_{t,d_0}^{\frac{2}{3}} Sc^2 \left(\frac{P}{P_0}\right)^{-0.19} \left(\frac{T}{T_0}\right)^{-3.0} \tag{2.13}$$

Researchers have also used the spherical chamber to conduct combustion studies. Birouk and Toth [182,188] investigated the turbulent burning characteristics of alkane and biodiesel fuel droplets at elevated pressure. Droplets adhered to the $d^2$ law for all test conditions. The indifference of $K$ with respect to turbulence intensity as noted by Birouk et al. [176] is confirmed at atmospheric pressure, regardless of ambient temperature. At elevated pressure, $K$ begins to increase with $q^{0.5}$. Interestingly, at a fixed value of intensity, $K$ increases with pressure. The increase is more dramatic for low values of $q^{0.5}$ and is the opposite of the evaporative relationship between $K$ and $P$. Continuing to increase the turbulence intensity will eventually result in a peak, followed by a subsequent reduction, in the burning rate. This finding agrees with Ohta et al. [127]. The precise value of $q^{0.5}$ which corresponds to the peak is a function of pressure, where higher pressure has less tolerance for increasing intensity before the burning rate begins to drop. The reduction in $K$ that results from excessive intensity can be so dramatic that the turbulent burning

rate may fall below the corresponding quiescent value, $K_0$. The sub-$K_0$ burning rate indicates that the turbulence effect has negatively countered the impact of natural convection, which is significant for large burning droplets. In a further illustration of the contrast between evaporation and burning, heptane experienced higher peak turbulent burning rates than decane. Excessive heat loss from the flame is considered responsible for the eventual reduction in burning rate with turbulence intensity, and this phenomenon will eventually result in a transition to pure evaporation as the flame becomes unstable and disappears.

In all reviewed studies involving isolated droplet evaporation or combustion, the initial droplet size is on the order of 1000 μm. Since actual spray combustion generates droplets in the range of 10 – 100 μm [42], the oft-examined size exceeds realistic application by one to two orders of magnitude. Furthermore, variation in the examined sizes was either non-existent, the result of the finite precision of experimental repetition, or considered unimportant and neglected in the analysis. To the authors knowledge, the only experimental investigation into the effect of zero mean turbulence and initial droplet size (490 – 850 μm) on evaporation is the preliminary report by Birouk and Toews [33] at room temperature and pressure. The authors discovered that evaporation rates of heptane and decane improve significantly as the initial diameter increases when turbulence is present. Stagnant ambiences did not feature any observable size effect. Further details regarding the effect of droplet size on evaporation rates are deferred to Section 2.8. Table 2.1 provides a summary of the key parameters in the above studies.

**Table 2.1**
Experimental parameters of turbulent droplet studies with negligible mean flow.

| Study | Type | Fuel | $P_\infty$ [bar] | $T_\infty$ [K] | $q^{0.5}$ [m/s] | $L$ [mm] | $d_0$ [μm] | Notes |
|---|---|---|---|---|---|---|---|---|
| Ohta et al. [127] | Evap. | ? | 1 | 293.5 | 0.3 – 1.2 | 1.9, 3.1 | 1000 | *unknown method of calculating intensity, no details on suspension* |
| Ohta et al. [127] | Comb. | hexane | 1 | 293.5 | 0.1 – 1.7 | 1.9, 3.1 | 3200 – 9200 | *porous spheres* |
| Birouk et al. [175] | Evap. | hexane – decane | 1 | 298 | 0.3 – 1.2 | 8.6 | 1500 | *quartz vertical suspending fiber, $d_f^*$ = 200 μm* |
| Birouk et al. [176] | Comb. | hexane – decane, heptane/decane | 1 | 298 | 0.25 – 0.4 | 8.6 | 1300 | *quartz vertical suspending fiber, $d_f$ = 200 μm* |
| Birouk and Gökalp [28] | Evap. | hexane – decane, heptane/decane | 1 | 298 | 0.3 – 1.2 | 8.6 | 1500 | *quartz vertical suspending fiber, $d_f$ = 200 μm* |
| Birouk and Fabbro [30] | Evap. | heptane | 1 – 21 | 298 | 0.4 – 4.62 | 22 | 1000 | *quartz vertical suspending fiber, $d_f$ = 150 – 290 μm, $d_n^\dagger$ = 400 μm* |
| Birouk [31] | Evap. | heptane, decane | 1 – 16 | 298 – 423 | 0.31 – 3.1 | 22 | 1000 | *quartz vertical suspending fiber, $d_f$ = 150 – 290 μm, $d_n$ = 400 μm* |
| Birouk and Toth [182] | Comb. | heptane, decane | 1 – 11 | 295 – 353 | 0.13 – 1.12 | 22 | 1000 – 1500 | *quartz vertical suspending fiber, $d_f$ = 150 – 290 μm, $d_n$ = 400 μm* |
| Birouk and Toth [188] | Evap. | soybean biodiesel | 1 – 16 | 473 | 0.31 – 1.86 | 22 | 1000 – 1500 | *quartz vertical suspending fiber, $d_f$ = 150 – 290 μm, $d_n$ = 400 μm* |
| Birouk and Toth [188] | Comb. | soybean biodiesel | 1 – 6 | 295 – 423 | 0.31 – 1.30 | 22 | 1000 – 1500 | *quartz vertical suspending fiber, $d_f$ = 150 – 290 μm, $d_n$ = 400 μm* |
| Birouk and Toews [33] | Evap. | heptane, decane | 1 | 298 | 0.31 – 1.86 | 22 | 490 – 850 | *SiC 90° cross-fiber, $d_f$ = 14 μm* |

*$^*d_f$ = diameter of the suspending fiber*
*$^\dagger d_n$ = diameter of the fiber nodule*

## 2.8 Initial droplet size

The effect of initial droplet size on fuel evaporation and combustion is a matter of great practical relevance. Investigations may proceed in one of two general directions: the evaluation of isolated droplets (or small structured arrays) or the determination of size characteristics in a spray. The former, being the subject of the present study, is emphasized in this section while the latter provides insight into the impact of droplet size distribution in actual spray combustion systems. For instance, Chiu et al. [52] identified four modes of droplet spray (or cloud) combustion: external sheath, external group, internal group, and single droplet. The primary determination of burning mode depends on a parameter called the group combustion number, $G$, which is proportional to the droplet density and size [8]. Furthermore, the radial distribution of size within a cloud can affect the burning rate, where a radially decreasing droplet size distribution results in faster burning [8]. The Sauter Mean Diameter (SMD) can influence the axial development of emissions (such as unburned hydrocarbons, carbon monoxide, and oxides of nitrogen) in a combusting spray (e.g., [51,189]). Flame speed is typically enhanced by reducing the SMD (e.g., [146,190]) and is particularly affected when the mass fraction of vaporized fuel to total fuel is low. Smaller droplet distribution, while generally strived for in practice, is not necessarily ideal from all combustion-related perspectives. For example, Datta and Som [191] numerically investigated a range of initial mean diameters (34 to 96 μm) and discovered that larger SMD resulted in improved turbine inlet pattern factor, while an intermediate SMD maximized combustion efficiency. Wang et al. [32] performed a Direct Numerical Simulation (DNS) study on a turbulent spray with smaller initial droplet sizes (7, 10, and 12 μm) and found that the interacting droplets still obey the $d^2$ law. Additionally, a transition from non-premixed to premixed combustion occurs earlier at high levels

of turbulence intensity and lower droplet diameter. The effect of initial droplet size is obviously of great importance in predicting the characteristics of spray combustion.

Investigations into the size effect of single droplets are split fairly evenly between combustion and evaporation. Combustion is discussed first from the perspective of droplet vaporization rate; arrays and other size-dependent topics such as ignition delay (e.g., [192]) and flame extinction (e.g., [73]) are avoided. Droplet combustion introduces several complicating factors with clear implications for size effect such as natural convection, soot shell formation, radiative exchange, and chemical kinetics. Natural convection is strongly dependent on the droplet size, where $Gr \propto d^3$, and is driven by the flame-enhanced temperature gradients. Monaghan et al. [94] recognized that most previous single droplet combustion studies used large ($d_0$ > 1000 μm) initial diameters (the study by Ohta et al. [127], although occurring after the Monaghan et al. [94] investigation, is an excellent example of using large porous spheres) which are not representative of a realistic size distribution in a spray. They successfully generated a wide range of suspended fuel droplets (150 – 2000 μm) and discovered that the burning rate increased with initial droplet diameter in normal gravity. The authors theorize that the initial diameter controls the burning rate due to the creation of a strong natural convective field which does not dissipate even as the droplet evaporates. Kumagai et al. [59] implicitly confirmed the theory of natural convection by performing microgravity combustion tests on free-floating heptane droplets in a similar initial droplet range and finding only minor variation in burning rate with droplet diameter. Poor free convection in microgravity conditions is the attributable cause of the weak size effect. This finding was further confirmed by the same group utilizing a different droplet generation technique [193] and for droplets down to 70 μm [60].

In contrast, Jackson and Avedisian [35] report a significant reduction in $K$ with increasing $d_0$ and reason that the soot shell, which is clearly defined in microgravity and sits between the droplet and flame, reduces heat and, more plausibly, mass transfer between the droplet and flame front. Large droplets provide increased time for soot to form, and early establishment of a soot shell may sustain further formation later in the droplet lifetime. Lee et al. [194] performed quantitative sooting measurements on large burning heptane droplets and confirmed that initially larger droplets provide greater opportunity for soot formation than smaller ones. This increase in soot level is attributed to the greater residence time of fuel vapor prior to reaching the flame which results in high levels of fuel pyrolysis and carbonization. Soot is a significant emitter of broadband radiation which contributes to heat loss and results in the lower burning rate of large droplets. The relationship between droplet size and sooting may reverse at very large droplet diameters (> 2000 μm) [195]. Xu et al. [36] determined that increasing the ambient temperature reduced and eventually reversed the net radiative losses, hence the effect of increasing initial droplet diameter in high-temperature ambiences is to increase the burning rate. Convective flows may sweep away the soot shell surrounding the droplet, which reduces the impact of radiative exchange and thus renders the burning rate relatively independent of the initial diameter [196]. Recent studies continue to evaluate the interplay regarding soot formation and radiative exchange and the subsequent relationship between evaporation rate and initial diameter (e.g., [34,197]). Like ambient temperature, the composition of the inert gas may affect the $K$ vs. $d_0$ relationship, although the mechanism involves soot formation rather than net heat exchange (e.g., [198–200]). Although the assumption of rapid chemical kinetics is a cornerstone of classic droplet combustion theory, numerical studies by Awasthi et al. [201,202] indicate that finite chemical kinetics become increasingly important as the droplet size decreases. At small initial droplet size ($d_0 \lesssim 60$ μm), the

authors found that diffusion can outpace chemical kinetics, based on the evaluation of a Damköhler number, for burning methanol droplets in a 1200 K ambience [201]. The average burning rate, $K$, peaks at approximately $d_0$ = 200 μm. $K$ decreases rapidly for smaller droplets due to the transition to a kinetically controlled regime while a gentler decrease occurs for larger droplets because of radiative losses.

The preceding discussion illustrates the complexity of size effect on the burning rate of individual droplets. Evaporation, on the other hand, appears to be impervious to many combustion-associated phenomena such as soot formation and chemical kinetics. In the absence of a soot shell, thermal radiation plays a reduced role in determining the droplet evaporation rate. The potential for strong natural convection is similarly mitigated without a flame. For these reasons, the evaporation rate of a single droplet isn't inherently a function of initial size. However, certain environmental factors such as intense pressure can introduce size dependency (e.g., [26,81,97]). The explanation, either explicit or presumptive, is natural convection (discussed in Section 2.7.2) since the Grashof number is proportional to the product $P^2 d^3$. Gogos et al. [97] developed a numerical code to assess the effect of natural convection and initial droplet size and calculated that normalized droplet lifetimes, $t_e/d_0^2$, decrease with pressure in normal gravity. The most dramatic reduction in lifetime occurs in subcritical pressure environments, where initially large droplets (e.g., $d_0$ = 1600 μm) are affected to a far greater extent than initially small droplets (e.g., $d_0$ = 100 μm). This finding indicates that moderate pressure ($P_r$ < 1) can have a profound impact on the lifetime of an evaporating droplet, at least when the ambient temperature is also elevated (800 K). The experimental results of Khan et al. [26] confirm that elevating the ambient pressure and temperature will improve the rate of $K$ gain with respect to initial droplet size for large ($d_0$ > 770 μm) kerosene fuel droplets. Small droplets are not well represented in the experimental

literature concerned with the evaluation the size-evaporation relationship, perhaps due to the belief that small, practically-sized droplets will experience little to no natural convection regardless of the surrounding conditions. Aside from enhancing natural convection, supercritical pressure can induce a size effect because of the transient nature of high-pressure evaporation. By virtue, initially larger droplets will feature longer lifetimes and thus greater potential for the surface to reach the critical mixing state [24]. Thus, in certain cases of extreme ambient pressure, larger droplets may experience transcritical evaporation, whereas smaller droplets evaporate strictly in the subcritical regime.

Droplet size may affect the rate controlling mechanism for evaporation. Several researchers have analyzed the potential for kinetic effects to take precedent over hydrodynamic diffusion (e.g., [118,203,204]). Kinetic effects (not to be confused with chemical kinetics) refer to the non-continuum processes which govern the detachment of liquid molecules from the surface of the droplet. Kinetic models may be developed independently and compared to diffusion models (e.g., [203,204]), or kinetic and diffusion approaches may be coupled by assuming dynamic mass balance between the kinetically-controlled region (Knudsen layer close to the droplet surface) and the diffusion-controlled region at farther radial locations where continuum assumptions regarding heat and mass transfer are valid (e.g., [118]). Kryukov et al. [203] assert that kinetic effects are always important (at least for the elevated temperature and small droplets of diesel fuel simulated in the study), especially as the initial droplet diameter decreases (5 μm vs. 20 μm). Pati et al. [204] confirmed that model disagreement (kinetic vs. diffusion) increases as the droplet size decreases using the same initial diameters as Kryukov et al. [203] but for water instead of diesel. Borodulin et al. [118] also evaluated water droplets with a range of sizes using both a classic diffusion model and a kinetic-influenced emission-diffusion model. At room temperature, the complex emission-

diffusion model predicts a rapid spike in droplet surface temperature near the end of the droplet lifetime. The temperature spike is noticeably absent in the standard diffusion model. This phenomenon impacts the lifetime of small droplets ($d_0$ < 250 μm) and predictions of longer evaporation times result. While Borodulin et al. [118] was able to confirm the temperature spike for larger ($d_0$ > 1000 μm) droplets using infrared thermography, experimental confirmation of results from the Kryukov et al. [203] and Pati et al. [204] studies are unlikely due to the exceedingly small size of the simulated droplets.

Of particular relevance to the present study is the potential for forced convective flow, either laminar or turbulent, to introduce evaporation rate size dependence. It is often difficult to isolate the effect of droplet size on evaporation rate in complicated studies such as the one by Honnery et al. [64] in which small ($d_0$ < 100 μm) droplets of nonane, decane, and dodecane are evaporated at low Reynolds number under the condition of steadily increasing ambient temperature. Although the study reports data on variably-sized droplets, the lack of explicit $d^2$ information, narrow initial size range, and inconsistent temperature field (though by design) make drawing conclusions regarding size effect somewhat futile. A similar point of view can be adopted when analyzing the results of a study by Kim et al. [205] in which a rapid compression process aided in the evaporation of a single heptane droplet. In that study, the authors discovered that smaller droplets attained higher bulk temperatures due to their superior surface area-to-volume ratio and, despite the transient nature of the temperature and pressure field, the middle portion of the droplet lifetime adhered to $d^2$ evaporation regardless of initial size. The steady-state evaporation constant decreased linearly with $d_0$ (in the range of 450 – 700 μm) at all tested conditions. In this instance, the finite compression period, which is accompanied by a large ambient temperature spike, take precedence in determining the size effect over natural convection.

Nguyen et al. [27] did not find a significant initial size effect for small free-falling droplets ($d_0$ < 90 μm) after an initial preheating stage. Yin et al. [100] compared 15 and 300 μm droplets exposed to a free-stream of constant convection coefficient in a numerical study. However, the authors contrast only the temperature profiles, and the paper provides no information regarding the expected rate of evaporation or droplet lifetime. There is thus surprisingly little information relating initial droplet diameter and evaporation rate under laminar flow conditions, and the relative flow between droplet and ambient is often the result of the droplet generation technique employed rather than a focal point of the study.

The scarcity of data relating initial droplet diameter and evaporation rate under turbulent, as compared to laminar, flow conditions is perhaps less surprising. The studies by Eckartsberg and Kapat [155] and Abou Al-Sood and Birouk [162] analyzed droplet evaporation in turbulence with a mean component while the investigation by Birouk and Toews [33] generated quasi-zero mean flow turbulence. Eckartsberg and Kapat hypothesized that only turbulent eddies which are smaller than the droplet can affect the evaporation rate. Furthermore, these eddies must contain significant kinetic energy to destabilize the boundary layer for any effect to be witnessed. The authors experimentally tested this hypothesis by exposing two large water droplets ($d_0$ = 2000 μm and 3500 μm) to identical laminar and turbulent (14% intensity) flows. The smaller of the two droplets evaporated at approximately the same rate in both laminar and turbulent flows. On the other hand, the turbulence increased the evaporation rate of the large droplet. The authors attribute the improvement to a greater proportion of energetic eddies smaller than the droplet, at least temporarily (the proportion reduces as the droplet shrinks in size). Abou Al-Sood and Birouk [162] compared 100-μm and 1500-μm droplets in a numerical study featuring intensities up to 60%. Turbulence is shown to improve $K$ at all conditions but is more effective for the larger droplet. $K$

is larger for the 1500-μm droplet than the 100-μm droplet at equal intensities. The disparity in evaporation rate between the two droplets increases with the intensity of the turbulence. The authors suggest that the reduced surface temperature of the larger droplet is responsible for the improvement in $K$, since this allows for a greater temperature gradient $T_\infty - T_s$, although it is not made clear as to why increased turbulence lowers the surface temperature. Logically, the reduced $T_s$ could be the result of improved vaporization and not necessarily the cause. Furthermore, the disparity between initial droplet sizes makes comparisons at equivalent instantaneous size impossible as the figures only report data for the larger droplet until $d \approx 475$ μm.

Although discussed in Section 2.7.5.2, it is worth reiterating the findings of Birouk and Toews [33] as this study is the first and only serious attempt (at the start of the research reported in this thesis) to quantify the effect of droplet size on evaporation rate in turbulence without a strong mean component. Turbulence was found to be effective in increasing $K$ for a range of heptane and decane droplet sizes (490 – 850 μm) at room temperature and pressure. At each turbulence intensity level, $K$ is a linearly increasing function of $d_0$ where higher intensity groups feature a steeper $K$ vs. $d_0$ slope. Because their study is preliminary in nature, few reasons are provided to explain the observed relationship between initial size, turbulence, and evaporation rate. However, the authors produce a Damköhler correlation which appears promising in its ability to predict turbulent evaporation rates. The present report is largely a continuation and expansion of the discovery in the paper by Birouk and Toews [33].

## 2.9 Summary

To summarize, investigations into single droplet evaporation have clear utility for contributing to the advancement of spray combustion theory and application. In particular, the experimental technique of suspending a droplet at the intersection of two micro-fibers is finding acceptance amongst researchers and offers many benefits. Perhaps the most important capability provided by the cross-fiber, as oppose to a large single fiber, is the ability to anchor small droplets on the order of 100 μm in diameter. A thorough review of the literature revealed that droplets of this size are not well represented, especially by experiment. Furthermore, while a small group of researchers have investigated the effect of turbulence on droplet evaporation, most experiments (and essentially all numerical codes) feature a strong mean flow. In turbulent studies which generate homogeneous and isotropic turbulence with quasi-zero mean flow, the initial droplet diameter is typically large (~1000 μm). It is difficult to elucidate the effect of pure turbulence on realistic droplet sizes based on the available research. Therefore, a parametric experimental investigation into the effect of turbulence and droplet size (particularly in the small range) on evaporation rate appears well-positioned to fill a large gap in the knowledge base related to spray combustion.

# CHAPTER 3
# EXPERIMENTAL SETUP AND PROCEDURE

## 3.1 Spherical chamber test rig and general accessories

All droplet evaporation studies were performed in a large fan-stirred spherical chamber. This test rig was developed to study the effect of turbulence on single droplet vaporization and combustion, as well as flame speed and spray atomization. The design of the chamber is the subject of [187] and the chamber has been utilized several times since then in comprehensive thesis studies (e.g., [206–208]). Due to the abundance of literature available regarding the specifics of the spherical chamber, this section provides only a cursory outline. Elements of the experimental setup which are unique to the current study, such as the cross-fiber frame and the capillary tube injector, are discussed in greater detail in Section 3.2.

The chamber was fabricated from two 12.7 mm thick stainless-steel hemispheres pressed from plate stock to form a sphere with an approximate volume of 29 L. From this basic welded shape, several extrusions for ports and flanges were added. The chamber features four window ports (two of 100-mm diameter and two of 125-mm diameter) arranged around the horizontal equator to enable optical access. Quartz glass windows of 40-mm thickness are clamped in place in the viewing ports using high-pressure gaskets. The window ports are the primary points of access for working inside the chamber and can accommodate other accessories such as block-off plates and heating elements. Eight fan ports of 115-mm diameter are arranged symmetrically around the circumference. When installed, the fans form axially opposed pairs which direct their flow towards the center of the chamber. A servomotor, matched to an independent servo amplifier, drives each six-bladed fan. The maximum angular velocity of the fans is 8000 RPM. Ten small

accessory ports are spread throughout the chamber to accept a variety of equipment and instrumentation such as pressure relief valves, fill and vacuum valves, thermocouples, pressure transducers, ignition electrodes, and fuel injectors. Fan control, as well as pressure and temperature feedback, is interfaced through LabVIEW software. Additional details regarding the design can be found in [187], and Fig. 3.1 provides a rendering of the chamber without any accessories installed.

The chamber is also capable of heating and pressurizing the contained gas. Previous studies have successfully achieved temperatures and pressures as high as 200°C and 21 bar (e.g., [187,206]). For all present studies, the chamber is pressurized by first vacuuming the air (as discussed in [208]) and then filling with nitrogen to the desired pressure. The heating system, developed and discussed in [206], can then be activated to perform a study at elevated temperature. The cross-fiber support frame is suspended from a threaded connection in the center top accessory port, while the injector is installed in one of the off-axis upper accessory ports.

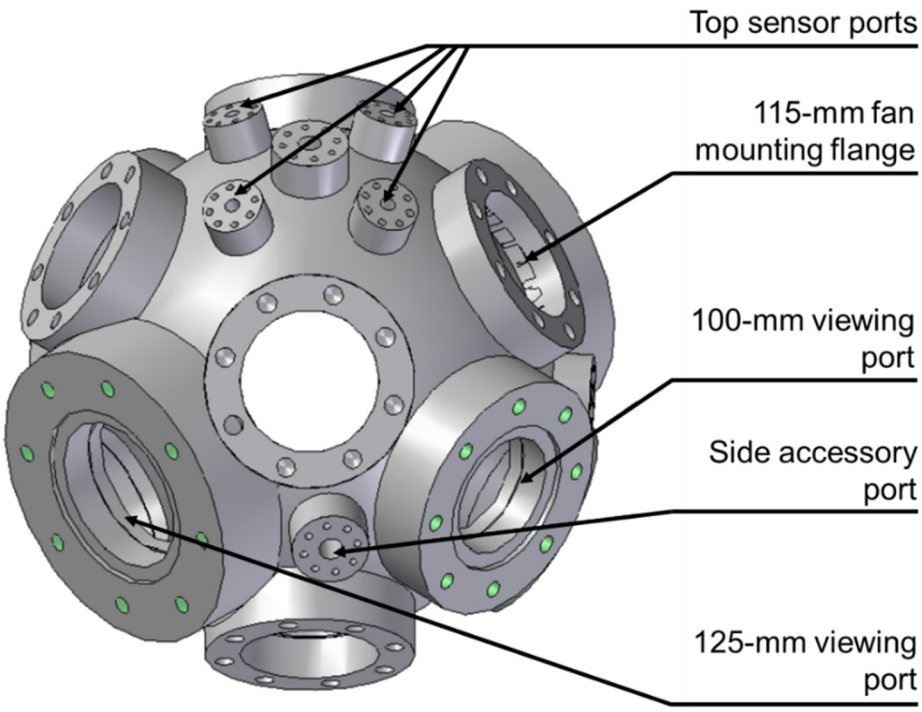


**Fig. 3.1.** Rendering of the stainless-steel spherical chamber used for all droplet evaporation studies [187].

## 3.2 Cross-fiber support frame and injector

The primary difference between the present investigation and previous studies in the spherical chamber (e.g., [187,206–208]) is the implementation of a cross-fiber support frame to anchor the droplets. As discussed in Section 2.3, suspending droplets on two small intersecting fibers has many benefits as compared to a single fiber. Several frames were machined from aluminum and fitted with threaded fiber holders to adjust the tension of the 14-μm silicon carbide (SiC) fibers. The fibers are epoxied to the holders prior to the frame's installation into the chamber. The square cross-sectional profile of the frame is minimal (3.175 mm × 3.175 mm) while the overall length and height (100 mm × 100 mm) are the largest allowable by the constraint of window port size based on the requirement to insert the frame through the port for installation.

As originally designed, the frame was secured to the chamber wall at three points; the top and both sides [33]. The two side supports were concluded to be largely redundant during testing. The single upper support is sufficient to secure the frame at all tested fan speeds. Attempting to attach the side supports dramatically increased the chance of breaking or loosening a fiber. A broken fiber requires significant time to replace due to the adhesive drying time and the sequential steps of epoxying a fiber to both holders, whereas a loose fiber will not support a droplet and hence necessitates a difficult in-chamber adjustment or complete removal and reinstallation of the frame. Furthermore, the side mounts increase the asymmetry of the frame with respect to the fans and can make alignment a challenge. The downside of the single support technique is that the frame appears to experience increased vibration. Although the vibration does not affect the integrity of the mount (provided the hardware is sufficiently tight) or image capture, it may induce droplet detachment from the fiber intersection. It is recommended that future iterations of the design retain the single-support approach and take into consideration the vibration issue (see Section 5.2.1).

Figure 3.2 illustrates the relative size of the spherical chamber and the cross-fiber support frame from a two-dimensional side perspective. The blades of the eight axial fans rotate in the shell demarcated by the dashed red line. The fans are thus in proximity to the frame. The large major dimensions of the frame result in the flow field at the center of the chamber remaining relatively undisturbed by the frame's presence. To ensure that the droplet is exposed to the highest quality turbulence (homogeneous and isotropic), it is important to ensure that the fiber intersection is coincident with the geometric center of the chamber. Section D.1 outlines the recommended alignment procedure. Figure 3.3 provides additional details of the cross-fiber frame.

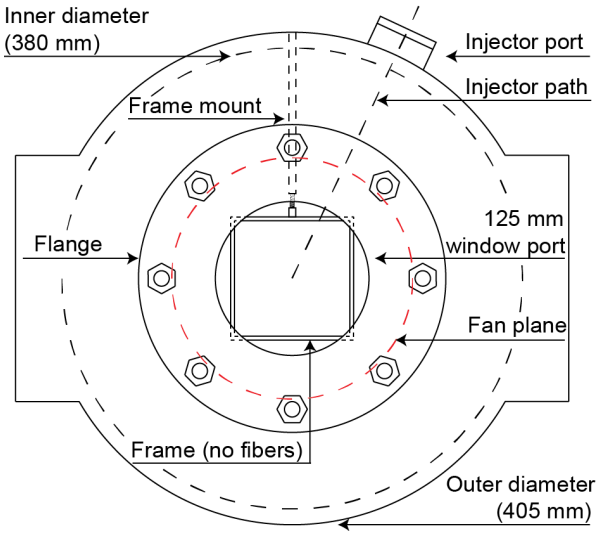


**Fig. 3.2.** Side view of the chamber with the cross-fiber frame installed (roughly to scale). The frame is rotated slightly about its support to accommodate the injector, PIV laser sheet, and camera.

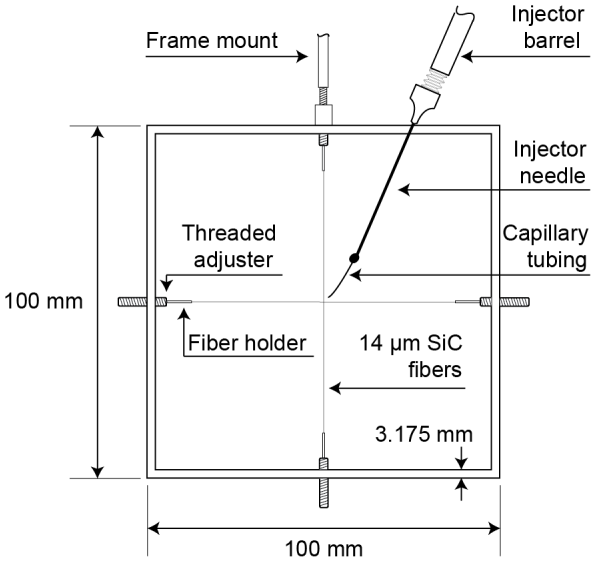


**Fig. 3.3.** Details and dimensions of the aluminum cross-fiber support frame.

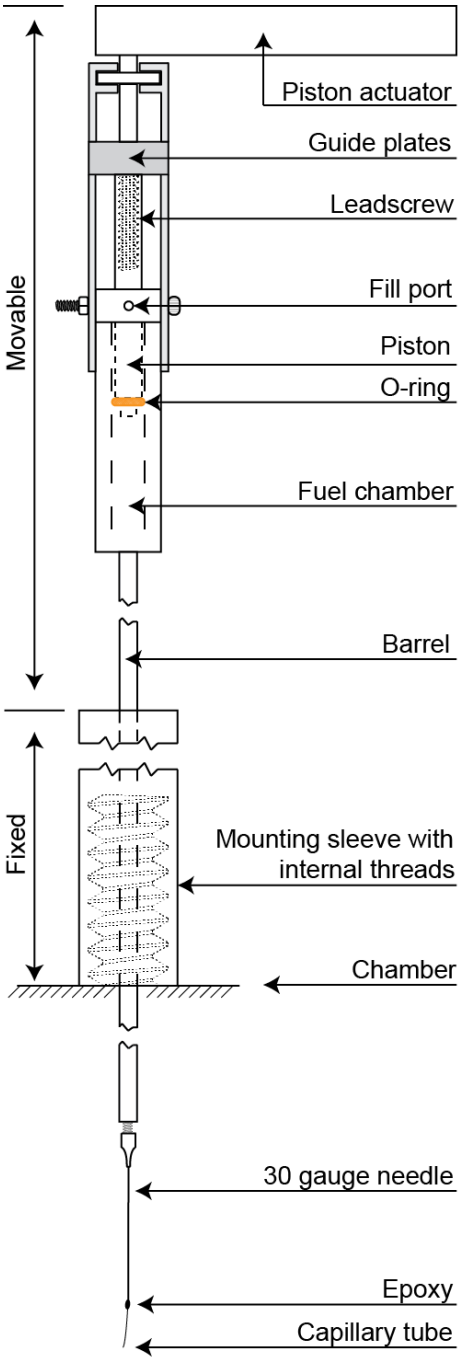


**Fig. 3.4.** Schematic of the fuel injector assembly (roughly to scale).

A schematic of the fuel injector is shown to the left. The mounting sleeve attaches to a threaded fitting located near the top of the chamber and provides a sealed sliding surface for insertion and retraction of the barrel and needle. To form a droplet, the piston actuator, which is attached to a leadscrew, is rotated. The guide plates ensure linear motion of the piston into the fuel chamber. An o-ring provides a seal between the piston and chamber wall, and the piston forces fuel through the barrel of the injector assembly. With sufficient pressure applied via the piston, fuel flows through the needle, resulting in the formation of small droplets at the end of the capillary tube. All tests were performed using polycarbonate capillary tubing with an inner diameter of 25 μm and an outer diameter of 50 μm. Once the injector places a droplet on the cross-fiber, the barrel is retracted and pressure is relieved by rotating the actuator in the opposite direction. Completely withdrawing the piston results in the exposure of the fill port which is used to add fuel to the chamber via a syringe. The injector is modular and can be broken down into pieces for thorough cleaning and parts replacement.

## 3.3 Test fuels and their properties

The two fuels used in this study are *n*-heptane and *n*-decane. These straight-chain alkanes (paraffins) have in tandem been the subject of dozens of studies because they belong to the same hydrocarbon family yet feature highly disparate volatilities. Pragmatically, it is beneficial to use common fuels in experiments to facilitate comparisons with other research findings. Both heptane and decane are widely available in high purity (> 99%). Furthermore, heptane and decane are common components in fuels such as gasoline, diesel, and aviation kerosene [209]. Heptane, for example, is used in reference mixtures for determining the octane rating of gasoline [210] and is one of the primary constituents of military-grade JP-4 jet fuel [211]. Decane, on the other hand, is an important lighter component in diesel fuel [212]. Between 70 and 85% of commercial aviation fuel is composed of paraffins [213]. For these reasons, the development of surrogate compounds for the modelling of complex real fuels often use heptane and decane. The key thermophysical properties of *n*-heptane and *n*-decane are provided in Table 3.1 [119].

**Table 3.1**
Thermophysical properties of *n*-heptane and *n*-decane.

| Fuel | $MW$ [g/mol] | $T_b$ [K] | $h_{fg}^{*}$ [kJ/mol] | $T_c$ [K] | $P_c$ [bar] | $P_{v,25°C}^{\dagger}$ [bar] |
|---|---|---|---|---|---|---|
| *n*-heptane $C_7H_{16}$ | 100.204 | 371.57 | 31.77 | 540.20 | 27.40 | 0.0611 |
| *n*-decane $C_{10}H_{22}$ | 142.285 | 447.30 | 38.75 | 617.70 | 21.10 | 0.00184 |

**at the normal boiling point*
*†calculated using Wagner relation*

Every effort is made to avoid cross-contamination of the fuels. Strategies include the designation of some apparatus and equipment parts, such as injection needle assemblies and transfer syringes, as fuel-type-exclusive. In these cases, only one type of fuel is allowed to come

in contact with the part. In situations where this is not feasible, such as the injector assembly which must accommodate both fuels, the part is disassembled, cleaned, rinsed with water, and dried prior to reassembly and use with a new fuel.

## 3.4 Particle image velocimetry

Two-dimensional Particle Image Velocimetry (2D-PIV) was performed at every fan speed to assess the turbulent flow field in the center of the chamber. Additional runs were also performed at elevated pressure and temperature. The typical layout, shown from above, is pictured in Fig. 3.5. A Dantec Dynamics DualPower 135-15 Nd:YAG laser and a FlowSense EO 4M camera interfaced with DynamicStudio software was used to perform all PIV measurements. The "Camera C Laser B" configuration illustrated in Fig. 3.5 was the standard layout. However, "Camera D Laser A" and "Camera D Laser C" arrangements were used to confirm the PIV results. A LaVision aerosol generator introduced micro-sized olive oil seeder droplets through a fitting in the bottom of the chamber. Sufficient time was allocated between seeding and image capture to allow for the dissipation of any transient flow effects caused by the influx of seeding particles. Additional post-processing of the data to extract correlation coefficients and compile multiple tests runs utilized an in-house MATLAB code (Section B.2). Section D.3 details the alignment and calibration procedure of the PIV system.

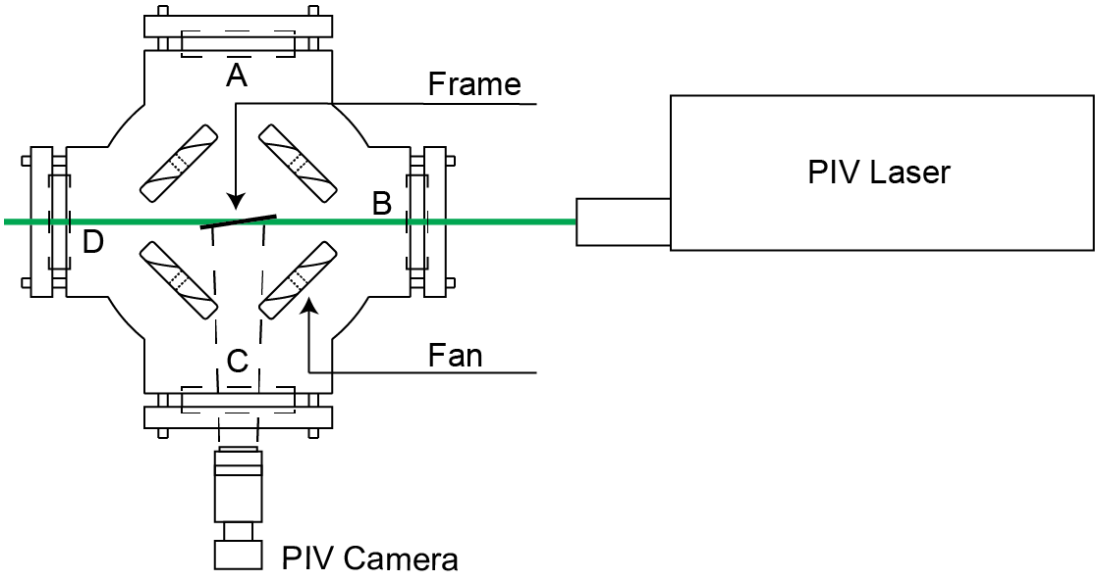


**Fig. 3.5.** Overhead view of the chamber (cross-sectional) and PIV equipment (roughly to scale).The PIV laser is shown closer to the chamber than in actual experiments for compactness, and the details of the fan motors and hubs are omitted for clarity. The cross-fiber frame is slightly angled to allow passage of the laser sheet.

Table 3.2 summarizes the main PIV settings. Pulse delay is determined by inspection for each fan speed such that the displacement of a seeding particle which occurs between two consecutive pulses is maintained in the range of ⅓ to ¼ of the interrogation area length, as recommended by [214]. The appropriate delay time was roughly inversely proportional to fan speed. The maximum number image pairs attainable in a single PIV run is 3000. However, it is possible to compile the results of multiple runs to obtain superior convergence of turbulent statistics. Nevertheless, it is advantageous to minimize the number of image pairs (while maintaining acceptable convergence) due to time and storage space restrictions. When a comparison was made between the velocity fluctuation RMS values from 6000 pairs to their counterparts collected using only 3000 pairs, the maximum percent difference in the central region ($\pm$ 10 mm) is less than 5% and 4% for 500 and 3000 RPM, respectively. Therefore, all PIV data reported in this research used 3000 image pairs. Due to the extremely small nature of the

evaporating fuel droplet, it is desirable to zoom the camera as much as possible to resolve the smaller scales. Because of the geometric constraints imposed by the large chamber and thick windows, the smallest field of view (and therefore greatest magnification) is approximately 70 mm × 70 mm. The camera resolution, combined with the interrogation area and window overlap, yielded 16,129 instantaneous velocity vectors for each pair of laser pulses.

**Table 3.2**
Summary of PIV specifications.

| | |
|---|---|
| **Repetition rate [Hz]** | 10 |
| **Pulse delay [μs]** | 50 – 370 |
| **Image pairs [#]** | 3000 |
| **Camera resolution [px.]** | 2048 × 2048 |
| **Field of view [mm]** | ~70 × 70 |
| **Scale factor [μm/px.]** | ~33 |
| **Interrogation area [px.]** | 32 × 32 |
| **Overlap [%]** | 50 |

A stroboscope was used to check the fans after every speed change. This rigorous inspection was necessary due to the appreciable drift in speed which can occur during lengthy runs. In general, the fans will slowly drop in RPM over time. The reason for this is unknown. Fortunately, the loss of RPM is consistent across all fans. However, it is important to ensure all fans are initially at the approximate same speed. All fans were set to within $\pm$ 1% of the commanded speed, and at no time were the minimum and maximum fan speeds allowed to exceed

1% difference. The *SIGNAL* potentiometer at the servo amplifier is used to adjust the speed of an individual fan if it differs substantially from the commanded value.

## 3.5 Droplet evaporation and image processing

The evolution of the droplet evaporating on the cross-fiber is captured in 8-bit grayscale using a Dantec Dynamics NanoSense MkIII high-speed camera with a Lowel Pro-light 250 W backlight. Fig. 3.6 illustrates the general layout from a top view. MotionStudio software controls camera settings and triggering/acquisition. The camera has a maximum resolution of 1280 px. × 1080 px. and is capable of a shooting 1040 fps at this resolution. Cropped images at lower frame rates are used for droplet evaporation studies because the small droplets studied here do not require a large field of view. Furthermore, due to the fixed buffer capacity, lower frame rates result in longer record times which is important for droplets that may take over 30 minutes to evaporate. The camera is equipped with a 3× teleconverter, a 70 – 210 mm zoom lens, and a +4 close-up filter to enable highly magnified images from a standoff distance exceeding 250 mm. This combination of lenses achieved a scale factor below 5 μm/px. Lower scale factors reduce error in the post-processing phase of image capture, as each pixel represents a physically smaller area and thus lessens the impact of missing (or including) a single pixel when calculating droplet size. Table 3.3 provides a summary of the recommended camera settings. Setting up the camera this way has consistently proven to yield high-contrast images with excellent clarity. Fig. 3.7 compares an example of a high-quality cross-fiber image with a comparative image from a single fiber study. The increased level of sphericity for the cross-fiber droplet is obvious. Section D.2 outlines the techniques of camera alignment and calibration. Accurate calibration was found to be paramount for obtaining repeatable data, as calculated droplet size and, hence, evaporation rate is far more

sensitive to this parameter than threshold value or the morphological structuring elements in the image processing code.

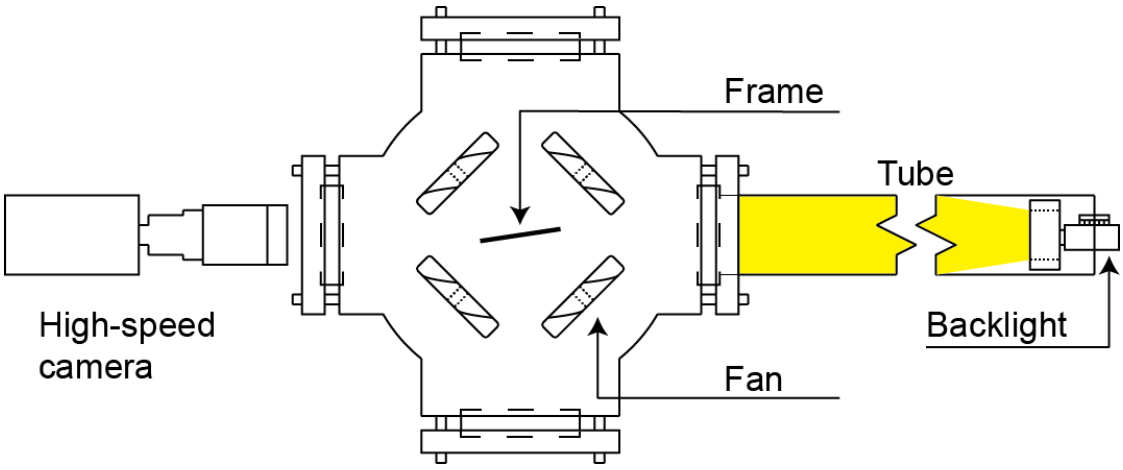


**Fig. 3.6.** Overhead view of the chamber (cross-sectional) and droplet imaging equipment (roughly to scale). The details of the fan motors and hubs are omitted for clarity.

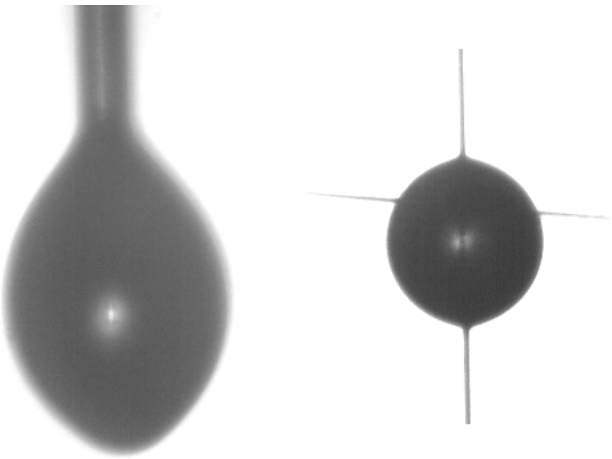

**Fig. 3.7.** Comparison of droplets suspended by a single fiber (left) and the cross-fiber (right).

**Table 3.3**
Camera specifications and settings.

| | |
|---|---|
| **Cropped resolution [px.]** | 256 × 256 |
| **Maximum images*** **[#]** | ~3200 |
| **Exposure [µm]** | ~800 |
| **Zoom [mm]** | 210 |
| ***f*# [-]** | 22 |
| **Scale factor [µm/px.]** | 4.6 – 5.0 |
| **Frame rate [fps]** | 1 – 120 |

**at 256 px. × 256 px. resolution*

Thoroughly cleaning the chamber prior to commencing droplet evaporation studies is imperative, especially following PIV tests due to the oily residue which remains. Dust and debris can affect the evaporative results by becoming embedded in the droplet surface. Droplets which fail to evaporate completely are a clear indication of this effect. Although it is not feasible to completely disassemble the interior of the chamber and clean with a degreaser every day, this is recommended as the first step of a prolonged evaporative study. Furthermore, vacuuming the chamber with the fans running and refilling with clean and dry nitrogen (multiple times in succession if necessary) should be done at least once a day to mitigate the effects of particulates in the air.

From the standpoint of image capture, variation of the experimental parameters (pressure, temperature, initial droplet size, fuel type, and turbulence level) required only the alteration of the frame rate and the number of images captured. For example, small heptane droplets at high temperature or high turbulence may evaporate in a matter of seconds and therefore require a high frame rate whereas a large decane droplet in a stagnant environment under high pressure could take close to 60 minutes to disappear completely. The maximum number of frames stored is a function of the total image resolution. It is desirable to store enough frames to capture the entire droplet lifetime, but not so many that the capture process and storage transfer become unduly time-consuming. The fact that the camera begins recording before the formation and placement of the droplet at the cross-fiber adds variability to the time estimation process. The camera begins recording before the formation of the droplet to avoid any lag between the manually-performed generation and camera trigger events. If too much time passes, the calculated initial droplet size could be significantly smaller than the actual value, especially for small, rapidly evaporating droplets. Starting the camera first removes any issue with manual injection and triggering.

The camera frame rate should be selected based not only upon the predicted evaporation time but also to avoid oscillations in the processed data. Experience has indicated that certain frame rates produce highly oscillatory behaviour in the plots of the extracted $d^2$ data. Interaction with the backlight frequency is the assumed cause of this phenomenon. Although the overall trend (i.e., $K$) is generally retained, it is best to avoid frequencies which promote undue fluctuations in the results. Trial runs allowed for the determination of appropriate camera frame rates. Table 3.4 lists the recommended frame rates for heptane droplets at standard conditions.

**Table 3.4**
Recommended frame rates for heptane at standard conditions.

| RPM | fps |
|---|---|
| 0 | 30 |
| 500 | 60 |
| 1000 | 60 |
| 2000 | 60 |
| 3000 | 120 |

The images are transferred to a PC for processing after they have been captured and stored in the camera. The image processing code (Section B.1) uses an automatic thresholding routine to separate the foreground and background. Two successive erosions and dilations are performed to remove the cross-fibers, and disk filtering cleans up the fiber-droplet contact points. The projected planar droplet area is equated to that of an equivalent circle with diameter $d$ to extract the initial size and surface regression information. The resultant plot of $d^2$ vs. $t$ is then assessed for linearity, and $K$ is calculated by placing a line of best fit through the linear portion of the profile.

As discussed in Section 3.4, the fans must be checked with a stroboscope prior to and following a series of evaporation tests at a given fan speed. Consistent fan inspection ensures that all tests adhered to the strict precision of the $\pm$ 1% fan speed criteria which was also applied to PIV runs.

# CHAPTER 4
# RESULTS AND DISCUSSION

The organization of this chapter follows the chronological order of the experimental process, and the material is presented in the same manner as in the two journal papers which resulted from the thesis material [215,216]. Section 4.1 reports the results of turbulence characterization and droplet evaporation at room temperature and pressure, while Section 4.2 expands the dataset to include ambient temperatures up to 100°C and pressures up to 10 bar. Due to the number of varied parameters, the evaporation results in Section 4.2 are further divided by quiescent, elevated pressure, and elevated temperature criteria. Data from the standard conditions tests in Section 4.1 are included in the figures and correlations in Section 4.2 where necessary, as the room pressure and temperature findings provide a baseline for the elevated conditions investigations.

## 4.1 Droplet evaporation at standard conditions

The following sections present the results and analysis of the PIV investigation and droplet evaporation of heptane and decane at 1 bar and 25°C. The ambient gas is nitrogen, and the fan speeds range from 0 – 3000 RPM.

### 4.1.1 Turbulence characterization

Previous investigations (e.g., [30,182]) have characterized the turbulent flow field in the chamber. However, further characterization of the flow in the middle of the vessel was repeated in the presence of the droplet-suspending cross-fiber frame. The frame is positioned such that the flow

along the fans' centerlines will not impact the frame or its mounting hardware, although some degree of anti-symmetry is inevitable as dictated by the requirements of image capture and PIV measurements (see Figs. 3.5 and 3.6). Regardless, the results obtained within a small central volume of the vessel (diameter of about 20 mm) revealed little difference as compared to findings reported earlier without the presence of the frame [30,182]. Flow field consistency is attributed to the fact that the frame is relatively thin and has sufficiently large dimensions as compared to the integral length scale, ensuring that the frame does not affect the turbulence in the central region of the chamber. Figure 4.1 illustrates the magnitude of the mean velocity field at 500 RPM while Fig. 4.2 depicts the field at 3000 RPM. These figures represent the entire PIV field of view while the dashed circles demarcate the central region of 20-mm diameter where the support frame has little effect on the flow. Figure 4.3 plots the mean and RMS fluctuating velocity components along the horizontal axis for the two extreme fan speeds (500 and 3000 RPM). In both cases, the mean flow is a very small fraction of the fluctuating component in the central (20 mm in diameter) region. Figure 4.3 is also indicative of a high level of isotropy ($U_{rms} \approx V_{rms}$) and homogeneity (the spatial independence of turbulent statistics) near the center of the field of view; Fig. 4.4 quantifies these measures. The horizontal lines drawn at 1.1 and 0.9 (representing $\pm$ 10% anisotropy and inhomogeneity) bound both $U_{rms}/V_{rms}$ and $q^{0.5}/q_{avg}^{0.5}$ ratios for at least a diameter of 20 mm in the central flow region which is more than sufficient for the present study. The $\pm$ 10% criteria is somewhat arbitrary but agrees with studies that used similar fan-stirred chambers and comparable regions of interest (e.g., [174,183,184]). Furthermore, both 500 and 3000 RPM fan speeds feature similar spatial patterns in Fig. 4.4, revealing consistent isotropy and homogeneity over the entire fan speed range explored here. Turbulent statistics plotted along the vertical axis agree with the trends established in Figs. 4.3 and 4.4.

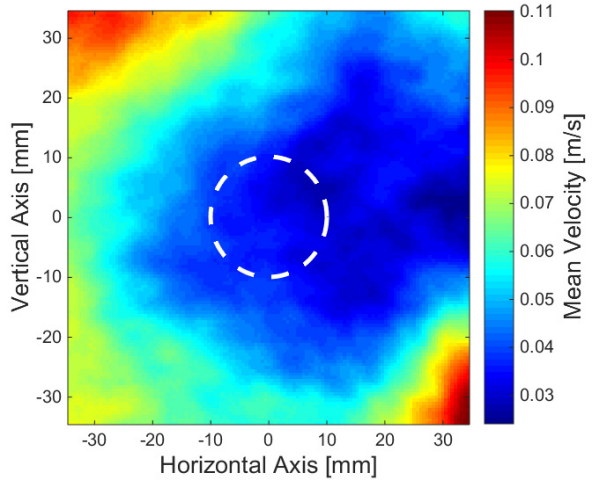


**Fig. 4.1.** Mean velocity magnitude at 500 RPM in field of view (70 mm × 70 mm).

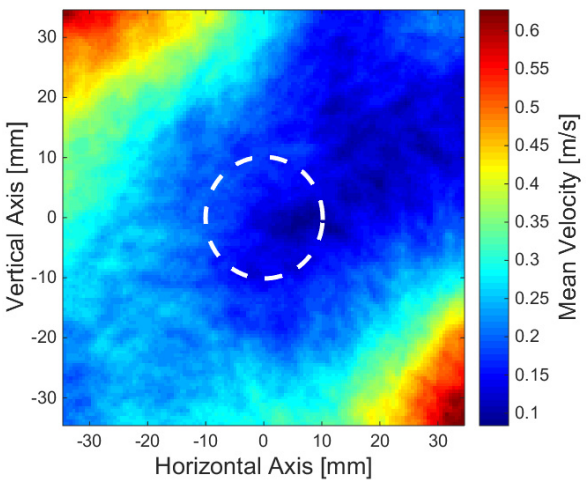


**Fig. 4.2.** Mean velocity magnitude at 3000 RPM in field of view (70 mm × 70 mm).

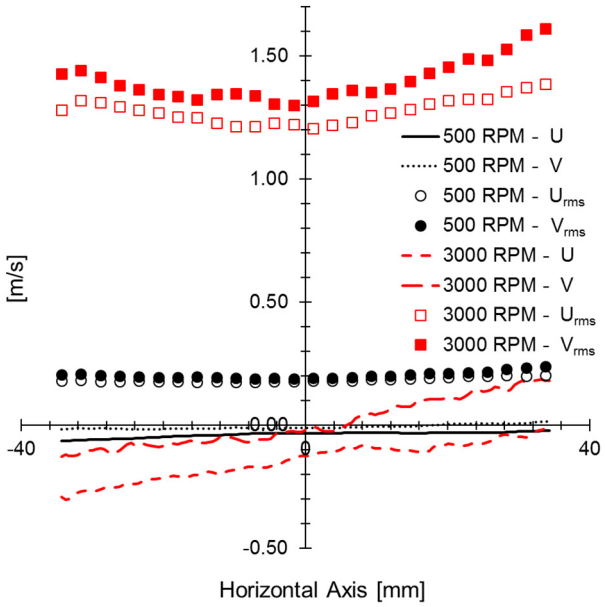


**Fig. 4.3.** Profiles of the mean velocity and RMS fluctuations at 500 and 3000 RPM.

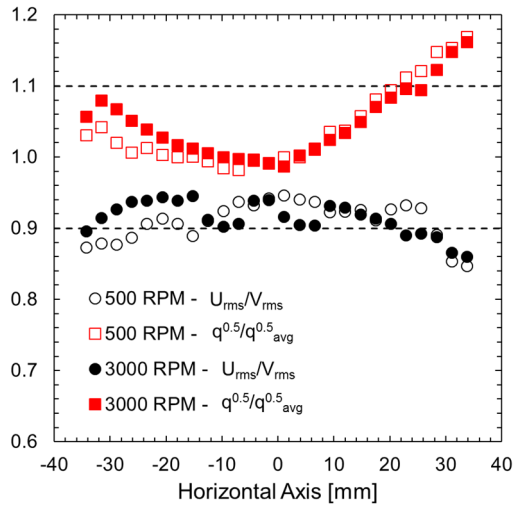


**Fig. 4.4.** Profiles of the isotropy and homogeneity ratios at 500 and 3000 RPM.

The turbulence kinetic energy, $q$, is defined as follows:

$$q = \frac{1}{2}\overline{u_i u_i} \approx \frac{1}{2}(2U_{rms}^2 + V_{rms}^2) \approx \frac{1}{2}(U_{rms}^2 + 2V_{rms}^2) \quad \textbf{(4.1)}$$

Due to the expected isotropy of the flow and the lack of data in the third dimension, it is assumed that $U_{rms} \approx V_{rms} \approx W_{rms}$. Experience has shown that both right-hand side formulations in Eq. (4.1) yield highly comparable values. The turbulence intensity, defined here as the square root of $q$, is directly proportional to fan speed. This important relationship is commonly observed in fan-stirred chambers (e.g., [174,175,178,184]). Turbulence intensity as a function of fan RPM, $N$, is plotted in Fig. 4.5 for the $\pm$ 10-mm region surrounding the origin, and the resulting best-fit equation is expressed as $q^{0.5} = 0.000509 \times N$. The integral length scale, $L$, is calculated by averaging the numerical integrations of the longitudinal correlation coefficient plots [182]. Following the notation of Davidson [217], Eq. (4.2) defines the integral length scale:

$$L = \int_0^\infty f(r)dr \tag{4.2}$$

The integral length scale provides a rough measure of the correlation distance for turbulent structures. The quantity $f(r)$ is the longitudinal correlation coefficient and may be calculated in both the horizontal ($f_x(r)$) and vertical ($f_y(r)$) directions.

$$f_x(r) = \frac{\overline{u(x_0, y_0)u(x_0 + r, y_0)}}{U_{rms}(x_0, y_0)U_{rms}(x_0 + r, y_0)} \tag{4.3}$$

$$f_y(r) = \frac{\overline{v(x_0, y_0)v(x_0, y_0 + r)}}{V_{rms}(x_0, y_0)V_{rms}(x_0, y_0 + r)} \tag{4.4}$$

Due to the high level of isotropy and homogeneity of the flow, the calculation of $L$ (Eq. (4.2)) may utilize either Eq. (4.3) or (4.4). Since the origin is centered in the field of view, the displacement distance $r$ can take on positive and negative values and thus both Eq. (4.3) and Eq.

(4.4) are plotted on either side of the origin. To calculate a representative integral length scale value, $f_x(r)$ and $f_y(r)$ are integrated for both positive and negative $r$, and the results averaged to find $L$. Due to the small field of view, the plots of $f_x(r)$ and $f_y(r)$ fail to de-correlate fully (reach zero). Thus, a simple linear extrapolation, similar to the approach of Ravi et al. [174], was performed on the tails of the correlation coefficient plots to yield a numerically integrable function. Figure 4.6 illustrates the extrapolation concept by plotting $f_x(r)$ for positive $r$ values at 500 and 3000 RPM. As evident in Fig. 4.6, there is little difference in correlation coefficients between 500 and 3000 RPM. Overall, $L$ was found to remain relatively consistent at all fan speeds and the average value, based on $f_x(r)$ and $f_y(r)$ for all $r$ and all fan speeds, is 20.55 mm. This value represents a length scale magnitude which could be expected in an actual combustor [174].

The integral length scale is one of three important characteristic turbulent length scales. The Kolmogorov length scale, $\eta$, provides a measure of the smallest eddies in the flow and is expected to be much closer to the droplet size than $L$. The Kolmogorov length scale cannot be resolved directly with the current PIV data and is calculated using the following relationship (e.g., [218,219]):

$$\eta \sim L\left(Re_{t,L}^{-\frac{3}{4}}\right) = L\left(\frac{q^{0.5}L}{\nu}\right)^{-\frac{3}{4}} \tag{4.5}$$

The Kolmogorov length scale is thus a strong function of intensity but a weak function of $L$. The third length scale typically used in the characterization of turbulence is the Taylor microscale, $\lambda$, which falls between $\eta$ and $L$. As with $L$, it may be calculated using the correlation coefficient plots (Fig. 4.6), however, $\lambda$ is estimated by extending a parabola fitted to the data points near the origin. By definition, the intercept of the extrapolated parabola is the Taylor microscale. Although the

PIV data compiler code (Section B.2) has the capability to calculate $\lambda$, the following discussion and correlations do not further reference the Taylor microscale. Accurate determination of $\lambda$ requires high-resolution PIV data near the origin, and it is questionable whether the current setup can provide sufficient data density to resolve the Taylor scale properly using the parabolic fit method. Table 4.1 provides additional turbulent flow field characteristics and test conditions.

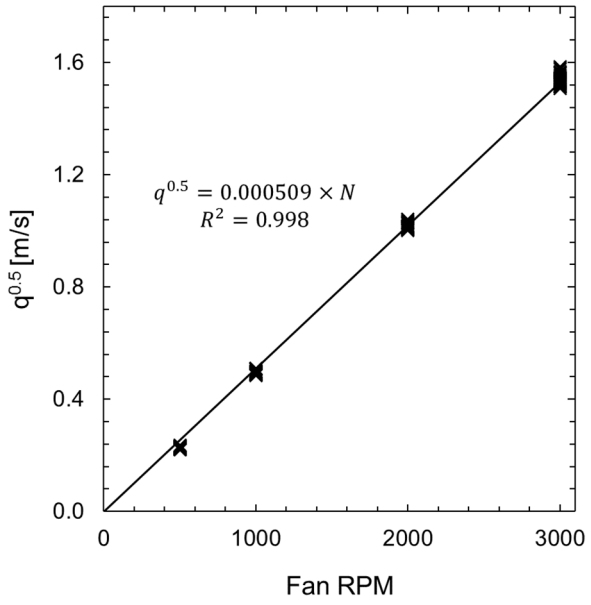


**Fig. 4.5.** Intensity gain with fan speed in the central spherical region ($d$ = 20 mm).

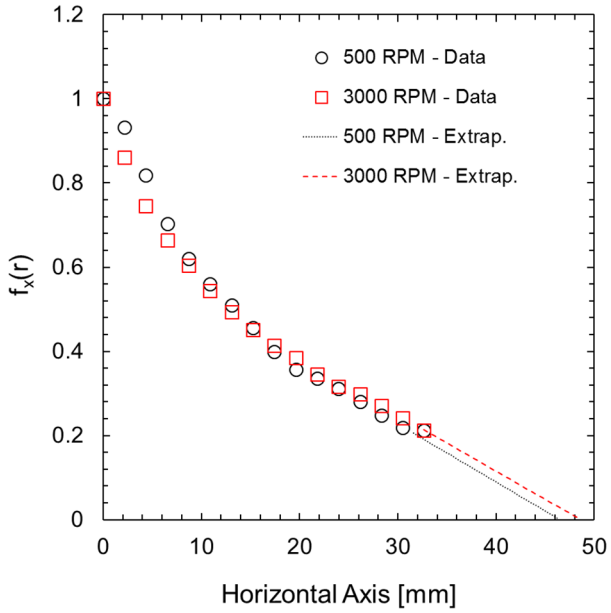


**Fig. 4.6.** Longitudinal correlation coefficient data with extrapolations.

**Table 4.1**
Summary of test conditions at standard temperature and atmospheric pressure.

| $d_0$ [µm] | $q^{0.5}$ [m/s] | $T_\infty$ [°C] | $P_\infty$ [bar] | $L/d_0$ [-] | $\eta/d_0$ [-] | $Re_{t,d_0}$ [-] |
|---|---|---|---|---|---|---|
| 145 – 730 | 0 – 1.53 | 25 | 1 | 28 – 141 | 0.13 – 2.00 | 0 – 53 |

### 4.1.2 Droplet evaporation

Figures 4.7 and 4.8 illustrate the time histories of selected heptane droplets. The quasi-linear temporal variation of the normalized squared diameter demonstrates that a suspended droplet on the cross-fiber adheres to the $d^2$ law under both quiescent (Fig. 4.7) and turbulent (Fig. 4.8) ambient conditions. More importantly, these figures reveal that the normalized lifetime does not vary with the initial droplet size, $d_0$, in a quiescent atmosphere (Fig. 4.7), whereas there is an apparent change in a turbulent environment (Fig. 4.8). The present finding in stagnant conditions is in line with classic theory and the results of Khan et al. [26], which predict minimal droplet size effect at low temperature. In the absence of a significant temperature gradient (where large gradients are associated with high-temperature environments, such as combustion), there is negligible flow induced by natural convection. Larger droplets tend to promote greater free convection while burning due to the strong characteristic length dependence of the Grashof number and the substantial temperature variation near the droplet surface. The improved heat transfer in a convective field may persist throughout the droplet lifetime, despite the rapid and progressive reduction in droplet size [94]. However, for droplet evaporation at room temperature and pressure, there is negligible potential for free convection to affect the heat or mass transfer and, consequently, the overall evaporation rate.

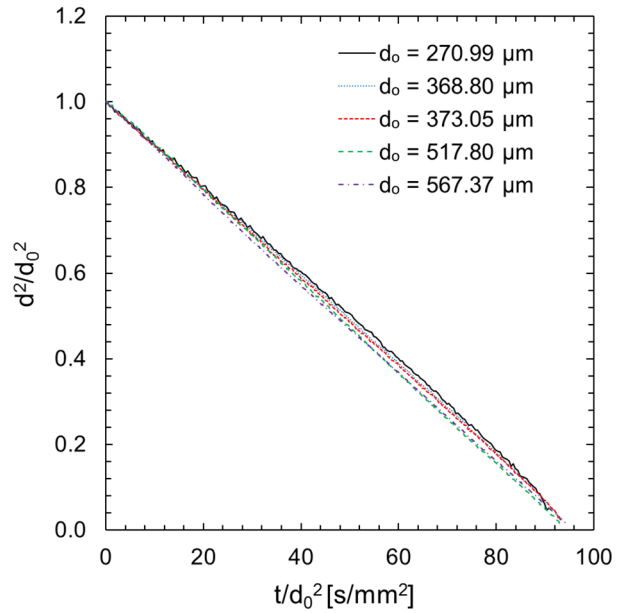


**Fig. 4.7.** Time history of heptane droplet evaporation in quiescent environment.

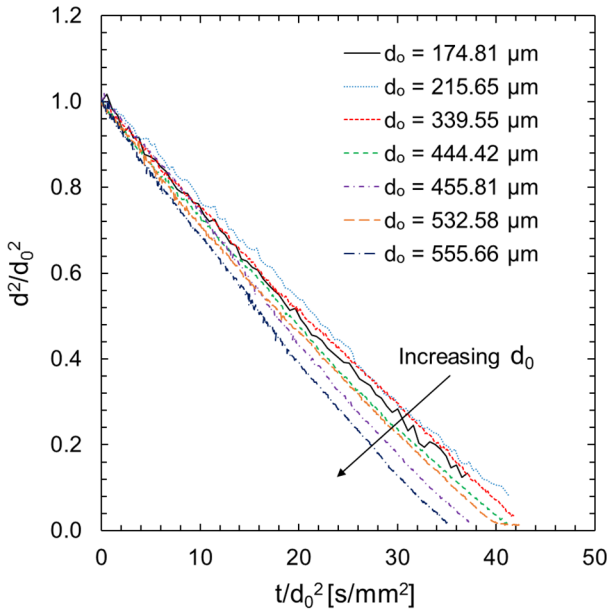


**Fig. 4.8.** Time history of heptane droplet evaporation in turbulent environment (2000 RPM).

Figure 4.9 presents the evaporation rate of heptane as a function of $d_0$ for different turbulence intensity levels (fan speed), while Fig. 4.10 plots the same data for decane. The evaporation rate, $K$, is defined as the slope of the temporal linear variation of $(d/d_0)^2$ shown in Figs. 4.7 and 4.8 using the classical $d^2$ law (i.e., $(d/d_0)^2 = 1 - K(t/d_0^2)$). In all cases, linearity begins immediately and is maintained throughout the majority of the droplet's lifetime. These figures clearly show a strong relationship between the evaporation rate and $d_0$ in turbulent environments. It is evident in Fig. 4.8 that the effect of the initial droplet size prevails in the presence of a convective turbulent flow field around the droplet, where the slope of the temporal variation of $(d/d_0)^2$ depends on the droplet initial size $d_0$ rather than the instantaneous diameter. For example, a droplet having an initial size of $d_0$ = 555.66 µm still has a higher $K$ when it shrinks to an intermediate size (say, $d(t)$ = 339.55 µm) than a droplet with an initial size of $d_0$ = 339.55 µm. The separation of $K$ from instantaneous size suggests the establishment of a

mechanism at the time of droplet formation/injection that subsequently controls the vaporization process throughout the droplet lifetime. The mechanism is still unknown, but all collected experimental data demonstrate the existence of this phenomenon. Furthermore, since the turbulence integral length scale remains constant throughout the experiment, the increasing turbulence intensity is responsible for the enhancement of the vaporization rate with fan speed. However, this finding does not imply that the integral length scale has no effect on the vaporization rate, as increasing the ratio of $L/d_0$ has been found to reduce $K$ [16] and the Nusselt number [220]. This ratio may, therefore, assume a secondary importance in predicting droplet evaporation rate [13].

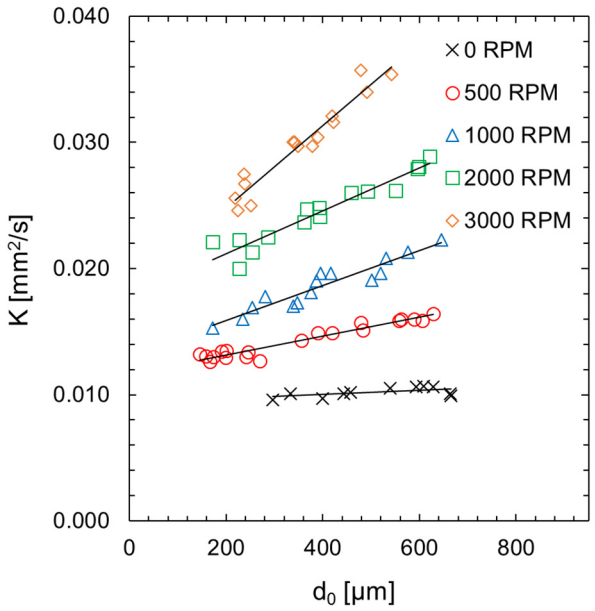


**Fig. 4.9.** Variation of heptane droplet vaporization rate as a function of initial diameter.

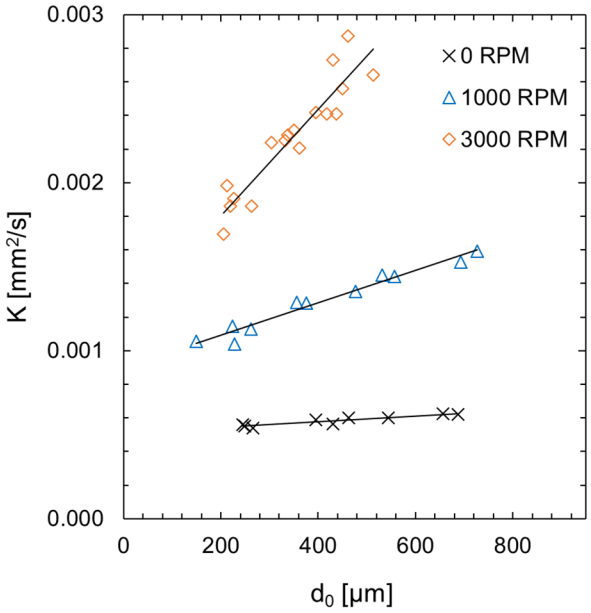


**Fig. 4.10.** Variation of decane droplet vaporization rate as a function of initial diameter.

Nonetheless, the enhancement in the evaporation rate with larger droplets is strongly dependent on the turbulence intensity, as evidenced by the greater slopes in Figs. 4.9 and 4.10 at higher fan speed (i.e., higher turbulence intensity). This experimental finding corroborates the

numerical simulation results reported by Abou Al-Sood and Birouk [162], where a 1500-μm droplet evaporated at a faster rate than a 100-μm droplet when exposed to a turbulent flow field with the same turbulence intensity. In Abou Al-Sood and Birouk [162], the effect of $d_0$ on $K$ is largely attributed to the lower surface temperature (wet-bulb temperature) of the larger droplet, which in turn enhances heat transfer into the droplet and consequently improves its evaporation rate. They also showed that increased turbulence intensity further lowers the droplet surface temperature. While heat transfer effect is considered dominant for droplet vaporization at high temperature [18], the present experiment is conducted with the droplet and its surrounding environment initially set at standard conditions. Although Abou Al-Sood and Birouk [162] found a significant increase in $K$ for a larger droplet in high-temperature environments, the difference in $K$ between these two distinct droplets (1500 μm vs. 100 μm) becomes insignificant as $T_\infty$ approaches 300 K, regardless of turbulence intensity. Similar studies have indicated that the attainable steady-state surface temperatures for both heptane and decane in a room temperature environment are completely independent of turbulence intensity level at standard pressure [159]. Thus, the interaction between droplet size and turbulence observed in the present experiment is believed to extend beyond the dependence on the droplet surface temperature gradient.

Additional observations from Figs. 4.9 and 4.10 are made concerning the improvement in droplet evaporation rate with increasing turbulence intensity. This relationship has been reported to reach a plateau (e.g., [28,31,160,175]); however, the range of turbulence intensity and droplet size tested here produced no such limit. For instance, when plotting the normalized evaporation rate, $K/K_0$, for droplets of similar size against turbulence intensity in Fig. 4.11, the relationship appears linear. Increasing the turbulence intensity further may eventually lead to asymptotic behaviour (i.e., a limiting $q^{0.5}$ value), especially at smaller droplet sizes. The droplet normalized

evaporation rate data indicate that decane, being a substantially less volatile fuel, experiences greater relative enhancement in vaporization with turbulence. This effect of volatility on the normalized evaporation rate under turbulent conditions is well established in the literature (e.g., [16,28,154]). Furthermore, the percent increase in $K/K_0$ with turbulence intensity is a function of $d_0$ and fuel type. An assessment of this effect can be made based on the quasi-linear variation exhibited in Figs. 4.9 and 4.10. For example, a smaller heptane droplet (e.g., $d_0$ = 100 μm) exhibits a 50% increase in $K/K_0$ when the fan speed varies from 1000 RPM ($q^{0.5} \approx 0.51$ m/s) to 3000 RPM ($q^{0.5} \approx 1.53$ m/s); a similar value is found for decane. However, for a larger droplet (e.g., $d_0$ = 700 μm), the increase in $K/K_0$ from 1000 to 3000 RPM is 80% and 115% for heptane and decane, respectively. This concept is illustrated graphically in Fig. 4.12. Thus, as $d_0$ increases, decane appears to experience a substantially greater improvement in the normalized evaporation rate than heptane as the turbulence intensity rises. The following section provides further discussion and proposed correlations.

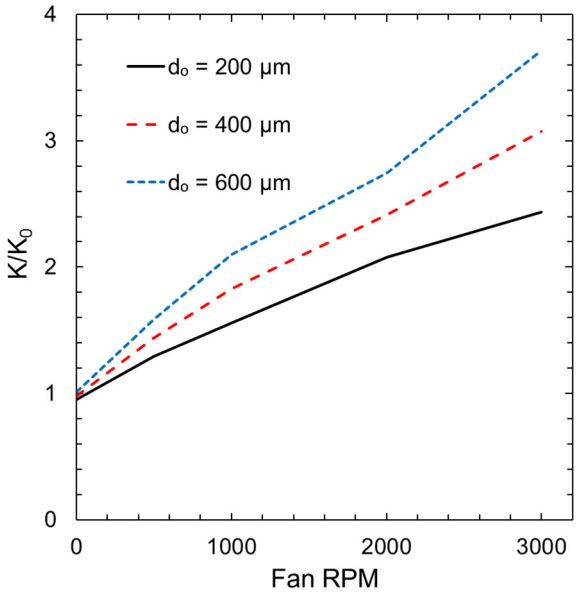


**Fig. 4.11.** Variation in normalized evaporation rate for heptane as a function of fan speed (based on best fit trends).

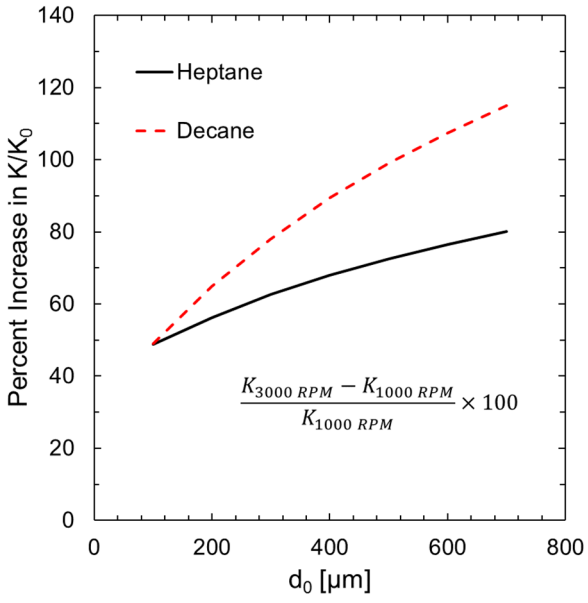


**Fig. 4.12.** Predicted percent increase in normalized evaporation vs. initial diameter (1000 to 3000 RPM).

### 4.1.3 Discussion and correlations

The results presented above reveal the existence of a well-established relationship between turbulence, droplet size ($d_0$), and evaporation rate ($K$). One approach, adopted in the literature, correlates the effect of turbulence on droplet vaporization rate in terms of a turbulent Reynolds number, $Re_t$ (e.g., [13]). A second methodology involves the use of a vaporization Damköhler number, $Da_v$, which represents a ratio between the characteristic time scales of flow and evaporation. Damköhler correlations are versatile and have been used to predict burning droplet extinction (e.g., [176]), optimize combustion intensity and efficiency (e.g., [150,221]) and, of particular relevance, gauge the effectiveness of turbulence on the evaporation of mono-sized droplets (e.g., [16,87,158]). Both approaches will be analyzed here because the development of correlations is useful in a predictive sense, as well as helping to address the issue of why droplet size is a factor in a turbulent environment.

A correlation based on $Re_t^{2/3}$ has shown promise in predicting the evaporation rate of mono-sized droplets in a purely turbulent flow in standard (e.g., [13,28]) and high-pressure environments (e.g., [30,31]). However, this correlation was developed based on data obtained with single hydrocarbon droplets having a size averaging around 1000 μm, yet the present results revealed the dependence of turbulent vaporization rate on droplet size. The predictive capability of the Reynolds number, combined with the interpretation of Reynolds number as a measure of scale separation, alludes to the potential importance of the Kolmogorov length scale, $\eta$, to droplet turbulent evaporation rate. While the ratio of the integral length scale to droplet size may assume a secondary role as a controlling factor, the ratio of Kolmogorov length scale to droplet diameter is much closer to unity in the present investigation, in agreement with realistic conditions (e.g., [12]). This proximity may result in the Kolmogorov length scale asserting precedence over the

larger, more energetic scales from the perspective of droplet-turbulence interaction (e.g., [151]). Adopting the scale relation $\eta/L \sim Re_{t,L}^{-3/4}$, where $Re_{t,L} = q^{0.5}L/\nu$, it can easily be shown that $\eta$ is a strong function of the turbulence intensity $q^{0.5}$ while having only a weak dependency on $L$ (e.g., [222]). As $K$ is proportional to $q^{0.5}$ (Figs. 4.9 and 4.10), it is worth investigating the relationship between the smallest eddies in the flow and the droplet size. Figure 4.13 plots the normalized evaporation rate of heptane droplets with different sizes as a function of $\eta/d_0$.

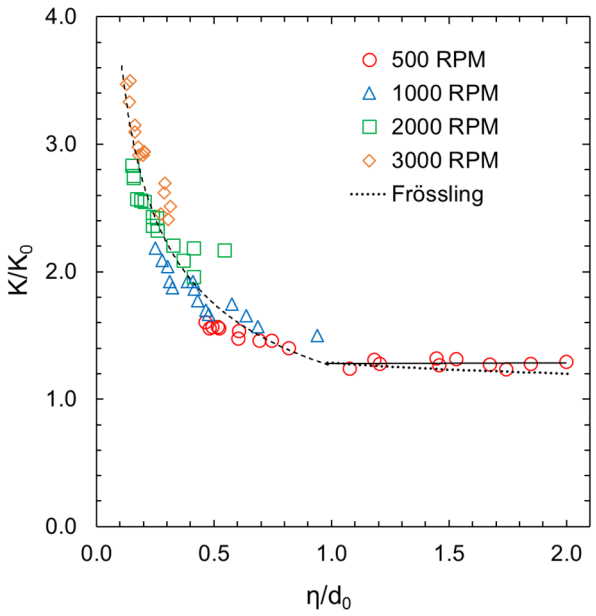


**Fig. 4.13.** Normalized evaporation rate of heptane droplet vs. non-dimensional length. The dashed line represents the best fit for data corresponding to abscissa values less than 1, and values exceeding 1 are fitted with the solid line. The dotted line represents a Frössling correlation prediction of $K_l/K_0$ based on the average mean velocity field at 500 RPM.

It is clear from Fig. 4.13 that the effectiveness of the turbulence, as quantified by its ability to increase the evaporation rate beyond the stagnant (no flow) value, is lessened as $\eta/d_0$ increases. Experiments on decane droplets found a similar relationship. For a Kolmogorov length scale to droplet size ratio ($\eta/d_0$) below unity, the normalized evaporation rate follows a decaying power trend. As $\eta/d_0$ exceeds unity, which occurs for the smallest droplets at the lowest turbulence

intensity level, the normalized evaporation rate levels off and no further change of $K/K_0$ is observed. It is interesting to note that the evaporation rate in this region is still slightly higher than the stagnant case, as $K/K_0 \approx 1.3$. This minor increase is potentially due to the residual mean flow velocity which, although negligible compared to its corresponding fluctuating components, could still contribute to increasing $K$. Based on a simple Frössling correlation ($K_l/K_0 \propto Re_l^{1/2}$) [13], the expected $K_l/K_0$ for small droplets exposed to a similar mean flow present in the center of the chamber is estimated to range between 1.20 and 1.29, which is reasonably close to the residual $K/K_0$ found when the Kolmogorov length scale exceeds $d_0$ (see Fig. 4.13). The present results indicate the existence of two distinct evaporation regimes in a turbulent flow; one for larger droplets which are affected by turbulent fluctuations, and another for small droplets (within the sub-Kolmogorov scale range) which only experience the relative effect of the mean flow. These findings are well in line with the theory that length scale disparity is critical. However, it is the relative size of the Kolmogorov length scale, and not the integral, which should be contrasted with the range of droplet size explored here.

While $d_0$ provides a convenient scaling parameter, it is reasonable to expect that the dynamic interaction between the Kolmogorov length scale and the droplet size persists throughout the evaporation lifetime. Furthermore, this length scale relationship could offer insight into the deviation from the $d^2$ law which some turbulent evaporation studies have witnessed (e.g., [28,175]). Although researchers have attributed this phenomenon to the effect of the suspending fiber (e.g., [28]), the small fibers used in the present study are expected to produce negligible impact (especially at standard/room temperature conditions), yet deviation in the temporal variation of $d^2$ is witnessed as a slight reduction in evaporation rate near the end of the droplet lifetime. This behaviour is only observed under turbulent conditions, as droplets evaporating in

quiescent environments retain a perfectly linear $d^2$ profile throughout their lifetime. It is possible that this departure from linearity represents a transition from turbulence-enhanced evaporation to a phase in which turbulence becomes less effective. This ineffectiveness of turbulence may result from evaporation reducing the droplet diameter to a size smaller than the Kolmogorov length scale. Regardless, it is clear that turbulence effect is important long before the droplet has shrunk to a size approaching the Kolmogorov scale, a result similar to that found by Gökalp et al. [87]. The conclusion reached here is that turbulence becomes ineffective once the initial droplet size (and perhaps the instantaneous diameter) falls below that of the smallest turbulent scales.

Using $d_0$ as the length scale for a turbulent Reynolds number seems ideal based on the above discussion, where $Re_{t,d_0} = q^{0.5} d_0/\nu$. Figure 4.14 plots the normalized evaporation rate of heptane vs. $Re_{t,d_0}^{2/3}$ arranged in groups of similar $d_0$. While the correlation can account for various turbulence intensity levels within each droplet size group ($R^2$ values in Fig. 4.14 are in the range of 0.94 – 0.99), there is an obvious trend disparity between these size groups. The groups can be forced to collapse by including an additional non-dimensional parameter in the form of $L/d_0$. The resultant correlation, expressed as $K/K_0 - 1 \propto Re_{t,d_0}^{2/3}(L/d_0)^p$ where the exponent $p$ has a positive value, does not reflect the typical relationship between $L/d_0$ and $K$ (e.g., [16,87]). Specifically, $K$ is expected to decrease as $L/d_0$ increases, which is not the case for $p > 0$. In addition, using $Re_{t,d_0} = q^{0.5} d_0/\nu$ instead of $Re_{t,L} = q^{0.5} L/\nu$ eliminates the direct link to the Kolmogorov scale, which is related to $L$ though the length scale-based turbulent Reynolds number as $\eta \sim L(Re_{t,L}^{-3/4})$. For these reasons, a correlation based on $Re_{t,L}$ is suggested and Fig. 4.15 plots the result. The inclusion of the Schmidt number, $Sc = D_{AB}/\nu$, is required to account for the difference in fuel vapor diffusivity, where $\nu$ and $D_{AB}$ are, respectively, the kinematic viscosity of

the ambient gaseous phase (nitrogen in the present study), and the vapor-nitrogen diffusivity coefficient. Based on the predominance of nitrogen mole fraction at the surface of the droplet ($X_{N_2,s}$ > 0.92 for both fuels), the kinematic viscosity is considered to be that of only nitrogen. All liquid and gas properties are evaluated using the temperature-dependent formulas provided in [158]. The proposed empirical correlation is expressed as follows:

$$\frac{K}{K_0} = 1 + 0.0142 Re_{t,L}^{\frac{2}{3}} \left(\frac{L}{d_0}\right)^{-0.52} Sc^{2.37} \tag{4.6}$$

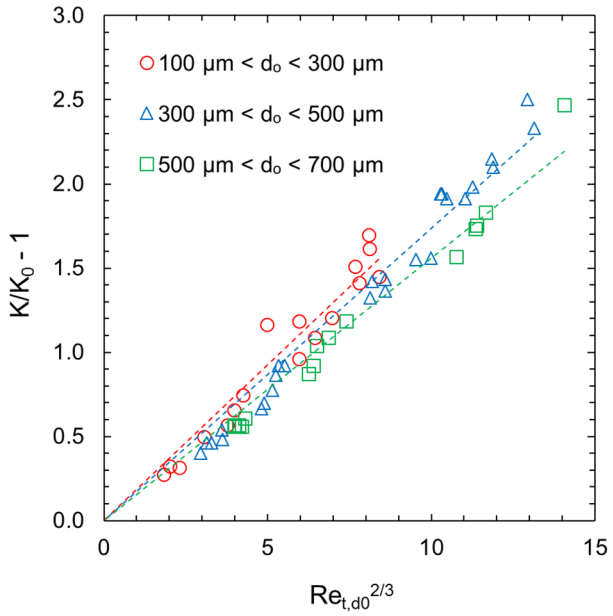


**Fig. 4.14.** Normalized evaporation rate of heptane droplet vs. turbulent Reynolds number.

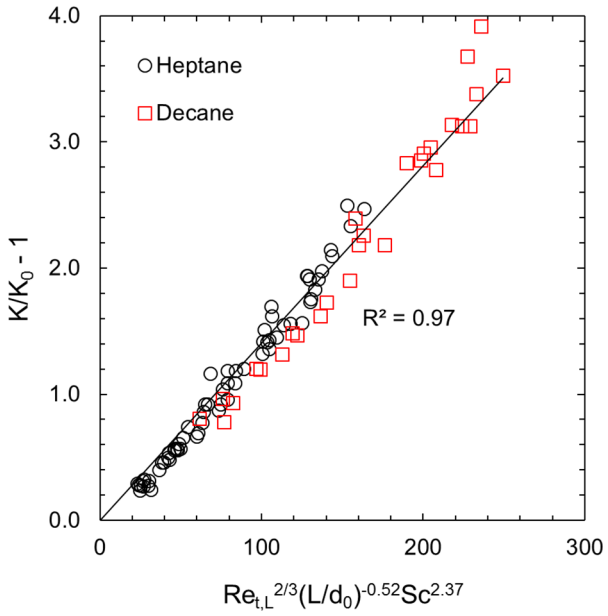


**Fig. 4.15.** Normalized evaporation rate vs. non-dimensional groupings.

This correlation is similar to the relationship developed by Birouk and Gökalp [28], with the added capability of accounting for the influence of $d_0$. The strength of this correlation lies in the intuitive interpretation of the dimensionless groups, as the droplet evaporation rate is expected to increase with turbulent Reynolds number, decrease with $L/d_0$, and increase with $Sc$ due to the unique turbulence-volatility relationship (heavier fuels, which are affected by turbulence to a

greater extent, tend to have lower mass diffusion coefficients and therefore higher Schmidt numbers). In fact, the Schmidt number exponent in Eq. (4.6) greatly exceeds the equivalent exponent in a Frössling-type correlation for pure laminar flow (i.e., 1/3 [13]). Clearly, the influence of fuel volatility on the normalized evaporation rate is a more significant factor for purely turbulent flows than it is for laminar flows, where $Sc$ variation is relatively unimportant in the prediction of $K_l/K_0$. This evidence suggests the possibility of a turbulence-droplet interface interaction in which the smaller-scale eddies promote greater vapor production at the surface of a low-volatility droplet. If the kinetic energy contained within the small-scale eddies interacts with the droplet surface to directly increase evaporation, large droplets are likely to be the primary beneficiaries due to the greater droplet interface-eddies interaction.

A second approach to correlate droplet size, turbulence, and evaporation rate can be achieved using a vaporization Damköhler number, $Da_v$. As defined by Gökalp et al. [87], the Damköhler number represents the ratio of a turbulent flow characteristic time scale, $t_{flow}$, to a time scale which represents the physics of evaporation, $t_{vap}$. It can be defined as follows:

$$Da_v = \frac{t_{flow}}{t_{vap}} \tag{4.7}$$

Where,

$$t_{flow} = \frac{d_0}{q^{0.5}} \tag{4.8}$$

And,

$$t_{vap} = \frac{r_0}{V_r} \tag{4.9}$$

In defining these characteristic time scales, a slightly simpler approach than the one introduced by Gökalp et al. [28], which is based on the concept derived by Abramzon and

Sirignano [125], is adopted in the present analysis. Instead of using the vapor film thickness, $\delta_M$, as the length scale for calculating $t_{vap}$, the initial droplet radius, $r_0$, is incorporated. The usage of $\delta_M$ is controversial as it is derived based on laminar flow considerations, and its applicability to pure turbulence is unknown [13]. The calculation of the characteristic radial velocity is also simplified by using the method of Chauveau et al. [77]. This approach (Eq. (4.10)) is based upon simple liquid-vapor continuity considerations at the droplet interface and replaces the technique of evaluating $V_r$ using purely theoretical formulations for a stagnant environment (e.g., [87]) or laminar flow (e.g., [16]).

$$\rho_v V_r = -\rho_l \left(\frac{dr}{dt}\right) = -\rho_l \left(\frac{1}{4d}\right)\left(\frac{d(d^2)}{dt}\right) \tag{4.10}$$

Droplet evaporation obeys the $d^2$ law in the present study. Therefore, the differential term in Eq. (4.10) is a constant value; that is, $K = -d(d^2)/dt$. The mass density of vapor at the surface, $\rho_v$, is calculated assuming saturation at thermodynamic equilibrium. Because $V_r$ is characteristic of the diffusion process, Eq. (4.10) uses $K_0$. In this manner, $V_r$ represents the expected velocity of the vapor diffusing into a stagnant environment; this development is equivalent to the radial velocity representation in Gökalp et al. [87] and Wu et al. [16]. Furthermore, to define a single unique radial velocity, the diameter term is set to be the droplet initial size. This approach is also consistent with the aforementioned relevant literature. Substitution of Eqs. (4.8) – (4.10) into Eq. (4.7) reveals that $Da_v$ is proportional to $d_0^{-1}$ which confirms that the droplet size dependency of the Damköhler expression developed above is nearly equivalent to the original Gökalp et al. [87] formulation.

The normalized evaporation rate of heptane and decane is plotted against the Damköhler number (Eq. (4.7)) in Fig. 4.16. This approach yields a correlation which is based on a characteristic time scale perspective instead of a ratio of characteristic length scales as in Eq. (4.6), although the two are analogous as proven by Birouk and Gökalp [13]. The equation of best fit has the following form:

$$\frac{K}{K_0} = 1 + 0.0948(Da_v)^{-0.765} \tag{4.11}$$

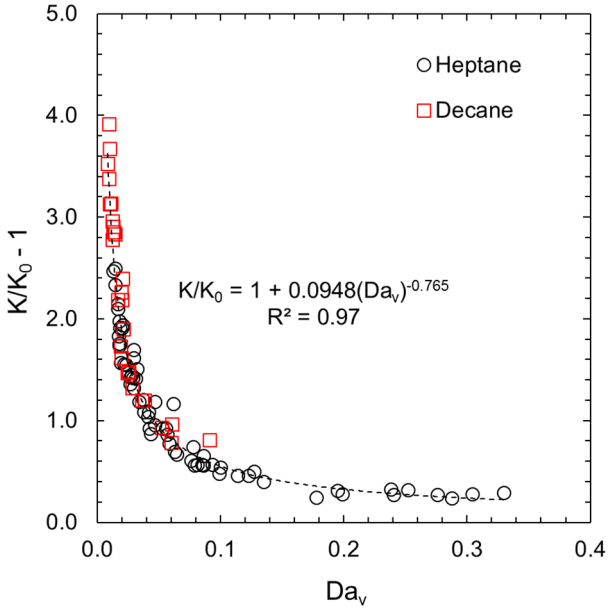


**Fig. 4.16.** Normalized evaporation rate vs. vaporization Damköhler number.

Smaller Damköhler number is clearly associated with greater levels of turbulent interaction, as the increase in droplet vaporization is diminished at higher $Da_v$. Higher turbulence intensity leads to a shorter $t_{flow}$, and therefore small $Da_v$, while greater $Da_v$ are more likely to be associated with high volatility fuels due to their inherently short vaporization time scale. The ineffectiveness of turbulence when the Damköhler number approaches unity agrees with the

findings of Wu et al. [16,29], despite the alternate approach used therein to calculate $Da_v$. Separation of scale is once again shown to be of paramount importance in predicting turbulence effect on droplet evaporation.

Although the approaches adopted by Wu et al. [16,29] and Birouk and Gökalp [13] can collapse several alkane fuels in the same Damköhler correlation, there are good reasons why the methodology set out here may yet represent an improvement to the concept of the Damköhler method. Specifically, the correlation developed by Wu et al. [16,29] predicts the normalized evaporation rate with respect to the laminar flow value rather than $K_0$. Furthermore, the turbulent flow generated in these studies feature a significant mean component ($\overline{U} > U_{rms}$) which may dominate the effect of turbulence and make comparisons with purely turbulent flows difficult. As previously mentioned, the Damköhler correlation developed by Birouk and Gökalp [13] cannot account for variations in droplet size and, in light of the significant size dependency witnessed in the present study, is inappropriate for correlating the current data. One point of consistency across all proposed Damköhler relations is the clear ineffectiveness of turbulence at higher $Da_v$.

These correlations provide two distinct prediction approaches; one based on the separation of characteristic length scales (Eq. (4.6)) and another on the separation of time scales (Eq. (4.11)). In the case of the Damköhler correlation, the distinction between whether turbulence serves purely as a diffusion enhancer, or engages in an as-of-yet unspecified mechanism to promote non-equilibrium vapor production at the surface, is an important one. Invoking the Clausius-Clapeyron assumption to calculate the mass density of the fuel at the droplet surface, $\rho_v$, requires the implicit belief that the interface condition is indeed one of thermodynamic equilibrium. While the enhancement of vapor diffusion is almost certainly a result of turbulence, the possibility of small-scale eddy interaction with the liquid in a manner which increases the vapor fraction at the droplet

surface is speculative at this point, although other studies have suggested it (e.g., [16]). The existence of such a phenomenon would act in concert with the improved diffusion gradient, as there would be a physically greater amount of vapor to diffuse. Indeed, if turbulence only aided in diffusion, an argument could be made that fuels with higher vapor fractions at the surface would be the primary beneficiaries; this is precisely the opposite of the observed effect. The vapor mass density at the surface of a decane droplet is 90% less than that of heptane, meaning that there may not be much vapor diffusion improvement for decane as the available vapor at the droplet surface is exceedingly low in comparison with that of heptane.

## 4.2 Droplet evaporation at elevated pressure and temperature

Additional PIV and droplet evaporation tests were performed at elevated conditions to compliment and expand upon the experimental discoveries at standard pressure and temperature. This section investigates the evaporation characteristics of both heptane (up to 10 bar and 75°C) and decane (up to 10 bar and 100°C) droplets. As in Section 4.1, the ambient gas is nitrogen and fan speeds range from 0 – 3000 RPM. Figure 4.17 provides a graphical summary of the evaporative test conditions (including those in Section 4.1).

The primary difference in apparatus setup for elevated conditions is the addition of a heating coil plate in an unused window port (Fig. 4.18). The control system maintained the desired ambient temperature to within $\pm 1\%$ of the set point. Comparative tests with multiple thermocouples (Fig. 4.18) indicated that the temperature field was consistent across the horizontal midplane, which is where the droplet was formed and evaporated (the long thermocouple is thus removed for PIV and evaporative studies). Fan-induced mixing helps promote temperature field

consistency of the gaseous phase inside the chamber. For experiments performed under stagnant conditions, the fans were briefly run immediately before each test to promote uniform thermal distribution. The chamber is well insulated and upon reaching thermal equilibrium the energy input from the heating element, and thus the potential for radiative influence, is low. Compressed nitrogen supplied from a commercial cylinder was used to pressurize the chamber. As with the temperature, the pressure inside the chamber was held at $\pm$ 1% throughout the course of the experiments. Due to the quality of the gaskets and seals, very little leak-down occurred (~0.002 bar/min. at a nominal pressure of 6.9 bar). A vacuum pump was periodically activated to purge and refill the chamber to reduce the build-up of fuel vapor.

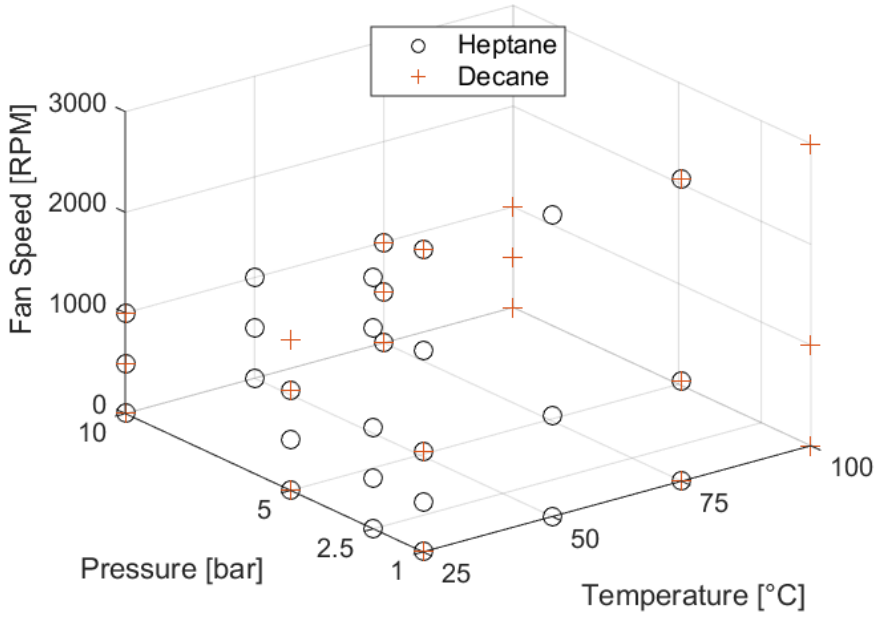


**Fig. 4.17.** Graphical summary of all ambient test conditions.

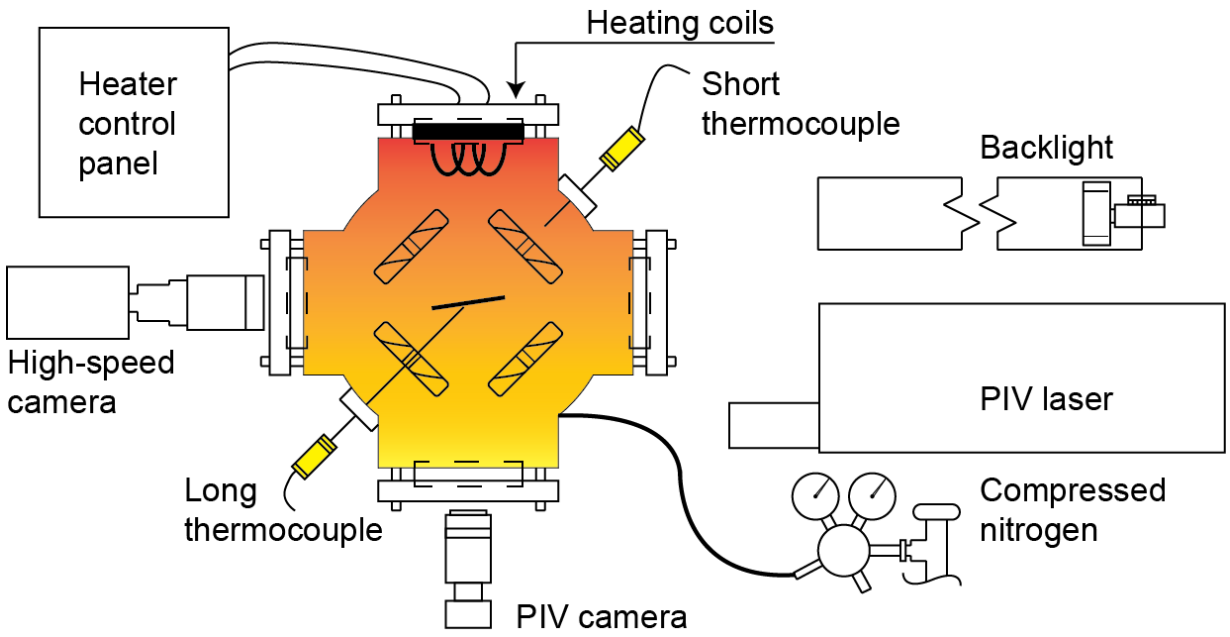


**Fig. 4.18.** Overhead view of the heated chamber (cross-sectional) with PIV and droplet imaging equipment shown (roughly to scale). The details of the fan motors and hubs are omitted for clarity. The right-hand window accommodates either the PIV laser for flow field characterization or the backlight for droplet imaging. Thermocouple and pressure transducer (not shown) output is sent to a PC.

### 4.2.1 Turbulence characterization

Particle image velocimetry experiments were repeated under high pressure and temperature test conditions to evaluate any changes in the flow field. The flow field characteristics are documented for fan speeds ranging from 1000 to 3000 RPM at 10 bar and 25°C, and 10 bar and 100°C. In most cases, increasing the pressure and temperature slightly improved the homogeneity and isotropy of the flow field, as the ratio measures of these qualities attained values closer to unity. Spatially, the region which could be considered homogeneous and isotropic is thus expanded beyond the 20-mm diameter established at room conditions, although this diameter meets or exceeds the integral length scale, $L$, and is therefore considered inconsequential for studies on micro-sized droplets.

Figure 4.19 illustrates the linear relationship between fan speed, $N$, and $q^{0.5}$ at all test conditions. There is a slight difference in trend at elevated test conditions, but the difference

between the minimum and maximum intragroup slopes is only 6%. The average relationship between the fan speed and turbulence intensity is expressed as $q^{0.5} = 0.000526 \times N$. Instantaneous velocity vectors observed during elevated pressure tests indicate the presence of smaller-scale eddies and less-coherent structures (compared with those at standard test conditions) as the kinematic viscosity, $\nu$, of the gaseous phase decreases (Figs. 4.20 and 4.21). From the perspective of turbulence, increasing pressure acts to reduce the size of the smallest eddies as $L$ remains constant, yet the turbulent Reynolds number, which governs scale separation, increases as $\nu$ decreases. Ambient temperature has the opposite effect. In this way, the effect of turbulence intensity and the Kolmogorov scale are separated, as altering the pressure and temperature can create a range of small-scale eddy size at any given turbulence intensity (fan speed).

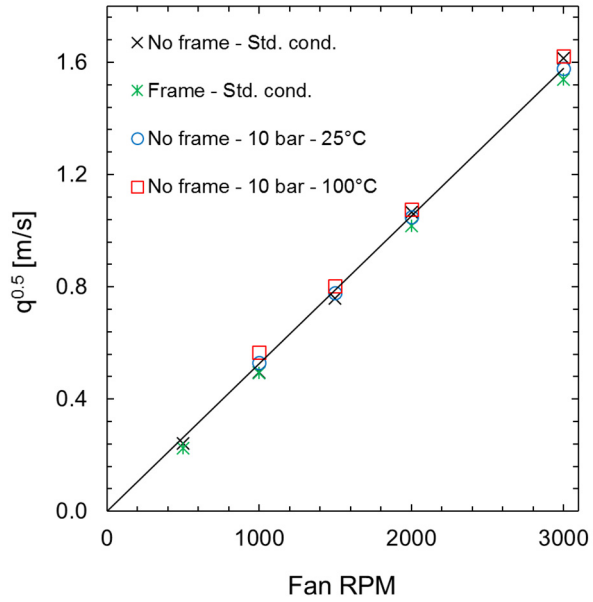


**Fig. 4.19.** Evolution of turbulence intensity with fan speed – elevated conditions comparison.

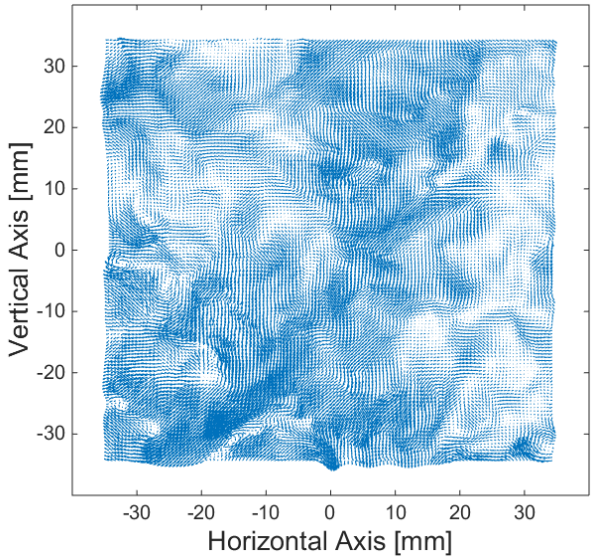


**Fig. 4.20.** Instantaneous flow field vectors at 1 bar and 1000 RPM.

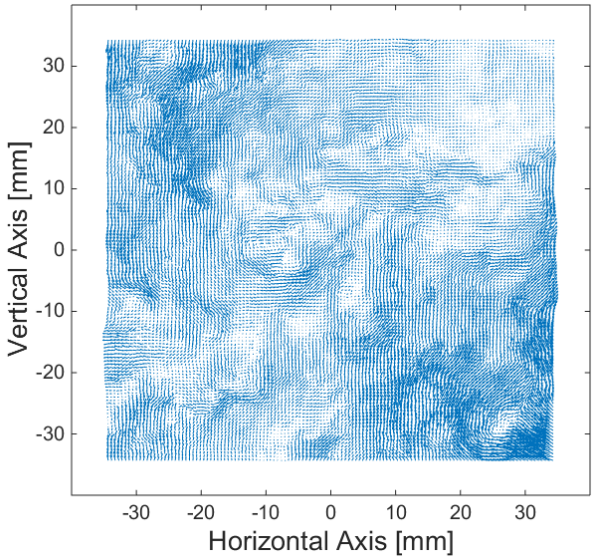


**Fig. 4.21.** Instantaneous flow field vectors at 10 bar and 1000 RPM.

The measured integral length scales at elevated pressure and temperature are randomly scattered around an average value of 21.35 mm. The integral length scale is thus assumed independent of ambient turbulence intensity, pressure, and temperature. This value compares favorably to the integral length scale determined at standard pressure and temperature conditions (20.55 mm) in Section 4.1.1. The combination of all collected PIV data, including at standard test conditions, results in an average length scale of 21.23 mm. Table 4.2 summarizes the parameters for droplet evaporation at elevated conditions.

**Table 4.2**
Summary of test conditions at elevated pressure and temperature.

| $d_0$ [µm] | $q^{0.5}$ [m/s] | $T_\infty$ [°C] | $P_\infty$ [bar] | $L/d_0$ [-] | $\eta/d_0$ [-] | $Re_{t,d0}$ [-] |
|---|---|---|---|---|---|---|
| 110 – 730 | 0 – 1.58 | 25 – 100 | 1 – 10 | 29 – 188 | 0.05 – 1.34 | 0 – 175 |

### 4.2.2 Droplet evaporation at elevated pressure

#### *4.2.2.1 Stagnant (natural convection) conditions*

The results and discussion in Section 4.1.2 emphasize that the evaporation rate of heptane and decane droplets does not vary significantly with initial size in a stagnant ambience. The elevated pressure condition provides an opportunity to re-evaluate this conclusion. Indeed, one apparent consequence of the elevated pressure is the increased size effect at quiescent conditions. Figure 4.22 graphically illustrates the expected percent increase in $K$ for 700-µm droplets as compared to 100-µm droplets. Although the heptane data, in particular, is fairly scattered, a rough trend comparison can still be made. At standard pressure, heptane and decane feature a 10% and 20% increase, respectively, in evaporation rate for a 700-µm droplet as opposed to a 100-µm droplet. At a pressure of 10 bar, the percent increase exceeds 50% for both fuels. This improvement is not a trivial increase and indicates that size may influence droplets in the sub 100-µm range even without turbulence or flame.

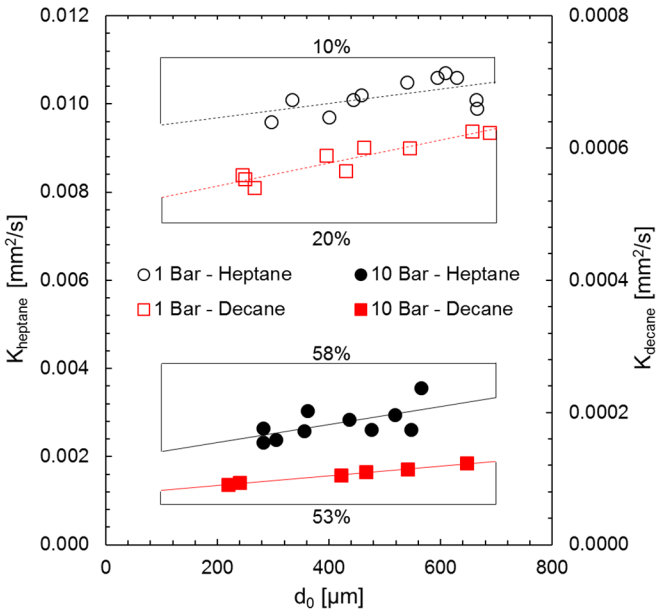


**Fig. 4.22.** Percent increase in $K_0$ with initial droplet size at 1 and 10 bar.

With no turbulent eddies interacting with the droplets, it is likely that natural convection is the reason for the size effect in a stagnant pressurized atmosphere. Although the temperature of the gas and liquid are initially equal (or approximately so), the evaporative cooling at the surface will lower the temperature at this location, resulting in a small temperature variation across the interface. Hegseth et al. [223] measured the temperature gradient of an evaporating methanol droplet and concluded that even the small temperature gradients experienced at room conditions can lead to major discrepancies in the characteristic time scales of liquid conduction and natural convection. While studies have examined or acknowledged the role of natural convection in elevated pressure environments (e.g., [81,97,224]), the temperature is typically elevated as well. Thus, it is interesting to note that even at room temperature, moderate ambient pressure appears to be sufficient to induce meaningful natural convection. In the absence of temperature gradients, the inherent variation in density between heavy fuel vapor and nitrogen is enough to drive a downward convective flow. As the Grashof number, $Gr$, is proportional to the square of pressure, increasing the pressure to 10 bar has effectively multiplied the natural convection "potential" by 100. Coupled with the fact that $Gr$ is proportional to the characteristic length, $d_0$, to the third power, this could be evidence of a minor, but clear, natural convection effect at moderate pressure and room temperature.

Analyzing the temporal $d^2$ profiles grants additional insight into the issue of natural convection in a quiescent environment. At room temperature, heptane exhibits excellent linearity ($d^2$ adherence) regardless of droplet size or pressure. On the other hand, decane droplets show higher incidences of $d^2$ deviation, which appear as a reduction in droplet evaporation rate at later stages of the lifetime profile. Although it is always possible to identify a significant linear portion of the droplet's lifetime (from which $K$ is assigned), large decane droplets, in particular, tend to

demonstrate late-stage deviation for all tested pressures. As the pressure increases, smaller droplets begin to show non-linear evaporation behaviour at earlier stages of their lifetime. For example, Figs. 4.23 and 4.24 compare the lifetimes of two similarly-sized (and reasonably small) decane droplets in a stagnant room temperature environment at two different pressures. Figure 4.23 plots the evaporation of a droplet at 1 bar and is a classic example of $d^2$ adherence. In Fig. 4.24, the pressure has been increased to 10 bar, and the departure from linearity is obvious. As discussed above, pressure dramatically increases the potential for natural convection to become a contributing factor in determining the overall evaporation rate. Due to the inherently poor vapor production and subsequent weak diffusion of decane, this fuel is likely to be impacted by natural convection to a greater extent than lighter fuels with high volatility. In other words, the fraction of total vapor dispersion attributed to natural convection could be significantly higher for decane than heptane. This would help explain the deviation witnessed in Fig. 4.24; that is, the contribution of natural convection is significant enough for decane at 10 bar that when the instantaneous droplet size becomes sufficiently small, the effect, which is strongly dependent on size, begins to waver. Furthermore, the reason for witnessing such behaviour in decane, but not for heptane, is contained within this explanation.

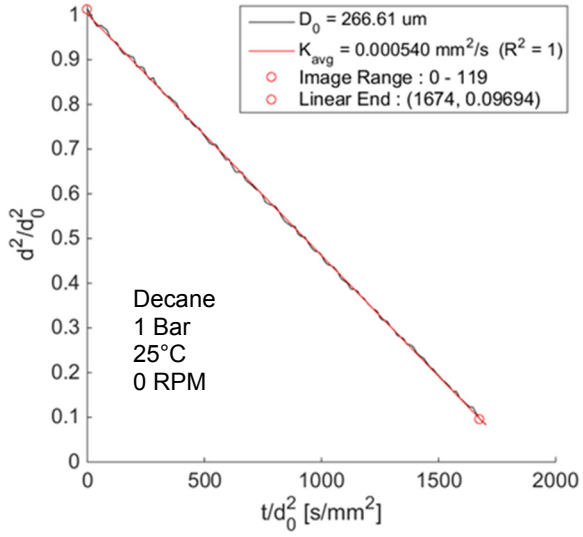


**Fig. 4.23.** Temporal $d^2$ profile of decane droplet at standard atmospheric pressure.

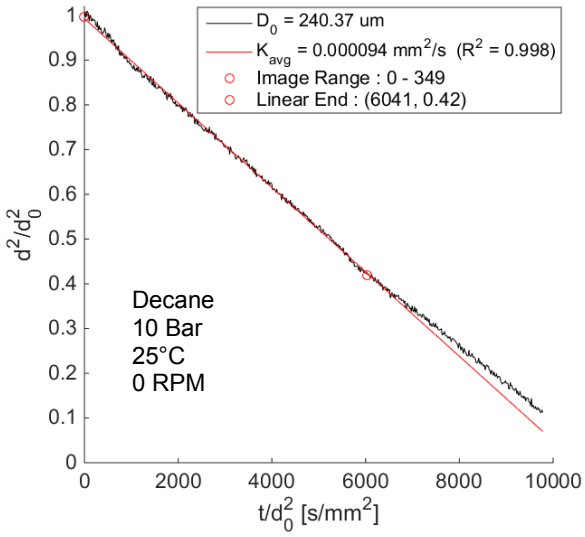


**Fig. 4.24.** Temporal $d^2$ profile of decane droplet at elevated pressure (10 bar).

The reason previous studies have failed to notice this effect is likely attributed to the predominant utilization of single suspending fibers, as well as the lack of evaporation studies (as compared to combustion) which take advantage of the cross-fiber. It is not possible to observe instantaneous droplet diameters approaching extinction with single fibers, as the minimum observable size is similar in scale to the supporting fiber nodule, which can measure several hundred micrometers in diameter (e.g., [20,31,87]). In one of the only cross-fiber experiments to focus on pure evaporation, Chauveau et al. [77] presents decane vaporization data with clear $d^2$ deviation in normal gravity at an elevated temperature. Extending the analysis to microgravity results in even more exaggerated two-stage $d^2$ behaviour until the ambient temperature approaches 1000 K. The authors propose that the lack of buoyancy at microgravity reduces natural convection to an extent that introduces transient vapor build-up effects. It is therefore apparent that poor natural convection can result in transient evaporation characteristics. However, in the present case,

the transient behaviour is introduced at normal gravity due to the reduction in droplet size. Section 4.2.4 discusses instances of $d^2$ deviation under turbulence.

*4.2.2.2 Turbulent conditions*

Figures 4.25 and 4.26 present the vaporization rate of heptane and decane droplets, respectively, as a function of the initial droplet size for zero (quiescent) and higher fan speeds at 10 bar and room temperature. These figures clearly show the evaporation rate, $K$, increases linearly with the initial droplet size, $d_0$. This is observed throughout the entire elevated pressure range (2.5 – 10 bar). The maximum fan speed which enables droplet formation at 10 bar was found to be approximately 1000 RPM.

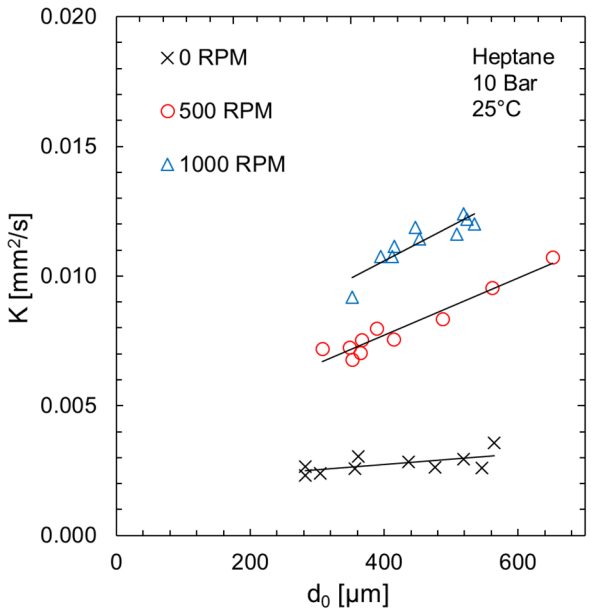


**Fig. 4.25.** Heptane evaporation rate as a function of initial droplet size at 10 bar.

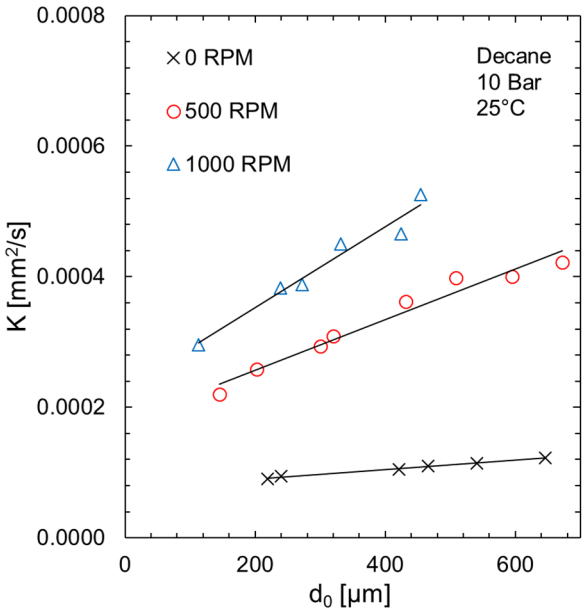


**Fig. 4.26.** Decane evaporation rate as a function of initial droplet size at 10 bar.

The present results reveal that increasing the pressure while holding other parameters (initial droplet size, fan speed, and temperature) constant results in a decrease of the evaporation rate. This decrease is a consequence of the low range of temperatures tested in the present study

and is in accordance with published results. Of greater interest is the variation of the normalized evaporation rate, which is defined as the turbulent evaporation rate divided by the corresponding stagnant evaporation rate, $K/K_0$, at the same temperature and pressure condition. This ratio may be interpreted as the effectiveness of turbulence. Consistent with the findings of Birouk and Fabbro [30], the effectiveness of turbulence increases with pressure as illustrated in Fig. 4.27 for typical turbulence intensity (1000 RPM). The variation of the ratio $K/K_0$ as a function of droplet size is also dependent on pressure, as the slope of each pressure group increases from 1 to 10 bar. This behaviour hints at the importance of the Kolmogorov length scale, $\eta$, and its magnitude compared to the initial droplet diameter (i.e., $\eta/d_0$), where smaller ratios correspond to higher normalized evaporation rates (Section 4.1.3). Figure 4.28 shows an excellent correlation between $K/K_0$ of heptane droplet and $\eta/d_0$ for all collected data at various initial diameter, turbulence intensity, and ambient pressure (which reduce the small-scale eddies significantly). This figure further demonstrates the importance and predictive potential of scale separation between the Kolmogorov eddy size and the initial droplet diameter, first established in Section 4.1.3. A similar trend is witnessed for decane, although the data is slightly more scattered. Gökalp et al. [87] reached a similar conclusion regarding the improvement in mass transfer as the characteristic turbulent scales are reduced in size, although the authors compared the integral length scale, not the Kolmogorov scale, to the initial droplet diameter. The generation of smaller turbulent structures utilizing elevated pressure has essentially separated the effects of turbulence intensity (which does not vary with pressure, see Fig. 4.19) and the Kolmogorov length scale. Turbulence intensity helps increase $K/K_0$ because it generates smaller eddies; however, the fundamental reason behind the intensity effect is the size of the Kolmogorov scale itself and its ratio to the initial droplet size. This interpretation reinforces the conclusion of Eckartsberg and Kapat [155] who reasoned that the

strength of eddies smaller than the droplet size, and not the turbulence intensity, is the appropriate parameter responsible for controlling the enhancement of turbulent droplet evaporation. The stabilization of $K/K_0$ as $\eta/d_0$ exceeds unity in Fig. 4.28 is attributed to the transition from turbulence-enhanced evaporation to pure background laminar effect, as discussed in Section 4.1.3.

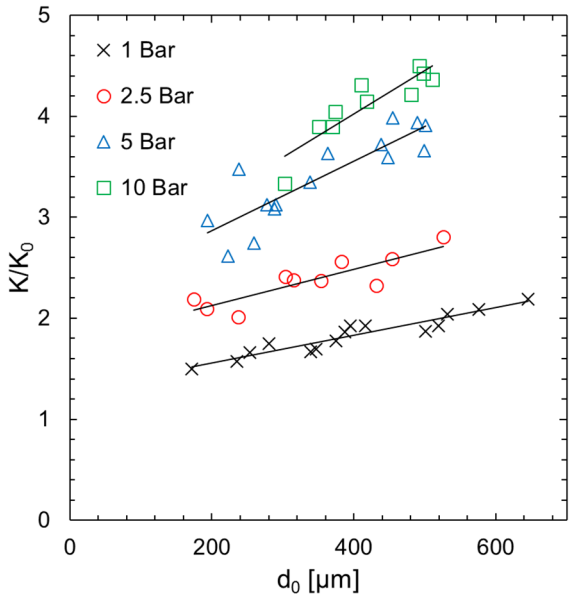


**Fig. 4.27.** Normalized evaporation rate of heptane droplet vs. $d_0$ at various pressures (1000 RPM).

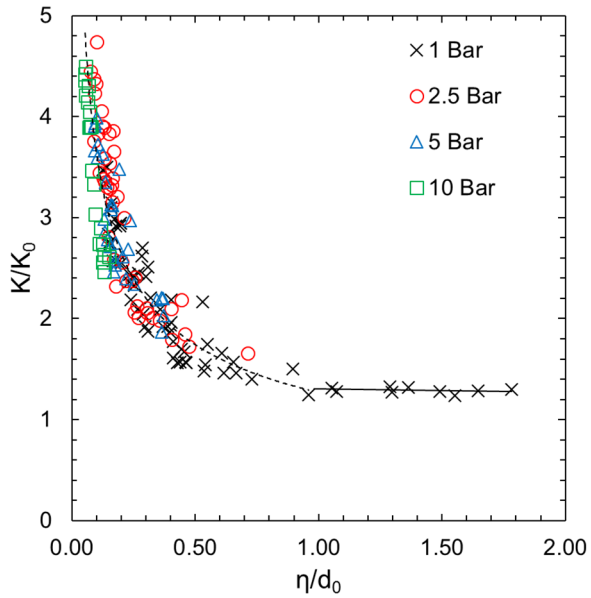


**Fig. 4.28.** Normalized evaporation rate of heptane droplet vs. non-dimensional length (all RPM and initial size).

The results plotted in Figs. 4.27 and 4.28 suggest that the enhancement of turbulent evaporation rate slows down with further increase in ambient pressure. Birouk and Fabbro [30] observed that the decrease in $K$ (or the plateau of $K/K_0$) with increasing the ambient pressure appears to reach a limiting value at approximately 10 bar. They tested relatively large ($d_0 >$ 1000 μm) mono-sized droplets, thus it is important to evaluate the trend across the range of smaller droplets created presently. Based on the established dependency of $K$ on the initial droplet size at all studied pressures, it appears helpful to segregate the droplets into groups of similar initial size. Figures 4.29 and 4.30 illustrate the measured vaporization rates of heptane and decane droplets

having an initial size smaller than 300 µm and greater than 500 µm, respectively. In all cases, as expected, the evaporation rate drops rapidly with pressure but levels off around 10 bar, confirming the findings of Birouk and Fabbro [30]. Interestingly, the reduction in $K$ for heptane and decane in a stagnant environment follows a very similar trend. However, at 1000 RPM, decane droplets experience a quicker decrease in $K$ as the pressure rises. This finding provides a different perspective on the issue of turbulence effectiveness for different fuels, where the advantage held by decane at atmospheric pressure (that is, enhanced $K/K_0$) lessens at higher pressure. Figure 4.31 summarizes these results and reveals that turbulence effectiveness reversal for heptane and decane occurs only for small droplets, whereas droplets which are initially large maintain the relationship established at atmospheric pressure. This finding could not be evaluated at higher levels of turbulence due to the difficulty in anchoring droplets on the cross-fiber in a high-pressure turbulent environment. Based on the trend agreement between the data in Birouk and Fabbro [30] and the data presented here, the results at higher fan speeds are expected to be similar.

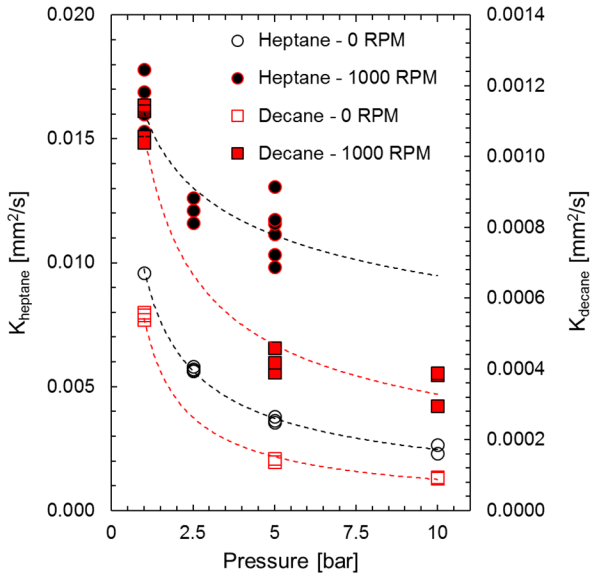


**Fig. 4.29.** Effect of pressure on the vaporization rate for small droplets ($d_0$ < 300 µm).

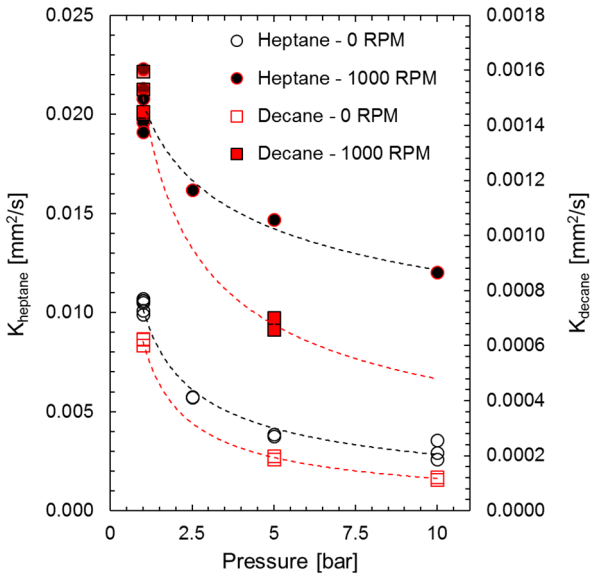


**Fig. 4.30.** Effect of pressure on the vaporization rate for large droplets ($d_0$ > 500 µm).

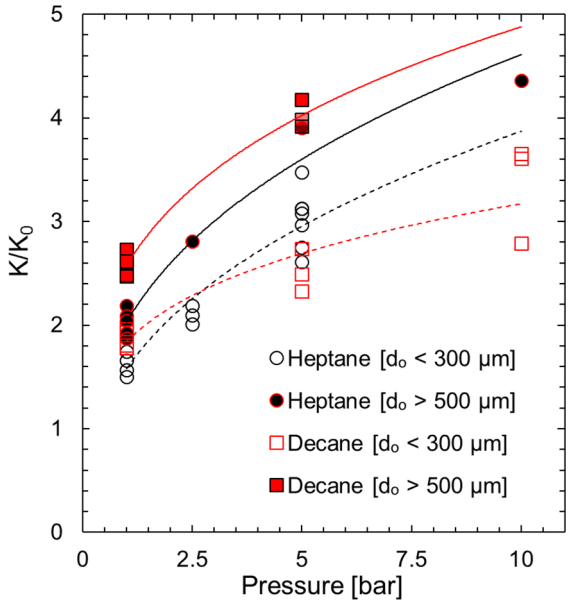


**Fig. 4.31.** Normalized evaporation rate vs. pressure at 1000 RPM.

Figures 4.29 and 4.30 suggest that regardless of fuel type, environment (quiescent or turbulent), or initial droplet size, the vaporization rate decreases with pressure until approximately 10 bar, at which point the trend begins to flatten out. The finding of pressure insensitivity exists in the literature (e.g., [21]) but in these cases, the elevated temperature is positioned such that a balance is established between the increase in the droplet surface temperature, $T_s$, and the decrease in $h_{fg}$ as the pressure rises, thereby maintaining the expected droplet lifetime. Such a temperature is hundreds of degrees higher than the ambient temperature tested here; thus, heat transfer is unlikely to be the dominant reason for the observed behaviour. In the absence of turbulence, it might be possible to assess the physics as a balance of a different kind between the reduced diffusion and increased natural convection which accompany high pressure. However, the fact that droplet vaporization behaves in the same relative manner under turbulence largely refutes this possibility. While natural convection appears to play a significant role in a stagnant environment

(Section 4.2.2.1), it is unlikely to compete with the effect of strong turbulence. Therefore, the answer must lie elsewhere.

It is clear that increasing the ambient pressure at low temperature reduces the potential for diffusion, as the available molar fraction of fuel on the surface, based on thermodynamic equilibrium, varies as $X_{F,S} \propto 1/P$. Thus, a plot of $X_{F,S}$ against pressure strongly replicates the trends in Figs. 4.29 and 4.30. To further illustrate in a more rigorous fashion, the evaporation rate, as predicted by classic diffusion theory, is plotted in Fig. 4.32 against pressure for heptane and decane. The classic theory relation for determining $K$ considers both pure diffusion and bulk motion of the vapor, as follows:

$$K = \frac{8\bar{\rho}_g D_{AB}}{\rho_l} \ln(1 + B) \tag{4.12}$$

In Eq. (4.12), the Clapeyron approximation is used to estimate molar fuel fractions at the droplet surface, while gas-phase ideality is assumed when calculating the averaged gas density. Liquid density is held constant, and the mass diffusion coefficient is determined via the method proposed by Fuller et al. [119]. Equation (4.12) typically does not provide quality predictions when compared to experimental results for several reasons (e.g., natural convection, difficulty in assigning a temperature to calculate the constant thermophysical properties, and questionable validity at high reduced pressures), but it is used here to illustrate the relative change in theoretical evaporation rate in a stagnant environment over a range of pressure.

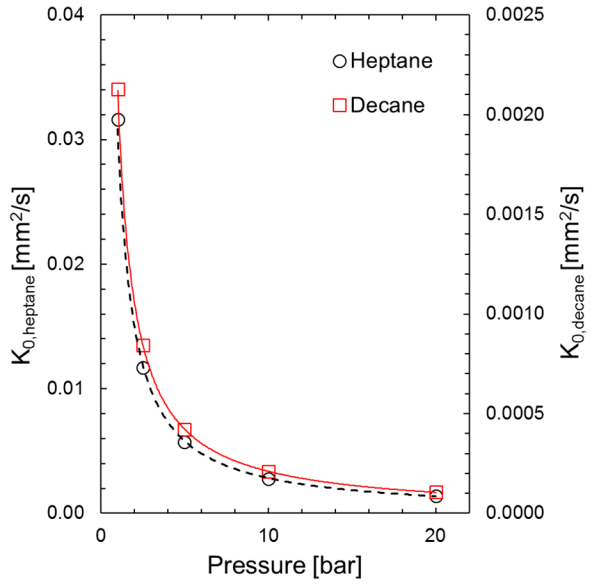


**Fig. 4.32.** Theoretical stagnant room temperature evaporation rate for heptane and decane as a function of ambient pressure.

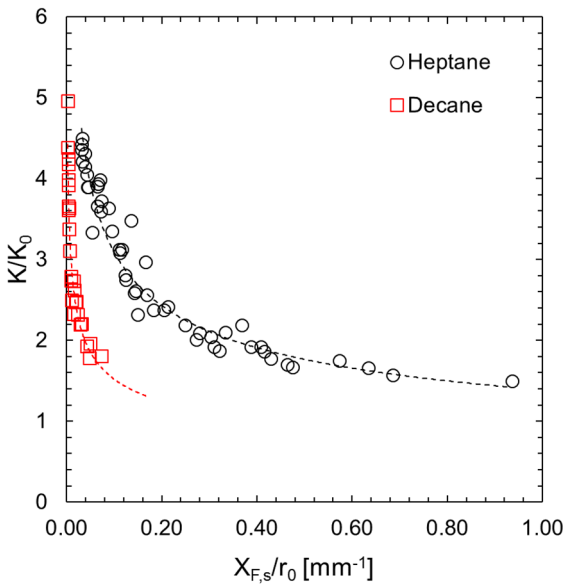


**Fig. 4.33.** Normalized evaporation rate vs. predicted stagnant fuel concentration gradient at surface of droplet (1000 RPM).

The similarity between the predicted $K$ plotted in Fig. 4.32 and the evaporation trends in Figs. 4.29 and 4.30 is obvious. At 10 bar, pressure has suppressed the potential for diffusion to such an extent that further increasing the ambient pressure has little effect. It is hypothesized that this is the reason for the stabilization of evaporation rates (with and without turbulence) observed at high pressure in Figs. 4.29 and 4.30. The agreement between theory and experiment is not surprising for the stagnant environment, as the conditions closely match those which formulate the theoretical prediction of Eq. (4.12); however, the compliance witnessed for the turbulent results is interesting. If indeed the role of turbulence is to improve the diffusion of pre-existing vapor, one interpretation is that there is simply not enough gaseous fuel produced at high pressure to allow for any additional enhancement. This reasoning, based on vapor-liquid equilibrium, is substantially different from the explanation provided by Birouk and Fabbro [30], which emphasized heat transfer (or lack thereof) as the reason for the eventual ineffectiveness turbulence-enhanced vaporization at elevated pressure. This concept is extended further in Fig. 4.33 which illustrates

the effectiveness of turbulence at 1000 RPM against the expected fuel concentration gradient magnitude on the surface of a droplet in a quiescent environment. The solution of the mass diffusion equation in the radial direction with the two quasi-steady boundary conditions ($X_F(r = r_s) = X_{F,s}; X_F(r \to \infty) = 0$) leads to a simple representative expression for the concentration gradient at the surface as:

$$\left.\frac{dX_F}{dr}\right|_{r=r_s} = -\frac{X_{F,s}}{r_s} \tag{4.13}$$

Equation (4.13) uses the initial droplet radius to calculate the abscissa values in Fig. 4.33 and as with Eq. (4.12), Eq. (4.13) should be considered useful for comparative purposes only. There are several notable features in Fig. 4.33. Clearly, low stagnant concentration gradients at the surface result in higher turbulence effectiveness – to a certain point. This occurs because a low concentration gradient represents a scenario which can be improved significantly by turbulence, whereas a droplet which is already evaporating rapidly via the diffusion mechanism has less potential for enhancement. Although $K/K_0$ monotonically increases with a reduction in gradient, a limiting value for both fuels is reached at approximately $K/K_0$ = 5 as the gradient approaches zero. For a given value of $X_{F,s}/r_0$, heptane exhibits higher turbulence effectiveness. If heptane and decane were to have similar gradient values, the heptane droplet would either need to be much larger or at a higher pressure, both of which increase $K/K_0$ (Fig. 4.27).

Overall, the complex issue of size, pressure, fuel type, and evaporation rate is best described from two perspectives: the ratio of Kolmogorov length scale to the initial droplet diameter and the molar fuel gradient at the surface of the droplet. The first group, $\eta/d_0$, represents the turbulent potential based on a length scale ratio. The second group, $X_{F,s}/r_0$, provides a measure

of the mass diffusion potential in the absence of turbulence. Small values of both $\eta/d_0$ and $X_{F,s}/r_0$ maximize the overall effectiveness of turbulence. These values are not independent of one another, as both include the initial size of the droplet, and pressure is also a common factor. This theory helps explain why the droplet size ($d_0$) becomes an increasingly important parameter in predicting the evaporation rate in a turbulent environment.

The concepts developed above are illustrated schematically in Fig. 4.34, where a) and b) represent an initially large and small droplet of heptane, respectively, while c) and d) depict a large and small droplet of decane. The small droplet diameter, $d_2$, is some fraction, $f$, of the large size, $d_1$. The length $\delta_{vap}$ represents a characteristic thickness of the region surrounding the droplet in which a significant vapor fraction exists based on diffusion considerations. For example, if the vapor concentration is considered negligible when it reaches 10% of the saturated surface value, then $CX_{F,s} = 0.1X_{F,s}$ and $\delta_{vap} = (1/0.1 - 1)r_1 = 9r_1$. Although decane has a much lower value of $X_{F,s}$ than heptane at the same ambient conditions, the theoretical vapor thickness as defined above is only a function of droplet size. Smaller droplets (Fig. 4.34 b) and d)) for a given fuel have the same fuel molar fraction at the surface as a large droplet but a smaller value of $\delta_{vap}$, leading to increased surface gradients and less potential for turbulence to enhance the vaporization. On the other hand, large droplets (Fig. 4.34 a) and c)) have small gradients at the surface, leading to an opportunity for turbulence to strongly improve the diffusion of vapor. The rapid reduction in turbulent vaporization rate with pressure for decane (as witnessed in Figs. 4.29 – 4.31) can be interpreted using Fig. 4.34. At low pressure, large decane droplets benefit from the poor theoretical gradient at their surface, and turbulence enhances $K$ significantly. For a similarly-sized droplet at high pressure, the further reduced gradient implies even greater potential for turbulent enhancement. However, when the droplet is small, the gradient is improved. Pressure reduces the

gradient, but at this point, there is very little decane vapor available at the surface for turbulence to diffuse and disperse. On the other hand, heptane at 10 bar has a greater mole fraction available at the surface than decane at 1 bar, which means it is not affected to the same extent when the droplet becomes small and the pressure rises. The small decane droplet under high pressure, therefore, represents a worst-case scenario for turbulence enhancement; a relatively high diffusion gradient (due to the small size) and an extremely low vapor concentration at the surface (due to the pressure).

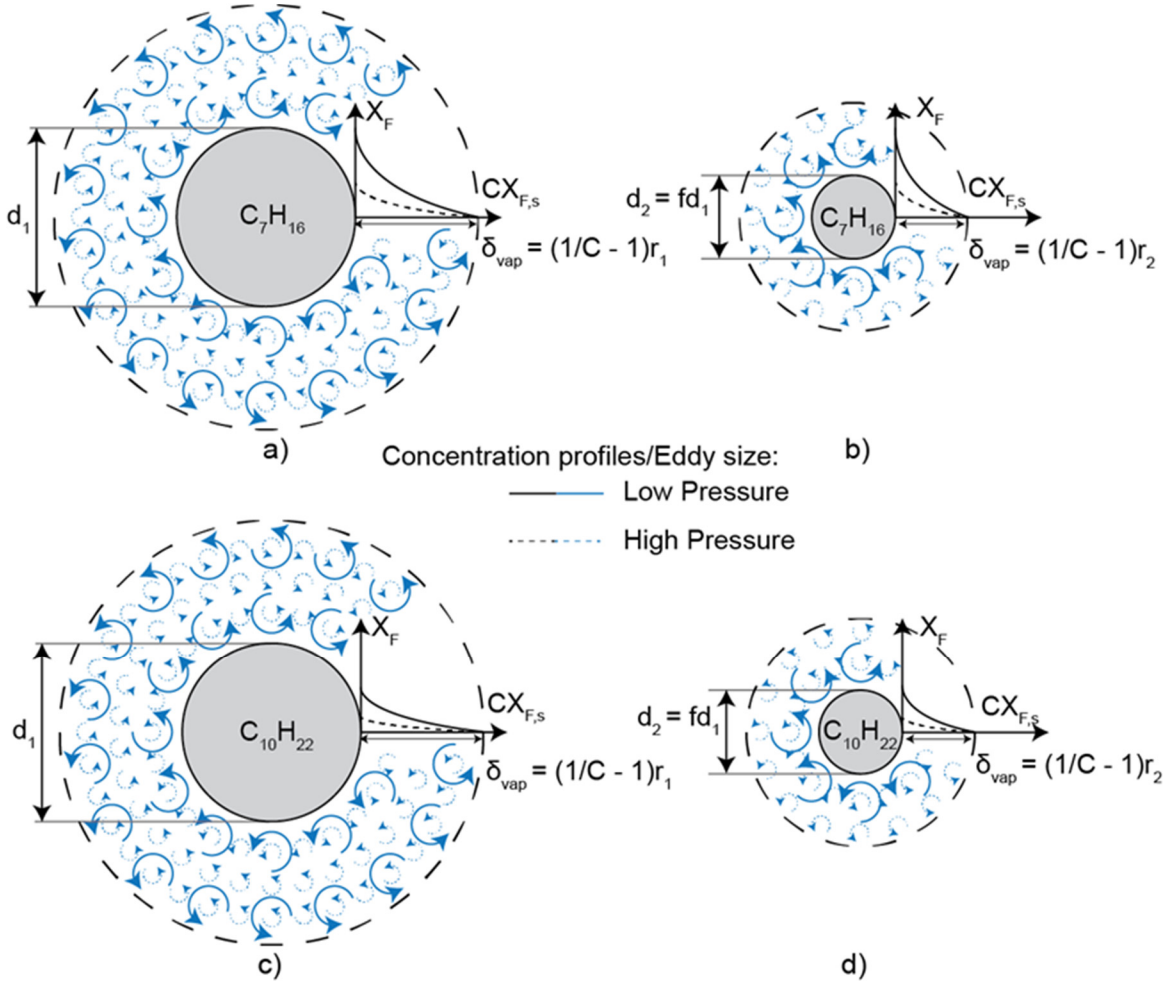


**Fig. 4.34.** Illustration of droplet size, fuel type, pressure, and vapor concentration profile (not to scale): a) large heptane droplet, b) small heptane droplet, c) large decane droplet, and d) small decane droplet. Smaller turbulent structures are potentially more efficient in dispersing vapor near the droplet.

Figure 4.34 also illustrates the relative size of the smallest eddies. The Kolmogorov scale reduces with pressure and turbulence intensity, although the decrease with pressure is not as rapid as the reduction in expected molar fuel fraction at the surface of the droplet. One possible reason for the increase in $K/K_0$ as $\eta/d_0$ ratio decreases is the greater packing of turbulent structures surrounding the droplet. The positive influence of small eddies could be attributed to a surface interaction effect or the ratio of scale size to the aforementioned vapor thickness shell. The actual fuel concentration profile that develops upon droplet exposure to turbulence will be different than the illustrations in Fig. 4.34, as the above schematics are representations of the situation that would exist in the absence of turbulence. It is likely that the vapor shell, as defined above, would become thinner with turbulence as the gradient intensifies at the surface and the flow rapidly disperses fuel such that negligible quantities exist in close vicinity to the droplet (e.g., [154]). Smaller eddies are potentially more efficient at this dispersion process. Hiromitsu and Kawaguchi [154] reached a similar conclusion and attributed the turbulence effect to small-scale eddies breaking down the concentration boundary layer of the evaporating droplet, although their experiment differs substantially from the present investigation insofar as it incorporated a strong mean flow and no pressure variation. The superposition of a mean flow and turbulent fluctuations may also account for Eckartsberg and Kapat [155] concluding that droplet enhancement does not occur if $d_0$ is smaller than the Taylor scale instead of the Kolmogorov scale. In other words, purely turbulent evaporation, as studied presently, appears to be influenced by smaller scales (i.e., Kolmogorov length scale) of turbulence, presumably due to the absence of a thick, viscous boundary layer surrounding the droplet.

Considering the above discussion regarding the dynamics of interacting length scales and concentration gradients, it is surprising that the temporal $d^2$ profile remains linear throughout the

majority of the droplet lifetime. For all conditions studied here, $d^2$ behaviour generally lasts until at least half of the droplet (as measured by $d^2$) is consumed (evaporated). As an example of the counter-intuitive adherence to $d^2$ linearity, also discussed in Section 4.1.2, consider that a droplet with $d_0$ = 500 μm will continue to evaporate at the same rate when it has reduced in size to 400 μm. However, another droplet with $d_0$ = 400 μm will evaporate slower than the first droplet which was reduced to 400 μm from an initially larger size, despite (seemingly) identical surrounding conditions. In other words, turbulent evaporation is associated with predictive ratios in the form $\eta/d_0$ and $X_{F,s}/r_0$ rather than $\eta/d(t)$ and $X_{F,s}/r(t)$, at least until $d^2$ deviation occurs.

Although the above discussion establishes the conditions under which turbulence is best positioned to enhance droplet evaporation, the exact controlling mechanism is still elusive. Performing the tests at room temperature has essentially mitigated heat transfer effect, and thus mass transfer phenomena are dominant. While there is no doubt that turbulence enhances the gradient for diffusion mass transfer (e.g., [161]), it is unclear as to whether the net improvement is due to the diffusion mechanism taking advantage of this gradient, or if the turbulence itself simply convects enough vapor to render the diffusion process negligible. This question is not likely to be resolved by experiment, and additional numerical study on the vapor concentration surrounding droplets is required. Previous studies have suggested the possibility that turbulence may increase the evaporation rate of the fuel at the surface of the droplet as opposed to simply improving the mass diffusion and convection (e.g., [16]). These claims are typically predicated upon the observation that heavier fuels, such as decane, are affected by turbulence to a greater extent than lighter ones, such as heptane. The results presented here have proved that this is not always true, especially for high-pressure environments or smaller droplets. This revelation, however, does not disprove the theory of vapor production. The process of evaporation is, at its

core, the escape of molecules from the liquid phase due to the acquirement of sufficient kinetic energy. The kinetic energy dissipation at the surface of the droplet could theoretically induce phase change in a manner analogous to the formation of droplets from a jet via turbulent primary breakup, which requires eddies with kinetic energy comparable to the surface energy to break a droplet free from the liquid core [7]. A modern DNS study by Shinjo et al. [225] revealed that the regions near the droplet surface strongly increase the dissipation rate of the turbulence kinetic energy, which may extend the credibility of the vapor production theory. Overall, it should be emphasized that while turbulence may increase vapor production at the surface, a definitive conclusion cannot yet be reached based on the available data.

### 4.2.3 Droplet evaporation at elevated temperature

For each fuel, two elevated temperatures were tested at 1 and 10 bar; 50 and 75°C for heptane, and 75 and 100°C for decane. These values were selected based on experimental limitations, as well as the desire to keep the temperature below the boiling point of the fuel. In all cases, the evaporation rate increases with initial droplet size in turbulence but remains relatively unaffected in quiescent environments as illustrated in Figs. 4.35 and 4.36. Thus, the overall qualitative trend established at room temperature is maintained. In many ways, the effect of temperature as it relates to turbulence can be considered the inverse of pressure. For example, increasing the ambient temperature always improves the rate of vaporization, yet the effectiveness of turbulence, $K/K_0$, tends to decrease as the temperature rises. The kinematic viscosity of the gas surrounding the droplet increases with temperature, resulting in an increase in the size of the smallest eddies due to a smaller turbulent Reynolds number. The predicted fuel vapor fraction at the surface of the fuel droplet also increases with temperature which improves the driving gradient for diffusive mass

transfer. In the case of decane, the average value of $K_0$ increases by a factor of 30 when the ambient temperature increases from 25 to 100°C through the combined effects of greater vapor production and diffusion (as $D_{AB} \propto T^{3/2}$). The improved ability of the droplet to vaporize via diffusion combined with the larger Kolmogorov scale results in relatively poor vaporization enhancement with turbulence.

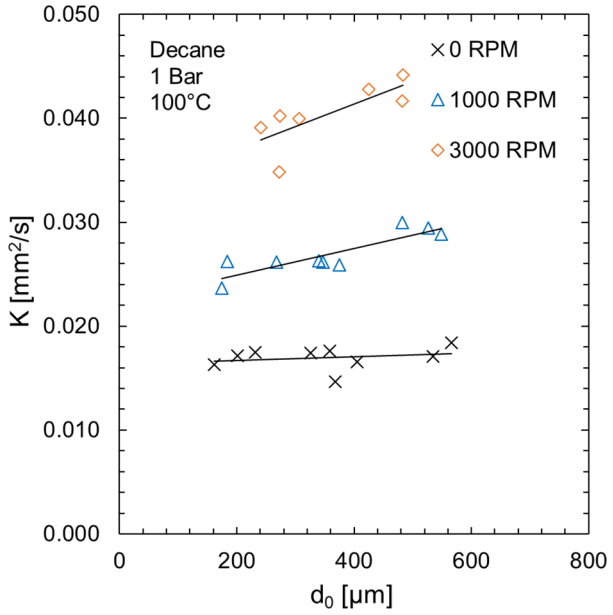


**Fig. 4.35.** Decane evaporation rate as a function of initial droplet size at 100°C and 1 bar.

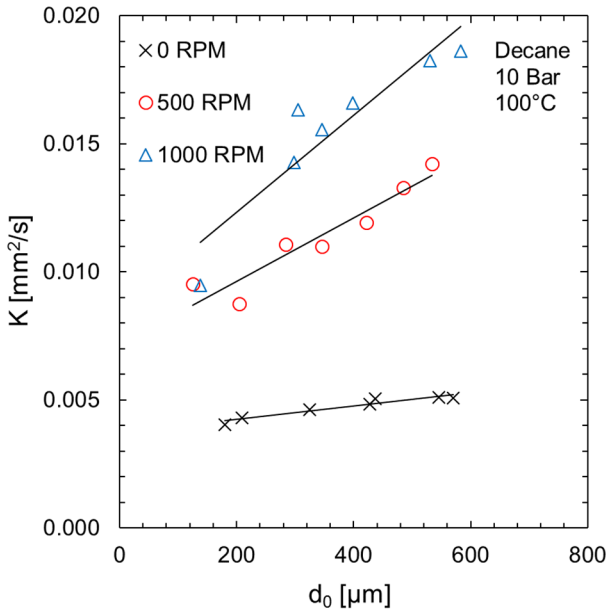


**Fig. 4.36.** Decane evaporation rate as a function of initial droplet size at 100°C and 10 bar.

As with the trials at room temperature, high pressure tends to increase the quiescent evaporation rate dependence on initial size as evident in Fig. 4.36, although the relationship is clearly minor compared to the turbulent runs. At 1 bar and 100°C (Fig. 4.35), a 700-μm droplet can be expected (based on the line of best fit) to feature a stagnant evaporation constant which is only 7% greater than that of a 100-μm droplet. At 10 bar and 100°C, the expected improvement in $K_0$ climbs to 39%. A similar spread in improvement was witnessed at 25°C, indicating that this is largely a pressure-dominated phenomenon. In fact, at any given pressure, we can expect to see

lower percent increases in evaporation rate at elevated temperature as compared to room temperature. This is true for both heptane and decane and is likely attributed to diffusion becoming increasingly dominant at higher temperature rather than a reduction in the effect of natural convection. An unexpected finding for heptane with no turbulence at 10 bar and elevated temperature is the increased incidents of $d^2$ deviation, despite the fact that heptane generally remained linear at 10 bar and 25°C. On the other hand, stagnant decane features improved $d^2$ adherence at 10 bar at high temperature. Based on the above discussion regarding the decreased dependency of $K_0$ on initial size at elevated temperature, the deviation does not appear to be related to natural convection. Despite the lack of explanation, this is further evidence that a significant portion of a small droplet's lifetime may be transient at elevated conditions. The exact nature of the transient may depend significantly on the fuel type.

Increasing the ambient temperature attenuates the effect of droplet size on the normalized evaporation rate. Figure 4.37 indicates that elevated temperature not only decreases $K/K_0$, but it also reduces the slope of the linear relationship between $K/K_0$ and $d_0$. In this figure, the slope of $K/K_0$ vs. $d_0$ is twice as large at 25°C than it is at 100°C for 1000 RPM. This difference increases to four times at 3000 RPM. In Section 4.2.2.2, it was asserted that the effect of turbulence and droplet size on the evaporation rate depend primarily on two interrelated factors; namely, the ratio of the smallest length scale eddies to initial droplet size, $\eta/d_0$, and the stagnant concentration fuel gradient at the droplet surface, $X_{F,s}/r_0$. $K/K_0$ was found to increase with a reduction in both ratios. Higher temperature increases both ratios, thus leading to decreased turbulence effectiveness as witnessed in Fig. 4.37. The general trend of $K/K_0$ as a function of the ambient pressure, established in Fig. 4.31, is reproduced including high-temperature data in Figs. 4.38 and 4.39 for small and

large droplets, respectively. At $T_\infty$ = 75°C, the effectiveness of turbulence continues to increase with pressure, but the trend is shifted to lower $K/K_0$.

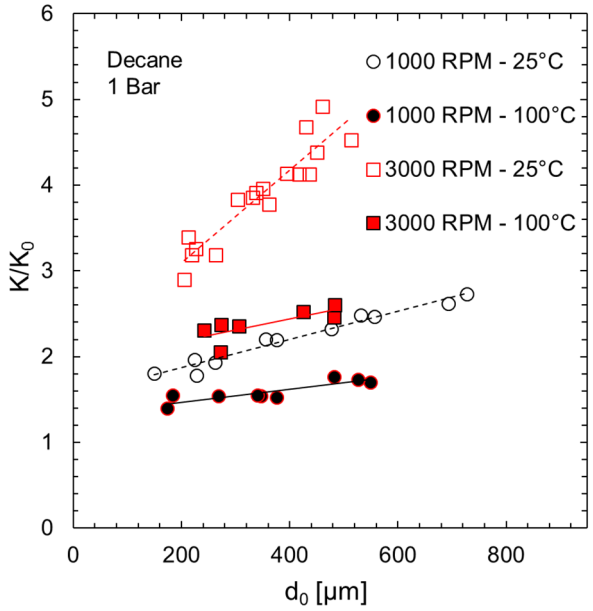


**Fig. 4.37.** The effect of ambient temperature on the droplet size-turbulence relationship for decane at 1 bar.

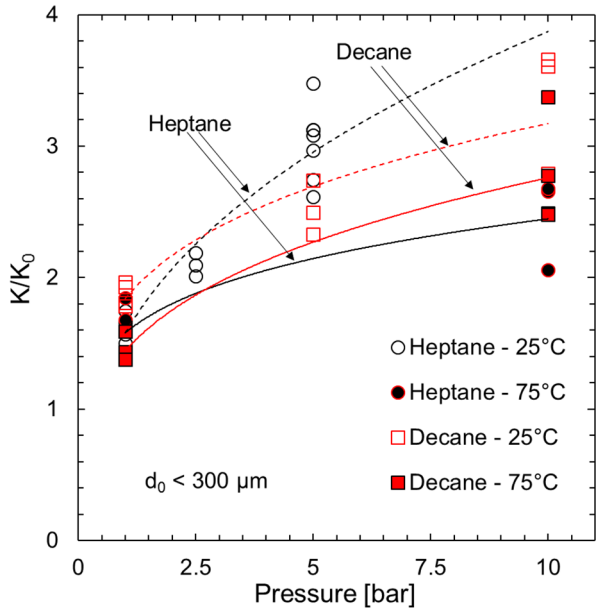


**Fig. 4.38.** $K/K_0$ vs. $P$ for small droplets (< 300 µm) at various temperatures (1000 RPM).

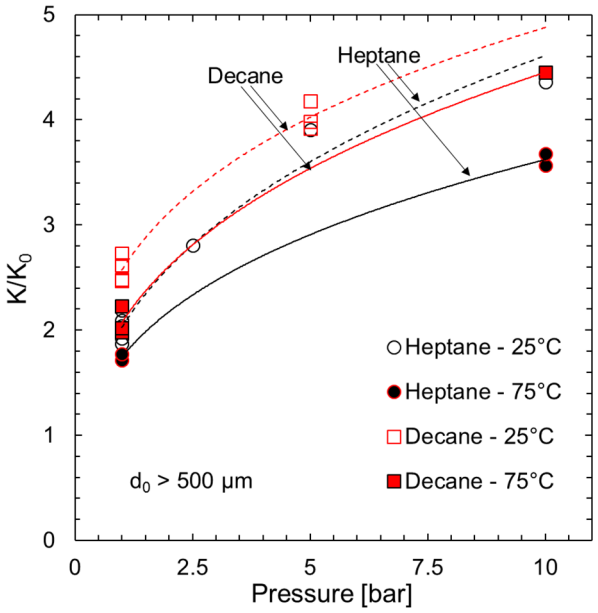


**Fig. 4.39.** $K/K_0$ vs. $P$ for large droplets (> 500 µm) at various temperatures (1000 RPM).

The importance of the ratio of Kolmogorov length scale over the initial droplet diameter, $\eta/d_0$, to the prediction of the evaporation rate is further illustrated in Fig. 4.40, which portrays the normalized evaporation rate vs. $\eta/d_0$ for both fuels at all examined elevated temperatures. Compared to Fig. 4.28, which depicts the same variables but for only heptane at room temperature, there are similarities and differences. A clear power relationship is evident, although the data contains more outliers (circled) in Fig. 4.40. In general, these are the result of unusually large $K$ for small droplets at elevated temperature. It is not known if there is a physical reason for this, as while the finding appears repeatable for heptane at 1 bar and 75°C, it is not systematically witnessed at the other elevated temperatures. In a theoretical study comparing the predictive capability of the standard hydrodynamic evaporation model to one based upon rigorous kinetic effects, Borodulin et al. [118] found that evaporating water droplets as large as 250 μm exhibited noticeable differences in evaporation time between the two investigated models. Although speculative, it is possible that phenomena other than pure diffusion at least influence the smallest droplets generated here. Despite the environmental differences between the present study and that of Borodulin et al. [118] (most importantly, their usage of water instead of a hydrocarbon fuel), a precedent has been established such that the critical diameter which splits "large" from "small" droplets (based on the controlling evaporative mechanism) may be larger (~250 μm) than originally thought. More importantly, Fig. 4.40 shows that the transition from turbulence-enhanced evaporation to the region where evaporation is largely unaffected by turbulence occurs at a smaller value of $\eta/d_0$ – approximately 0.5 to 0.6 – as compared to Fig. 4.28 which predicts a transitional $\eta/d_0$ value of approximately unity. Thus, turbulence may lose effectiveness before the Kolmogorov scale exceeds the initial droplet diameter at elevated temperatures.

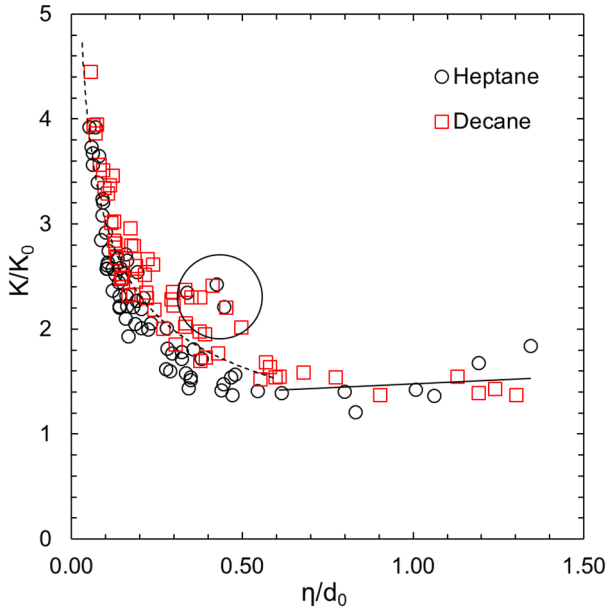


**Fig. 4.40.** $K/K_0$ vs. non-dimensional length for all pressures at elevated temperature. The data points within the circled region show high deviation from the expected trend, both here and in the individual $K$ vs. $d_0$ plots.

### 4.2.4 Deviation from linear $d^2$ behaviour

The timing of linear deviation is another area of interest. Analysis of the various temporal $d^2$ profiles reveal that droplets generally will not feature fully linear lifetimes under turbulent conditions unless the droplet is very small. As with the prediction of $K/K_0$, the diameter at which deviation occurs, $d_{dev}$, is strongly linked to initial diameter for all tested conditions, with $d_{dev}$ appearing as a linearly increasing function of $d_0$. This discovery indicates that turbulent $d^2$ deviation does not coincide with the droplet shrinking below the Kolmogorov length scale, as this would occur independent of the droplet initial size and at a constant value for each pressure/temperature/intensity combination. Beyond this observation, it is difficult to present quantitative data due to the inherent scatter in data, as well as the difficulty in assigning the specific location of deviation. Indeed, relatively quick evaporation times result in the possibility of two similarly-sized droplets being exposed to different flow fields simply due to the randomness of

turbulence over short observation periods. Thus, this section provides only a preliminary qualitative assessment. As a general rule, $d_{dev}$ is relatively independent of turbulence intensity level (fan speed) at low pressure as depicted in Fig. 4.41 for heptane at 2.5 bar. As the pressure increases, the slope of the $d_{dev}$ vs. $d_0$ line becomes greater, and by 10 bar the various fan speed groups may begin to separate. For heptane at low pressure, the minimum initial droplet diameter for which deviation is witnessed increases with temperature. For example, the smallest heptane droplet which displays deviation at 1 bar and 25°C is ~200 μm. At 50°C, this value is ~300 μm, and by 75°C, no deviation is witnessed for droplets under 400 μm in initial diameter. This trend is not well reproduced at high pressure (it has already been discussed in Section 4.2.3 how increasing the temperature actually increases deviation for stagnant heptane at 10 bar). Conversely, decane at high pressure benefits from increasing the temperature from the perspective of $d^2$ adherence for both stagnant and turbulent runs.

As noted previously, the number of studies which utilize the cross-fiber methodology in a moderate evaporative environment is small. While deviation has been perceived using the cross-fiber approach in stagnant combustion (e.g., [199]) and high-temperature microgravity (e.g., [77,226]), the reasons provided are specific to those particular environments (approach to flame extinction and lack of natural convection, respectively) and are not applicable here. Thus, these results may be some of the first reported instances of $d^2$ deviation in a turbulent, diffusion-controlled environment. Additionally, since the droplet remains anchored in place, it is exposed to drag forces which would normally not be present if the droplet was immediately transported "in the mean." Both the background mean velocity (albeit minor compared to the fluctuations) and the large integral scales are responsible for promoting relative motion between the droplet and the stationary apparatus. This relative motion induces oscillations during image processing which is

quite evident in Fig. 4.42. It is interesting to note that the onset of linear deviation appears to correspond to where the $d^2$ profile becomes smooth, indicating that the droplet has shrunk to a size which is not significantly affected by drag forces. This is potentially another reason for the observance of $d^2$ deviation in many turbulent runs. Although it is difficult to draw firm conclusions based on the available data (especially as it relates to high-pressure deviation due to the 10 bar maximum pressure studied here), it is clear that transient effects are present for turbulent droplet evaporation at elevated pressures and temperatures well below the respective critical values.

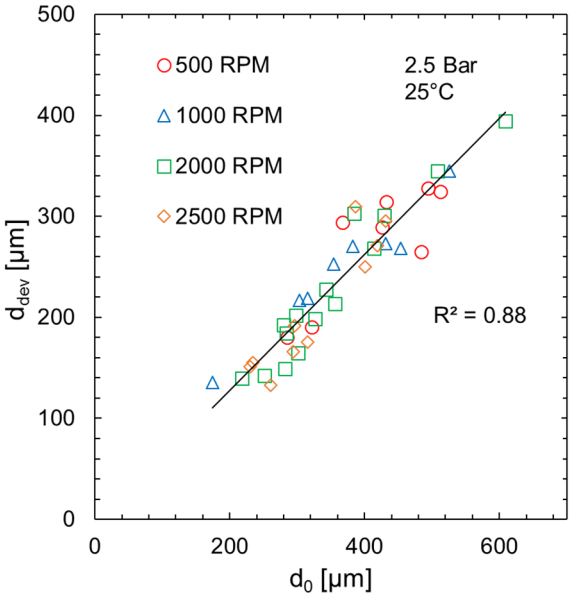


**Fig. 4.41.** Deviation diameter vs. initial droplet diameter for heptane droplets at 2.5 bar.

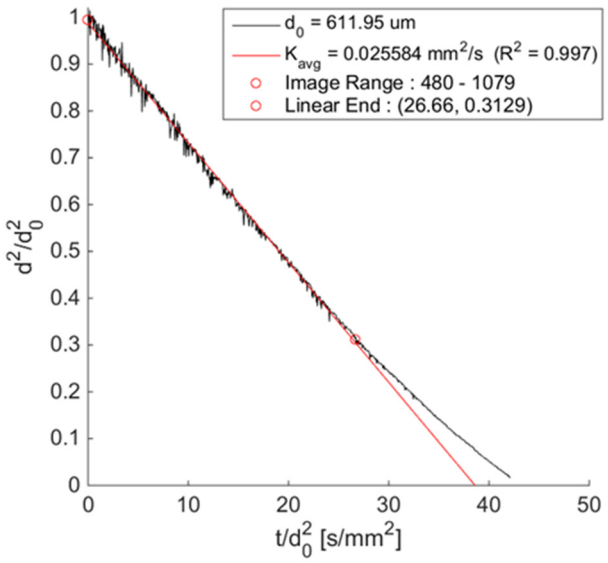


**Fig. 4.42.** Illustration of rapid fluctuation associated with the linear portion of a $d^2$ profile.

### 4.2.5 Further discussion and comprehensive correlations

Two different correlation approaches were developed to predict turbulent evaporation rates at standard conditions in Section 4.1.3. The novelty of these correlations is the inclusion of droplet size; a feature which had been lacking in the literature. The generalization of these correlations to include elevated pressure and temperature is evaluated below using all 476 measured data points.

Following the methodology of Birouk [31], additional non-dimensional temperature and pressure groups in the form of $T/T_0$ and $P/P_0$ are added to the turbulent Reynolds correlation. The resultant expression, obtained using least squares regression based on the data presented in Fig. 4.43, has the following form:

$$\frac{K}{K_0} = 1 + 0.0439 Re_{t,L}^{\frac{2}{3}} \left(\frac{L}{d_0}\right)^{-0.53} Sc^{1.16} \left(\frac{T}{T_0}\right)^{-1.42} \left(\frac{P}{P_0}\right)^{-0.19} \quad \textbf{(4.14)}$$

Equation (4.14) retains almost identical dependence on the dimensionless length scale ratio, $L/d_0$, as presented in Eq. (4.6) for standard conditions, while the dependence on the Schmidt number has decreased. Interestingly, the exponent of $P/P_0$ in Eq. (4.14) is the same as the one presented by Birouk [31], indicating that the addition of variably-sized droplets has little impact on the overall evaporation characteristics at elevated pressure. This conclusion is readily observed by comparing the qualitative similarities between Fig. 4.29 ($d_0$ < 300 μm) and Fig. 4.30 ($d_0$ > 500 μm).

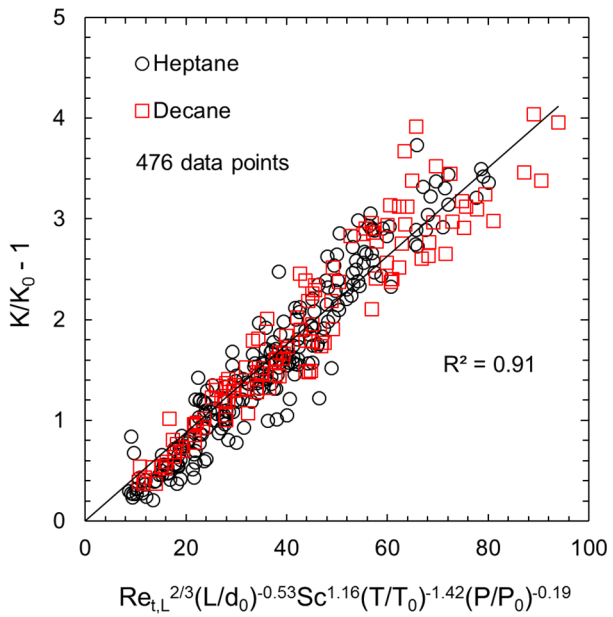


**Fig. 4.43.** Normalized evaporation rate vs. a turbulent Reynolds correlation (all data) featuring several non-dimensional parameters.

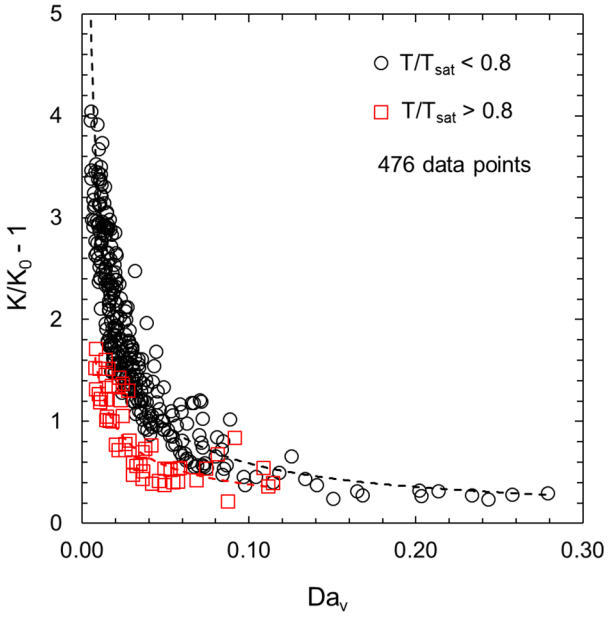


**Fig. 4.44.** Normalized evaporation rate vs. vaporization Damköhler number (all data).

A vaporization Damköhler number, $Da_v$, has also been used to predict the droplet normalized evaporation rate, but only at standard pressure (e.g., [13,16,87,154]). It is therefore questionable whether the Damköhler approach is suitable for correlating turbulent droplet vaporization at elevated pressure and temperature conditions. In fact, Hiromitsu and Kawaguchi [154] expressed doubt, based upon their experimental findings, that the $Da_v$ formulation proposed by Gökalp et al. [87] would work at high temperature. Fig. 4.44 provides a plot of the normalized evaporation rate vs. $Da_v$ using the present data and the definition of $Da_v$ outlined in Eqs. (4.7) – (4.10). Despite the significant scatter, two data groupings can be identified: one comprised of data at high pressure and/or low temperature ($T/T_{sat}$ < 0.8) and another, smaller data group which has a high ratio of $T/T_{sat}$, where $T_{sat}$ is the saturation temperature (i.e., boiling point) corresponding to the specific fuel and pressure. Saturation temperature is estimated utilizing the Wagner approach [119]. The distinction between high and low $T/T_{sat}$ ratio is approximately 0.8 based upon

observation of all plotted data, but it is unknown if an evaporation mechanism change (for example, a potential shift from diffusion-limited to heat transfer limited) occurs at or near this value. One plausible explanation involves the common difficulty of property evaluation at high temperature. Indeed, a goal of the Damköhler definition developed in Section 4.1.3 was to minimize the impact of temperature-dependent thermophysical property calculation (e.g., thermal conductivity, specific heat, etc.) and instead utilize reliable experimental evaporation data which would be known a priori where, upon substation and simplification:

$$Da_v = \frac{1}{2}\left(\frac{\rho_l}{\rho_v}\right)\left(\frac{K_0}{d_0 q^{0.5}}\right) \tag{4.15}$$

In Eq. (4.15), only the mass density of vapor at the droplet interface, $\rho_v$, is both realistically unmeasurable and strongly temperature dependent. The accuracy of the Damköhler calculation thus rests upon evaluating $\rho_v$ at an appropriate interface temperature, $T_i$. All data presented in Fig. 4.44 is calculated based on the assumption that the ambient temperature reasonably approximates the interface temperature. This approach is partially justified by maintaining the liquid and surrounding environment at an equivalent temperature prior to droplet evaporation. However, the real interface temperature is expected to be lower due to the evaporative cooling effect. At low ambient temperatures, the difference between $T_i$ and $T_\infty$ is correspondingly low as well. However, the theoretical findings of Sobac et al. [101] show that the temperature gradient developed near the droplet surface at high ambient temperatures is significant, even if $T_\infty$ remains below the boiling point of the liquid. Furthermore, the steady-state temperature difference, $T_\infty - T_i$, grows substantially at high ambient temperature which indicates that the real vapor mass density is considerably lower than the value predicted at $T_\infty$. Based on Eq. (4.15), smaller $\rho_v$ values would lead to higher $Da_v$ predictions, resulting in the second group of data points merging

with the first. The reason high-pressure data is not affected (even at equivalent $T_\infty$ values) could be due to the slower evaporation rate which leads to less evaporative cooling and interface temperatures which are more comparable to the ambient value, $T_\infty$. Although Hiromitsu and Kawaguchi [154] may be partially correct in asserting that Damköhler numbers are ill-suited to correlating data at high temperature, the reason could be inadequate property calculation due to a lack of knowledge regarding the temperature profile in the droplet interface region.

# CHAPTER 5
# CONCLUSIONS AND RECOMMENDATIONS FOR FUTURE WORK

## 5.1 Concluding remarks

This thesis focused on obtaining experimental evaporation rate data for single isolated alkane fuel droplets of small, realistic sizes under turbulent conditions. Droplets with initial diameters of 110 – 770 μm were suspended on a 14-μm cross-fiber in the center of a large, fan-stirred spherical vessel. The droplets were exposed to various levels of turbulence (0 – 1.5 m/s), pressure (1 – 10 bar), and temperature (25 – 100°C) to gauge how the droplet evaporation rate, with respect to initial droplet size, was affected by the parametrically-varying environment. Particle image velocimetry revealed that the turbulence had a quasi-zero mean velocity and high levels of isotropy and homogeneity. This experimental study may, therefore, be interpreted as a fundamental investigation into the effect of pure turbulent fluctuations on the evaporation characteristics of small fuel droplets. Almost 500 unique droplet evaporation tests were performed throughout the course of this study. Initial efforts focused on determining the relationship between turbulence, droplet size, and evaporation rate at standard room conditions. Additional experiments were then performed to assess the impact of elevated pressure and temperature. The inclusion of elevated conditions allowed for the modification of the turbulent flow field in ways which altering the fan speed could not achieve. The procedures employed maintained tight control of all experimental variables, while both $d^2$ law adherence and the resultant $K$ were of primary interest when interpreting the data. The crucial observations and conclusions derived from this study are presented as follows:

1) The turbulence integral length scale, $L$, is relatively independent of the chamber fan speed, temperature, and pressure. The average integral length scale, based on 21 individual PIV runs, is 21.23 mm. Similarly, the relationship between $q^{0.5}$ and fan speed is not a strong function of ambient condition. On average, the linear equation is expressed as $q^{0.5} = 0.000526 \times N$. The isotropy and homogeneity ratios remained between 0.9 and 1.1 for a central spherical volume with a diameter of at least 20 mm. Evaporating droplets were thus exposed to a controlled turbulent flow field with a quasi-zero mean velocity.
2) The $d^2$ law is confirmed for the entire range of droplet sizes, turbulence, and ambient conditions tested here. Linearity begins almost immediately and remains until much of the droplet has evaporated. However, $d^2$ deviation eventually sets in for most droplets, especially under turbulent conditions and for initially large droplets. The deviation data is difficult to interpret other than the fact that the deviation diameter is a strong linear function of $d_0$.
3) In a turbulent convective environment at room conditions, the initial droplet diameter controls the rate of evaporation, $K$. In all cases, $K$ increases with $d_0$. The rate of increase is stronger for higher turbulence levels. However, under stagnant conditions, there is no apparent size effect as all droplets evaporate at roughly the same rate. This suggests a persistent turbulent mechanism which is sensitive to the initial condition of droplet size, rather than the instantaneous size, for the majority of the droplet's existence.
4) The ratio of Kolmogorov length scale to initial diameter, $\eta/d_0$, is an excellent predictor of the effectiveness of turbulence, $K/K_0$. Turbulence is far more effective when this length scale ratio is small. Once $\eta/d_0$ exceeds approximately unity, $K/K_0$ maintains a steady value which corresponds to the small background mean velocity based on simple laminar

predictions. Therefore, turbulence appears to have no effect on $K$ when the smallest of scales (Kolmogorov) exceed the initial droplet diameter. The generation of small turbulent structures thus improves droplet evaporation. For a fixed value of $L$, as in the present case, $\eta$ may be reduced by increasing $Re_{t,L}$. The relationship between $\eta/d_0$ and $K/K_0$ was confirmed for elevated pressure and temperatures. A physical explanation is elusive, but the tight packing of small turbulent structures around the droplet could induce a surface effect or break down the vapor shell more effectively.

5) Pressures of 10 bar appear high enough to generate meaningful natural convection at the low temperatures studied here. While $K_0$ hardly increases with size at room pressure, the percent improvement in $K_0$ for a large droplet vs. a smaller one is significant at 10 bar.
6) Although $K$ always reduces with pressure and increases with temperature, the ratio of $K/K_0$ exhibits the opposite effect. In other words, the effectiveness of turbulence increases with pressure yet decreases with temperature. Eventually, the pressure will reduce the available molar fuel fraction at the droplet surface to a point where turbulence is no longer effective, but prior to this occurrence, $K/K_0$ increases as the theoretical molar concentration gradient, $X_{F,s}/r_0$, decreases. This finding helps explain why turbulence is more effective at high pressure and low temperature, as $X_{F,s}/r_0$ decreases and increases with pressure and temperature, respectively. The molar concentration gradient also reduces with droplet size, which further addresses the issue of why evaporation rate increases with droplet size. Overall, the two ratios $\eta/d_0$ and $X_{F,s}/r_0$ are excellent predictors of turbulent evaporation rate.
7) Collapsing all evaporation data is achieved through either a turbulent Reynolds number correlation or a vaporization Damköhler number correlation. Relevant literature has

established both techniques to a certain extent, but not for droplets of variable initial size. Furthermore, simplifying improvements are suggested to assist in calculating certain variables, such as the radial vaporization velocity $V_r$, which are components of the above correlations. Both the turbulent Reynolds approach, centered around $Re_{t,L}^{2/3}$, and the vaporization Damköhler number technique, which requires a single term $Da_v^n$, provide reasonable estimates for $K/K_0$ throughout the range of conditions studied here.

## 5.2 Recommendations for future work

Throughout the processes of reviewing the literature, gathering experimental data, writing papers, and compiling this thesis, several areas of improvement, as well as potential future research directions, were revealed. The nine most pertinent categories are discussed below.

### 5.2.1 Improvements to frame design

The cross-fiber frame, as developed by Birouk and Toews [33], remained entirely serviceable throughout hundreds of hours of experiment which speaks to the quality of the original design. However, a modified frame design is recommended to simplify setup and decrease experimental downtime. Frame enhancements related to the inclusion of an ignition system are discussed in Section 5.2.3 whereas the present section is dedicated to improvements which should be implemented regardless of ignition considerations. Figure 5.1 provides a sketch of proposed features. While it is recommended to retain the major dimensions of the frame, the next generation of models should consider the following points:

1) *Circular frame tubing*

Circular tubing would provide a streamlined frame cross-section and theoretically reduce the impact of the frame on the flow field in the center of the chamber. Solid round aluminum bar could be bent into the frame shape. The smoothly radiused corners (dashed lines in Fig. 5.1) could further mitigate flow field disruption, and a frame bent from a single piece of round bar would be easier to manufacture. An assessment of the plausibility of this design, including drilling accurate fiber holes, has not yet been made.

2) *Offset fiber bores*

The current frame features holes for the fiber holders drilled directly in the center of the square tube face. In theory, this should result in the fibers passing through the frame in the same plane and thus intersecting at the center. However, it is impossible to ensure that the holders perfectly center the 14-μm fibers. Furthermore, the fiber holders are not completely straight, and even a small amount of offset can result failed fiber contact. In many cases, the only way to fix this issue is to remove one fiber and invert its orientation with respect to the other fiber. If each pair of holes is drilled slightly offset from the center in opposite directions and the fibers properly installed, they will be forced to intersect. The side view in Fig. 5.1 illustrates the concept.

3) *Spring loaded tensioners*

The current frame implementation uses small screws to adjust the fiber tension (Fig. 3.3). Although the original design incorporated a small spring for each fiber (to be used in conjunction with the screw) [33], none of the experiments reported here utilized the springs

(for a variety of practical reasons). The inclusion of a spring will help maintain consistent fiber tension, especially during the heating and cooling cycles in elevated temperature tests. Observation of the fibers following high-temperature runs revealed that tension was repeatedly lost upon chamber cool down. The fiber anchor opposite the spring-loaded holder is simply a small hole drilled in the frame. Regardless of the anchor type (spring loaded or fixed), the fiber can completely pass through the holder or frame and is epoxied in two locations at each support (Fig. 5.1). Spring selection would be crucial, and some degree of trial-and-error testing is probable.

4) *Modified upper mount*

The current method of suspending the frame from the top of the chamber involves a series of threaded connections. Integration of a sturdier, one piece mount is recommended for use with a new frame design. Figure 5.1 illustrates a mount which contacts the frame in two locations for greater support. A sliding insert attachment is recommended (see the fiber holder in [207] for an example) to replace the threaded connections at the top of the chamber. In this type of design, the frame mount would slide into a slightly larger tube suspended from the chamber roof. Set screws in the tubing would secure the frame mount in position. Section 3.2 describes the issue of frame vibration; the use of vibration-reducing material in the new mount should therefore be considered.

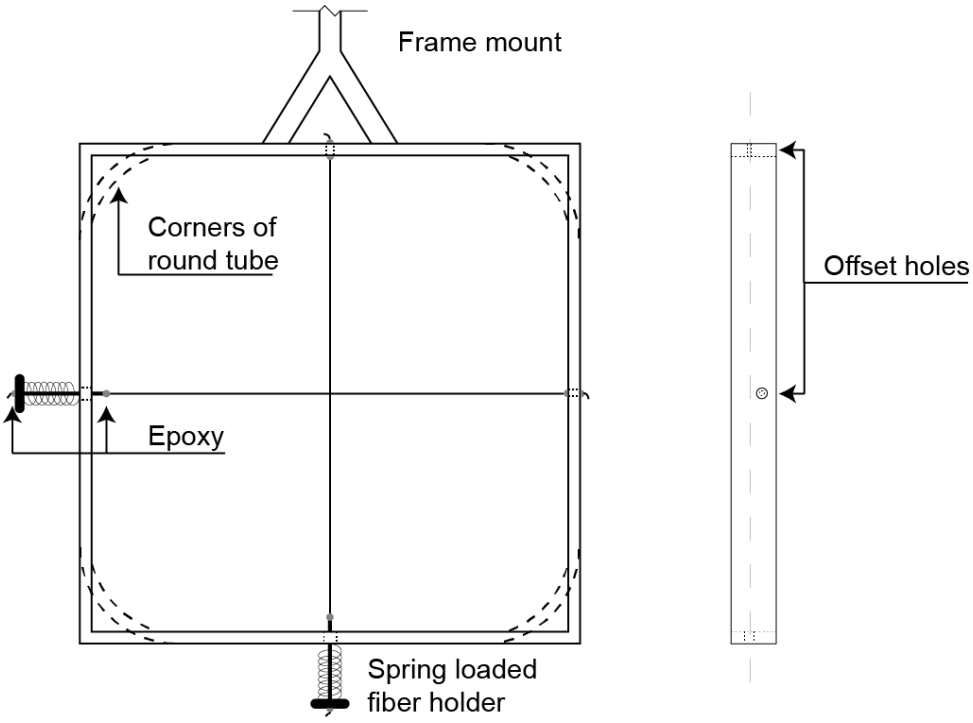


**Fig. 5.1.** Sketch of the proposed frame alterations including spring loaded tensioners, integral frame mount, offset fiber holes, and rounded corners – front and side views (not to scale).

### 5.2.2 Assessment of chamber symmetry

Although the chamber generates low mean velocities and acceptable levels of isotropy and homogeneity, there may be room for improvement. PIV results consistently show the mean flow field oriented in the same direction, which could be an indication of certain fans affecting the flow more than others. A simple visual inspection revealed that some fans appear to extend further towards the center than others. A thorough investigation into the fan symmetry is recommended to address the following concerns:

1) *Distance from fan to chamber center*

   The distance between each fan face and the center of the chambers should be precisely measured. The intersection of perpendicular strings running through precision drilled holes in the side port fittings could effectively locate dead center (this is analogous to the frame

alignment technique discussed in Section D.1 but with string instead of lasers to provide a physical measuring point). Fans which are too close or too far from the center can be machined or shimmed to obtain the proper location.

2) *Degree of alignment between fan pairs*

Each fan pair should be coaxial. If the two opposing fans are not directing flow precisely towards each other, the quality of the turbulent flow field will suffer. Performing measurements to assess this will be challenging. It may be possible to visualize the direction of flow by attaching a small laser to one fan shaft. If the laser point does not appear on the opposite fan shaft, then the fans are not sufficiently aligned, and corrective action must be taken. The chief difficulty will be ensuring that the laser accurately represents the axial path of the airflow.

3) *Fan shaft runout*

Radial runout in the fan shafts could cause poor flow characteristics due to the fan blade wobbling in the plane of rotation. Failed bearings or shaft warpage, potentially due to overheating, can cause runout. The runout can be measured with a dial indicator and should become standard practice following every hub removal and bearing replacement. An assembly with new bearings and shaft can establish the nominal runout value. Whenever a hub assembly runout is found to exceed this nominal value by a predetermined amount, steps should be taken to fix the issue.

### 5.2.3 Incorporation of ignition system

Ignition and combustion of small droplets is the next logical step in assessing the effect of turbulence. The spherical chamber is currently compatible with two types of ignition systems. The first approach makes use of two long electrodes inserted through the chamber's side ports to initiate a central flame in a homogeneous gaseous mixture [208]. The electrodes are not retractable post-ignition and may interfere with the turbulent flow field at the center of the chamber. The second method, used in conjunction with single fiber droplet suspension [187,206], is an injector-mounted heating element pictured in Fig. 5.2. The attachment slides over the injector needle and barrel and connects to two electrical wires, embedded in the barrel, which carry current to the element. The equipment necessary to perform the sequential processes of droplet formation and ignition are thus combined into one device. The attachment pictured in Fig. 5.2 cannot be used with the cross-fiber, as its operation requires the heating coil to first pass by the fiber and then return to heat and ignite the vapor. While this is possible for a single, vertically suspended filament, intersecting fibers do not allow this procedure.

The limitations of the current ignitions mandate the development a new cross-fiber compatible system. Fabbro [187] commented on the difficulty of igniting low-volatility fuels in turbulent environments with a spark and, based on this observance, developed the heating element in Fig. 5.2. High-pressure environments may also result in unreliable spark ignition (e.g., [132]). Spark ignition is preferable due to its instantaneous nature and, unlike resistance heating, a spark will not affect the temperature distribution of the droplet and surrounding gas prior to ignition. Aggarwal [45] has reviewed single droplet ignition, including the ignition induced by a spark. Researchers have successfully implemented spark ignition systems for the combustion of single droplets, even in turbulent environments (e.g., [176]). However, the ignition process is expected

to become more difficult as the droplet size decreases due to the lower amount of available vapor. If preliminary tests of a spark ignition system are unsuccessful, it is recommended to move to a heating coil ignitor.

Figure 5.3 illustrates a proposed design concept for the ignition system. The design does not include any sizing or cost estimation of parts and is therefore preliminary in nature. The new design proposes the incorporation of the electrodes into the frame. This feature will ease alignment, reduce install and removal time, and should provide more reliable ignition. The frame would be installed and aligned as before, with a single additional step of attaching the main wiring harness connector. The chamber-side harness would exit through an accessory port to interface with the necessary support hardware (ignition coil, actuator controller, etc.). Micro linear actuators support the electrodes to enable automatic retraction once the spark has fired. The synchronization could be implemented using the currently installed LabVIEW software. Furthermore, synchronizing the firing of the ignition system to the retraction of the injector is theoretically possible (for example, once the injector has been pulled back 25 mm from the fiber intersection, the system could be programmed to fire and retract the electrodes). Automatic triggering of the camera would be the final step in realizing a highly efficient laboratory setup for analyzing the burning characteristics of small droplets. Frame usage in elevated conditions would need to carefully consider the effect of temperature and pressure on the ignition system.

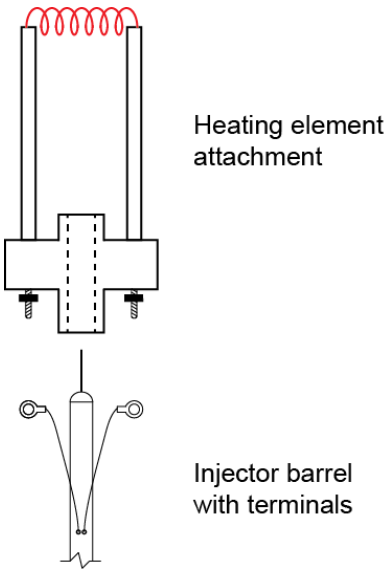


**Fig. 5.2.** Illustration of the detachable injector heating element (not to scale).

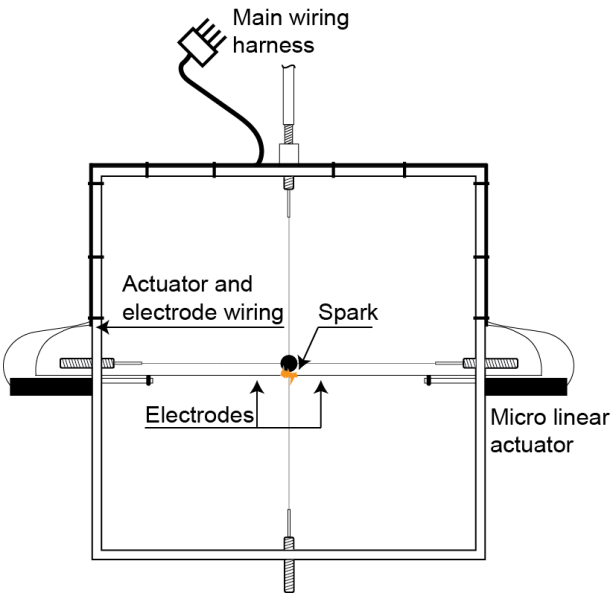


**Fig. 5.3.** Schematic of the proposed frame with integrated spark ignition (not to scale).

### 5.2.4 Modifications to injection, suspension, and imaging systems

The present experimental setup consistently generated droplet diameters in the 150 – 200 µm range, while the occasional sub 150-µm droplet required a great deal of persistence and luck. Several changes are suggested to aid in the pursuit of creating and analyzing smaller droplets.

All experiments exclusively used polycarbonate capillary tubing of 25/50-µm inner/outer diameter for injection. Both the inner diameter and wall thickness are important factors in determining how small of a droplet can be released consistently. The testing of smaller tubing is therefore recommended. While cutting 25/50-µm tubing to size with a razor blade to avoid crimping is dependable, preliminary tests on 22.5/25-µm tubing were repeatedly unsuccessful. Different sizes, materials, and cutting procedures should be evaluated in the future.

Another issue with tracking the lifetime of extremely small droplets is the diamond-like appearance which occurs near the end of the droplet lifetime. This distortion is presumably due to

the adhesion of the liquid to the 14-µm SiC fibers. Although 14-µm fiber is quite thin, researchers have successfully implemented fibers of 7 and 2.5 µm in the cross-fiber configuration (e.g., [76,227]). Any future endeavour to generate smaller droplets should replace the existing fibers with smaller ones to help maintain sphericity and, by extension, improve image processing at small droplet diameters.

Finally, the image processing program no longer recognizes droplets once they fall below ~75 µm in diameter. Droplet disappearance at this size is not problematic in the current study, as the droplets are typically quite distorted by this point, as discussed above, leading to unreliable calculation of an equivalent diameter. Furthermore, the smallest droplets generated in this study are approximately 150 µm. Even for this size of droplet, three-quarters of the lifetime, as measured by $d^2$, is processed by the time the diameter reaches the cut-off size of ~75 µm. For $d_0$ = 500 µm, the code processes over 97% of the lifetime. However, if the eventual goal is to generate sub 100-µm droplets, the current state of image processing will be inaccurate. Distortion of the spherical droplet shape into a diamond should be rectified by using smaller fibers (discussed above), and the image processing code can be modified to use less-aggressive morphological processing operations, if necessary (see [228] for details regarding image processing techniques). The greatest gains related to small droplet imaging and processing are likely to be achieved using a new camera or updated accessories capable of high-resolution macro-photography. The current setup uses a 3× teleconverter, a 70 – 210 mm zoom lens, and a +4 close-up filter to attain a scale factor of 4.6 – 5 µm/px. This spatial resolution is not acceptable for tracking sub 100-µm droplets as they evaporate to completion. If a scale factor of 5 µm/px. is assumed, a 50-µm diameter droplet will be represented by ~80 px. A single pixel erroneously missed or included in the image processing phase represents over 1% of the entire droplet projected area. It is therefore recommended to

upgrade the camera with a unit capable of high-quality macro-photography and spatial resolutions significantly lower than 5 μm/px. No recommendation regarding frame rate is made since droplet evaporation does not require a particularly fast camera, although combustion studies would benefit from frame rates which exceed the capabilities of the current optical system.

### 5.2.5 Infrared thermography

Infrared thermography is a technique used to measure the temperature field of an object by detecting emitted infrared radiation. Infrared cameras produce spatial heat maps, or thermograms, of the field of view. The present study made no attempt to measure the temperature of the droplet using intrusive methods such as thermocouples. Section 2.3 discussed the numerous ways in which a support fiber or thermocouple can interfere with droplet evaporation, including the provision of an additional conductive path and the modification of liquid and gas convective flows near the droplet-thermocouple interface. However, knowledge of the droplet surface temperature evolution would be a significant asset in developing a comprehensive theory of turbulent droplet vaporization. The application of thermography to droplet evaporation is relatively new, and researchers have used infrared cameras to determine heat flux and thermal profiles associated with droplet-wall impacts (e.g., [229,230]) and track sprays against a uniformly heated background (e.g., [231]). Studies have also utilized infrared thermography in conjunction with traditional imaging techniques to simultaneously gather data on surface temperature and droplet regression (e.g., [118,232]).

Preliminary thermal imaging tests were performed with a FLIR I60 camera. The I60 is designed for large-scale hand-held operation, such as finding heat loss in a building insulation, and was therefore determined unsuitable for macro-imaging of small fuel droplets. For example, the

spatial resolution at the minimum focus distance is ~300 μm/px. The spatial resolution decreases to ~600 μm/px. at the actual stand-off distance of 240 mm (as dictated by the chamber geometry). A typical 500-μm droplet would not fill the space of a single pixel. Every study cited above used FLIR cameras [233], therefore it is recommended to contact the company to discuss the specific requirements of droplet thermal imaging due to their extensive product line.

### 5.2.6 Variable fan geometry

As discussed in Sections 4.1.1 and 4.2.1, the integral length scale, $L$, remains constant throughout all test conditions and fan speeds. While the invariability of $L$ is desirable to isolate the effects of other parameters such as turbulence intensity and Kolmogorov length scale, the controlled ability to generate disparate integral length scales would be useful in gauging the impact of the $L/d_0$ ratio on the evaporation rate. The integral length scale is geometry-driven, and in that sense, the fixed physical characteristics of the chamber may limit the range of plausible $L$. On the other hand, Ravi et al. [174] illustrated the potential to vary $L$ by altering the fan blade count and pitch angle. It should be noted that whether the altering the blades achieved significant variation in length scale depended on the method of calculating $L$. Regardless, it would be a useful endeavour to design and manufacture new fan blades in an attempt to modify the integral length scale. The results of Ravi et al. [174] suggest that adjusting the blade pitch is preferable to blade count, as increasing the blades on each hub from three to six led to a decrease in flow isotropy. In proceeding with additional droplet studies in the present chamber, the development of two new sets of fan assemblies with differing integral length scales would be highly advantageous. Variable integral length scale associated with zero mean velocity turbulence is a novel area and would be beneficial in validating correlations for predicting turbulent droplet evaporation.

### 5.2.7 Evaluation of cross-fiber effect

Section 2.3 revealed that while researchers have extensively studied the effect of large single fibers on droplet evaporation, only a handful of investigations have compared single fibers to cross-fibers (e.g., [57,58,73,77]). Furthermore, none of these studies have varied the diameter or material of the crossed fibers. It may, therefore, be useful to perform a parametric study on the cross-fiber effect by testing various fiber types and diameters. In this way, it would be possible to determine the maximum allowable fiber diameter which induces no unwanted effects. Although it is clearly possible to perform cross-fiber tests with fibers of very small diameter (Pan and collaborators [76,227] have used extremely thin fibers with diameters of 7 and 2.5 μm), it may be advantageous in some cases (for example, in high pressure or highly turbulent environments) to use larger fibers to improve droplet anchoring. Thus, future investigations should consider gathering experimental data on the variation of droplet evaporation rate with respect to cross-fiber material and diameter.

### 5.2.8 Background fuel vapor

Liquid droplets in combustion systems might not evaporate into pure ambient air of infinite expanse but rather into some mixture of air and previously vaporized fuel. While a handful of numerical studies (e.g., [204,234,235]) have analyzed the evaporation of a liquid droplet into an ambience saturated with its vapor, a serious lack of experimental data is evident. Pati et al. [204] compared the performance of diffusion- and kinetic-based models for predicting the lifetime of small water droplets evaporating into humid air at various pressure and temperature. Although the authors used a simple empirical model to benchmark the solutions, no experimental data was available for comparative purposes. Similarly, Abarham and Wichman [234] report interesting numerical and analytical findings regarding the condensation of background fuel vapor on droplets

prior to classic $d^2$ evaporation but, in their conclusion, concede that no experimental evidence exists for any of the processes examined in the paper. Recently, Gavhane et al. [235] extended the analysis of background fuel vapor to multicomponent fuels yet, once again, the authors were unable to provide comparisons against experimental data. Experimental data is critical in assessing the predictive capability of numerical codes, and investigations using the current spherical chamber could help bridge the knowledge gap. As discussed in [208], methods exist to introduce vaporized fuel into the chamber in a controlled and measurable manner. In summary, the chamber is first thoroughly vacuumed, and vaporized fuel is subsequently added. The chamber is equipped with a low range pressure transducer (0 – 5 psia) which can precisely measure the pressure of the vapor which, upon addition of air or nitrogen, becomes the partial vapor pressure. In this way, careful variation of the background fuel vapor concentration is possible. This procedure could be adapted to study the effect of background vapor on the evaporation of fuel droplets at various partial and total pressures as well as different temperatures.

### 5.2.9 Inclusion of a strong mean flow component

As presently equipped, the spherical chamber produces high levels of turbulence with quasi-zero mean velocity. In the future, it would be useful to combine the turbulence with a strong mean flow. The preliminary design of an additional fan, to be installed in one of the window ports, was the subject of a recent internal report [236]. The inclusion of this central fan would greatly extend the capability of the chamber. Currently, most studies with a strong mean component are carried out in a wind tunnel with grid-generated turbulence. Relatively low turbulence intensities handicap such approaches (Section 2.7.4). However, the combination of the existing eight fans with an additional centrally-located fan should produce turbulence intensities, defined as $U_{rms}/\overline{U}$,

exceeding 100%. Experiments of this nature would offer insight into the balance between mean convection and turbulent fluctuations and thus represent a novel pursuit in the field of droplet evaporation dynamics.

# REFERENCES


[1] U.S. Energy Information Administration, International energy outlook 2016, 2016.

[2] R.D. Reitz, Directions in internal combustion engine research, Combust. Flame. 160 (2013) 1–8.

[3] Intergovernmental Panel on Climate Change, IPCC Special report: Aviation and the global atmosphere, 1999.

[4] International Energy Agency, World energy outlook special report: Energy and air pollution, 2016.

[5] J.D. Murphy, T. Thamsiriroj, What will fuel transport systems of the future?, Mater. Today. 14 (2011) 518–524.

[6] National Research Council of the National Academies, Assessment of fuel economy technologies for light-duty vehicles, 2011.

[7] G.M. Faeth, Spray combustion phenomena, Symp. Combust. 26 (1996) 1593–1612.

[8] H.H. Chiu, T.M. Liu, Group combustion of liquid droplets, Combust. Sci. Technol. 17 (1977) 127–142.

[9] V. Deprédurand, G. Castanet, F. Lemoine, Heat and mass transfer in evaporating droplets in interaction: Influence of the fuel, Int. J. Heat Mass Transf. 53 (2010) 3495–3502.

[10] W.P. Jones, A.J. Marquis, K. Vogiatzaki, Large-eddy simulation of spray combustion in a gas turbine combustor, Combust. Flame. 161 (2014) 222–239.

[11] A.H. Lefebvre, D.R. Ballal, Gas turbine combustion: Alternative fuels and emissions, 3rd ed., Taylor and Francis Group, Boca Raton, FL, 2010.

[12] W.A. Sirignano, Fuel droplet vaporization and spray combustion theory, Prog. Energy Combust. Sci. 9 (1983) 291–322.

[13] M. Birouk, I. Gökalp, Current status of droplet evaporation in turbulent flows, Prog. Energy Combust. Sci. 32 (2006) 408–423.

[14] A. Williams, Combustion of droplets of liquid fuels: A review, Combust. Flame. 21 (1973) 1–31.

[15] A.L. Sánchez, J. Urzay, A. Liñán, The role of separation of scales in the description of spray combustion, Proc. Combust. Inst. 35 (2015) 1549–1577.

[16] J.-S. Wu, Y.-J. Liu, H.-J. Sheen, Effects of ambient turbulence and fuel properties on the evaporation rate of single droplets, Int. J. Heat Mass Transf. 44 (2001) 4593–4603.

[17] S.M. Correa, Power generation and aeropropulsion gas turbines: From combustion science to combustion technology, Symp. Combust. 27 (1998) 1793–1807.

[18] G.A.E. Godsave, Studies of the combustion of drops in a fuel spray - The burning of single drops of fuel, Symp. Combust. 4 (1953) 818–830.

[19] D.B. Spalding, The combustion of liquid fuels, Symp. Combust. 4 (1953) 847–864.

[20] H. Ghassemi, S.W. Baek, Q.S. Khan, Experimental study on evaporation of kerosene droplets at elevated pressures and temperatures, Combust. Sci. Technol. 178 (2006) 1669–1684.

[21] H. Nomura, Y. Ujiie, H.J. Rath, J. Sato, M. Kono, Experimental study on high-pressure droplet evaporation using microgravity conditions, Symp. Combust. 26 (1996) 1267–1273.

[22] T. Kitano, J. Nishio, R. Kurose, S. Komori, Effects of ambient pressure, gas temperature and combustion reaction on droplet evaporation, Combust. Flame. 161 (2014) 551–564.

[23] H. Kim, N. Sung, The effect of ambient pressure on the evaporation of a single droplet and a spray, Combust. Flame. 135 (2003) 261–270.

[24] G.-S. Zhu, R.D. Reitz, S.K. Aggarwal, Gas-phase unsteadiness and its influence on droplet vaporization in sub- and super-critical environments, Int. J. Heat Mass Transf. 44 (2001) 3081–3093.

[25] J. Bellan, Supercritical (and subcritical) fluid behavior and modeling: drops, streams, shear and mixing layers, jets and sprays, Prog. Energy Combust. Sci. 26 (2000) 329–366.

[26] Q.S. Khan, S.W. Baek, S.Y. Lee, Effect of droplet initial diameter on droplet vaporization regimes for kerosene fuel droplet, in: 45th Aerosp. Sci. Meet. Exhib., Reno, NV, 2007: pp.

14163–14170.

[27] D. Nguyen, D. Honnery, J. Soria, Measuring evaporation of micro-fuel droplets using magnified DIH and DPIV, Exp. Fluids. 50 (2011) 949–959.

[28] M. Birouk, I. Gökalp, A new correlation for turbulent mass transfer from liquid droplets, Int. J. Heat Mass Transf. 45 (2002) 37–45.

[29] J.-S. Wu, K.-H. Hsu, P.-M. Kuo, H.-J. Sheen, Evaporation model of a single hydrocarbon fuel droplet due to ambient turbulence at intermediate Reynolds numbers, Int. J. Heat Mass Transf. 46 (2003) 4741–4745.

[30] M. Birouk, S.C. Fabbro, Droplet evaporation in a turbulent atmosphere at elevated pressure - Experimental data, Proc. Combust. Inst. 34 (2013) 1577–1584.

[31] M. Birouk, A hydrocarbon droplet evaporating in turbulent environment at elevated ambient pressure and temperature, Combust. Sci. Technol. 186 (2014) 1295–1308.

[32] H. Wang, K. Luo, J. Fan, Effects of turbulent intensity and droplet diameter on spray combustion using direct numerical simulation, Fuel. 121 (2014) 311–318.

[33] M. Birouk, P. Toews, Effect of the initial diameter on the vaporization rate of a fuel droplet in a turbulent atmosphere: Experimental data, in: 25th Int. Colloq. Dyn. Explos. React. Syst., Leeds, UK, 2015.

[34] Y. Xu, M.C. Hicks, C.T. Avedisian, The combustion of iso-octane droplets with initial diameters from 0.5 to 5 mm: Effects on burning rate and flame extinction, Proc. Combust. Inst. 36 (2017) 2541–2548.

[35] G.S. Jackson, C.T. Avedisian, The effect of initial diameter in spherically symmetric droplet combustion of sooting fuels, Proc. R. Soc. London A. 446 (1994) 255–276.

[36] G. Xu, M. Ikegami, S. Honma, K. Ikeda, X. Ma, H. Nagaishi, D.L. Dietrich, P.M. Struk, Inverse influence of initial diameter on droplet burning rate in cold and hot ambiences: A thermal action of flame in balance with heat loss, Int. J. Heat Mass Transf. 46 (2003) 1155–1169.

[37] W.A. Sirignano, Fluid dynamics and transport of droplets and sprays, 2nd ed., Cambridge

University Press, New York, NY, 2014.

[38] S.P. Lin, R.D. Reitz, Drop and spray formation from a liquid jet, Annu. Rev. Fluid Mech. 30 (1998) 85–105.

[39] H.I.H. Saravanamuttoo, G.F.C. Rogers, H. Cohen, P.V. Straznicky, Gas turbine theory, 6th ed., Pearson Prentice Hall, Harlow, U.K., 2009.

[40] S.D. Givler, J. Abraham, Supercritical droplet vaporization and combustion studies, Prog. Energy Combust. Sci. 22 (1996) 1–28.

[41] I. Treager, Aircraft gas turbine engine technology, 3rd ed., Glencoe, New York, NY, 1996.

[42] A.H. Lefebvre, Atomization and sprays, Taylor and Francis Group, New York, NY, 1989.

[43] J.B. Heywood, Internal combustion engine fundamentals, McGraw-Hill, Inc., United States, 1988.

[44] P. Marmottant, E. Villermaux, On spray formation, J. Fluid Mech. 498 (2004) 73–111.

[45] S.K. Aggarwal, Single droplet ignition: Theoretical analyses and experimental findings, Prog. Energy Combust. Sci. 45 (2014) 79–107.

[46] M. Chaker, C.B. Meher-Homji, Gas turbine power augmentation: Parametric study relating to fog droplet size and its influence on evaporative efficiency, J. Eng. Gas Turbines Power. 133 (2011) 92001–92010.

[47] H. Barrow, C.W. Pope, Droplet evaporation with reference to the effectiveness of water-mist cooling, Appl. Energy. 84 (2007) 404–412.

[48] K. Harstad, J. Bellan, Modeling evaporation of Jet A, JP-7, and RP-1 drops at 1 to 15 bars, Combust. Flame. 137 (2004) 163–177.

[49] M.R.G. Zoby, S. Navarro-Martinez, A. Kronenburg, A.J. Marquis, Turbulent mixing in three-dimensional droplet arrays, Int. J. Heat Fluid Flow. 32 (2011) 499–509.

[50] N.A. Chigier, The atomization and burning of liquid fuel sprays, Prog. Energy Combust. Sci. 2 (1976) 97–114.

[51] J.A. Nicholls, C.W. Kauffman, D.G. Pelaccio, D.R. Glass, J.F. Driscoll, The effect of fuel

sprays on emissions from a research gas turbine combustor, Combust. Sci. Technol. 23 (1980) 203–213.

[52] H.H. Chiu, H.Y. Kim, E.J. Croke, Internal group combustion of liquid droplets, Symp. Combust. 19 (1982) 971–980.

[53] W.A. Sirignano, Advances in droplet array combustion theory and modeling, Prog. Energy Combust. Sci. 42 (2014) 54–86.

[54] H. Nomura, H. Takahashi, Y. Suganuma, M. Kikuchi, Droplet ignition behavior in the vicinity of the leading edge of a flame spreading along a fuel droplet array in fuel-vapor/air mixture, Proc. Combust. Inst. 34 (2013) 1593–1600.

[55] G.M. Faeth, Evaporation and combustion of sprays, Prog. Energy Combust. Sci. 9 (1983) 1–76.

[56] E.W. Curtis, P. V. Farrell, A numerical study of high-pressure droplet vaporization, Combust. Flame. 90 (1992) 85–102.

[57] M. Mikami, H. Oyagi, N. Kojima, M. Kikuchi, Y. Wakashima, S. Yoda, Microgravity experiments on flame spread along fuel-droplet arrays using a new droplet-generation technique, Combust. Flame. 141 (2005) 241–252.

[58] Y.C. Liu, Y. Xu, C.T. Avedisian, M.C. Hicks, The effect of support fibers on micro-convection in droplet combustion experiments, Proc. Combust. Inst. 35 (2015) 1709–1716.

[59] S. Kumagai, T. Sakai, S. Okajima, Combustion of free fuel droplets in a freely falling chamber, Symp. Combust. 13 (1971) 779–785.

[60] H. Hara, S. Kumagai, The effect of initial diameter on free droplet combustion with spherical flame, Symp. Combust. 25 (1994) 423–430.

[61] G. Castanet, P. Lavieille, F. Lemoine, M. Lebouché, A. Atthasit, Y. Biscos, G. Lavergne, Energetic budget on an evaporating monodisperse droplet stream using combined optical methods: Evaluation of the convective heat transfer, Int. J. Heat Mass Transf. 45 (2002) 5053–5067.

[62] C. Maqua, G. Castanet, F. Lemoine, Bicomponent droplets evaporation: Temperature

measurements and modelling, Fuel. 87 (2008) 2932–2942.

[63] T. Kristyadi, V. Deprédurand, G. Castanet, F. Lemoine, S.S. Sazhin, A. Elwardany, E.M. Sazhina, M.R. Heikal, Monodisperse monocomponent fuel droplet heating and evaporation, Fuel. 89 (2010) 3995–4001.

[64] D. Honnery, D. Nguyen, J. Soria, Microdroplet evaporation under increasing temperature conditions: Experiments and modelling, Fuel. 105 (2013) 247–257.

[65] G.O. Langstroth, C.H.H. Diehl, E.J. Winhold, The evaporation of droplets in still air, Can. J. Res. 28A (1950) 580–595.

[66] A.T. Shih, C.M. Megaridis, Suspended droplet evaporation modeling in a laminar convective environment, Combust. Flame. 102 (1995) 256–270.

[67] J.-R. Yang, S.-C. Wong, On the discrepancies between theoretical and experimental results for microgravity droplet evaporation, Int. J. Heat Mass Transf. 44 (2001) 4433–4443.

[68] J.-R. Yang, S.-C. Wong, An experimental and theoretical study of the effects of heat conduction through the support fiber on the evaporation of a droplet in a weakly convective flow, Int. J. Heat Mass Transf. 45 (2002) 4589–4598.

[69] K. Han, G. Song, X. Ma, B. Yang, An experimental and theoretical study of the effect of suspended thermocouple on the single droplet evaporation, Appl. Therm. Eng. 101 (2016) 568–575.

[70] P. Seers, W. Thomas, S. Bruyere-Bergeron, Determination of fuel droplet evaporation based on multiple thermocouple sizes, in: 49th Aerosp. Sci. Meet. Exhib., Orlando, FL, 2011.

[71] H.L. Rehman, J. Weiss, P. Seers, Effect of heat conduction on droplet life time and evaporation rate under forced convection at low temperatures, Exp. Therm. Fluid Sci. 72 (2016) 59–66.

[72] D. Shringi, H.A. Dwyer, B.D. Shaw, Influences of support fibers on vaporizing fuel droplets, Comput. Fluids. 77 (2013) 66–75.

[73] M.C. Hicks, V. Nayagam, F.A. Williams, Methanol droplet extinction in carbon-dioxide-enriched environments in microgravity, Combust. Flame. 157 (2010) 1439–1445.

[74] T. Farouk, F.L. Dryer, Microgravity droplet combustion: Effect of tethering fiber on burning rate and flame structure, Combust. Theory Model. 15 (2011) 487–515.

[75] C.T. Avedisian, B.J. Callahan, Experimental study of nonane/hexanol mixture droplet combustion without natural or forced convection, Proc. Combust. Inst. 28 (2000) 991–997.

[76] K.-L. Pan, J.-W. Li, C.-P. Chen, C.-H. Wang, On droplet combustion of biodiesel fuel mixed with diesel/alkanes in microgravity condition, Combust. Flame. 156 (2009) 1926–1936.

[77] C. Chauveau, M. Birouk, I. Gökalp, An analysis of the d2-law departure during droplet evaporation in microgravity, Int. J. Multiph. Flow. 37 (2011) 252–259.

[78] P.M. Struk, M. Ackerman, V. Nayagam, D.L. Dietrich, On calculating burning rates during fiber supported droplet combustion, Microgravity Sci. Technol. XI (1998) 144–151.

[79] S.S. Sazhin, Advanced models of fuel droplet heating and evaporation, Prog. Energy Combust. Sci. 32 (2006) 162–214.

[80] S.S. Sazhin, Modelling of droplet heating and evaporation: Recent results and unsolved problems, Fuel. 196 (2017) 69–101.

[81] R.L. Matlosz, S. Leipziger, T.. Torda, Investigation of liquid drop evaporation in a high temperature and high pressure environment, Int. J. Heat Mass Transf. 15 (1972) 831–852.

[82] R.P. Probert, The influence of spray particle size and distribution in the combustion of oil droplets, Philos. Mag. 37 (1946) 94–105.

[83] C.K. Law, Recent advances in droplet vaporization and combustion, Prog. Energy Combust. Sci. 8 (1982) 171–201.

[84] L.W. Huang, C.H. Chen, Flame stabilization and blowoff over a single droplet, Numer. Heat Transf. Part A Appl. 27 (1995) 53–71.

[85] C.G. McCreath, N.A. Chigier, Liquid-spray burning in the wake of a stabilizer disc, Symp. Combust. 14 (1973) 1355–1363.

[86] J. Sato, M. Tsue, M. Niwa, M. Kono, Effects of natural convection on high-pressure droplet combustion, Combust. Flame. 82 (1990) 142–150.

[87] I. Gökalp, C. Chauveau, O. Simon, X. Chesneau, Mass transfer from liquid fuel droplets in turbulent flow, Combust. Flame. 89 (1992) 286–298.

[88] J.C. Maxwell, The scientific papers of James Clerk Maxwell, Vol. II, Cambridge University Press, 1890.

[89] Stefan, Unknown title, Wien. Ber. 65 (1872) 323.

[90] N. Fuchs, Concerning the velocity of evaporation of small droplets in a gas atmosphere, 1934.

[91] T.L. Bergman, A.S. Lavine, F.P. Incropera, D.P. Dewitt, Fundamentals of heat and mass transfer, 7th ed., John Wiley & Sons, Inc., Hoboken, NJ, 2011.

[92] G. Juncu, Unsteady heat transfer from an oblate/prolate spheroid, Int. J. Heat Mass Transf. 53 (2010) 3483–3494.

[93] J. Li, J. Zhang, A theoretical study of the spheroidal droplet evaporation in forced convection, Phys. Lett. A. 378 (2014) 3537–3543.

[94] M.T. Monaghan, R.G. Siddall, M.W. Thring, The influence of initial diameter on the combustion of single drops of liquid fuel, Combust. Flame. 12 (1968) 45–53.

[95] H. Isoda, S. Kumagai, New aspects of droplet combustion, Symp. Combust. 7 (1958) 523–531.

[96] M.K. King, H.D. Ross, Overview of the NASA microgravity combustion program, AIAA J. 36 (1998) 1337–1345.

[97] G. Gogos, S. Soh, D.N. Pope, Effects of gravity and ambient pressure on liquid fuel droplet evaporation, Int. J. Heat Mass Transf. 46 (2003) 283–296.

[98] E.M. Sparrow, J.L. Gregg, The variable fluid-property problem in free convection, Trans Am. Soc. Mech. Eng. 80 (1958) 879–886.

[99] G.L. Hubbard, V.E. Denny, A.F. Mills, Droplet evaporation: Effects of transients and variable properties, Int. J. Heat Mass Transf. 18 (1975) 1003–1008.

[100] C. Yin, Modelling of heating and evaporation of n-Heptane droplets: Towards a generic

model for fuel droplet/particle conversion, Fuel. 141 (2015) 64–73.

[101] B. Sobac, P. Talbot, B. Haut, A. Rednikov, P. Colinet, A comprehensive analysis of the evaporation of a liquid spherical drop, J. Colloid Interface Sci. 438 (2015) 306–317.

[102] A.J. Marchese, F.L. Dryer, The effect of non-luminous thermal radiation in microgravity droplet combustion, Combust. Sci. Technol. 124 (1997) 371–402.

[103] H.H. Chiu, Advances and challenges in droplet and spray combustion. I. Toward a unified theory of droplet aerothermochemistry, Prog. Energy Combust. Sci. 26 (2000) 381–416.

[104] G.M. Faeth, Current status of droplet and liquid combustion, Prog. Energy Combust. Sci. 3 (1977) 191–224.

[105] C.C. Tseng, R. Viskanta, Effect of radiation absorption on fuel droplet evaporation, Combust. Sci. Technol. 177 (2005) 1511–1542.

[106] B. Abramzon, S. Sazhin, Droplet vaporization model in the presence of thermal radiation, Int. J. Heat Mass Transf. 48 (2005) 1868–1873.

[107] H. Wise, G.A. Agoston, Burning of a liquid droplet, Lit. Combust. Pet. 20 (1958) 116–135.

[108] M. Goldsmith, S.S. Penner, On the burning of single drops of fuel in an oxidizing atmosphere, J. Jet Propuls. 24 (1954) 245–251.

[109] N. Frössling, Evaporation of falling drops, Gerlands Beitr. Geophys. 52 (1938) 170–216.

[110] W.E. Ranz, W.R. Marshall, Evaporation from drops: Part I, Chem. Eng. Prog. 48 (1952) 141–146.

[111] W.E. Ranz, W.R. Marshall, Evaporation from drops: Part II, Chem. Eng. Prog. 48 (1952) 173–180.

[112] M.E. How, The influence of turbulence on the burning rates of fuel suspensions, J. Inst. Fuel. 39 (1966) 150–158.

[113] C. Borgnakke, R.E. Sonntag, Fundamentals of thermodynamics, 7th ed., John Wiley & Sons, Inc., Hoboken, NJ, 2009.

[114] V. Yang, Modeling of supercritical vaporization, mixing, and combustion processes in

liquid-fueled propulsion systems, Proc. Combust. Inst. 28 (2000) 925–942.

[115] G. Fang, C.A. Ward, Temperature measured close to the interface of an evaporating liquid, Phys. Rev. E. 59 (1999) 417–428.

[116] A.J.H. McGaughey, C.A. Ward, Temperature discontinuity at the surface of an evaporating droplet, J. Appl. Phys. 91 (2002) 6406–6415.

[117] E.Y. Gatapova, I.A. Graur, O.A. Kabov, V.M. Aniskin, M.A. Filipenko, F. Sharipov, L. Tadrist, The temperature jump at water - air interface during evaporation, Int. J. Heat Mass Transf. 104 (2017) 800–812.

[118] V.Y. Borodulin, V.N. Letushko, M.I. Nizovtsev, A.N. Sterlyagov, Determination of parameters of heat and mass transfer in evaporating drops, Int. J. Heat Mass Transf. 109 (2017) 609–618.

[119] B.E. Poling, J.M. Prausnitz, J.P. O'Connell, The properties of gases and liquids, 5th ed., McGraw-Hill, Inc., United States, 2001.

[120] G.S. Zhu, S.K. Aggarwal, Transient supercritical droplet evaporation with emphasis on the effects of equation of state, Int. J. Heat Mass Transf. 43 (2000) 1157–1171.

[121] J.S. Chin, A.H. Lefebvre, The role of the heat-up period in fuel drop evaporation, Int. J. Turbo Jet Engines. 2 (1985) 315–325.

[122] H. Jia, G. Gogos, High pressure droplet vaporization; effects of liquid-phase gas solubility, Int. J. Heat Mass Transf. 36 (1993) 4419–4431.

[123] C. Chauveau, X. Chesneau, I. Gökalp, High pressure vaporization and burning of methanol droplets in reduced gravity, Adv. Sp. Res. 16 (1995) 157–160.

[124] R.J. Tabaczynski, Turbulence and turbulent combustion in spark-ignition engines, Prog. Energy Combust. Sci. 2 (1976) 143–165.

[125] B. Abramzon, W.A. Sirignano, Droplet vaporization model for spray combustion calculations, Int. J. Heat Mass Transf. 32 (1989) 1605–1618.

[126] F. Marti, O. Martinez, D. Mazo, J. Garman, D. Dunn-Rankin, Evaporation of a droplet larger than the Kolmogorov length scale immersed in a relative mean flow, Int. J. Multiph.

Flow. 88 (2017) 63–68.

[127] Y. Ohta, K. Shimoyama, S. Ohigashi, Vaporization and combustion of single liquid fuel droplets in a turbulent environment, Bull. JSME. 18 (1975) 47–56.

[128] C.K. Law, G.M. Faeth, Opportunities and challenges of combustion in microgravity, Prog. Energy Combust. Sci. 20 (1994) 65–113.

[129] G.A. Agoston, H. Wise, W.A. Rosser, Dynamic factors affecting the combustion of liquid spheres, Symp. Combust. 6 (1957) 708–717.

[130] P. Balakrishnan, T. Sundararajan, R. Natarajan, Combustion of a fuel droplet in a mixed convective environment, Combust. Sci. Technol. 163 (2001) 77–106.

[131] C.K. Law, F.A. Williams, Kinetics and convection in the combustion of alkane droplets, Combust. Flame. 19 (1972) 393–405.

[132] T. Kadota, H. Hiroyasu, Combustion of a fuel droplet in supercritical gaseous environments, Symp. Combust. 18 (1981) 275–282.

[133] G.M. Faeth, D.P. Dominicis, J.F. Tulpinsky, D.R. Olson, Supercritical bipropellant droplet combustion, Symp. Combust. 12 (1969) 9–18.

[134] J. Sato, Studies on droplet evaporation and combustion in high pressure, in: 31st Aerosp. Sci. Meet. Exhib., Reno, NV, 1993.

[135] A. Daïf, M. Bouaziz, X. Chesneau, A. Ali Chérif, Comparison of multicomponent fuel droplet vaporization experiments in forced convection with the Sirignano model, Exp. Therm. Fluid Sci. 18 (1999) 282–290.

[136] C. Habchi, V. Ebrahimian, Gravitational effects on multi-component droplet evaporation, Microgravity Sci. Technol. 24 (2012) 229–235.

[137] M. Ackerman, F.A. Williams, Simplified model for droplet combustion in a slow convective flow, Combust. Flame. 143 (2005) 599–612.

[138] H. Zhang, G. Gogos, Numerical research on a vaporizing fuel droplet in a forced convective environment, Int. J. Multiph. Flow. 30 (2004) 181–198.

[139] M.R.G. Zoby, S. Navarro-Martinez, A. Kronenburg, A.J. Marquis, Evaporation rates of droplet arrays in turbulent reacting flows, Proc. Combust. Inst. 33 (2011) 2117–2125.

[140] R.S. Miller, K. Harstad, J. Bellan, Evaluation of equilibrium and non-equilibrium evaporation models for many-droplet gas-liquid flow simulations, Int. J. Multiph. Flow. 24 (1998) 1025–1055.

[141] Z. Zhifu, W. Guoxiang, C. Bin, G. Liejin, W. Yueshe, Evaluation of evaporation models for single moving droplet with a high evaporation rate, Powder Technol. 240 (2013) 95–102.

[142] S. Prakash, W.A. Sirignano, Liquid fuel droplet heating with internal circulation, Int. J. Heat Mass Transf. 21 (1978) 885–895.

[143] S. Prakash, W.A. Sirignano, Theory of convective droplet vaporization with unsteady heat transfer in the circulating liquid phase, Int. J. Heat Mass Transf. 23 (1980) 253–268.

[144] N. Ghata, B.D. Shaw, Computational modeling of the effects of support fibers on evaporation of fiber-supported droplets in reduced gravity, Int. J. Heat Mass Transf. 77 (2014) 22–36.

[145] D.L. Albernaz, G. Amberg, M. Do-Quang, Simulation of a suspended droplet under evaporation with Marangoni effects, Int. J. Heat Mass Transf. 97 (2016) 853–860.

[146] G.D. Myers, A.H. Lefebvre, Flame propagation in heterogeneous mixtures of fuel drops and air, Combust. Flame. 66 (1986) 193–210.

[147] M. Sommerfeld, H.-H. Qiu, Experimental studies of spray evaporation in turbulent flow, Int. J. Heat Fluid Flow. 19 (1998) 10–22.

[148] R.J. Sornek, R. Dobashi, T. Hirano, Effect of turbulence on vaporization, mixing, and combustion of liquid-fuel sprays, Combust. Flame. 120 (2000) 479–491.

[149] A. Sadiki, M. Chrigui, J. Janicka, M.R. Maneshkarimi, Modeling and simulation of effects of turbulence on vaporization, mixing and combustion of liquid-fuel sprays, Flow Turbul. Combust. 75 (2005) 105–130.

[150] M. Labowsky, D.E. Rosner, M. Arias-Zugasti, Turbulence effects on evaporation rate-controlled spray combustor performance, Int. J. Heat Mass Transf. 54 (2011) 2683–2695.

[151] B. Rauch, R. Calabria, F. Chiariello, P. Le Clercq, P. Massoli, M. Rachner, Accurate analysis of multicomponent fuel spray evaporation in turbulent flow, Exp. Fluids. 52 (2012) 935–948.

[152] P.R. Yearling, R.D. Gould, Convective heat and mass transfer from single evaporating water, methanol and ethanol droplets, in: Proc. ASME Heat Transf. Fluids Eng. Div., 1995: pp. 33–38.

[153] T.R. Galloway, B.H. Sage, Thermal and material transfer from spheres: Prediction of local transport, Int. J. Heat Mass Transf. 11 (1968) 539–549.

[154] N. Hiromitsu, O. Kawaguchi, Influence of flow turbulence on the evaporation rate of a suspended droplet in a hot air flow, Heat Transf. - Japanese Res. 24 (1995) 689–700.

[155] A.V. Eckartsberg, J.S. Kapat, Effect of flow turbulence on evaporation rate of a single droplet, in: 38th Aerosp. Sci. Meet. Exhib., Reno, NV, 2000.

[156] J. Park, K. Kontani, Numerical study for free-stream turbulence effects on a single droplet vaporization, SAE Tech. Pap. 901607 (1990).

[157] M. Masoudi, W.A. Sirignano, Collision of a vortex with a vaporizing droplet, Int. J. Multiph. Flow. 26 (2000) 1925–1949.

[158] M.M. Abou Al-Sood, M. Birouk, A numerical study of the effect of turbulence on mass transfer from a single fuel droplet evaporating in a hot convective flow, Int. J. Therm. Sci. 46 (2007) 779–789.

[159] M.M. Abou Al-Sood, M. Birouk, A numerical model for calculating the vaporization rate of a fuel droplet exposed to a convective turbulent airflow, Int. J. Numer. Methods Heat Fluid Flow. 18 (2008) 146–159.

[160] M.M. Abou Al-Sood, M. Birouk, Droplet heat and mass transfer in a turbulent hot airstream, Int. J. Heat Mass Transf. 51 (2008) 1313–1324.

[161] M. Birouk, M.M. Abou Al-Sood, I. Gökalp, Droplet evaporation in a turbulent environment at elevated pressure and temperature conditions, Combust. Sci. Technol. 180 (2008) 1987–2014.

[162] M.M. Abou Al-Sood, M. Birouk, 3D numerical simulation of the effect of droplet initial conditions on the evaporation process, Comput. Therm. Sci. 1 (2009) 159–187.

[163] M. Birouk, M.M. Abou Al-Sood, Droplet evaporation in a turbulent high-pressure freestream - A numerical study, Int. J. Therm. Sci. 49 (2010) 264–271.

[164] W. Hwang, J.K. Eaton, Creating homogeneous and isotropic turbulence without a mean flow, Exp. Fluids. 36 (2004) 444–454.

[165] K. Chang, G.P. Bewley, E. Bodenschatz, Experimental study of the influence of anisotropy on the inertial scales of turbulence, J. Fluid Mech. 692 (2012) 464–481.

[166] A. Srdic, H.J.S. Fernando, L. Montenegro, Generation of nearly isotropic turbulence using two oscillating grids, Exp. Fluids. 20 (1996) 395–397.

[167] M.M. Hoque, M.J. Sathe, S. Mitra, J.B. Joshi, G.M. Evans, Comparison of specific energy dissipation rate calculation methodologies utilising 2D PIV velocity measurement, Chem. Eng. Sci. 137 (2015) 752–767.

[168] A.A. Davani, P.D. Ronney, A Jet-Stirred Apparatus for Turbulent Combustion Experiments, in: 9Th Natl. Meet., Leeds, UK, 2015: pp. 1–6.

[169] T.D. Fansler, E.G. Groff, Turbulence characteristics of a fan-stirred combustion vessel, Combust. Flame. 80 (1990) 350–354.

[170] R.G. Abdel-Gayed, K.J. Al-Khishali, C. Bradley, Turbulent burning velocities and flame straining in explosions, Proc. R. Soc. London A. 391 (1984) 393–414.

[171] E.S. Semenov, Measurement of turbulence characteristics in a closed volume with artificial turbulence, Combust. Explos. Shock Waves. 1 (1965) 57–62.

[172] S. Kwon, M.-S. Wu, J.F. Driscoll, G.M. Faeth, Flame surface properties of premixed flames in isotropic turbulence: Measurements and numerical simulations, Combust. Flame. 88 (1992) 221–238.

[173] B. Leisenheimer, W. Leuckel, Self-generated acceleration of confined deflagrative flame fronts, Combust. Sci. Technol. 118 (1996) 147–164.

[174] S. Ravi, S.J. Peltier, E.L. Petersen, Analysis of the impact of impeller geometry on the

turbulent statistics inside a fan-stirred, cylindrical flame speed vessel using PIV, Exp. Fluids. 54 (2013) 1424.

[175] M. Birouk, C. Chauveau, B. Sarh, A. Quilgars, I. Gökalp, Turbulence effects on the vaporization of monocomponent single droplets, Combust. Sci. Technol. 113 (1996) 413–428.

[176] M. Birouk, C. Chauveau, I. Gökalp, Turbulence effects on the combustion of single hydrocarbon droplets, Proc. Combust. Inst. 28 (2000) 1015–1021.

[177] M. Birouk, B. Sarh, I. Gökalp, An attempt to realize experimental isotropic turbulence at low Reynolds number, Flow Turbul. Combust. 70 (2003) 325–348.

[178] Z. Dou, Z.K. Pecenak, L. Cao, S.H. Woodward, Z. Liang, H. Meng, PIV measurement of high-Reynolds-number homogeneous and isotropic turbulence in an enclosed flow apparatus with fan agitation, Meas. Sci. Technol. 27 (2016) 35305.

[179] S. Xu, S. Huang, R. Huang, W. Wei, X. Cheng, Y. Ma, Y. Zhang, Estimation of turbulence characteristics from PIV in a high-pressure fan-stirred constant volume combustion chamber, Appl. Therm. Eng. 110 (2017) 346–355.

[180] J. de Jong, J.P.L.C. Salazar, S.H. Woodward, L.R. Collins, H. Meng, Measurement of inertial particle clustering and relative velocity statistics in isotropic turbulence using holographic imaging, Int. J. Multiph. Flow. 36 (2010) 324–332.

[181] A. Hayakawa, Y. Miki, Y. Nagano, T. Kitagawa, Analysis of turbulent burning velocity of spherically propagating premixed flame with effective turbulence intensity, J. Therm. Sci. Technol. 7 (2012) 507–521.

[182] M. Birouk, S.L. Toth, Hydrocarbon droplet turbulent combustion in an elevated pressure environment, Flow Turbul. Combust. 94 (2015) 843–858.

[183] J. Goulier, N. Chaumeix, F. Halter, N. Meynet, A. Bentaïb, Experimental study of laminar and turbulent flame speed of a spherical flame in a fan-stirred closed vessel for hydrogen safety application, Nucl. Eng. Des. 312 (2017) 214–227.

[184] B. Galmiche, N. Mazellier, F. Halter, F. Foucher, Turbulence characterization of a high-

pressure high-temperature fan-stirred combustion vessel using LDV, PIV and TR-PIV measurements, Exp. Fluids. 55 (2014) 1636.

[185] P.O. Witze, Hot wire turbulence measurements in a motored internal combustion engine, in: 2nd Eur. Symp. Combust., Orleans, FR, 1975.

[186] E. Baum, B. Peterson, C. Surmann, D. Michaelis, B. Böhm, A. Dreizler, Investigation of the 3D flow field in an IC engine using tomographic PIV, Proc. Combust. Inst. 34 (2013) 2903–2910.

[187] S. Fabbro, An experimental test facility for studying the effects of turbulence on the evaporation of fuel droplets at elevated pressure and temperature conditions, M.Sc. thesis, University of Manitoba, 2012.

[188] M. Birouk, S.L. Toth, Vaporization and combustion of a soybean biodiesel droplet in turbulent environment at elevated ambient pressure, Combust. Sci. Technol. 187 (2015) 937–952.

[189] J.F. Driscoll, D.G. Pelaccio, Turbulent eddy diffusivity and mean eddy lifetimes measured in spray combusiton, Combust. Sci. Technol. 21 (1980) 205–212.

[190] D.R. Ballal, A.H. Lefebvre, Flame propagation in heterogeneous mixtures of fuel droplets, fuel vapor and air, Symp. Combust. 18 (1981) 321–328.

[191] A. Datta, S.K. Som, Effects of spray characteristics on combustion performance of a liquid fuel spray in a gas turbine combustor, Int. J. Energy Res. 23 (1999) 217–228.

[192] R. Nakanishi, H. Kobayashi, S. Kato, T. Niioka, Ignition experiment of a fuel droplet in high-pressure high-temperature ambient, Symp. Combust. 25 (1994) 447–453.

[193] H. Hara, S. Kumagai, Experimental investigation of free droplet combustion under microgravity, Symp. Combust. 23 (1990) 1605–1610.

[194] K.-O. Lee, S.L. Manzello, M.Y. Choi, The effects of initial diameter on sooting and burning behavior of isolated droplets under microgravity conditions, Combust. Sci. Technol. 132 (1998) 139–156.

[195] S.L. Manzello, M.U. Choi, A. Kazakov, F.L. Dryer, R. Dobashi, T. Hirano, The burning of

large n-heptane droplets in microgravity, Proc. Combust. Inst. 28 (2000) 1079–1086.

[196] G. Xu, M. Ikegami, S. Honma, K. Ikeda, D.L. Dietrich, P.M. Struk, Interactive influences of convective flow and initial droplet diameter on isolated droplet burning rate, Int. J. Heat Mass Transf. 47 (2004) 2029–2035.

[197] Y.C. Liu, Y. Xu, M.C. Hicks, C.T. Avedisian, Comprehensive study of initial diameter effects and other observations on convection-free droplet combustion in the standard atmosphere for n-heptane, n-octane, and n-decane, Combust. Flame. 171 (2016) 27–41.

[198] J.H. Bae, C.T. Avedisian, Experimental study of the effect of helium/nitrogen concentration and initial droplet diameter on nonane droplet combustion with minimal convection, Proc. Combust. Inst. 31 (2007) 2157–2164.

[199] J.H. Bae, C.T. Avedisian, Nonane droplet combustion with and without buoyant convection: Flame structure, burning rate and extinction in air and helium, Proc. Combust. Inst. 32 (2009) 2231–2238.

[200] S. Nakaya, K. Fujishima, M. Tsue, M. Kono, D. Segawa, Effects of droplet diameter on instantaneous burning rate of isolated fuel droplets in argon-rich or carbon dioxide-rich ambiences under microgravity, Proc. Combust. Inst. 34 (2013) 1601–1608.

[201] I. Awasthi, G. Gogos, T. Sundararajan, Effects of size on combustion of isolated methanol droplets, Combust. Flame. 160 (2013) 1789–1802.

[202] I. Awasthi, D.N. Pope, G. Gogos, Effects of the ambient temperature and initial diameter in droplet combustion, Combust. Flame. 161 (2014) 1883–1899.

[203] A.P. Kryukov, V.Y. Levashov, S.S. Sazhin, Evaporation of diesel fuel droplets: Kinetic versus hydrodynamic models, Int. J. Heat Mass Transf. 47 (2004) 2541–2549.

[204] S. Pati, S. Chakraborty, S.K. Som, Influence of ambient vapor concentration on droplet evaporation in a perspective of comparison between diffusion controlled model and kinetic model, Int. J. Heat Mass Transf. 54 (2011) 4580–4584.

[205] H. Kim, S.W. Baek, D. Chang, A single n-heptane droplet behavior in rapid compression machine, Int. J. Heat Mass Transf. 69 (2014) 247–255.

[206] S.L. Toth, Experimental study of droplet vaporization and combustion of diesel, biodiesel and their blends in a turbulent environment at elevated pressure and temperature conditions, M.Sc. thesis, University of Manitoba, 2014.

[207] A.M.I. Chowdhury, Experimental characterization of a bio-liquid fuel to be used as an additive for improving biodiesel combustion in cold weather conditions, M.Sc. thesis, University of Manitoba, 2015.

[208] C.A.G. Casanova, Experimental measurement of laminar flame speed of a novel liquid biofuel 1,3 dimethoxyoctane, M.Sc. thesis, University of Manitoba, 2015.

[209] T. Edwards, M. Colket, N. Cernansky, F. Dryer, F. Egolfopoulos, D. Friend, E. Law, D. Lenhert, P. Lindstedt, H. Pitsch, A. Sarofim, K. Seshadri, M. Smooke, W. Tsang, S. Williams, Development of an experimental database and kinetic models for surrogate jet fuels, in: 45th AIAA Aerosp. Sci. Meet. Exhib., Reno, NV, 2007.

[210] M. Al Qubeissi, S.S. Sazhin, J. Turner, S. Begg, C. Crua, M.R. Heikal, Modelling of gasoline fuel droplets heating and evaporation, Fuel. 159 (2015) 373–384.

[211] U.S. Department of Health and Human Services, Toxicological profile for jet fuels JP-4 and JP-7, 1995.

[212] Chevron Corporation, Diesel fuels technical review, 2007.

[213] S. Blakey, L. Rye, C.W. Wilson, Aviation gas turbine alternative fuels: A review, Proc. Combust. Inst. 33 (2011) 2863–2885.

[214] M. Raffel, C. Willert, S. Wereley, J. Kompenhans, Particle image velocimetry: A practical guide, 2nd ed., Springer, 2007.

[215] C. Verwey, M. Birouk, Experimental investigation of the effect of droplet size on the vaporization process in ambient turbulence, Combust. Flame. 182 (2017) 288–297.

[216] C. Verwey, M. Birouk, Fuel vaporization: Effect of droplet size and turbulence at elevated temperature and pressure (SUBMITTED), Combust. Flame. n/a (2017) n/a.

[217] P.A. Davidson, Turbulence: An introduction for scientists and engineers, 2nd ed., Oxford University Press, Oxford, UK, 2015.

[218] H. Tennekes, J.L. Lumley, A first course in turbulence, The MIT Press, Cambridge, MA, 1972.

[219] S.B. Pope, Turbulent flows, Cambridge University Press, New York, NY, 2000.

[220] G.D. Raithby, E.R.G. Eckert, The effect of turbulence parameters and support position on the heat transfer from spheres, Int. J. Heat Mass Transf. 11 (1968) 1233–1252.

[221] D.E. Rosner, M. Arias-Zugasti, M. Labowsky, Intensity and efficiency of spray fuel-fed well-mixed adiabatic combustors, Chem. Eng. Sci. 63 (2008) 3909–3922.

[222] C.P. Cho, H.Y. Kim, S.S. Yoon, Interaction of the burning spherical droplets in oxygen-enriched turbulent environment, Combust. Flame. 156 (2009) 14–24.

[223] J.J. Hegseth, N. Rashidnia, A. Chai, Natural convection in droplet evaporation, Phys. Rev. E. 54 (1996) 1640–1644.

[224] H. Nomura, H. Rath, J. Sato, M. Kono, Effects of ambient pressure and natural convection on fuel droplet evaporation, in: 4th Asian-Pacific Int. Symp. Combust. Energy Util., Bangkok, TH, 1997: pp. 266–271.

[225] J. Shinjo, J. Xia, A. Umemura, Droplet/ligament modulation of local small-scale turbulence and scalar mixing in a dense fuel spray, Proc. Combust. Inst. 35 (2015) 1595–1602.

[226] C. Chauveau, F. Halter, I. Gökalp, Vaporization in three-dimensional droplet arrays: Effects of the fuel vapor saturation, in: 10th Int. Conf. Liq. At. Spray Syst., Kyoto, JP, 2006.

[227] K.-L. Pan, M.-C. Chiu, Droplet combustion of blended fuels with alcohol and biodiesel/diesel in microgravity condition, Fuel. 113 (2013) 757–765.

[228] C. Solomon, T. Breckon, Fundamentals of digital image processing: A practical approach with examples in MATLAB, John Wiley & Sons, Inc., Chichester, UK, 2011.

[229] J. Jung, S. Jeong, H. Kim, Investigation of single-droplet/wall collision heat transfer characteristics using infrared thermometry, Int. J. Heat Mass Transf. 92 (2016) 774–783.

[230] F. Girard, M. Antoni, K. Sefiane, Infrared thermography investigation of an evaporating sessile water droplet on heated substrates, Langmuir. 26 (2010) 4576–4580.

[231] N.K. Akafuah, A.J. Salazar, K. Saito, Infrared thermography-based visualization of droplet transport in liquid sprays, Infrared Phys. Technol. 53 (2010) 218–226.

[232] S.B. Saharin, B. Lefort, C. Morin, C. Chauveau, L. Le Moyne, R. Kafafy, Vaporization characteristics of ethanol and 1-propanol droplets at high temperatures, At. Sprays. 22 (2012) 207–226.

[233] FLIR Systems Inc., www.flir.ca/home, (2017).

[234] M. Abarham, I.S. Wichman, Mono-component fuel droplet evaporation in the presence of background fuel vapor, Int. J. Heat Mass Transf. 54 (2011) 4090–4098.

[235] S. Gavhane, S. Pati, S.K. Som, Evaporation of multicomponent liquid fuel droplets: Influences of component composition in droplet and vapor concentration in free stream ambience, Int. J. Therm. Sci. 105 (2016) 83–95.

[236] G. Rigby, Examination of the effect of cross-flow turbulence on column trajectory and breakup of an injected liquid jet at high temperature and pressure, Energy and Combustion Laboratory, University of Manitoba, 2016.

# APPENDICES

## A. Complete data sheets

**Table A.1**
Heptane evaporation data – standard conditions.

| $P$ [bar] | $T$ [K] | $N$ [RPM] | $d_0$ [µm] | $K$ [mm²/s] | $K/K_0$ [-] | $d_{dev}$ [µm] |
|---|---|---|---|---|---|---|
| 1 | 298 | 0 | 664.89 | 0.0099 | 0.97 | - |
| 1 | 298 | 0 | 400.11 | 0.0097 | 0.95 | - |
| 1 | 298 | 0 | 539.15 | 0.0105 | 1.03 | - |
| 1 | 298 | 0 | 608.26 | 0.0107 | 1.05 | - |
| 1 | 298 | 0 | 443.22 | 0.0101 | 0.99 | - |
| 1 | 298 | 0 | 663.47 | 0.0101 | 0.99 | - |
| 1 | 298 | 0 | 628.62 | 0.0106 | 1.04 | - |
| 1 | 298 | 0 | 457.59 | 0.0102 | 1.00 | - |
| 1 | 298 | 0 | 593.26 | 0.0106 | 1.04 | - |
| 1 | 298 | 0 | 296.84 | 0.0096 | 0.94 | - |
| 1 | 298 | 0 | 333.45 | 0.0101 | 0.99 | - |
| 1 | 298 | 500 | 483.18 | 0.0151 | 1.48 | 205.00 |
| 1 | 298 | 500 | 589.54 | 0.0160 | 1.57 | - |
| 1 | 298 | 500 | 557.42 | 0.0159 | 1.56 | 334.45 |
| 1 | 298 | 500 | 479.01 | 0.0157 | 1.54 | 283.39 |
| 1 | 298 | 500 | 628.53 | 0.0164 | 1.61 | 371.84 |
| 1 | 298 | 500 | 605.52 | 0.0159 | 1.56 | 284.01 |
| 1 | 298 | 500 | 201.02 | 0.0135 | 1.32 | - |
| 1 | 298 | 500 | 246.11 | 0.0134 | 1.31 | - |
| 1 | 298 | 500 | 419.70 | 0.0149 | 1.46 | 229.88 |
| 1 | 298 | 500 | 389.78 | 0.0149 | 1.46 | 135.02 |
| 1 | 298 | 500 | 562.66 | 0.0160 | 1.57 | 342.25 |
| 1 | 298 | 500 | 355.43 | 0.0143 | 1.40 | 150.80 |
| 1 | 298 | 500 | 173.69 | 0.0130 | 1.28 | - |
| 1 | 298 | 500 | 269.67 | 0.0127 | 1.25 | - |
| 1 | 298 | 500 | 190.00 | 0.0134 | 1.32 | - |
| 1 | 298 | 500 | 145.41 | 0.0132 | 1.30 | - |

**Table A.1**
(Continued)

| $P$ [bar] | $T$ [K] | $N$ [RPM] | $d_0$ [µm] | $K$ [mm$^2$/s] | $K/K_0$ [-] | $d_{dev}$ [µm] |
|---|---|---|---|---|---|---|
| 1 | 298 | 500 | 166.70 | 0.0126 | 1.24 | - |
| 1 | 298 | 500 | 199.41 | 0.0130 | 1.27 | - |
| 1 | 298 | 500 | 157.43 | 0.0131 | 1.28 | - |
| 1 | 298 | 500 | 241.27 | 0.0130 | 1.28 | - |
| 1 | 298 | 1000 | 338.80 | 0.0170 | 1.67 | |
| 1 | 298 | 1000 | 531.42 | 0.0208 | 2.04 | 336.10 |
| 1 | 298 | 1000 | 171.97 | 0.0153 | 1.50 | - |
| 1 | 298 | 1000 | 280.65 | 0.0178 | 1.75 | - |
| 1 | 298 | 1000 | 234.76 | 0.0160 | 1.57 | 128.58 |
| 1 | 298 | 1000 | 519.44 | 0.0196 | 1.92 | 284.51 |
| 1 | 298 | 1000 | 375.20 | 0.0181 | 1.78 | 198.54 |
| 1 | 298 | 1000 | 346.85 | 0.0173 | 1.70 | 155.12 |
| 1 | 298 | 1000 | 501.20 | 0.0191 | 1.87 | 212.64 |
| 1 | 298 | 1000 | 415.86 | 0.0196 | 1.92 | 227.78 |
| 1 | 298 | 1000 | 575.91 | 0.0213 | 2.09 | 364.24 |
| 1 | 298 | 1000 | 253.78 | 0.0169 | 1.66 | - |
| 1 | 298 | 1000 | 387.10 | 0.0190 | 1.86 | 189.64 |
| 1 | 298 | 1000 | 645.11 | 0.0223 | 2.19 | 397.67 |
| 1 | 298 | 1000 | 394.74 | 0.0196 | 1.92 | - |
| 1 | 298 | 2000 | 366.46 | 0.0247 | 2.42 | 193.91 |
| 1 | 298 | 2000 | 254.79 | 0.0213 | 2.09 | - |
| 1 | 298 | 2000 | 620.96 | 0.0289 | 2.84 | 340.11 |
| 1 | 298 | 2000 | 392.93 | 0.0248 | 2.43 | 175.72 |
| 1 | 298 | 2000 | 361.35 | 0.0237 | 2.33 | 197.92 |
| 1 | 298 | 2000 | 551.05 | 0.0262 | 2.57 | 330.63 |
| 1 | 298 | 2000 | 172.76 | 0.0221 | 2.17 | - |
| 1 | 298 | 2000 | 458.52 | 0.0260 | 2.55 | 205.06 |
| 1 | 298 | 2000 | 598.58 | 0.0281 | 2.76 | 364.10 |
| 1 | 298 | 2000 | 596.23 | 0.0279 | 2.74 | 337.28 |
| 1 | 298 | 2000 | 393.28 | 0.0241 | 2.36 | 192.67 |
| 1 | 298 | 2000 | 227.47 | 0.0200 | 1.96 | - |
| 1 | 298 | 2000 | 286.92 | 0.0225 | 2.21 | 157.15 |

**Table A.1**
(Continued)

| $P$ [bar] | $T$ [K] | $N$ [RPM] | $d_0$ [µm] | $K$ [mm²/s] | $K/K_0$ [-] | $d_{dev}$ [µm] |
|---|---|---|---|---|---|---|
| 1 | 298 | 2000 | 227.02 | 0.0223 | 2.19 | 128.42 |
| 1 | 298 | 2000 | 492.60 | 0.0261 | 2.56 | 282.98 |
| 1 | 298 | 3000 | 542.49 | 0.0354 | 3.47 | - |
| 1 | 298 | 3000 | 389.31 | 0.0304 | 2.98 | 246.22 |
| 1 | 298 | 3000 | 250.85 | 0.0250 | 2.45 | 177.38 |
| 1 | 298 | 3000 | 419.68 | 0.0321 | 3.15 | 258.71 |
| 1 | 298 | 3000 | 377.97 | 0.0297 | 2.91 | 207.02 |
| 1 | 298 | 3000 | 490.70 | 0.0340 | 3.34 | 318.01 |
| 1 | 298 | 3000 | 224.49 | 0.0246 | 2.41 | 141.98 |
| 1 | 298 | 3000 | 349.02 | 0.0297 | 2.91 | 156.09 |
| 1 | 298 | 3000 | 339.40 | 0.0300 | 2.94 | 191.99 |
| 1 | 298 | 3000 | 236.76 | 0.0275 | 2.70 | 125.28 |
| 1 | 298 | 3000 | 479.33 | 0.0357 | 3.50 | 279.50 |
| 1 | 298 | 3000 | 422.55 | 0.0316 | 3.10 | 273.84 |
| 1 | 298 | 3000 | 341.21 | 0.0300 | 2.94 | 186.89 |
| 1 | 298 | 3000 | 218.79 | 0.0256 | 2.51 | 115.77 |
| 1 | 298 | 3000 | 238.29 | 0.0267 | 2.62 | - |

**Table A.2**
Decane evaporation data – standard conditions.

| $P$ [bar] | $T$ [K] | $N$ [RPM] | $d_0$ [µm] | $K$ [mm²/s] | $K/K_0$ [-] | $d_{dev}$ [µm] |
|---|---|---|---|---|---|---|
| 1 | 298 | 0 | 430.43 | 0.000565 | 0.97 | 210.87 |
| 1 | 298 | 0 | 266.21 | 0.000540 | 0.92 | - |
| 1 | 298 | 0 | 687.46 | 0.000623 | 1.07 | 400.85 |
| 1 | 298 | 0 | 656.78 | 0.000625 | 1.07 | 334.89 |
| 1 | 298 | 0 | 543.98 | 0.000600 | 1.03 | 292.94 |
| 1 | 298 | 0 | 462.38 | 0.000601 | 1.03 | 244.67 |
| 1 | 298 | 0 | 394.91 | 0.000589 | 1.01 | 201.37 |
| 1 | 298 | 0 | 245.12 | 0.000559 | 0.96 | - |
| 1 | 298 | 0 | 249.52 | 0.000553 | 0.95 | - |

**Table A.2**
(Continued)

| $P$ [bar] | $T$ [K] | $N$ [RPM] | $d_0$ [µm] | $K$ [mm$^2$/s] | $K/K_0$ [-] | $d_{dev}$ [µm] |
|---|---|---|---|---|---|---|
| 1 | 298 | 1000 | 692.57 | 0.00153 | 2.62 | 499.42 |
| 1 | 298 | 1000 | 556.07 | 0.00144 | 2.47 | - |
| 1 | 298 | 1000 | 477.27 | 0.00135 | 2.32 | 309.31 |
| 1 | 298 | 1000 | 375.69 | 0.00128 | 2.20 | 243.47 |
| 1 | 298 | 1000 | 355.52 | 0.00129 | 2.20 | 246.31 |
| 1 | 298 | 1000 | 726.87 | 0.00159 | 2.73 | 459.71 |
| 1 | 298 | 1000 | 261.59 | 0.00113 | 1.93 | 147.98 |
| 1 | 298 | 1000 | 149.74 | 0.00106 | 1.81 | - |
| 1 | 298 | 1000 | 227.82 | 0.00104 | 1.78 | - |
| 1 | 298 | 1000 | 224.32 | 0.00115 | 1.96 | 148.80 |
| 1 | 298 | 1000 | 530.77 | 0.00145 | 2.48 | 318.46 |
| 1 | 298 | 3000 | 417.51 | 0.00241 | 4.13 | - |
| 1 | 298 | 3000 | 394.67 | 0.00242 | 4.14 | 230.13 |
| 1 | 298 | 3000 | 331.71 | 0.00225 | 3.86 | 175.52 |
| 1 | 298 | 3000 | 460.69 | 0.00287 | 4.92 | 291.37 |
| 1 | 298 | 3000 | 263.53 | 0.00186 | 3.19 | 170.79 |
| 1 | 298 | 3000 | 513.73 | 0.00264 | 4.53 | - |
| 1 | 298 | 3000 | 361.95 | 0.00221 | 3.78 | 191.53 |
| 1 | 298 | 3000 | 226.75 | 0.00190 | 3.26 | - |
| 1 | 298 | 3000 | 337.33 | 0.00228 | 3.91 | 181.66 |
| 1 | 298 | 3000 | 449.75 | 0.00256 | 4.38 | 266.08 |
| 1 | 298 | 3000 | 213.17 | 0.00198 | 3.39 | - |
| 1 | 298 | 3000 | 430.73 | 0.00273 | 4.68 | 265.52 |
| 1 | 298 | 3000 | 205.10 | 0.00169 | 2.90 | - |
| 1 | 298 | 3000 | 436.89 | 0.00241 | 4.13 | 296.31 |
| 1 | 298 | 3000 | 218.93 | 0.00186 | 3.19 | 134.96 |
| 1 | 298 | 3000 | 303.73 | 0.00224 | 3.83 | 201.47 |
| 1 | 298 | 3000 | 350.70 | 0.00231 | 3.96 | 219.01 |

**Table A.3**
Heptane evaporation data – elevated pressure and standard temperature.

| $P$ [bar] | $T$ [K] | $N$ [RPM] | $d_0$ [µm] | $K$ [mm$^2$/s] | $K/K_0$ [-] | $d_{dev}$ [µm] |
|---|---|---|---|---|---|---|
| 2.5 | 298 | 0 | 554.67 | 0.00571 | 0.99 | - |
| 2.5 | 298 | 0 | 451.05 | 0.00570 | 0.99 | - |
| 2.5 | 298 | 0 | 496.49 | 0.00597 | 1.03 | - |
| 2.5 | 298 | 0 | 430.40 | 0.00588 | 1.02 | - |
| 2.5 | 298 | 0 | 227.76 | 0.00581 | 1.01 | - |
| 2.5 | 298 | 0 | 362.12 | 0.00582 | 1.01 | - |
| 2.5 | 298 | 0 | 376.12 | 0.00587 | 1.02 | - |
| 2.5 | 298 | 0 | 292.08 | 0.00563 | 0.98 | - |
| 2.5 | 298 | 0 | 506.36 | 0.00574 | 0.99 | - |
| 2.5 | 298 | 0 | 281.43 | 0.00567 | 0.98 | - |
| 2.5 | 298 | 0 | 181.47 | 0.00572 | 0.99 | - |
| 2.5 | 298 | 500 | 494.38 | 0.0123 | 2.12 | 331.64 |
| 2.5 | 298 | 500 | 483.70 | 0.0116 | 2.01 | 241.85 |
| 2.5 | 298 | 500 | 274.49 | 0.0100 | 1.72 | - |
| 2.5 | 298 | 500 | 321.76 | 0.0104 | 1.80 | 203.50 |
| 2.5 | 298 | 500 | 512.91 | 0.0119 | 2.06 | 324.39 |
| 2.5 | 298 | 500 | 284.99 | 0.0107 | 1.85 | 180.24 |
| 2.5 | 298 | 500 | 426.28 | 0.0119 | 2.06 | 285.96 |
| 2.5 | 298 | 500 | 431.92 | 0.0122 | 2.10 | 311.46 |
| 2.5 | 298 | 500 | 183.04 | 0.0096 | 1.66 | - |
| 2.5 | 298 | 500 | 367.47 | 0.0115 | 1.99 | - |
| 2.5 | 298 | 1000 | 431.30 | 0.0134 | 2.32 | 255.16 |
| 2.5 | 298 | 1000 | 525.67 | 0.0162 | 2.81 | - |
| 2.5 | 298 | 1000 | 193.01 | 0.0121 | 2.10 | - |
| 2.5 | 298 | 1000 | 453.90 | 0.0149 | 2.59 | 264.67 |
| 2.5 | 298 | 1000 | 382.16 | 0.0148 | 2.56 | 270.23 |
| 2.5 | 298 | 1000 | 354.00 | 0.0137 | 2.38 | 250.32 |
| 2.5 | 298 | 1000 | 315.54 | 0.0137 | 2.38 | 218.61 |
| 2.5 | 298 | 1000 | 174.73 | 0.0126 | 2.19 | 134.21 |
| 2.5 | 298 | 1000 | 236.68 | 0.0116 | 2.01 | - |
| 2.5 | 298 | 1000 | 303.17 | 0.0139 | 2.41 | 214.37 |
| 2.5 | 298 | 2000 | 413.64 | 0.0199 | 3.44 | 251.61 |

**Table A.3**
(Continued)

| $P$ [bar] | $T$ [K] | $N$ [RPM] | $d_0$ [µm] | $K$ [mm$^2$/s] | $K/K_0$ [-] | $d_{dev}$ [µm] |
|---|---|---|---|---|---|---|
| 2.5 | 298 | 2000 | 508.50 | 0.0217 | 3.75 | 321.60 |
| 2.5 | 298 | 2000 | 429.28 | 0.0221 | 3.83 | 297.41 |
| 2.5 | 298 | 2000 | 343.27 | 0.0194 | 3.35 | 225.10 |
| 2.5 | 298 | 2000 | 326.74 | 0.0191 | 3.30 | 193.30 |
| 2.5 | 298 | 2000 | 280.29 | 0.0196 | 3.39 | 188.02 |
| 2.5 | 298 | 2000 | 282.12 | 0.0182 | 3.16 | 149.28 |
| 2.5 | 298 | 2000 | 297.73 | 0.0204 | 3.54 | 199.72 |
| 2.5 | 298 | 2000 | 384.80 | 0.0234 | 4.06 | 298.06 |
| 2.5 | 298 | 2000 | 355.60 | 0.0195 | 3.38 | 210.38 |
| 2.5 | 298 | 2000 | 300.97 | 0.0190 | 3.29 | 159.26 |
| 2.5 | 298 | 2000 | 218.26 | 0.0173 | 3.00 | 136.30 |
| 2.5 | 298 | 2000 | 284.39 | 0.0192 | 3.32 | 182.10 |
| 2.5 | 298 | 2000 | 608.87 | 0.0257 | 4.45 | 375.33 |
| 2.5 | 298 | 2000 | 251.49 | 0.0185 | 3.21 | 137.75 |
| 2.5 | 298 | 2500 | 296.13 | 0.0207 | 3.59 | 182.55 |
| 2.5 | 298 | 2500 | 418.67 | 0.0244 | 4.23 | 271.33 |
| 2.5 | 298 | 2500 | 430.94 | 0.0253 | 4.38 | 292.28 |
| 2.5 | 298 | 2500 | 315.36 | 0.0226 | 3.91 | 172.73 |
| 2.5 | 298 | 2500 | 387.02 | 0.0274 | 4.74 | 309.62 |
| 2.5 | 298 | 2500 | 293.87 | 0.0225 | 3.90 | 166.24 |
| 2.5 | 298 | 2500 | 260.84 | 0.0221 | 3.83 | 130.42 |
| 2.5 | 298 | 2500 | 230.62 | 0.0211 | 3.65 | 149.46 |
| 2.5 | 298 | 2500 | 234.34 | 0.0223 | 3.86 | 155.44 |
| 2.5 | 298 | 2500 | 400.55 | 0.0250 | 4.32 | 219.39 |
| 5 | 298 | 0 | 480.69 | 0.00383 | 1.02 | - |
| 5 | 298 | 0 | 539.26 | 0.00386 | 1.03 | - |
| 5 | 298 | 0 | 416.85 | 0.00397 | 1.06 | - |
| 5 | 298 | 0 | 355.24 | 0.00349 | 0.93 | - |
| 5 | 298 | 0 | 352.95 | 0.00344 | 0.91 | - |
| 5 | 298 | 0 | 221.81 | 0.00356 | 0.95 | - |
| 5 | 298 | 0 | 199.67 | 0.00379 | 1.01 | - |
| 5 | 298 | 0 | 317.24 | 0.00393 | 1.04 | - |

**Table A.3**
(Continued)

| $P$ [bar] | $T$ [K] | $N$ [RPM] | $d_0$ [µm] | $K$ [mm²/s] | $K/K_0$ [-] | $d_{dev}$ [µm] |
|---|---|---|---|---|---|---|
| 5 | 298 | 0 | 556.59 | 0.00375 | 1.00 | - |
| 5 | 298 | 0 | 308.83 | 0.00411 | 1.09 | - |
| 5 | 298 | 0 | 216.73 | 0.00364 | 0.97 | - |
| 5 | 298 | 500 | 537.11 | 0.01046 | 2.78 | 379.79 |
| 5 | 298 | 500 | 595.41 | 0.01123 | 2.99 | 433.47 |
| 5 | 298 | 500 | 213.61 | 0.00703 | 1.87 | - |
| 5 | 298 | 500 | 338.02 | 0.01010 | 2.69 | 224.22 |
| 5 | 298 | 500 | 306.71 | 0.00880 | 2.34 | 198.77 |
| 5 | 298 | 500 | 438.38 | 0.00953 | 2.53 | 196.05 |
| 5 | 298 | 500 | 499.62 | 0.01019 | 2.71 | 278.18 |
| 5 | 298 | 500 | 444.42 | 0.00966 | 2.57 | 288.02 |
| 5 | 298 | 500 | 207.71 | 0.00764 | 2.03 | 131.37 |
| 5 | 298 | 500 | 577.75 | 0.01074 | 2.86 | 365.40 |
| 5 | 298 | 500 | 457.78 | 0.00926 | 2.46 | 183.11 |
| 5 | 298 | 500 | 224.35 | 0.00821 | 2.18 | 134.61 |
| 5 | 298 | 500 | 210.21 | 0.00826 | 2.20 | 154.47 |
| 5 | 298 | 500 | 353.78 | 0.00900 | 2.39 | 212.27 |
| 5 | 298 | 500 | 212.39 | 0.00830 | 2.21 | - |
| 5 | 298 | 1000 | 489.44 | 0.0148 | 3.93 | 379.12 |
| 5 | 298 | 1000 | 499.15 | 0.0138 | 3.66 | 366.80 |
| 5 | 298 | 1000 | 448.39 | 0.0135 | 3.59 | 317.06 |
| 5 | 298 | 1000 | 222.26 | 0.0098 | 2.61 | - |
| 5 | 298 | 1000 | 287.91 | 0.0116 | 3.08 | 205.61 |
| 5 | 298 | 1000 | 337.77 | 0.0126 | 3.35 | 224.05 |
| 5 | 298 | 1000 | 500.82 | 0.0147 | 3.91 | 374.78 |
| 5 | 298 | 1000 | 258.78 | 0.0103 | 2.75 | 157.41 |
| 5 | 298 | 1000 | 237.99 | 0.0131 | 3.48 | 176.50 |
| 5 | 298 | 1000 | 363.20 | 0.0137 | 3.63 | 264.41 |
| 5 | 298 | 1000 | 454.47 | 0.0150 | 3.99 | 283.82 |
| 5 | 298 | 1000 | 438.71 | 0.0140 | 3.72 | 291.01 |
| 5 | 298 | 1000 | 277.78 | 0.0117 | 3.12 | 180.02 |
| 5 | 298 | 1000 | 289.63 | 0.0118 | 3.13 | 192.12 |

**Table A.3**
(Continued)

| $P$ [bar] | $T$ [K] | $N$ [RPM] | $d_0$ [µm] | $K$ [mm²/s] | $K/K_0$ [-] | $d_{dev}$ [µm] |
|---|---|---|---|---|---|---|
| 5 | 298 | 1000 | 193.76 | 0.0112 | 2.97 | - |
| 10 | 298 | 0 | 361.29 | 0.00304 | 1.10 | - |
| 10 | 298 | 0 | 564.46 | 0.00357 | 1.29 | - |
| 10 | 298 | 0 | 282.01 | 0.00265 | 0.96 | - |
| 10 | 298 | 0 | 282.45 | 0.00232 | 0.84 | - |
| 10 | 298 | 0 | 546.39 | 0.00261 | 0.95 | - |
| 10 | 298 | 0 | 476.31 | 0.00262 | 0.95 | - |
| 10 | 298 | 0 | 355.78 | 0.00258 | 0.94 | - |
| 10 | 298 | 0 | 518.53 | 0.00294 | 1.07 | - |
| 10 | 298 | 0 | 304.61 | 0.00239 | 0.87 | - |
| 10 | 298 | 0 | 436.69 | 0.00285 | 1.03 | - |
| 10 | 298 | 500 | 364.74 | 0.00705 | 2.56 | 252.70 |
| 10 | 298 | 500 | 487.28 | 0.00835 | 3.03 | 407.69 |
| 10 | 298 | 500 | 366.23 | 0.00754 | 2.73 | 256.36 |
| 10 | 298 | 500 | 388.60 | 0.00799 | 2.90 | 320.45 |
| 10 | 298 | 500 | 561.30 | 0.00955 | 3.47 | 469.62 |
| 10 | 298 | 500 | 414.19 | 0.00756 | 2.74 | 333.93 |
| 10 | 298 | 500 | 352.52 | 0.00679 | 2.46 | 246.76 |
| 10 | 298 | 500 | 348.06 | 0.00725 | 2.63 | 260.46 |
| 10 | 298 | 500 | 307.49 | 0.00721 | 2.61 | 215.24 |
| 10 | 298 | 500 | 651.51 | 0.01073 | 3.89 | 545.09 |
| 10 | 298 | 1000 | 302.75 | 0.0092 | 3.33 | 211.93 |
| 10 | 298 | 1000 | 480.66 | 0.0116 | 4.21 | 304.00 |
| 10 | 298 | 1000 | 374.31 | 0.0112 | 4.05 | 259.33 |
| 10 | 298 | 1000 | 351.17 | 0.0107 | 3.90 | 230.28 |
| 10 | 298 | 1000 | 417.78 | 0.0114 | 4.15 | 280.26 |
| 10 | 298 | 1000 | 492.60 | 0.0124 | 4.50 | 344.82 |
| 10 | 298 | 1000 | 498.00 | 0.0122 | 4.42 | 294.62 |
| 10 | 298 | 1000 | 510.81 | 0.0120 | 4.36 | 319.00 |
| 10 | 298 | 1000 | 370.51 | 0.0107 | 3.90 | 222.31 |
| 10 | 298 | 1000 | 410.39 | 0.0119 | 4.31 | 224.78 |

**Table A.4**
Decane evaporation data – elevated pressure and standard temperature.

| $P$ [bar] | $T$ [K] | $N$ [RPM] | $d_0$ [µm] | $K$ [mm$^2$/s] | $K/K_0$ [-] | $d_{dev}$ [µm] |
|---|---|---|---|---|---|---|
| 5 | 298 | 0 | 713.94 | 0.000199 | 1.18 | 478.93 |
| 5 | 298 | 0 | 620.58 | 0.000186 | 1.11 | 402.18 |
| 5 | 298 | 0 | 262.11 | 0.000146 | 0.87 | - |
| 5 | 298 | 0 | 414.11 | 0.000163 | 0.97 | 248.47 |
| 5 | 298 | 0 | 165.75 | 0.000137 | 0.82 | - |
| 5 | 298 | 0 | 498.77 | 0.000177 | 1.05 | 352.68 |
| 5 | 298 | 1000 | 641.98 | 0.000669 | 3.98 | 458.47 |
| 5 | 298 | 1000 | 209.46 | 0.000419 | 2.49 | - |
| 5 | 298 | 1000 | 461.73 | 0.000611 | 3.63 | 326.49 |
| 5 | 298 | 1000 | 328.54 | 0.000522 | 3.11 | 220.39 |
| 5 | 298 | 1000 | 228.19 | 0.000460 | 2.74 | 142.50 |
| 5 | 298 | 1000 | 551.36 | 0.000702 | 4.18 | 389.87 |
| 5 | 298 | 1000 | 557.16 | 0.000658 | 3.92 | 401.77 |
| 5 | 298 | 1000 | 142.27 | 0.000391 | 2.33 | - |
| 5 | 298 | 1000 | 370.58 | 0.000567 | 3.38 | 272.32 |
| 5 | 298 | 1500 | 441.13 | 0.000750 | 4.46 | 341.70 |
| 5 | 298 | 1500 | 355.73 | 0.000689 | 4.10 | 256.52 |
| 5 | 298 | 1500 | 234.16 | 0.000591 | 3.52 | - |
| 5 | 298 | 1500 | 337.24 | 0.000693 | 4.13 | 228.73 |
| 5 | 298 | 1500 | 224.78 | 0.000572 | 3.40 | - |
| 5 | 298 | 1500 | 459.86 | 0.000847 | 5.04 | 331.61 |
| 5 | 298 | 1500 | 285.16 | 0.000667 | 3.97 | 186.99 |
| 10 | 298 | 0 | 646.26 | 0.000123 | 1.16 | 466.02 |
| 10 | 298 | 0 | 466.07 | 0.000110 | 1.04 | 287.30 |
| 10 | 298 | 0 | 240.37 | 0.000094 | 0.89 | 140.16 |
| 10 | 298 | 0 | 218.94 | 0.000090 | 0.85 | 127.66 |
| 10 | 298 | 0 | 540.34 | 0.000114 | 1.07 | 305.66 |
| 10 | 298 | 0 | 421.22 | 0.000105 | 0.99 | 266.40 |
| 10 | 298 | 500 | 672.16 | 0.000422 | 3.98 | 511.90 |
| 10 | 298 | 500 | 594.75 | 0.000400 | 3.77 | 441.08 |
| 10 | 298 | 500 | 319.78 | 0.000309 | 2.91 | 226.12 |
| 10 | 298 | 500 | 144.77 | 0.000220 | 2.07 | - |

**Table A.4**
(Continued)

| $P$ [bar] | $T$ [K] | $N$ [RPM] | $d_0$ [µm] | $K$ [mm²/s] | $K/K_0$ [-] | $d_{dev}$ [µm] |
|---|---|---|---|---|---|---|
| 10 | 298 | 500 | 300.72 | 0.000294 | 2.77 | 201.73 |
| 10 | 298 | 500 | 431.92 | 0.000362 | 3.42 | 334.56 |
| 10 | 298 | 500 | 201.96 | 0.000259 | 2.44 | 127.73 |
| 10 | 298 | 500 | 508.50 | 0.000399 | 3.76 | 393.88 |
| 10 | 298 | 1000 | 424.27 | 0.000465 | 4.39 | 323.11 |
| 10 | 298 | 1000 | 113.03 | 0.000296 | 2.79 | - |
| 10 | 298 | 1000 | 271.98 | 0.000388 | 3.66 | 182.45 |
| 10 | 298 | 1000 | 454.35 | 0.000526 | 4.96 | 351.94 |
| 10 | 298 | 1000 | 331.19 | 0.000450 | 4.24 | 236.52 |
| 10 | 298 | 1000 | 238.92 | 0.000383 | 3.61 | 141.35 |

**Table A.5**
Heptane evaporation data – elevated temperature.

| $P$ [bar] | $T$ [K] | $N$ [RPM] | $d_0$ [µm] | $K$ [mm²/s] | $K/K_0$ [-] | $d_{dev}$ [µm] |
|---|---|---|---|---|---|---|
| 1 | 323 | 0 | 361.12 | 0.0229 | 1.02 | - |
| 1 | 323 | 0 | 503.55 | 0.0221 | 0.98 | - |
| 1 | 323 | 0 | 208.72 | 0.0214 | 0.95 | - |
| 1 | 323 | 0 | 586.80 | 0.0229 | 1.02 | - |
| 1 | 323 | 0 | 141.96 | 0.0233 | 1.03 | - |
| 1 | 323 | 1000 | 491.86 | 0.0341 | 1.52 | 340.77 |
| 1 | 323 | 1000 | 500.64 | 0.0324 | 1.44 | 264.91 |
| 1 | 323 | 1000 | 515.39 | 0.0357 | 1.58 | 236.18 |
| 1 | 323 | 1000 | 365.84 | 0.0310 | 1.38 | - |
| 1 | 323 | 1000 | 595.52 | 0.0361 | 1.60 | 285.60 |
| 1 | 323 | 1000 | 367.88 | 0.0347 | 1.54 | 156.08 |
| 1 | 323 | 1000 | 206.50 | 0.0274 | 1.21 | - |
| 1 | 323 | 1000 | 161.94 | 0.0308 | 1.37 | - |
| 1 | 323 | 1000 | 314.91 | 0.0318 | 1.41 | - |
| 1 | 323 | 1000 | 391.99 | 0.0320 | 1.42 | 156.80 |
| 1 | 323 | 3000 | 406.73 | 0.0462 | 2.05 | 190.77 |

**Table A.5**
(Continued)

| $P$ [bar] | $T$ [K] | $N$ [RPM] | $d_0$ [µm] | $K$ [mm$^2$/s] | $K/K_0$ [-] | $d_{dev}$ [µm] |
|---|---|---|---|---|---|---|
| 1 | 323 | 3000 | 416.65 | 0.0499 | 2.22 | 220.47 |
| 1 | 323 | 3000 | 537.05 | 0.0501 | 2.22 | 294.15 |
| 1 | 323 | 3000 | 234.50 | 0.0402 | 1.78 | - |
| 1 | 323 | 3000 | 336.30 | 0.0451 | 2.00 | 161.28 |
| 1 | 323 | 3000 | 211.81 | 0.0408 | 1.81 | - |
| 1 | 323 | 3000 | 367.85 | 0.0453 | 2.01 | 164.51 |
| 1 | 323 | 3000 | 589.51 | 0.0568 | 2.52 | 408.42 |
| 1 | 348 | 0 | 533.38 | 0.0356 | 1.02 | - |
| 1 | 348 | 0 | 460.95 | 0.0341 | 0.98 | - |
| 1 | 348 | 0 | 340.60 | 0.0343 | 0.99 | - |
| 1 | 348 | 0 | 251.79 | 0.0342 | 0.98 | - |
| 1 | 348 | 0 | 570.87 | 0.0365 | 1.05 | - |
| 1 | 348 | 0 | 186.60 | 0.0340 | 0.98 | - |
| 1 | 348 | 1000 | 644.48 | 0.0617 | 1.77 | 341.03 |
| 1 | 348 | 1000 | 586.42 | 0.0598 | 1.72 | 315.80 |
| 1 | 348 | 1000 | 496.07 | 0.0598 | 1.72 | 361.14 |
| 1 | 348 | 1000 | 394.77 | 0.0545 | 1.57 | 246.53 |
| 1 | 348 | 1000 | 236.33 | 0.0490 | 1.41 | - |
| 1 | 348 | 1000 | 307.82 | 0.0484 | 1.39 | - |
| 1 | 348 | 1000 | 140.55 | 0.0642 | 1.84 | - |
| 1 | 348 | 1000 | 158.51 | 0.0584 | 1.68 | - |
| 1 | 348 | 1000 | 187.48 | 0.0496 | 1.43 | - |
| 1 | 348 | 1000 | 425.54 | 0.0514 | 1.48 | - |
| 1 | 348 | 3000 | 540.30 | 0.0879 | 2.53 | 285.90 |
| 1 | 348 | 3000 | 517.70 | 0.0807 | 2.32 | - |
| 1 | 348 | 3000 | 404.50 | 0.0762 | 2.19 | - |
| 1 | 348 | 3000 | 245.57 | 0.0818 | 2.35 | - |
| 1 | 348 | 3000 | 195.03 | 0.0845 | 2.43 | - |
| 1 | 348 | 3000 | 298.07 | 0.0701 | 2.01 | - |
| 1 | 348 | 3000 | 526.04 | 0.0945 | 2.71 | 368.23 |
| 1 | 348 | 3000 | 185.65 | 0.0770 | 2.21 | - |
| 1 | 348 | 3000 | 434.44 | 0.0790 | 2.27 | - |

**Table A.5**
(Continued)

| $P$ [bar] | $T$ [K] | $N$ [RPM] | $d_0$ [µm] | $K$ [mm$^2$/s] | $K/K_0$ [-] | $d_{dev}$ [µm] |
|---|---|---|---|---|---|---|
| 10 | 323 | 0 | 528.07 | 0.00777 | 1.08 | 258.70 |
| 10 | 323 | 0 | 394.80 | 0.00737 | 1.02 | 216.24 |
| 10 | 323 | 0 | 277.35 | 0.00658 | 0.91 | - |
| 10 | 323 | 0 | 373.21 | 0.00676 | 0.94 | 171.03 |
| 10 | 323 | 0 | 183.99 | 0.00648 | 0.90 | - |
| 10 | 323 | 0 | 591.30 | 0.00814 | 1.13 | 461.82 |
| 10 | 323 | 0 | 238.73 | 0.00662 | 0.92 | - |
| 10 | 323 | 0 | 518.40 | 0.00799 | 1.11 | 351.60 |
| 10 | 323 | 500 | 497.04 | 0.0186 | 2.58 | 233.13 |
| 10 | 323 | 500 | 593.96 | 0.0206 | 2.85 | 361.29 |
| 10 | 323 | 500 | 185.68 | 0.0117 | 1.62 | - |
| 10 | 323 | 500 | 366.99 | 0.0167 | 2.32 | - |
| 10 | 323 | 500 | 482.37 | 0.0190 | 2.64 | 277.10 |
| 10 | 323 | 500 | 268.83 | 0.0184 | 2.55 | 186.25 |
| 10 | 323 | 500 | 308.71 | 0.0140 | 1.93 | 138.06 |
| 10 | 323 | 1000 | 443.37 | 0.0283 | 3.93 | 283.90 |
| 10 | 323 | 1000 | 601.11 | 0.0283 | 3.92 | 355.62 |
| 10 | 323 | 1000 | 342.71 | 0.0234 | 3.24 | 202.75 |
| 10 | 323 | 1000 | 254.73 | 0.0186 | 2.58 | 176.48 |
| 10 | 323 | 1000 | 331.64 | 0.0232 | 3.21 | 229.77 |
| 10 | 323 | 1000 | 214.59 | 0.0186 | 2.58 | - |
| 10 | 323 | 1000 | 380.73 | 0.0264 | 3.65 | 243.79 |
| 10 | 323 | 1000 | 522.56 | 0.0269 | 3.73 | 290.95 |
| 10 | 348 | 0 | 514.77 | 0.0186 | 1.14 | 325.57 |
| 10 | 348 | 0 | 505.81 | 0.0191 | 1.16 | 327.80 |
| 10 | 348 | 0 | 514.69 | 0.0172 | 1.05 | 317.28 |
| 10 | 348 | 0 | 396.28 | 0.0156 | 0.95 | 202.06 |
| 10 | 348 | 0 | 337.07 | 0.0153 | 0.93 | - |
| 10 | 348 | 0 | 275.34 | 0.0149 | 0.91 | - |
| 10 | 348 | 0 | 212.47 | 0.0162 | 0.99 | 129.24 |
| 10 | 348 | 0 | 189.67 | 0.0143 | 0.87 | - |
| 10 | 348 | 0 | 513.39 | 0.0172 | 1.05 | 324.70 |

**Table A.5**
(Continued)

| $P$ [bar] | $T$ [K] | $N$ [RPM] | $d_0$ [µm] | $K$ [mm²/s] | $K/K_0$ [-] | $d_{dev}$ [µm] |
|---|---|---|---|---|---|---|
| 10 | 348 | 0 | 364.54 | 0.0155 | 0.95 | 182.27 |
| 10 | 348 | 500 | 554.54 | 0.0423 | 2.58 | 407.50 |
| 10 | 348 | 500 | 405.18 | 0.0362 | 2.21 | 210.54 |
| 10 | 348 | 500 | 357.56 | 0.0344 | 2.10 | - |
| 10 | 348 | 500 | 269.35 | 0.0377 | 2.30 | 182.68 |
| 10 | 348 | 500 | 407.51 | 0.0401 | 2.45 | 203.76 |
| 10 | 348 | 500 | 472.57 | 0.0388 | 2.37 | 236.29 |
| 10 | 348 | 500 | 347.21 | 0.0364 | 2.22 | 273.39 |
| 10 | 348 | 500 | 202.13 | 0.0298 | 1.82 | - |
| 10 | 348 | 500 | 568.4 | 0.0480 | 2.93 | 409.88 |
| 10 | 348 | 500 | 162.51 | 0.0253 | 1.55 | - |
| 10 | 348 | 1000 | 540.45 | 0.0585 | 3.57 | 305.72 |
| 10 | 348 | 1000 | 447.72 | 0.0558 | 3.40 | 272.34 |
| 10 | 348 | 1000 | 324.30 | 0.0428 | 2.61 | 177.63 |
| 10 | 348 | 1000 | 374.59 | 0.0506 | 3.09 | 275.27 |
| 10 | 348 | 1000 | 311.59 | 0.0450 | 2.75 | 152.65 |
| 10 | 348 | 1000 | 250.33 | 0.0439 | 2.68 | 166.05 |
| 10 | 348 | 1000 | 145.13 | 0.0337 | 2.06 | - |
| 10 | 348 | 1000 | 206.80 | 0.0436 | 2.66 | - |
| 10 | 348 | 1000 | 542.34 | 0.0603 | 3.68 | 320.85 |

**Table A.6**
Decane evaporation data – elevated temperature.

| $P$ [bar] | $T$ [K] | $N$ [RPM] | $d_0$ [µm] | $K$ [mm²/s] | $K/K_0$ [-] | $d_{dev}$ [µm] |
|---|---|---|---|---|---|---|
| 1 | 348 | 0 | 624.96 | 0.00801 | 1.05 | 279.49 |
| 1 | 348 | 0 | 240.98 | 0.00760 | 1.00 | - |
| 1 | 348 | 0 | 589.45 | 0.00779 | 1.02 | 322.86 |
| 1 | 348 | 0 | 380.71 | 0.00737 | 0.97 | - |
| 1 | 348 | 0 | 432.70 | 0.00763 | 1.00 | - |
| 1 | 348 | 0 | 280.18 | 0.00694 | 0.91 | - |

**Table A.6**
(Continued)

| $P$ [bar] | $T$ [K] | $N$ [RPM] | $d_0$ [µm] | $K$ [mm²/s] | $K/K_0$ [-] | $d_{dev}$ [µm] |
|---|---|---|---|---|---|---|
| 1 | 348 | 0 | 285.63 | 0.00693 | 0.91 | - |
| 1 | 348 | 0 | 145.20 | 0.00811 | 1.07 | - |
| 1 | 348 | 0 | 179.95 | 0.00806 | 1.06 | - |
| 1 | 348 | 1000 | 633.42 | 0.0170 | 2.23 | 490.65 |
| 1 | 348 | 1000 | 325.65 | 0.0125 | 1.64 | 198.09 |
| 1 | 348 | 1000 | 332.12 | 0.0128 | 1.69 | - |
| 1 | 348 | 1000 | 503.84 | 0.0151 | 1.98 | 363.32 |
| 1 | 348 | 1000 | 568.74 | 0.0154 | 2.02 | 429.39 |
| 1 | 348 | 1000 | 484.02 | 0.0148 | 1.95 | 345.66 |
| 1 | 348 | 1000 | 278.64 | 0.0121 | 1.59 | 210.37 |
| 1 | 348 | 1000 | 209.19 | 0.0105 | 1.38 | - |
| 1 | 348 | 1000 | 152.49 | 0.0109 | 1.44 | - |
| 1 | 348 | 1000 | 145.16 | 0.0105 | 1.38 | - |
| 1 | 348 | 3000 | 372.22 | 0.0203 | 2.67 | 263.20 |
| 1 | 348 | 3000 | 453.53 | 0.0212 | 2.79 | 307.60 |
| 1 | 348 | 3000 | 200.57 | 0.0184 | 2.41 | 138.96 |
| 1 | 348 | 3000 | 236.30 | 0.0175 | 2.31 | - |
| 1 | 348 | 3000 | 481.28 | 0.0225 | 2.96 | 322.85 |
| 1 | 348 | 3000 | 183.50 | 0.0168 | 2.21 | - |
| 1 | 348 | 3000 | 284.20 | 0.0174 | 2.29 | 150.38 |
| 1 | 348 | 3000 | 349.37 | 0.0199 | 2.62 | 231.75 |
| 1 | 373 | 0 | 534.46 | 0.0171 | 1.01 | 311.64 |
| 1 | 373 | 0 | 405.05 | 0.0166 | 0.98 | - |
| 1 | 373 | 0 | 231.55 | 0.0175 | 1.03 | 122.52 |
| 1 | 373 | 0 | 565.60 | 0.0184 | 1.08 | 423.26 |
| 1 | 373 | 0 | 367.91 | 0.0147 | 0.87 | 183.96 |
| 1 | 373 | 0 | 326.05 | 0.0174 | 1.03 | - |
| 1 | 373 | 0 | 358.04 | 0.0176 | 1.04 | - |
| 1 | 373 | 0 | 201.52 | 0.0172 | 1.01 | - |
| 1 | 373 | 0 | 160.93 | 0.0163 | 0.96 | - |
| 1 | 373 | 1000 | 548.89 | 0.0288 | 1.70 | 338.36 |
| 1 | 373 | 1000 | 375.36 | 0.0259 | 1.53 | 176.06 |

**Table A.6**
(Continued)

| $P$ [bar] | $T$ [K] | $N$ [RPM] | $d_0$ [µm] | $K$ [mm$^2$/s] | $K/K_0$ [-] | $d_{dev}$ [µm] |
|---|---|---|---|---|---|---|
| 1 | 373 | 1000 | 173.82 | 0.0237 | 1.40 | - |
| 1 | 373 | 1000 | 347.01 | 0.0262 | 1.54 | 183.62 |
| 1 | 373 | 1000 | 526.80 | 0.0294 | 1.74 | 364.98 |
| 1 | 373 | 1000 | 482.38 | 0.0300 | 1.77 | 319.97 |
| 1 | 373 | 1000 | 183.29 | 0.0262 | 1.55 | - |
| 1 | 373 | 1000 | 340.17 | 0.0263 | 1.55 | 170.09 |
| 1 | 373 | 1000 | 268.00 | 0.0261 | 1.54 | 146.79 |
| 1 | 373 | 3000 | 482.14 | 0.0417 | 2.46 | 360.80 |
| 1 | 373 | 3000 | 273.93 | 0.0403 | 2.37 | 191.75 |
| 1 | 373 | 3000 | 425.16 | 0.0428 | 2.52 | 300.63 |
| 1 | 373 | 3000 | 241.30 | 0.0391 | 2.31 | 183.77 |
| 1 | 373 | 3000 | 305.74 | 0.0399 | 2.35 | 240.74 |
| 1 | 373 | 3000 | 482.87 | 0.0442 | 2.61 | 358.11 |
| 1 | 373 | 3000 | 272.05 | 0.0348 | 2.05 | 153.89 |
| 10 | 348 | 0 | 534.97 | 0.00180 | 1.07 | 267.49 |
| 10 | 348 | 0 | 485.42 | 0.00177 | 1.05 | 299.23 |
| 10 | 348 | 0 | 427.59 | 0.00166 | 0.99 | 245.63 |
| 10 | 348 | 0 | 336.59 | 0.00166 | 0.99 | 212.88 |
| 10 | 348 | 0 | 239.84 | 0.00159 | 0.94 | - |
| 10 | 348 | 0 | 274.75 | 0.00164 | 0.97 | - |
| 10 | 348 | 0 | 221.46 | 0.00164 | 0.98 | - |
| 10 | 348 | 500 | 591.42 | 0.00562 | 3.35 | 401.12 |
| 10 | 348 | 500 | 430.30 | 0.00450 | 2.68 | 304.27 |
| 10 | 348 | 500 | 325.11 | 0.00470 | 2.80 | 266.11 |
| 10 | 348 | 500 | 459.74 | 0.00477 | 2.84 | 311.81 |
| 10 | 348 | 500 | 233.45 | 0.00368 | 2.19 | 127.87 |
| 10 | 348 | 500 | 340.32 | 0.00391 | 2.33 | 186.40 |
| 10 | 348 | 500 | 256.77 | 0.00386 | 2.30 | 192.15 |
| 10 | 348 | 1000 | 235.15 | 0.00417 | 2.48 | - |
| 10 | 348 | 1000 | 594.23 | 0.00748 | 4.45 | 467.90 |
| 10 | 348 | 1000 | 461.83 | 0.00663 | 3.95 | 326.56 |
| 10 | 348 | 1000 | 413.83 | 0.00600 | 3.57 | 295.53 |

**Table A.6**
(Continued)

| $P$ [bar] | $T$ [K] | $N$ [RPM] | $d_0$ [µm] | $K$ [mm²/s] | $K/K_0$ [-] | $d_{dev}$ [µm] |
|---|---|---|---|---|---|---|
| 10 | 348 | 1000 | 261.62 | 0.00466 | 2.78 | - |
| 10 | 348 | 1000 | 298.64 | 0.00567 | 3.38 | 219.45 |
| 10 | 348 | 1000 | 228.65 | 0.00418 | 2.49 | - |
| 10 | 373 | 0 | 545.84 | 0.00511 | 1.08 | 327.50 |
| 10 | 373 | 0 | 437.49 | 0.00504 | 1.07 | 262.49 |
| 10 | 373 | 0 | 324.32 | 0.00463 | 0.98 | - |
| 10 | 373 | 0 | 208.64 | 0.00431 | 0.91 | - |
| 10 | 373 | 0 | 180.42 | 0.00404 | 0.86 | - |
| 10 | 373 | 0 | 569.89 | 0.00508 | 1.08 | 279.19 |
| 10 | 373 | 0 | 427.11 | 0.00483 | 1.02 | 233.94 |
| 10 | 373 | 500 | 533.83 | 0.0142 | 3.01 | 250.39 |
| 10 | 373 | 500 | 485.42 | 0.0133 | 2.82 | 242.71 |
| 10 | 373 | 500 | 421.28 | 0.0119 | 2.53 | 230.74 |
| 10 | 373 | 500 | 346.10 | 0.0110 | 2.33 | 154.78 |
| 10 | 373 | 500 | 284.49 | 0.0111 | 2.35 | 165.88 |
| 10 | 373 | 500 | 204.22 | 0.0087 | 1.85 | - |
| 10 | 373 | 500 | 124.84 | 0.0095 | 2.02 | - |
| 10 | 373 | 1000 | 582.84 | 0.0186 | 3.94 | 382.19 |
| 10 | 373 | 1000 | 530.46 | 0.0182 | 3.87 | 375.09 |
| 10 | 373 | 1000 | 398.42 | 0.0166 | 3.52 | 284.53 |
| 10 | 373 | 1000 | 346.31 | 0.0156 | 3.30 | 254.48 |
| 10 | 373 | 1000 | 305.31 | 0.0163 | 3.46 | 232.52 |
| 10 | 373 | 1000 | 297.38 | 0.0143 | 3.03 | 210.28 |
| 10 | 373 | 1000 | 137.49 | 0.0095 | 2.01 | - |

**Table A.7**
Stagnant evaporation constant – heptane*.

| | | ***P* [bar]** | | | |
|---|---|---|---|---|---|
| | | **1** | **2.5** | **5** | **10** |
| | **298** | 0.0102 | 0.0058 | 0.0038 | 0.0028 |
| ***T* [K]** | **323** | 0.0225 | - | - | 0.0072 |
| | **348** | 0.0348 | - | - | 0.0164 |

*$K_0$ *is calculated based on the average value of all 0 RPM runs.*

**Table A.8**
Stagnant evaporation constant – decane*.

| | | ***P* [bar]** | | |
|---|---|---|---|---|
| | | **1** | **5** | **10** |
| | **298** | 0.000584 | 0.000168 | 0.000106 |
| ***T* [K]** | **348** | 0.00761 | - | 0.00168 |
| | **373** | 0.0170 | - | 0.00472 |

*$K_0$ *is calculated based on the average value of all 0 RPM runs.*

# B. MATLAB code listings

The following MATLAB codes were written solely by the author and were utilized in the data processing, analysis, or results presentation of this thesis or related material. Functional description and instructions are provided in the header block of each code.

## B.1 Image processing code

```
%=========================================================================================
% CROSS-FIBER IMAGE PROCESSING CODE (2016)
% CAMERON VERWEY
%=========================================================================================

% This program uses thresholding to convert the grayscale images to black and white.
% Two successive erosions remove the vertical and horizontal lines (remaining fibers)
% followed by two dilations to restore the droplet size. Disk filtering is used to
% smooth out the edges of the drop. The cross-sectional area of the droplet is
% calculated by counting pixels and multiplying the number of pixels by the square of
% the conversion factor. The diameter is found by assuming the droplet is a perfect
% sphere. Normalized d^2 values are then plotted against normalized time.
% Program detects an error and exits if more than one region remains at the end of
% processing, or if no regions exist (droplet has disappeared). Several lines of best
% fit may be interactively placed on the plot until good fit has been achieved. The
% image range is then re-specified for the final plot. The final plot is saved
% (optional) in the directory, along with an Excel file of the data (also optional).
% The point of d^2 deviation is calculated based on the criteria of average residuals.
% The instantaneous K value can also be plotted along with d^2 on a second axis
% (optional).

% INSTRUCTIONS
% 1) Specify the location of the folder containing the images to process.
% 2) Set flags which control file writing and data output.
% 3) Define the first and last image numbers to be read as well as the processing
%    interval. 'first_pic' will typically be the first image for which the injector
%    has just disappeared (i.e., the initial droplet). 'last_pic' can be set greater
%    than the total number of pictures, the program will automatically end when the
%    droplet has disappeared. There is little reason to use an interval other than
%    one (i.e., evaluate every image).
% 4) To evaluate how the image processing code works on a single image, set
%    'first_pic' equal to 'last_pic'. That single image will be processed and a figure
%    produced to illustrate.
% 5) Set 'freq' to camera fps and set the image resolution. 256x256 is typical.
% 6) Set how many pixels to trim from the edges of all images. Useful for removing
%    the timestamp and the injector if it is not retracted quickly.
% 7) Set the scale factor, 'pix_convert'. This is CRITICAL.
% 8) Set the number of time intervals to use in calculating the derivative (central
%    difference). For example, 'slope_points' = 20 will use 20 time intervals before
%    and after the point of interest find the derivative. In the case of 'pic_step' =
%    1 (most common), each time interval is an image.
% 9) When prompted, continue with curve fitting or terminate the program. Several
%    best fit lines can be generated for comparison purposes. End curve fitting when
%    satisfied with fitting.
% 10)Based on the previous curve fitting step, enter the starting and final images
```

```
%    for the linear region to be displaced on the final plot. Notes may also be
%    entered (optional). This figure is saved in the current directory if 'img_write'
%    is set to true.

% FUTURE REVISIONS
% 1) Insert a sample picture of the droplet (probably the first one
%    processed) into the final figure for reference.
% 2) If figure and excel file already exist, prompt user for name change,
%    or overwrite, or do nothing, similar to integral length scale program.
% 3) Test how the d^2 deviation criteria, based on average residuals, works on a
%    variety of data.

%==========================================================================================

clc
clear
close all

file_location = ['E:\Droplet data\November-December 2016 runs\12-07-2016\'...
                 '2.5 bar - 2000 RPM - 25 C - N2 (2)\TestSession\TestSession_006'];

%FLAGS
%------------------------------------------------------------------------------------------
img_write = false;     %true will overwrite if file already exists
data_write = false;    %true will overwrite if file already exists
sec_axis = true;       %include a secondary axis with image numbers and inst. K values
%------------------------------------------------------------------------------------------

%IMAGE PROCESSING PARAMETERS
%------------------------------------------------------------------------------------------
first_pic = 480;
pic_step = 1;
last_pic = 3000;

freq = 60;

res_horiz = 256;
res_vert = 256;

trim_top = 25;    %25 should be sufficient to remove the time stamp
trim_bottom = 0;
trim_right = 0;
trim_left = 0;

pix_convert = 4.8598;     %Dec. 16 - Dec. 19

slope_points = 20;  %calculate K_inst using central difference, +/- 'slope_points'
%------------------------------------------------------------------------------------------

%MISC.
%------------------------------------------------------------------------------------------
file_form = 'Cam_1306060055_000000';   %MotionStudio

img_view = false;
   if (first_pic == last_pic);
    img_view = true;
   end

diameters = zeros(1,length(first_pic:pic_step:last_pic)); %preallocate d vector
time = 0:(1/freq)*pic_step:(last_pic - first_pic)/freq;   %create the general t vector
image_num_act = first_pic:pic_step:last_pic;              %actual image numbers

img_count = 0;
```

```
cd(file_location);
disp(file_location);
%-------------------------------------------------------------------------------------

%IMAGE PROCESSING LOOP
%-------------------------------------------------------------------------------------
 for j = (first_pic + 1):pic_step:(last_pic + 1);  %file names start at zero

       file_name = strcat(file_form, num2str(j-1), '.tif');
       file_name(16:(length(file_name) - 10)) = '';         %MotionStudio

       if exist(file_name, 'file') == 0;
           fprintf('%s -- NO FILE FOUND; END LOOP\n', file_name);
           break
       end

       f = imread(file_name);

       %Crop images based on trim parameters
       f = imcrop(f, [1 (trim_top + 1) res_horiz (res_vert - trim_top)]);
       f = imcrop(f, [1 1 res_horiz (res_vert - trim_top - trim_bottom - 1)]);
       f = imcrop(f, [1 1 (res_horiz - trim_right - 1) ...
                 (res_vert - trim_top - trim_bottom)]);
       f = imcrop(f, [(trim_left + 1) 1 (res_horiz - trim_right) ...
                 (res_vert - trim_top - trim_bottom)]);

       f_bw = im2bw(f,graythresh(f));     %threshold image at global level
       %f_bw = im2bw(f, 0.99);            %manual threshold, for comparative purposes

       f_bw = ~f_bw;                      %invert black and white

       SE = ones(1,8);                    %define line structuring element
       bw_vert = imerode(f_bw,SE);        %remove vertical lines
       bw_horiz = imerode(bw_vert,SE');   %remove horizontal lines

       dilate_1 = imdilate(bw_horiz, SE'); %dilate twice to restore droplet size
       dilate_2 = imdilate(dilate_1, SE);

       im_fill = imfill(dilate_2,'holes'); %remove any holes in droplet (reflection)

       se_smooth = strel('disk',8);       %disc filter to smooth edges (minimal impact)
       im_fill = imopen(im_fill, se_smooth);

       %Check for connectivity errors
       conn = bwlabel(im_fill);
       num_regions = max(max(conn));   %number of connected regions

       if ~img_view            %do not end loop if troubleshooting single images
           if num_regions > 1;    %program is detecting two regions
               fprintf(['%s ERROR - more then 1 connected region:'...
                        'PROCESSING ENDED\n'], file_name);
               break
           end

           if num_regions == 0;   %droplet has disappeared, automatically end the loop
               fprintf('%s No droplet found: PROCESSING ENDED\n', file_name);
               break
           end
       end

       img_count = img_count + 1;              %count processed image
       fprintf('%s PROCESSED\n', file_name);    %print processed filename to screen
```

```
        white = find(im_fill == 1);              %find locations where pixels are white
        num_pix = length(white);                 %total number of white pixels
        area = num_pix*pix_convert*pix_convert;  %calculate area using scale factor
        dia = sqrt(4*area/pi);                   %calculate equivalent diameter
        diameters(1,img_count) = dia;            %store diameter data in vector

        %Generate troubleshooting images if 'img_view' is true
        if img_view
            figure
            subplot(2,2,1), imshow(f_bw), title('Thresholded');
            subplot(2,2,2), imshow(bw_horiz), title('Eroded');
            subplot(2,2,3), imshow(im_fill), title('Dilated');

            boundary = bwperim(im_fill); [I,J] = find(boundary);
            subplot(2,2,4), imshow(f), hold on, plot(J,I,'r.'), title('Boundary fit');

            fprintf('Image number: %d\n', first_pic);
            fprintf('Diameter: %f\n', dia);
        end
end
%-------------------------------------------------------------------------------------

%EXTRACT D^2 DATA
%-------------------------------------------------------------------------------------
if ~img_view     %remainder of program isn't necessary if looking at single images


    D_o = mean(diameters(1:3));   %set d_0 to be the average of the first three
    K = zeros(5,1);
    Rsq = zeros(5,1);

    %Extract name of folder for plot title
    path = strfind(file_location,'\');      %works if path looks like: C:\...\...\
                                            %DESIRED TITLE\TestSession\TestSession_00x
    path_cut = path(end-2:end-1);
    base_title = file_location(path_cut(1)+1:path_cut(2)-1);
    title_num = file_location(end-2:end);
    plot_title = [base_title,' - ','RUN ',title_num];

    %Process the diameters matrix for plotting and evaluating K values
    stop = find(diameters == 0, 1);           %find the first instance of d = 0
    diameters(stop:length(diameters)) = [];   %remove all elements after d = 0
    time(stop:length(time)) = [];             %remove same elements from time vector

    diam_squared = diameters.*diameters;                %calculate d^2
    diam_squared_norm = diam_squared./(D_o.*D_o);       %normalize d^2
    time_norm = (time./(D_o.*D_o))*1000000;             %normalize t, units mm^2/s

    image_num_proc = 1:length(diameters);
    image_num_act(length(image_num_proc) + 1:end) = [];
%-------------------------------------------------------------------------------------

%WRITE TO EXCEL FILE
%-------------------------------------------------------------------------------------
    if data_write == true;
        full_data = [image_num_act; image_num_proc; time; diameters;...
                     time_norm; diam_squared_norm]';
        col_headers = {'Img. #','Proc. Img. #' 't [s]', 'D [mm]',...
                       't/D0^2 [s/mm^2]', 'D^2/D0^2'};
        xlswrite(strcat(plot_title,'.xlsx'), col_headers, 'Sheet1', 'A1');
        xlswrite(strcat(plot_title,'.xlsx'), full_data, 'Sheet1', 'A2');
    end
```

```
%-------------------------------------------------------------------------------------

%LINEAR FIT
%-------------------------------------------------------------------------------------
    f = figure;
    set(f, 'name', 'Linear region evaluation', 'numbertitle', 'off');
    line(image_num_proc, diam_squared_norm, 'Color', 'k');
    ax1 = gca;
    ax1.XLabel.String = 'Processed images'; ax1.YLabel.String = 'd^2/d_0^2';
    ax1.XGrid = 'on'; ax1.XMinorGrid = 'on';
    ax1.YLim = [0 1.02];
    ax1.Title.String = plot_title;
    label{1} = ['Data', ' - Actual image range: ', num2str(first_pic), ' - ', ...
                num2str(image_num_act(end))];
    annotation('textbox', [0.15 0 0.2 0.2], 'String',...
              ['d_0 = ', num2str(D_o), ' um'], 'FitBoxToText', 'on',...
               'EdgeColor', 'none');

    linear_fit = input('\nContinute with linear fitting (Y/N)? ', 's');

    if linear_fit ~= 'Y' && linear_fit ~= 'y';
        if ishandle(f);
            close(f);
        end
        return
    end

    loop = 0;
    loop_count = 0;

    %Loop until desired fit has been achieved
    while loop ~= 1

        %Get user input on where to start and end the linear line of best fit
        linear_start = input('Start of linear region (1 and up): ');
        linear_end = input('End of linear region: ');

        if linear_start < 1 || linear_start > image_num_proc(end) || ...
           linear_end > image_num_proc(end) || linear_end < linear_start;
            disp('Values not in-range; re-enter...');
            continue
        end

        loop_count = loop_count + 1;

        fit = polyfit(image_num_proc(linear_start:linear_end), ...
              diam_squared_norm(linear_start:linear_end), 1);
        y1 = polyval(fit,image_num_proc);
        Kfit = polyfit(time_norm(linear_start:linear_end), ...
               diam_squared_norm(linear_start:linear_end), 1);

        %Calculate the R^2 value for each linear fit
        y_resid = diam_squared_norm(linear_start:linear_end) - ...
                  y1(linear_start:linear_end);
        sum_square_resid = sum(y_resid.^2);
        sum_square_total = length(diam_squared_norm(linear_start:linear_end) - 1)*...
                           var(diam_squared_norm(linear_start:linear_end));

        Rsq(loop_count) = 1 - sum_square_resid/sum_square_total;
        K(loop_count) = -Kfit(1);

        %Change the line style for each successive line of best fit
        switch loop_count
```

```
            case 1
                line_style = '-';
            case 2
                line_style = '--';
            case 3
                line_style = ':';
            otherwise
                line_style = '-.';
        end

        %Add lines and labels for each linear best fit
        line(image_num_proc, y1, 'Color', 'r', 'LineStyle', line_style);
        label{loop_count + 1} = [num2str(loop_count), '  ', 'Images: ', ...
                                 num2str(linear_start), ' - ', num2str(linear_end),...
                                 '   K = ', num2str(K(loop_count)),' mm^2/s',...
                                 '   R^2 = ', num2str(Rsq(loop_count))];
        legend(label);
        pass = input('End curve fitting (Y/N)? ', 's');

        if pass == 'y' || pass == 'Y'
            loop = 1;
            clear label;
        end

    end
%-------------------------------------------------------------------------------------------

%FINAL PLOT
%-------------------------------------------------------------------------------------------

    accept = false;

    %Ensure final plot points are within range
    while accept == false;
        actual_start = input('Starting image for final plot: ');
        actual_end = input('Final image for final plot: ');

        if actual_start < 1 || actual_start > image_num_proc(end) || ...
           actual_end > image_num_proc(end) || actual_end < actual_start;
            accept = false;
            disp('Values out of range; re-enter...');
        else
            accept = true;
        end
    end

    fig_notes = input('Notes for saved figure (may leave empty): ', 's');

    %Plot data as normalized D-squared vs. normalized time
    ff = figure;
    %set(ff, 'name', plot_title, 'numbertitle', 'off');
    line(time_norm, diam_squared_norm, 'Color', 'k');
    ax1 = gca;
    ax1.YLim = [0 1.02];
    ax1.XLabel.String = 't/d_0^2 [s/mm^2]'; ax1.YLabel.String = 'd^2/d_0^2';
    %ax1.Title.String = plot_title;
    ax1.Title.Position(2) = 0.94;
    ax1.Title.FontSize = 13;
    ax1.FontName = 'Arial'; ax1.FontSize = 14;

    final_fit = polyfit(time_norm(actual_start:actual_end), ...
                        diam_squared_norm(actual_start:actual_end), 1);
    y_final = polyval(final_fit, time_norm);
```

```
line(time_norm, y_final, 'Color', 'r');
K_final = -final_fit(1);

y_resid_f = diam_squared_norm(actual_start:actual_end)...
            - y_final(actual_start:actual_end);
sum_square_resid_f = sum(y_resid_f.^2);
sum_square_total_f = length(diam_squared_norm(actual_start:actual_end) - 1)*...
                     var(diam_squared_norm(actual_start:actual_end));
Rsq_final = 1 - sum_square_resid_f/sum_square_total_f;

%Calculate where deviation occurs based on average of maximum residuals
resid_avg = mean(abs(y_resid_f));  %average residual in the linear region
all_residuals = abs(diam_squared_norm(actual_start:end) -...
                    y_final(actual_start:end)); %calc. all residuals, inc.
                                                %those after linear region

res_exceed = find(all_residuals > resid_avg);   %find indices where residuals
                                                %exceed the average value
flag = 0;

%Determine where residual exceeds average and never falls below again
for i = 1:length(res_exceed);
    exceed_check = all_residuals(res_exceed(i):end) > resid_avg;

    if all(exceed_check);
        flag = 1;
        dev_index = actual_start + res_exceed(i);
        diam_squared_dev = diam_squared_norm(dev_index);
        diam_dev = diameters(dev_index);
        time_norm_dev = time_norm(dev_index);
        time_dev = time(dev_index);
        fprintf('\n\nDeviation data:\n')
        fprintf('    Normalized coordinates: (%.2f, %.2f)\n',...
                time_norm_dev, diam_squared_dev);
        fprintf('    Actual values         :  %.2f seconds, %.2f um \n',...
                    time_dev, diam_dev);
        break
    end
end

if flag == 0;
    fprintf('\n\nDeviation NOT detected!');
end

hold on

plot(time_norm(actual_start), diam_squared_norm(actual_start), 'ro');
plot(time_norm(actual_end), diam_squared_norm(actual_end), 'ro');
plot(time_norm(dev_index), diam_squared_norm(dev_index), 'g*', 'markersize', 10);

slope_points = int16(slope_points/pic_step);   %avoids expanding the slope range

k_inst = zeros(1,length(time_norm) - 2*slope_points);

for n = slope_points + 1: length(diam_squared_norm) - slope_points;
    P = polyfit(time_norm(n-slope_points:n+slope_points),...
                diam_squared_norm(n - slope_points:n + slope_points), 1);
    k_inst(n - slope_points) = abs(P(1));
end

fprintf('\nK range: %f mm^2/s - %f mm^2/s\n', min(k_inst), max(k_inst));
k_percent_diff = 100*((max(k_inst) - min(k_inst))/...
                 (0.5*(max(k_inst) + min(k_inst))));
```

```
    fprintf('K %%diff: %4.2f%% \n', k_percent_diff);

    legend_entry{1} = ['d_0 = ', num2str(D_o, '%6.2f'), ' um'];
    legend_entry{2} = ['K_{avg} = ', num2str(K_final,'%8.6f'),' mm^2/s  ',...
                       '(R^2 = ', num2str(Rsq_final, 3), ')'];
    legend_entry{3} = ['Image Range : ', num2str(image_num_act(actual_start)),...
                       ' - ', num2str(image_num_act(actual_end))];
    legend_entry{4} = ['Linear End : (', num2str(time_norm(actual_end),4),', ',...
                       num2str(diam_squared_norm(actual_end),4),')'];
    legend_entry{5} = 'Deviation point';

    if sec_axis == true;
        line(0,0,'Color','b');   %'fake' line to allow the K_inst plot (on a different
                                 %axes set) to be included in the main legend
        legend_entry{6} = 'K_{inst.} [mm^2/s]';
    end

    legend(legend_entry, 'Position', [0.7 0.66 0.1 0.2]);

    if sec_axis == true;
        %Set up second axes for plotting k_inst and showing image # info
        ax2 = axes('Position', ax1.Position, 'XAxisLocation', 'top',...
                   'YAxisLocation', 'right','Color', 'none');
        ax2.YLabel.String = 'mm^2/s';
        ax2.XLim = [first_pic, int16(ax1.XLim(2)*(D_o/1000)*(D_o/1000)*...
                    freq + first_pic)];
        ax2.XLabel.String = 'Image #';
        ax2.XGrid = 'on'; ax2.XMinorGrid = 'on';
        ax2.YColor = 'b';

        line(image_num_act(1 + slope_points):pic_step:...
             image_num_act(end - slope_points),k_inst, 'Color', 'b', 'Parent', ax2);
    end

    if ~isempty(fig_notes);
        annotation('textbox', [0.15 0 0.2 0.2], 'String', fig_notes,...
                   'FitBoxToText', 'on', 'EdgeColor', 'none');
    end

    if img_write == true;
        saveas(gcf, strcat(plot_title,'.fig'), 'fig'); %will overwrite existing figure
    end
%-------------------------------------------------------------------------------------

end
```

***OUTPUT***

```
E:\Droplet data\November-December 2016 runs\12-07-2016\2.5 bar - 2000 RPM - 25 C - N2
(2)\TestSession\TestSession_006
Cam_1306060055_000480.tif PROCESSED
Cam_1306060055_000481.tif PROCESSED
Cam_1306060055_000482.tif PROCESSED
Cam_1306060055_000483.tif PROCESSED
...
...
...

Cam_1306060055_001423.tif PROCESSED
```

```
Cam_1306060055_001424.tif PROCESSED
Cam_1306060055_001425.tif PROCESSED
Cam_1306060055_001426.tif PROCESSED
Cam_1306060055_001427.tif No droplet found: PROCESSING ENDED

Continue with linear fitting (Y/N)? Y
Start of linear region (1 and up): 1
End of linear region: 100
End curve fitting (Y/N)? N
Start of linear region (1 and up): 1
End of linear region: 600
End curve fitting (Y/N)? N
Start of linear region (1 and up): 500
End of linear region: 900
End curve fitting (Y/N)? Y
Starting image for final plot: 1
Final image for final plot: 600
Notes for saved figure (may leave empty): Example output


Deviation data:
    Normalized coordinates: (28.22, 0.28)
    Actual values         :  10.57 seconds, 322.84 um

K range: 0.013719 mm^2/s - 0.037387 mm^2/s
K %diff: 92.63%
```

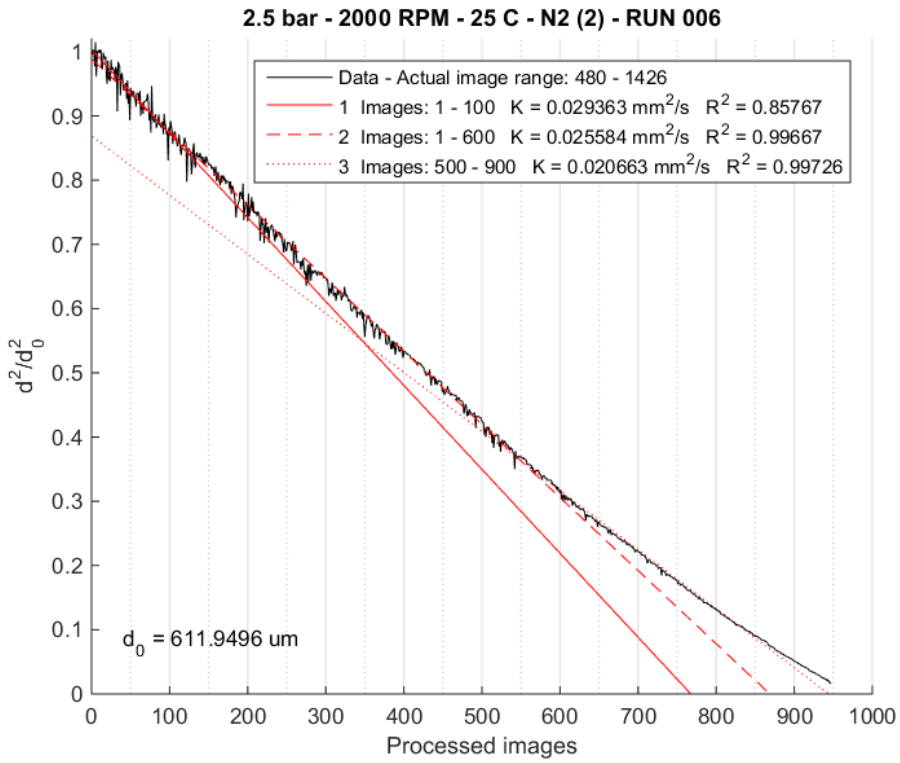

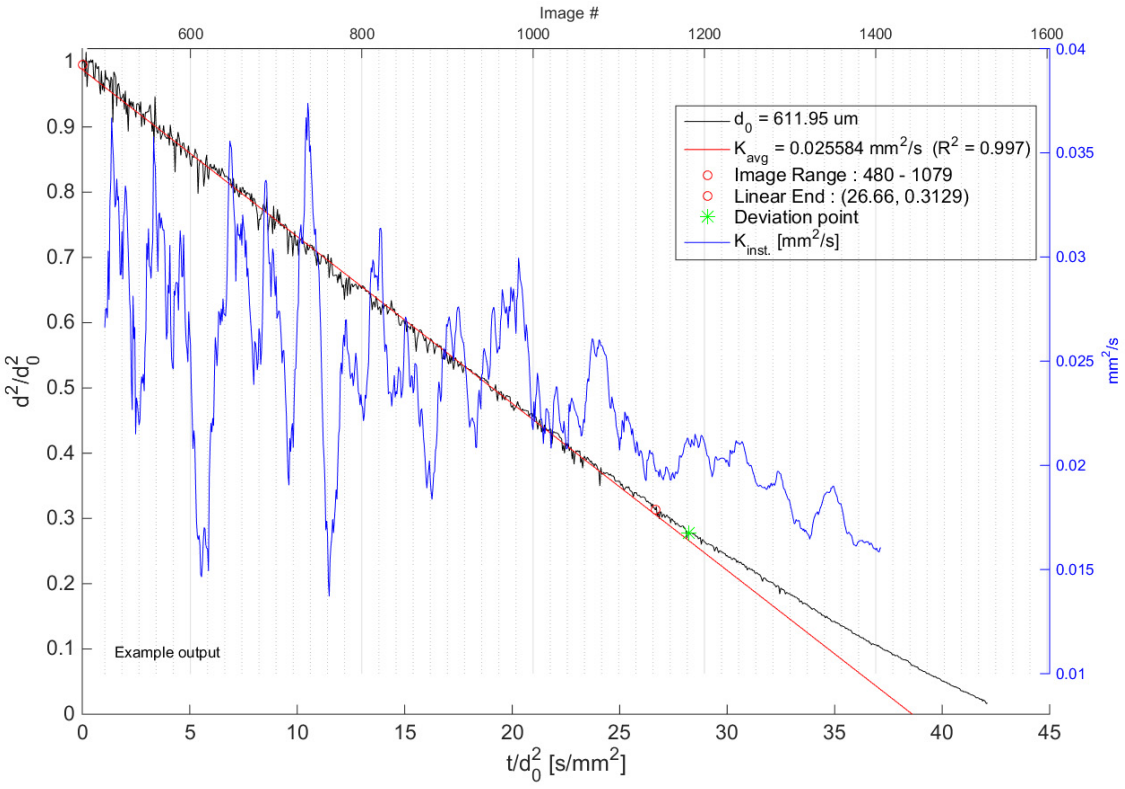


**output Excel file not shown*

## B.2 PIV data compiler

```
%=========================================================================================
% PIV MULTIPLE RUN DATA COMPILER (2016)
% CAMERON VERWEY
%=========================================================================================

% This program accepts up to three input folders, each containing the adaptive
% correlation output (.csv files) from a single PIV run. Up to three PIV runs can
% therefore be combined to yield the mean velocities and RMS values. Ensure that the
% .csv files have the first row of data in row 10, X and Y data in columns E and F,
% and U and V data in columns I and J (as viewed in Excel). This should be the default
% export format. The 'csvread' statements would need to be modified if this isn't the
% case. The program also sorts the data along the horizontal and vertical axis, and
% outputs this to the same Excel file in a separate worksheet to facilitate immediate
% plotting of the data. RMS to mean velocity ratio, isotropy ratio, the square root of
% TKE, the homogeneity ratio, and the correlation coefficients are automatically
% calculated and tabulated along each axis. This program also calculates the integral
% length scale by averaging the integrations of Rii and Rjj on both sides of the
% origin, using a simple linear extrapolation of the last few correlation points.

% INSTRUCTIONS
% 1) Specify the location of the parent folder which contains the individual run
```

```
%    folder(s).
% 2) Provide the output Excel file name and worksheet names for the full and sorted
%    output. The output file saves in the parent folder.
% 3) Set 'save_output' to false if you don't want to save the output (troubleshooting
%    runs, etc.).
% 4) If the origin is not centered in the FOV and is in the corner (i.e., all X and Y
%    values are positive starting from zero), set 'origin_cent' to 'false'. This will
%    center the data.
% 5) Enter number of data points in each direction (i.e., how many velocity vectors
%    along X or Y direction) in 'grid_size'.
% 6) Specify the range (mm) on either side of the origin for which q^0.5_avg is
%    calculated in 'homog_range'. Also specify how many points to skip for plotting
%    in 'skip_value' (e.g., if 'skip_value' = 4, a column in the sorted output
%    worksheet will appear containing every fourth position point).
% 7) Specify how many points on either side of the origin to include in calculating
%    the Taylor scale parabola in 'taylor_points'.
% 8) Select how many files to run from each folder (n1, n2, n3). Typically 3000 each,
%    which is the maximum per PIV run. These values act as flags, so be sure to set to
%    zero if you do not want the second or third folder to be looked at.
% 9) Specify the names of the individual folder(s). Name does not matter if n = 0
%    for that folder (it won't be looked at).
% 10)Specify the base name of the actual .csv files (the first file in each folder).
%    Name does not matter if n = 0 for that folder.
% 11)Double check that the read range for .csv files is correct.

% FUTURE REVISIONS
% 1) Performance has not been tested for grid sizes other than 127 x 127. This should
%    be investigated.
% 2) Allow user to select how many points/which points for the linear
%    extrapolation of the Rii/Rjj coefficients.
% 3) Evaluate the accuracy of the recently implemented Taylor scale calculation.
%=========================================================================================

clc
clear
close all

%INPUTS
%-----------------------------------------------------------------------------------------

folder_location = ['E:\PIV\October PIV runs\10-13-2016 - '...
                   'Camera C Laser B (Additional runs with frame and no frame)\'...
                   'Adaptive correlations\'];

%Output file info
excel_file = 'test.xlsx';
excel_sheet_full = 'Sheet1';    %'Sheet1' is default
excel_sheet_sorted = 'Sorted';

save_output = true;             %flag for writing output to excel file
origin_cent = true;             %is the origin ALREADY centered in the FOV?
grid_size = 127;                %depends on interrogation area and overlap

homog_range = 10;
skip_value = 4;                 %for plotting, retain every n'th value
taylor_points = 8;              %points on either side or origin for calc'ing Taylor

n1 = 3000;
n2 = 3000;
n3 = 0;
n = n1 + n2 + n3;

total_grid = grid_size*grid_size;
```

```
folder_1 = '3000 RPM No frame run 1 - ambient';
base_name_1 = '3000RPMnoFrameambientRun1.4quqlm2e.000000';

folder_2 = '3000 RPM No frame run 2 - ambient';
base_name_2 = '3000RPMnoFrameambientRun2.4quudyxf.000000';

folder_3 = '';
base_name_3 = '';
%-------------------------------------------------------------------------------------------

%MAIN DATA READ AND PROCESS
%-------------------------------------------------------------------------------------------

if n2 == 0;
    folder_2 = 'n/a';
end

if n3 == 0;
   folder_3 = 'n/a';
end

%Read range for .csv files
vel_range = [9 8 total_grid+8 9];
pos_range = [9 4 total_grid+8 5];

%Preallocate 3D matrices to store velocities
vel_array = zeros(total_grid, 2, n);
fluct_vel = zeros(total_grid, 2, n);

tic

%Read data from first file
cd(strcat(folder_location,folder_1));
fprintf('\nFirst folder..........\n');

for i = 1:n1
    file_name_1 = strcat(base_name_1, num2str(i-1),'.csv');
    file_name_1(length(base_name_1) - 5: length(file_name_1) - 10) = '';
    vel_array(:,:,i) = csvread(file_name_1, 9, 8, vel_range);
    fprintf('Folder 1: %s;  File: %s\n', folder_1, file_name_1);
end

pos_array = csvread(file_name_1,9,4, pos_range); %does not change throughout

%Center the origin in the FOV if the origin was originally in the corner
if origin_cent == false;
    [row, col] = size(pos_array);
    x_mid = pos_array(round(row/2), 1);
    x_mid_indices = find(pos_array(:,1) == x_mid);
    mid_values = pos_array(x_mid_indices,:);
    y_mid = pos_array(ceil(length(mid_values(:,2))/2),2);

    centered_x = pos_array(:,1) - x_mid;
    centered_y = pos_array(:,2) - y_mid;

    pos_array = [centered_x, centered_y];
end

%Read data from second file if required
if n2 ~= 0;
    cd(strcat(folder_location, folder_2));
    fprintf('\nSecond folder..........\n');
    for i = 1:n2
```

```
        file_name_2 = strcat(base_name_2, num2str(i-1),'.csv');
        file_name_2(length(base_name_2) - 5: length(file_name_2) - 10) = '';
        vel_array(:,:,n1 + i) = csvread(file_name_2, 9, 8, vel_range);
        fprintf('Folder 2: %s;  File: %s\n', folder_2, file_name_2);
    end
end

%Read data from third file if required
if n3 ~=0;
    cd(strcat(folder_location, folder_3));
    fprintf('\nThird folder..........\n');
    for i = 1:n3
        file_name_3 = strcat(base_name_3, num2str(i-1),'.csv');
        file_name_3(length(base_name_3) - 5: length(file_name_3) - 10) = '';
        vel_array(:,:,n1 + n2 + i) = csvread(file_name_3, 9, 8, vel_range);
        fprintf('Folder 3: %s;  File: %s\n', folder_3, file_name_3);
    end
end

mean_vel = sum(vel_array,3)./n;

%Subtract mean velocity from instantaneous velocities to find fluctuating component
for i = 1:n
    fluct_vel(:,:,i) = vel_array(:,:,i) - mean_vel;
end

%Add positional columns to fluctuating velocity array
pos_fluct_vel = [repmat(pos_array,1,1,n), fluct_vel];

%Calculate the RMS values, the RMS-to-mean velocity ratios, and the square root of TKE
square_fluct = fluct_vel.*fluct_vel;
mean_square = sum(square_fluct,3)./n;
rms = sqrt(mean_square);
rms_ratio = abs(mean_vel./rms);
isotropy = rms(:,1)./rms(:,2);                                    %u'/v'
sqrt_k = sqrt(0.5*(2.0*rms(:,1).*rms(:,1) + rms(:,2).*rms(:,2))); %sqrt(2*u'^2 + v'^2)

%Concatenate the position, mean velocity, RMS data and TKE arrays
full_array = [pos_array, mean_vel, rms, rms_ratio, isotropy, sqrt_k];
[abs_min_values, cl_index] = min(abs(full_array));
x_cl = full_array(cl_index(1),1);               %centerline X value
y_cl = full_array(cl_index(2),2);               %centerline Y value

%Sort the data along the vertical axis, add additional parameters to array
y_indices = find(full_array(:,1) == x_cl);
y_sorted = full_array(y_indices,:);

sqrt_k_cent = y_sorted(y_sorted(:,2) == y_cl, 10);  %same for both X and Y axes

%Calculate homogeneity based on centerline value of q^0.5
y_sorted(:,11) = y_sorted(:,10)/sqrt_k_cent;

%Calculate homogeneity based on average values of q^0.5 around center
sqrt_k_avg_y = mean(y_sorted((abs(y_sorted(:,2)) <= homog_range), 10));
y_sorted(:,12) = y_sorted(:,10)/sqrt_k_avg_y;

%Sort the data along the horizontal axis, add additional parameters to array
x_indices = find(full_array(:,2) == y_cl);
x_sorted = full_array(x_indices,:);

%Sort fluctuating velocity arrays
pos_fluct_vel_x = pos_fluct_vel(x_indices,:,:);
pos_fluct_vel_y = pos_fluct_vel(y_indices,:,:);
```

```
rms_x = rms(x_indices,:);
rms_y = rms(y_indices,:);

x_cent_ind = find(pos_fluct_vel_x(:,1) == x_cl);
y_cent_ind = find(pos_fluct_vel_y(:,2) == y_cl);

%Calculate homogeneity based on centerline value of q^0.5
x_sorted(:,11) = x_sorted(:,10)/sqrt_k_cent;

%Calculate homogeneity based on average values of q^0.5 around center
sqrt_k_avg_x = mean(x_sorted((abs(x_sorted(:,1)) <= homog_range), 10));
x_sorted(:,12) = x_sorted(:,10)/sqrt_k_avg_x;

%Calculate correlation coefficients
Rii = zeros(grid_size,1);
Rjj = zeros(grid_size,1);

for r = 1:grid_size;
    Qxx = sum(pos_fluct_vel_x(x_cent_ind,3,:).*pos_fluct_vel_x(r,3,:))./n;
    Rii(r,1) = Qxx/(rms_x(x_cent_ind,1)*rms_x(r,1));

    Qyy = sum(pos_fluct_vel_y(y_cent_ind,4,:).*pos_fluct_vel_y(r,4,:))./n;
    Rjj(r,1) = Qyy/(rms_y(y_cent_ind,2)*rms_y(r,2));
end

x_sorted(:,13) = Rii;
y_sorted(:,13) = Rjj;

%Add 'x_skip' and 'y_skip' columns for plotting purposes
x_skip = num2cell(x_sorted(:,1));
y_skip = num2cell(y_sorted(:,2));

%Modify cells to contain empty values
for i = 1:length(x_skip);
    r = rem(i,skip_value);

    if r ~= 0.0
        x_skip{i} = [];
        y_skip{i} = [];
    end
end
%-------------------------------------------------------------------------------------------

%CALCULATE INTEGRAL LENGTH SCALE
%-------------------------------------------------------------------------------------------

%Isolate Rii/Rjj with their corresponding spatial coordinates
Rii_sort = x_sorted;
Rii_sort(:,2:12) = [];
Rjj_sort = y_sorted;
Rjj_sort(:,1) = [];
Rjj_sort(:,2:11) = [];

%Pull end points off of Rii/Rjj curves to create linear fits
Rii_left = Rii_sort(3:15,:);
Rii_right =Rii_sort(length(Rii_sort)-14:length(Rii_sort)-2,:);

Rjj_lower = Rjj_sort(3:15,:);
Rjj_upper = Rjj_sort(length(Rjj_sort)-14:length(Rjj_sort)-2,:);

%Fit linear curves through end points for extrapolation
P1 = polyfit(Rii_left(:,1), Rii_left(:,2),1);
P2 = polyfit(Rii_right(:,1), Rii_right(:,2), 1);
```

```
P3 = polyfit(Rjj_lower(:,1), Rjj_lower(:,2), 1);
P4 = polyfit(Rjj_upper(:,1), Rjj_upper(:,2), 1);

%Find distance coordinate where Rii/Rjj = 0, based on linear fit
P1_int = -P1(2)/P1(1);
P2_int = -P2(2)/P2(1);
P3_int = -P3(2)/P3(1);
P4_int = -P4(2)/P4(1);

P1_2nd_point = polyval(P1, Rii_sort(2,1));
P1_2nd_pair = [Rii_sort(2,1), P1_2nd_point];
P2_2nd_point = polyval(P2, Rii_sort(length(Rii_sort) - 1,1));
P2_2nd_pair = [Rii_sort(length(Rii_sort) - 1,1), P2_2nd_point];
P3_2nd_point = polyval(P3, Rjj_sort(2,1));
P3_2nd_pair = [Rjj_sort(2,1), P3_2nd_point];
P4_2nd_point = polyval(P4, Rjj_sort(length(Rjj_sort) - 1,1));
P4_2nd_pair = [Rjj_sort(length(Rjj_sort) - 1,1), P4_2nd_point];

Rii_left_extrap = Rii_sort(3:find(Rii_sort == x_cl),:);
Rii_left_extrap = [[P1_int, 0]; P1_2nd_pair; Rii_left_extrap];

Rii_right_extrap = Rii_sort(find(Rii_sort == x_cl):length(Rii_sort) - 3,:);
Rii_right_extrap = [Rii_right_extrap; P2_2nd_pair; [P2_int, 0]];

Rjj_lower_extrap = Rjj_sort(3:find(Rjj_sort == y_cl),:);
Rjj_lower_extrap = [[P3_int, 0]; P3_2nd_pair; Rjj_lower_extrap];

Rjj_upper_extrap = Rjj_sort(find(Rjj_sort == y_cl):length(Rjj_sort) - 3,:);
Rjj_upper_extrap = [Rjj_upper_extrap; P4_2nd_pair; [P4_int, 0]];

L_Rii_left = trapz(Rii_left_extrap(:,1), Rii_left_extrap(:,2));
L_Rii_right = trapz(Rii_right_extrap(:,1), Rii_right_extrap(:,2));
L_Rjj_lower = trapz(Rjj_lower_extrap(:,1), Rjj_lower_extrap(:,2));
L_Rjj_upper = trapz(Rjj_upper_extrap(:,1), Rjj_upper_extrap(:,2));

L_avg = (L_Rii_left + L_Rii_right + L_Rjj_lower + L_Rjj_upper)/4.0;
%-------------------------------------------------------------------------------------------

%CALCULATE TAYLOR MICROSCALE
%-------------------------------------------------------------------------------------------
Rii_rhs_indices = find(Rii_sort(:,1) > 0);
Rii_rhs_indices = Rii_rhs_indices(1:taylor_points);
Rii_rhs = Rii_sort(Rii_rhs_indices,:);

Rii_lhs = Rii_sort((Rii_rhs_indices(1) - taylor_points):Rii_rhs_indices(1) - 1, :);
Rii_combine = [Rii_lhs;Rii_rhs];
Rii_taylor_parab = polyfit(Rii_combine(:,1), Rii_combine(:,2), 2);
Rii_taylor = roots(Rii_taylor_parab);

%Rjj
Rjj_upper_indices = find(Rjj_sort(:,1) > 0);
Rjj_upper_indices = Rjj_upper_indices(1:taylor_points);
Rjj_upper = Rjj_sort(Rjj_upper_indices,:);

Rjj_lower = Rjj_sort((Rjj_upper_indices(1) - taylor_points):...
                     Rjj_upper_indices(1) - 1,:);
Rjj_combine = [Rjj_lower; Rjj_upper];
Rjj_taylor_parab = polyfit(Rjj_combine(:,1), Rjj_combine(:,2), 2);
Rjj_taylor = roots(Rjj_taylor_parab);

Taylor_avg = (Rii_taylor(1) + abs(Rii_taylor(2)) + Rjj_taylor(1) +...
              abs(Rjj_taylor(2)))/4.0;
```

```
%-------------------------------------------------------------------------------------------

%PLOT DATA
%-------------------------------------------------------------------------------------------
subplot(1,2,1); plot(Rii_sort(:,1), Rii_sort(:,2), 'ko');
title('Rii Correlation Coefficients'), xlabel('X [mm]'), ylabel('Rii');
hold on
plot(Rii_right_extrap(:,1), Rii_right_extrap(:,2), 'r-');
plot(Rii_sort(:,1), polyval(Rii_taylor_parab, Rii_sort(:,1)));
plot(Rii_left_extrap(:,1), Rii_left_extrap(:,2), 'r-');

ax1 = gca;
ax1.YLim = [-0.1 1.1];
legend('Data', 'Data w/ linear extrapolation', 'Taylor parabola');

hold off

subplot(1,2,2); plot(Rjj_sort(:,1), Rjj_sort(:,2), 'ko');
title('Rjj Correlation Coefficients'), xlabel('Y [mm]'), ylabel('Rjj');
hold on
plot(Rjj_upper_extrap(:,1), Rjj_upper_extrap(:,2), 'r-');
plot(Rjj_sort(:,1), polyval(Rjj_taylor_parab, Rjj_sort(:,1)));
plot(Rjj_lower_extrap(:,1), Rjj_lower_extrap(:,2), 'r-');

legend('Data', 'Data w/ linear extrapolation', 'Taylor parabola');
ax2 = gca;
ax2.YLim = [-0.1, 1.1];

hold off
%-------------------------------------------------------------------------------------------

%WRITE OUTPUT DATA
%-------------------------------------------------------------------------------------------
cd(folder_location);

%If excel_write flag is not set, output is not saved and program ends
if save_output == 1;
    user_resp = 0;  %initialize variable

    if exist(excel_file, 'file') == 2;
        user_resp = input(['\nOUTPUT FILE ALREADY EXISTS! Enter 1 to remove old'...
                           'file and rewrite, 2 to select new file name,'...
                           'or any other # to exit: ']);

        if user_resp == 1;
            delete(excel_file);
            fprintf('\nDeleting old file.....\n');
        elseif user_resp == 2;
            unique_name = 0;
            while unique_name == 0;
                new_file = input('\nPlease enter unique file name: ', 's');
                new_file = strcat(new_file, '.xlsx');
                if exist(new_file, 'file') ~= 2;
                    unique_name = 1;
                    excel_file = new_file;
                else
                    disp('Name already taken!');
                end
            end

        else
            fprintf('\nFile exists but will not be changed.\n');
            return;
```

```
    end
end

disp('Writting file..........');

%Create and write output to specified Excel file
base_info = {'Directory:', folder_location};
folder_info = {'Folder 1:',folder_1,'',n1,'Pairs' ; 'Folder 2:', folder_2,...
               '', n2, 'Pairs' ; 'Folder 3', folder_3, '', n3, 'Pairs'};
col_header = {'x [mm]', 'y [mm]', '', 'U [m/s]', 'V [m/s]', '',...
              'Urms [m/s]', 'Vrms [m/s]'};
full_title = {'FULL DATA'};
xlswrite(excel_file, base_info, excel_sheet_full);
xlswrite(excel_file, folder_info, excel_sheet_full,'A2');
xlswrite(excel_file, full_title, excel_sheet_full, 'A5');
xlswrite(excel_file, col_header, excel_sheet_full, 'A6');
xlswrite(excel_file, pos_array, excel_sheet_full, 'A7');
xlswrite(excel_file, mean_vel, excel_sheet_full, 'D7');
xlswrite(excel_file, rms, excel_sheet_full, 'G7');

horiz_title = {'HORIZONTAL AXIS'};
vert_title = {'VERTICAL AXIS'};
horiz_col_header = {'X [mm] (sorted)', 'X_skip [mm]', 'y [mm]', 'U [m/s]',...
                    'V [m/s]', 'Urms [m/s]', 'Vrms [m/s]', 'U/Urms', 'V/Vrms',...
                    'Urms/Vrms', 'q^0.5 [m/s]', 'q^0.5/q^0.5cent',...
                    'q^0.5/q^0.5avg', 'Rii'};
vert_col_header = {'X [mm]', 'Y [mm] (sorted)', 'Y_skip [mm]', 'U [m/s]',...
                   'V [m/s]', 'Urms [m/s]', 'Vrms [m/s]', 'U/Urms', 'V/Vrms',...
                   'Urms/Vrms', 'q^0.5 [m/s]', 'q^0.5/q^0.5cent',...
                   'q^0.5/q^0.5avg', 'Rjj'};

xlswrite(excel_file, horiz_title, excel_sheet_sorted, 'A1');
xlswrite(excel_file, horiz_col_header, excel_sheet_sorted, 'A2');
xlswrite(excel_file, x_sorted(:,1), excel_sheet_sorted, 'A3');
xlswrite(excel_file, x_skip, excel_sheet_sorted, 'B3');
xlswrite(excel_file, x_sorted(:,2:13), excel_sheet_sorted, 'C3');

xlswrite(excel_file, vert_title, excel_sheet_sorted, 'P1');
xlswrite(excel_file, vert_col_header, excel_sheet_sorted, 'P2');
xlswrite(excel_file, y_sorted(:,1:2), excel_sheet_sorted, 'P3');
xlswrite(excel_file, y_skip, excel_sheet_sorted, 'R3');
xlswrite(excel_file, y_sorted(:,3:13), excel_sheet_sorted, 'S3');

length_title = {'INTEGRAL LENGTH SCALE'};
L_Rii_left_output = {'Rii (left) [mm]', L_Rii_left};
L_Rii_right_output = {'Rii (right) [mm]', L_Rii_right};
L_Rjj_lower_output = {'Rjj (lower) [mm]', L_Rjj_lower};
L_Rjj_upper_output = {'Rjj (upper) [mm]', L_Rjj_upper};
L_avg_output = {'Average [mm]', L_avg};

xlswrite(excel_file, length_title, excel_sheet_sorted, 'AF1');
xlswrite(excel_file, L_Rii_left_output, excel_sheet_sorted, 'AE2');
xlswrite(excel_file, L_Rii_right_output, excel_sheet_sorted, 'AE3');
xlswrite(excel_file, L_Rjj_lower_output, excel_sheet_sorted, 'AE4');
xlswrite(excel_file, L_Rjj_upper_output, excel_sheet_sorted, 'AE5');
xlswrite(excel_file, L_avg_output, excel_sheet_sorted, 'AE6');

taylor_title = {'TAYLOR MICRO SCALE'};
xlswrite(excel_file, taylor_title, excel_sheet_sorted, 'AI1');
xlswrite(excel_file, Rii_taylor(2), excel_sheet_sorted, 'AI2');
xlswrite(excel_file, Rii_taylor(1), excel_sheet_sorted, 'AI3');
xlswrite(excel_file, Rjj_taylor(2), excel_sheet_sorted, 'AI4');
xlswrite(excel_file, Rjj_taylor(1), excel_sheet_sorted, 'AI5');
```

```
    xlswrite(excel_file, Taylor_avg, excel_sheet_sorted, 'AI6');

    fprintf('\n\nOutput data has been written to: %s\n',...
            strcat(folder_location,excel_file));

else
    fprintf('\n\nOutput NOT SAVED!\n');
%--------------------------------------------------------------------------

end
```

***OUTPUT***

```
First folder..........
Folder 1: 3000 RPM No frame run 1 - ambient;  File:
       3000RPMnoFrameambientRun1.4quqlm2e.000000.csv
Folder 1: 3000 RPM No frame run 1 - ambient;  File:
       3000RPMnoFrameambientRun1.4quqlm2e.000001.csv
Folder 1: 3000 RPM No frame run 1 - ambient;  File:
       3000RPMnoFrameambientRun1.4quqlm2e.000002.csv
...
...
...
Folder 1: 3000 RPM No frame run 1 - ambient;  File:
       3000RPMnoFrameambientRun1.4quqlm2e.002997.csv
Folder 1: 3000 RPM No frame run 1 - ambient;  File:
       3000RPMnoFrameambientRun1.4quqlm2e.002998.csv
Folder 1: 3000 RPM No frame run 1 - ambient;  File:
       3000RPMnoFrameambientRun1.4quqlm2e.002999.csv

Second folder..........
Folder 2: 3000 RPM No frame run 2 - ambient;  File:
       3000RPMnoFrameambientRun2.4quudyxf.000000.csv
Folder 2: 3000 RPM No frame run 2 - ambient;  File:
       3000RPMnoFrameambientRun2.4quudyxf.000001.csv
Folder 2: 3000 RPM No frame run 2 - ambient;  File:
       3000RPMnoFrameambientRun2.4quudyxf.000002.csv
...
...
...

Folder 2: 3000 RPM No frame run 2 - ambient;  File:
       3000RPMnoFrameambientRun2.4quudyxf.002997.csv
Folder 2: 3000 RPM No frame run 2 - ambient;  File:
       3000RPMnoFrameambientRun2.4quudyxf.002998.csv
Folder 2: 3000 RPM No frame run 2 - ambient;  File:
       3000RPMnoFrameambientRun2.4quudyxf.002999.csv

OUTPUT FILE ALREADY EXISTS! Enter 1 to remove old file and rewrite, 2 to select new file
       name, or any other # to exit: 1

Deleting old file..........
Writing file..........
Warning: Added specified worksheet.
> In xlswrite>activate_sheet at 284
  In xlswrite>ExecuteWrite at 256
  In xlswrite at 213
  In PIV_Data_Compiler_mod_taylor at 432
```

```
Output data has been written to: E:\PIV\October PIV runs\10-13-2016 - Camera C Laser B
       (Additional runs with frame and no frame)\Adaptive correlations\test.xlsx
>>
```

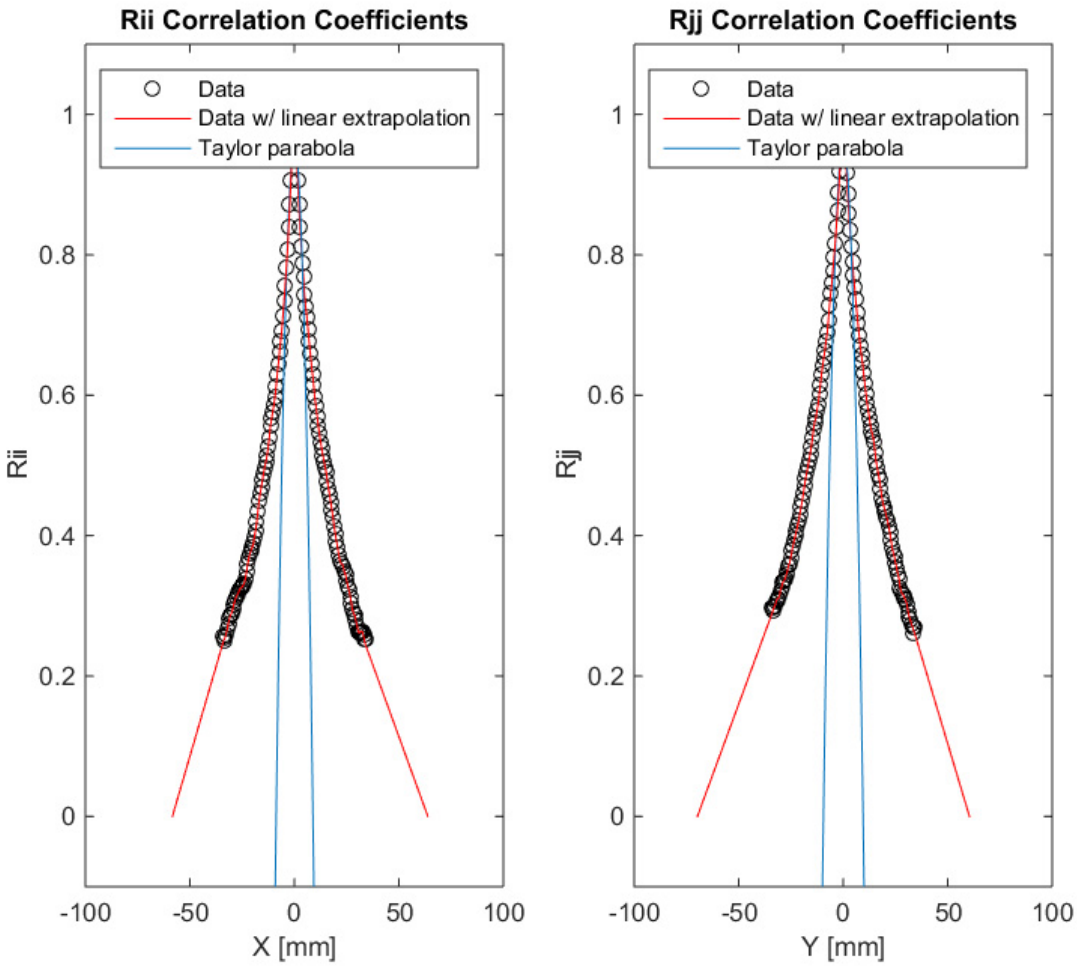


**Output Excel file (not shown) contains two worksheets, one of all the raw processed data, and a second with the data sorted and ready to plot (including isotropy ratio, intensity, etc.). The integral and Taylor scales are also output here.*

## B.3 Curve fitter

```
%=========================================================================================
% CURVE FITTING OPTIMIZATION - FIVE VARIABLES (2017)
% CAMERON VERWEY
%=========================================================================================

% This program automatically cycles through different exponents to find the
% combination which provides the best fit, based on maximizing R^2, for an equation
% which looks like:
%
%                          y = A*(B^m)*(C^n)*(D^o)*(E^p)
%
% The intercept can be forced to zero (simple regression) or 'polyfit' can be called,
% which generates the ideal intercept value. Other versions of this program exist for
% two and three variables.

% INSTRUCTIONS
% 1) Specify Excel file location, file, and worksheet which contains the data.
% 2) Specify whether to force intercept to zero ('zero_intercept' == true).
% 3) Specify range of data to read in. Note that if the Excel sheet is altered
%    (i.e., columns or rows are deleted or added), the inputs must
%    be changed as well.
% 4) Set how often to update progress with text output ('prog_update'), does not
%    affect execution of program.
% 5) Remove certain rows of data based on any relevant criteria (for example, we often
%    wish to remove 0 RPM data).
% 6) Ensure the proper columns are being assigned to the Y variable and the various
%    X components.
% 7) Specify the minimum and maximum exponent range for each independent variable, as
%    well as their individual increments. Start with wide range and fairly large
%    increment (for example, +/- 5 with an increment of 0.1) to narrow down the
%    exponent range. Then narrow the range based on the first run and lower the
%    increment (e.g., 0.01) to increase the accuracy of the correlation.
% 8) Modify the X-axis formula in the loop, as well as 'x_best' for plotting,
%    depending on the combination of variables.

% FUTURE REVISIONS
% 1) Instead of having separate programs for different numbers of independent
%    variables, combine into a single script. Flags could be set depending on number
%    of variables to control program execution.

%=========================================================================================

clc
clear
close all

tic

file_location = ['C:\Users\Cam\Desktop\MECH\Graduate\Project\'...
                 'Writing and publishing\Journal papers\Elevated conditions '...
                 'article(s)\Article separation\Turbulence only\'];
input_file = 'Elevated conditions - Turbulence - Graphs and analysis.xlsx';
input_sheet = 'Reynolds corr.';

zero_intercept = true;   %true == force thru zero

cd(file_location);

%INPUTS
%-----------------------------------------------------------------------------------------
```

```
main_array = xlsread(input_file, input_sheet, 'A6:P481');

fprintf('Data has been read, processing.....\n\n');
prog_update = 50000; %display progress after this many combinations

%Data exclusions
main_array((main_array(:,5) == 0), :) = [];    %remove 0 RPM rows
%main_array((main_array(:,14) >= 1), :) = [];  %remove n/d0 >= 1 rows

%Select the column containing the dependent variable (Y axis)
y = main_array(:,11);            % K/K0 - 1

%Select the columns which contain values that make up the X-axis data
x_comp_1 = main_array(:,12);    % Ret,L
x_comp_2 = main_array(:,14);    % L/D0
x_comp_3 = main_array(:,15);    % Sc
x_comp_4 = main_array(:,16);    % T/T0
x_comp_5 = main_array(:,3);     % P/P0

%Set the exponent ranges and increment for each variable
exp_2_low = -0.6;
exp_2_high = -0.4;
exp_div_2 = 0.01;

exp_3_low = 1.1;
exp_3_high = 1.3;
exp_div_3 = 0.01;

exp_4_low = -1.5;
exp_4_high = -1.3;
exp_div_4 = 0.01;

exp_5_low = -0.3;
exp_5_high = -0.1;
exp_div_5 = 0.01;

%EXECUTION
%-------------------------------------------------------------------------------------------
num_combo = int32(((exp_2_high - exp_2_low)/exp_div_2 + 1)*...
                  ((exp_3_high - exp_3_low)/exp_div_3 + 1)*...
                  ((exp_4_high - exp_4_low)/exp_div_4 + 1)*...
                  ((exp_5_high - exp_5_low)/exp_div_5 + 1));

fprintf('Analyzing %d possible combinations.\n', num_combo);

output = zeros(num_combo, 7);

count = 0;

for i = 1:ceil((exp_2_high - exp_2_low)/exp_div_2 + 1);
    m = exp_2_low + exp_div_2*i - exp_div_2;

    for j = 1:ceil((exp_3_high - exp_3_low)/exp_div_3 + 1);
        n = exp_3_low + exp_div_3*j - exp_div_3;

        for k = 1:ceil((exp_4_high - exp_4_low)/exp_div_4 + 1);
            o = exp_4_low + exp_div_4*k - exp_div_4;

            for l = 1:ceil((exp_5_high - exp_5_low)/exp_div_5 + 1);
                p = exp_5_low + exp_div_5*l - exp_div_5;

            count = count + 1;
```

```
            output(count,1) = m;
            output(count,2) = n;
            output(count,3) = o;
            output(count,4) = p;

            %X-axis formula: Re^c * (L/d0)^m * Sc^n * (T/To)^o * (P/P0)^p
            x = (x_comp_1.^(0.6666666)).*(x_comp_2.^m).*(x_comp_3.^n).*...
                (x_comp_4.^o).*(x_comp_5.^p);

            if zero_intercept == true;      %perform simple linear regression
                b1 = x\y;                   %slope
                yfit = b1.*x;
                output(count,5) = b1;
            elseif zero_intercept == false; %use polyfit, return an intercept
                p = polyfit(x,y,1);
                output(count,5) = p(1);     %slope
                output(count,6) = p(2);     %intercept
                yfit = polyval(p,x);
            end

            %Calculate the R^2 value
            yresid = y - yfit;
            SSresid = sum(yresid.^2);
            SStotal = (length(y) - 1)*var(y);
            rsq = 1 - SSresid/SStotal;

            output(count,7) = rsq;

            if rem(count/prog_update, 1) == 0;
                fprintf('%d combinations analyzed; %.2f percent complete.\n',...
                count, (count/double(num_combo))*100);
                toc
            end

            end
        end
    end
end

[value, location] = max(output(:,7));      %find maximum R^2 value
best_fit_data = output(location,:);        %pull the data from the row with R^2 max

%Best fit data
disp('Exponents:');
fprintf('  m = %f\n', best_fit_data(1));
fprintf('  n = %f\n', best_fit_data(2));
fprintf('  o = %f\n', best_fit_data(3));
fprintf('  p = %f\n', best_fit_data(4));

disp('Data:');
fprintf('  slope = %f\n', best_fit_data(5));
fprintf('  intercept = %f\n', best_fit_data(6));
fprintf('  r-squared = %f\n', best_fit_data(7));

%OUTPUT PLOT
%-------------------------------------------------------------------------------------
x_best = (x_comp_1.^(0.666)).*(x_comp_2.^best_fit_data(1)).*...
         (x_comp_3.^best_fit_data(2)).*(x_comp_4.^best_fit_data(3)).*...
         (x_comp_5.^best_fit_data(4));

y_best = best_fit_data(5).*x_best + best_fit_data(6);   %line of best fit plot
```

```
x_title =
sprintf('Re_t_,_L^2^/^3(L/d_0)^{%4.2f}Sc^{%4.2f}(T/T_0)^{%4.2f}(P/P_0)^{%4.2f}',...
                    best_fit_data(1), best_fit_data(2), best_fit_data(3),
best_fit_data(4));

plot(x_best,y, 'ko');
xlabel(x_title);
ylabel('K/K_0 - 1');
hold on
plot(x_best, y_best, 'r-');
%-------------------------------------------------------------------------------------

toc
```

***OUTPUT***

```
Data has been read, processing.....

Analyzing 194481 possible combinations.
50000 combinations analyzed; 25.71 percent complete.
Elapsed time is 16.465426 seconds.
100000 combinations analyzed; 51.42 percent complete.
Elapsed time is 31.132808 seconds.
150000 combinations analyzed; 77.13 percent complete.
Elapsed time is 45.897990 seconds.
Exponents:
  m = -0.530000
  n = 1.160000
  o = -1.420000
  p = -0.190000
Data:
  slope = 0.043868
  intercept = 0.000000
  r-squared = 0.906859
Elapsed time is 59.105156 seconds.
```

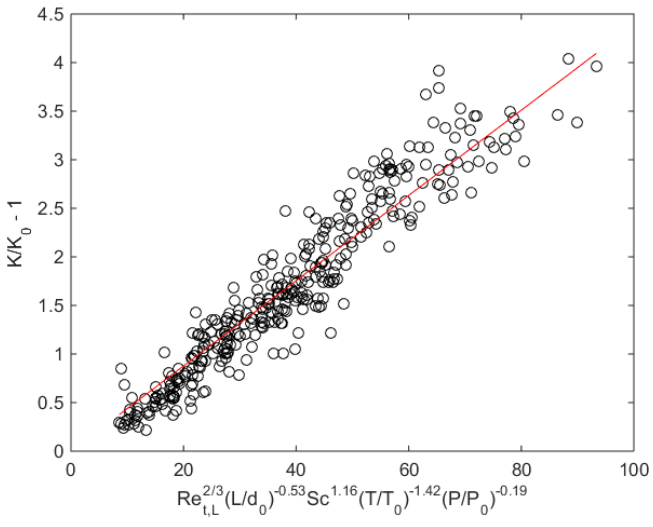

## B.4 PIV heat map generator

```
%=========================================================================================
% PIV HEAT MAP GENERATOR (2017)
% CAMERON VERWEY
%=========================================================================================

% Takes PIV data organized in a table as follows...

% X Y value
% - -    -
% - -    -
%    etc.

% ...and creates the following matrix:

%    .
%    .
%    .
% Y3   value(X1,Y3) value(X2,Y3) value (X3,Y3)
% Y2   value(X1,Y2) value(X2,Y2) value (X3,Y2)
% Y1   value(X1,Y1) value(X2,Y1) value (X3,Y1) ...
%          X1           X2           X3

% Data in this format is then plotted as a heat map. Will typically be used with
% averaged data (vector statistics) but could also be employed with instantaneous data
% (i.e., individual adaptive correlation .csv files).

% INSTRUCTIONS
% 1) Change directory to the location of the Excel vector statistics .csv file.
% 2) Ensure file name and range is correct for reading in the data.
% 3) Assign columns to correct variable (x, y, U, V, Urms, Vrms, etc.)
% 4) Specify 'grid_size', the number of points in either direction. Has not been
%    tested for grids other than 127 x 127 (interrogation area 32 x 32 px., 50%
%    overlap).
% 5) Calculate variable to plot in a heat map if necessary (e.g., velocity magnitude,
%    turbulence kinetic energy, etc.)
% 6) Assign 'map_data' to the variable to be plotted in a heat map.
% 7) Double-check heat map against 'output_matrix' and original data table to ensure
%    that the data is being calculated and displayed properly.

%=========================================================================================

clear
clc
close all

cd(['E:\PIV\October PIV runs\10-12-2016 - Camera C Laser B (Frame at all RPM)\'...
   'Vector statistics\']);

data = csvread('Frame3000rpmRun1.4qt2lzip.000000.csv', 9, 0);

x = data(:,5);
y = data(:,6);
U = data(:,9);
V = data(:,10);
u_rms = data(:,13);
v_rms = data(:,14);

grid_size = 127;

u_rms_ratio = abs(U./u_rms);
```

```
V_mag = sqrt(U.*U + V.*V);

output_matrix = zeros(grid_size, grid_size);
map_data = V_mag;                  %'map_data' will be plotted as a heat map

%Rearrange 'map_data' in matrix form
for n = 1:grid_size;
    temp = map_data((1 + (n-1)*grid_size):(127 + (n-1)*grid_size));
    temp_flip = flipud(temp);
    output_matrix(:,n) = temp_flip;
end

%Output matrix needs to be flipped to use with 'imagesc'
imagesc(x,y,flipud(output_matrix));

%Plot heat map
ax = gca;
xlabel('Horizontal Axis [mm]', 'FontSize', 16);
ylabel('Vertical Axis [mm]', 'FontSize', 16);
ax.YDir = 'normal';
ax.FontName = 'Arial'; ax.FontSize = 12;

colormap('jet');
h = colorbar;
xlabel(h, 'Mean Velocity [m/s]', 'FontSize', 16);
h.FontName = 'Arial'; h.FontSize = 12;
```

***OUTPUT***

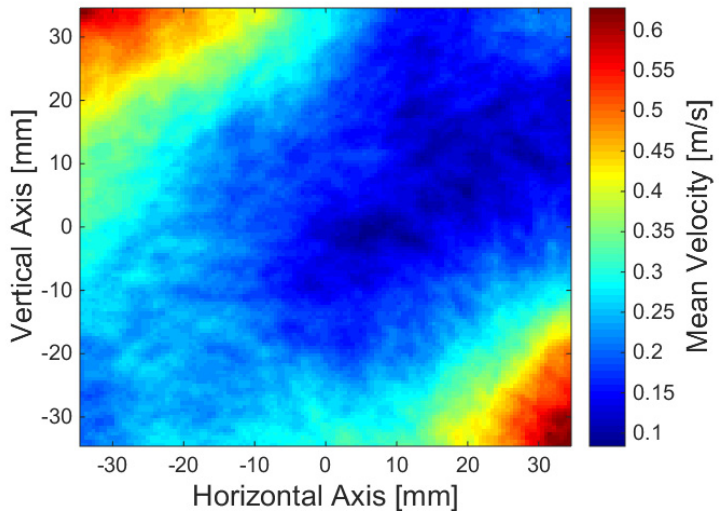

## C. Error analysis

Calibration of the high-speed camera presents the greatest potential for error. Fortunately, the calibration technique, discussed in Section D.2, is highly repeatable. A series of calibrations performed sequentially revealed that the width of the calibration needle can be determined, conservatively, to within $\pm$ 0.5 pixels. The average reported thickness for the calibration needle is ~63.7 px., based on the final 12 calibrations. Assuming a repeatability of 0.5 pixels:

$$\%error_{cam.\ calib.} = \frac{64.2 - 63.2}{\frac{1}{2}(64.2 + 63.2)} \times 100 = 1.57\% \tag{C.1}$$

Conservatively, the uncertainty of the camera scale factor is approximately 2%.

The image processing code presents another source of error. Previous investigations (e.g., [187,206,207]) have placed the edge detection error at $\pm$ 2 pixels which lead to surface area estimation errors of 5 – 8% for droplets in the 500 – 600 μm range. Edge detection is a function of the thresholding operation which separates foreground from background. The choice of threshold level becomes more significant as the droplet shrinks in size. Otsu's method of determining the threshold value helps avoid the requirement of manually determining a threshold value for each run. Furthermore, it assigns individual threshold levels for each image rather than applying a global value to all images. Otsu's method, used throughout, is compared to global thresholding in Fig. C.1. Values of $d_0$ and $K$ for one large and one small heptane droplet are plotted against the global threshold level used to calculate them, while a large circle symbolizes the results of Otsu's method. Since the threshold value can change for each image using Otsu's method, the circles are plotted corresponding to the average threshold level. The range of global threshold which return results within $\pm$ 5% of Otsu's method are designated by horizontal error bars. The large droplet is

insensitive to threshold level as any value from approximately 0.3 to 0.9 would produce results within $\pm$ 5% of either $d_0$ or $K$ determined via Otsu's method. The calculation of $d_0$ for the small droplet is still relatively independent of threshold over a small range. On the other hand, the predicted $K$ of the small droplet using Otsu's method is significantly smaller than what would be predicted if a constant threshold, similar in magnitude to the Otsu average value, were used. Additionally, the relationship between $K$ and threshold level is much steeper for the smaller droplet than the larger one. This is a clear indication of greater error associated with small droplets but does not necessarily imply that Otsu's method is error-prone, as Fig. C.1 could also be used to condemn the ability of global thresholds. Further analysis of image processing techniques is recommended, especially in association with small droplets approaching 100 µm.

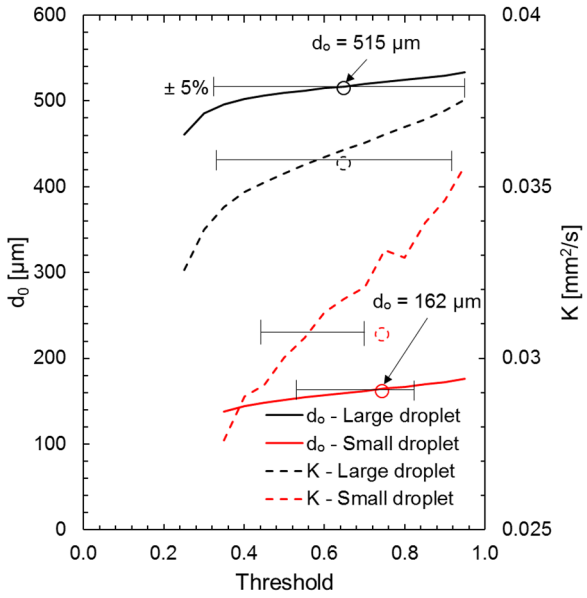


**Fig. C.1.** Comparison of calculated $d_0$ and $K$ for various threshold values – large and small droplet. The circles represent the value returned via Otsu's method.

# D. Recommended techniques for alignment and calibration

## D.1 Frame alignment

The cross-fiber support frame must be aligned so that the fiber intersection coincides with the geometric center of the chamber. The primary issue is the vertical height of the frame as the connection is threaded and therefore continuously adjustable. Furthermore, the mounting hardware is not perfectly straight, and radial alignment must also be verified. A technique using an inexpensive red laser pointer is recommended. This approach involves removing the threaded plugs (5/8-inch) from two opposing side accessory ports. A laser is fixed at one side using either a stand or a fitting in the threaded bore and adjusted until the beam cleanly travels through the opposite port. Because the ports are machined along the center plane of the chamber, the laser path passes through the center of the chamber with a maximum error of half the port opening (5/16-inch or 8 mm). However, it is not difficult to ensure that the laser is passing through the approximate center of the threaded bore on both sides to minimize error. Once the laser is aligned, the frame is installed and adjusted until the beam is visible on the cross-fiber intersection. This does not preclude the potential for the frame to be off center along the beam axis and thus for a truly rigorous alignment, two lasers are recommended. The two beams would then intersect at the center of the chamber. Lasers of different colors and higher strength would be necessary to avoid ambiguity in assessing the reflection off the small cross-fibers. It is recommended that future iterations of this method use lasers with visible beams and adapters which ensure the laser is situated in the precise center of the side port bore. Figure D.1 diagrams the single laser approach used in the present study.

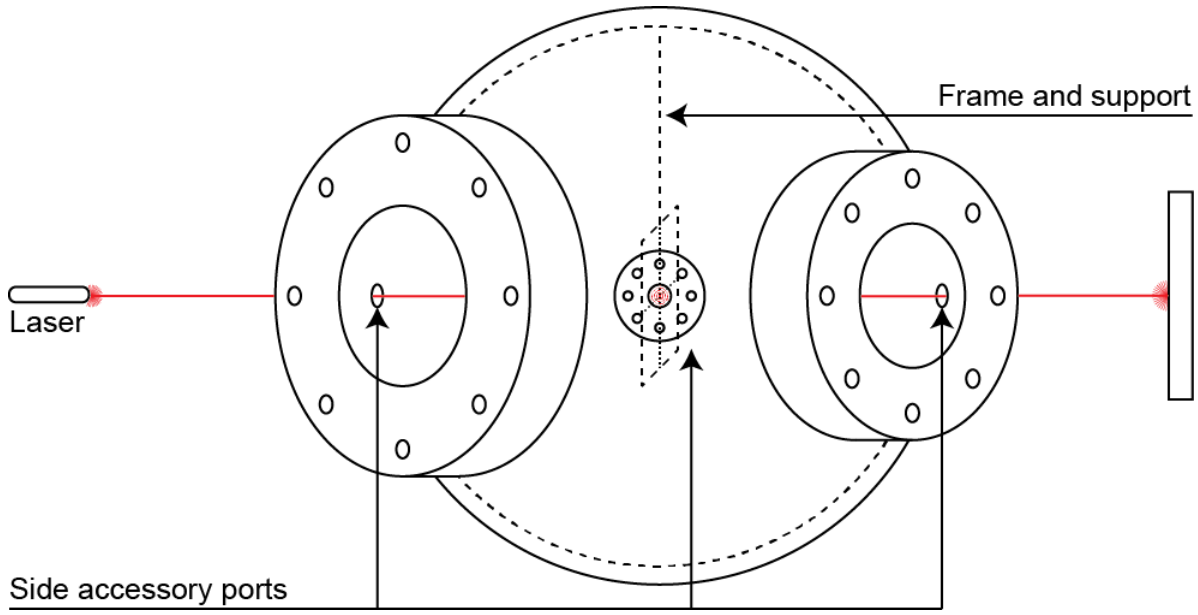


**Fig. D.1.** Simplified schematic of the laser alignment technique. The beam is shown as visible for illustrative purposes. For greater accuracy, a second laser could be installed in the middle port.

## D.2 Camera alignment and calibration

The camera and backlight must be aligned to capture high-quality images. It is best to begin by leveling the camera on the scissor platform about the pitch and roll axes. The camera, with zoom lens fully extended, is advanced and stopped just before the lens contacts the quartz window. It is recommended to set the initial field of view to the maximum resolution (1280 px. × 1080 px.) to assist in finding the cross-fiber intersection (note that resetting the camera field of view does not impact the calibration as it only crops the image). The camera should then be adjusted such that the fiber intersection appears roughly in the center of the field of view. The camera achieves proper focus when the fibers appear crisp, the horizontal fiber visibly extends an equal distance on either side of the vertical fiber, and the lens is almost touching the chamber window.

Similarly, the backlight tube should be initially set perpendicular to the window flange. Once the adjustment of the camera is complete (described above), the rear of the tube should be

slightly moved in all directions to find the position which results in the best image quality. Small angular displacements can yield major differences in how the camera represents the droplet. To aid in the thresholding procedure, the entire circumference of the droplet should appear uniform with as little gray transition (shadow) as possible. The position of the backlight inside the tube should also be optimized. Once the camera and backlight alignment is complete, great care should be taken to avoid touching either object. Subtle movements of the backlight/tube may not be perceptible, however, if by accident a slight alteration of the camera position occurs, immediate re-calibration should be considered.

Previous calibration techniques utilized a ruler installed in place of the cross-fiber frame to measure scale. There are several issues with this strategy. First, it requires the complete removal and reinstallation of the cross-fiber frame. Second, the use of several different frames and mounting hardware throughout the experiment ensures that the fiber intersection will not always coincide with the position of the calibration ruler. Third, the ruler must be perfectly perpendicular to the camera for accurate calibration using the gradient marks. Finally, at the high level of magnification featured in this study, the ruler tick marks appear wide and blurry, and it is difficult to extract a consistent scale factor.

The following recommended technique solves most of these problems. For all data reported in this study, calibration was performed by first installing the cross-fiber frame and then placing a stainless-steel needle of 305-μm diameter at the intersection of the cross-fiber. In this way, the frame receives a calibration tailored to its exact position before the subsequent droplet tests. Furthermore, the needle is circular which mitigates the issue of angular misalignment (lack of perpendicularity to the camera). The needle is epoxied to a length of solder while a window stud is used to secure the opposite end of the solder to the chamber. The needle is then inserted into the

chamber and gently placed directly above the fiber intersection. The ductility of the solder will cause the needle to fall slowly, and a calibration image is taken at the instant when the needle contacts the intersection. The needle and solder are then quickly retracted to avoid moving or damaging the fibers. Figure D.2 provides an example of a typical calibration image. The greyscale calibration image is converted to a binary representation by thresholding using Otsu's method (the result is illustrated in Fig. D.3). Both droplet and calibration file use the same methodology to separate foreground from background. The diameter of the needle is measured in pixels using the built-in interactive image tool in MATLAB. For example, the diameter of the needle in Figs. D.2 and D.3 is 63.00 pixels which results in a scale factor of 4.8413 µm/px. The diameter must be measured perpendicular to the needle edges (hence the inclusion of the long blue lines which demarcate the upper and lower surface of the needle) at the location where the needle contacts the fibers.

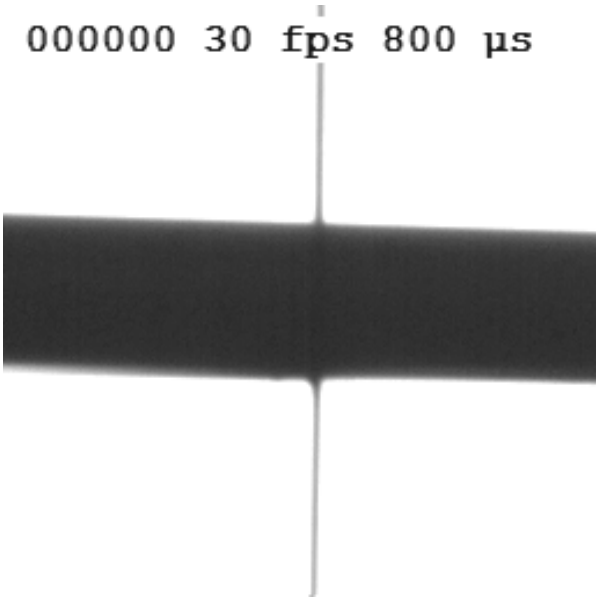


**Fig. D.2.** Typical camera calibration image. The stainless-steel needle has a diameter of 305 µm and rests at the fiber intersection.

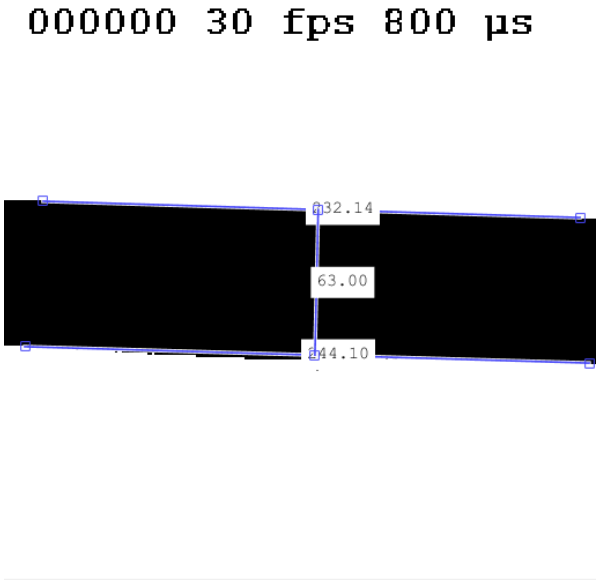


**Fig. D.3.** Thresholded calibration image. The measured diameter is 63 pixels, which corresponds to a scale factor of ~4.8 µm/px.

Camera calibration is extremely important for the acquisition and processing of droplet data. For a typical droplet (~600 μm), scale factors which differ by $\pm$ 3% from the nominal value can result in instantaneous diameter calculations varying by $\pm$ 3% and overall evaporation rates ($K$) varying by $\pm$ 6%. The inclusion or exclusion of only one to two pixels when measuring the calibration object can result in a $\pm$ 3% error in the scale factor, making this a very realistic scenario. Fortunately, calibration of the camera using the needle technique has proven to be highly repeatable. Repetitive measurements on the same frame are typically precise to within 1 pixel. As a further example, tests at high temperature typically resulted in the fibers losing tension upon cool down. The corrective action, either tightening the fibers or installing a new frame, required re-calibration. The time period corresponding to the high-temperature experiments required the acquisition of 12 different calibration images, and the percent difference between the highest and lowest scale factor was less than 3%. This level of precision in measurement is indicative of consistency in both frame placement and calibration technique.

## D.3 PIV alignment and calibration

Proper alignment of the PIV laser and camera is crucial, and several criteria must be satisfied simultaneously. The laser sheet should be vertical and pass through the center of the chamber, while the camera must be aligned perpendicular to the sheet. Failure to achieve perpendicularity can result in particles which appear blurry instead of as sharp points of light. The camera field of view must also be centered around the point of droplet suspension and properly calibrated.

To ensure that the camera is both centered and perpendicular to the laser sheet, an approach utilizing strings to find the window port centers was adopted. Figure D.4 illustrates a length of

string tightly wrapped around the extruding studs for both the foreground and background window ports. When properly wrapped, the intersection of all portions of string which pass across the window conveniently locates the port center. The camera position and focus is then adjusted to center the string intersection of the foreground window in the camera field of view. When the camera is subsequently adjusted to bring the background window into focus, the point of string intersection should coincide with that of the foreground window. If this criterion is satisfied, the camera field of view is passing perfectly through the chamber. If, conversely, the background and foreground string intersections are not coincident, some degree of angular misalignment is present. The camera is then adjusted until both intersections coincide and correspond to the center of the field of view.

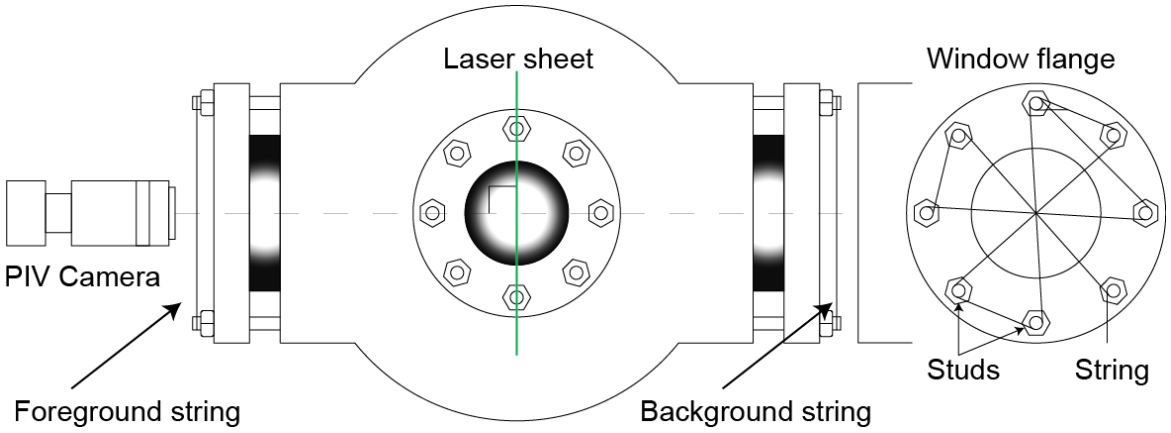


**Fig. D.4.** Illustration of the string method for aligning the PIV camera.

Alignment of the laser should begin by leveling the laser on its tripod, both fore and aft and side to side. Laser centering is achieved using the string method described above. The laser is centered in the window ports when the sheet is observed to pass through both the foreground and background string intersections. Once both the camera and laser are individually aligned, it is recommended to perform a PIV test run to evaluate the image quality. If the camera focus can be

adjusted such that the seeding appears crisp around the entire image periphery as well as in the center, the laser and camera are sufficiently aligned.

The final step is to calibrate the camera by establishing a scale factor in the center of the chamber. Calibration proceeds by installing a cross-fiber frame with a transparent ruler suspended through its center. The positioning of the cross-fiber frame is equivalent to the frame's location in a droplet evaporation study. Because the camera focus is already adjusted to match the location of the laser sheet, care must be taken to avoid touching the camera. Instead, the frame should be pushed forward or backward, if necessary, to bring the ruler into focus. The camera then captures a calibration image. If the frame is to remain installed for the PIV test, is should be aligned as discussed in Section D.1. A cardboard insert with accurate grid markings may be used to find the exact center of the frame rather than the intersection of the fibers (fibers are typically not present for PIV studies). If purpose of the frame is simply to aid in calibration, the exact height is not important as removal of the frame will occur after calibration is complete.

## E. Summary of experimental equipment

The following tables provide part numbers and details for much of the experimental equipment used for this thesis. The lists are not exhaustive, and consultation/confirmation with previous thesis reports [187,206–208] is recommended when possible.

**Table E.1**
Chamber parts and accessories.

| Part description | Part details | Notes |
|---|---|---|
| Fan motors | SEM HR70E4-32S w/ E07 encoder | *blades, shafts, keys, heatsinks, and mounting accessories are manufactured in house [187]* |
| Servo amplifiers | Servo Dynamics DynaDrive 1224-BLS | |
| Fan bearings | R8-2RS low temp. / SR8Z high temp. | *most fan assemblies still have R8-2RS bearings installed – replace with SR8Z when necessary* |
| Fan hub o-rings* | AS568A-244 | *4-1/4 × 4-1/2 × 1/8†* |
| Intermediate fan shaft o-rings | AS568A-018 | *to be used with in-house seal machined from polyamide-filled Teflon round stock [187]*<br>*3/4 × 7/8 × 1/16* |
| Quartz windows | ? | *40 mm thick, unknown manufacturer/supplier* |
| Flange window gaskets | NA-60 gasket sheet | *not required to hold pressure*<br>*5 in. window: 5 × 5-15/16 × 1/16*<br>*4 in. window: 4 × 4-15/16 × 1/16* |
| Chamber window seals | SKF rotary seal R12-F | *holds chamber pressure, torque nuts to 150 in-lbs.*<br>*5 in. window: 5.080 × 5.920 × 0.181*<br>*4 in. window: 4.080 × 4.920 × 0.181* |
| Droplet suspension fibers | NCK Hi-Nicalon continuous silicon carbide fiber - 14 µm | |
| Fiber holders | McMaster-Carr 22-gauge needle – 75165A758 | *cut into pieces approx. 1/2 in. long with wire EDM to avoid crimping, available from chemistry stores* |
| Capillary tubing | Paradigm Optics CTPC025-050 | *polycarbonate capillary tubing, 25-µm inner diameter, 50-µm outer diameter* |
| Injection needle | McMaster-Carr 30-gauge needle – 6710A38 | *base must be threaded with 10-32 tap to facilitate connection with injector barrel* |
| Injector piston o-rings | AS568A-112<br>AS568A-204 | *-112 (first o-ring): 1/2 × 11/16 × 3/32*<br>*-204 (second o-ring): 3/8 × 5/8 × 1/8* |
| Window plate o-rings | AS568A-253<br>AS568A-245 | *-253 (5 in. port): 5-3/8 × 5-5/8 × 1/8*<br>*-245 (4 in. port): 4-3/8 × 4-5/8 × 1/8* |
| Accessory port o-ring | AS568A-118 | *7/8 × 1-1/16 × 3/32* |

**all o-rings made from Viton (Fluorocarbon Type A)*
*†inner diameter × outer diameter × cross section (thickness), units are inches (aerospace size standard)*

**Table E.2**
Data acquisition and measurement.

| Part description | Part details | Notes |
|---|---|---|
| High-speed camera | IDT XS5-M-1 (branded Dantec NanoSense MkIII) | *max. 1280 px. × 1080 px. @ 1040 fps mounted on large metal scissor stand* |
| Backlight | Lowel Pro-light 250 W | *inserted into long metal duct, cooled with basic commercial fan* |
| Teleconverter | Sears Auto 3× Teleconverter N/AI | *no longer produced* |
| Telescopic lens | Nikon AF 70 – 210 mm zoom lens | *no longer produced* |
| Close-up filter | Nikon +4 close-up filter | |
| PIV laser | Dantec Dynamics DualPower 135-15 | *Nd:YAG laser, 135 mJ per pulse, 532 nm wavelength, 10 Hz repetition rate* |
| PIV power supply unit | Litron Lasers LPU 550 | |
| PIV camera | Dantec Dynamics FlowSense EO 4M | *2048 px. × 2048 px.* |
| PIV camera lens | Nikon AF Micro 60 mm | *replaced by Nikon AF-S 60 mm* |
| PIV lens filter | ? | *unknown make/model* |
| PIV seeder | La Vision aerosol generator 1108926 | *olive oil, ~1-µm particle diameter* |
| DAQ chassis | NI cDAQ 9172 | *USB connectivity, legacy, current models 917x or 918x* |
| Analog voltage input module | NI 9205 | *receives pressure transducer input* |
| Temperature input module | NI 9211 | *receives thermocouple input* |
| Analog voltage output modules | NI 9263 | *controls fan servos, camera timing* |
| Thermocouples | Omega KQXL-18G-[**] | *$^1/_8$ in. sheath diameter, grounded junction, [**] designates length in inches* |
| Pressure transducer | Kavlico P155-150G-F1A | *high pressure transducer (0-150 psia)* |
| Pressure transducer | Kulite XTEL-190 | *low pressure transducer (0-5 psia)* |
| Signal conditioner | Omega DMD4059 | *amplifies the signal from the low-pressure transducer* |
| Signal generator | BK Precision 1670A power supply | *powers the pressure transducers* |

# F. Supporting literature

The following resources may be useful for those undertaking similar work to that found in this thesis, as the documentation relates to experimental equipment or procedure. Table F.1 provides the location of online availability where possible at the time of thesis publication. Interested readers may contact the author regarding unavailable material.

**Table F.1**
Supporting literature for equipment and experimental procedure.

| Title | Available |
|---|---|
| Technical Data Manual – HR/HRS Brushless AC Servomotors (TD HRM 1.1, Issue No. 10.0) | http://www.sem.co.uk/_Resources/Persistent/7f54cf5db6d9584ea430f4883fe9ebdde63fc9f2/HR_Technical_Data_Manual_Issue_10.0.pdf |
| User Guide – Servo Dynamics 1224-BLS Servo Drive | http://www.servodynamics.com/wp-content/uploads/2014/10/1224bls_manual.pdf |
| Monarch Instrument – Using a stroboscope to measure RPM | http://www.monarchinstrument.com/KB/Stroboscopes/Strobe_for_RPM.pdf |
| MPF – Fused silica window cleaning notes | http://mpfpi.com/Portals/0/PDFS/Fused-Silica-Window-Cleaning-Notes.pdf |
| Cutting polymer tubes | *upon request* |
| COI Ceramics, Inc. – Hi-Nicalon ceramic fiber brochure | http://www.coiceramics.com/pdfs/Hi-nicalon_1-17-06.pdf |
| Lowel Pro-light instructions | http://lowel.tiffen.com/download/LowelProLightInstrs_0510_4web.pdf |
| IDT – MotionStudio User Manual (latest release) | http://media.idtvision.com/docs/manuals/mstudio_man_en.pdf |
| Dantec Dynamics – DynamicStudio v3.12 User's Guide | *upon request* |

## G. Servo wiring diagram

The following schematic illustrates the proper wiring of the servo drive and encoder harness. It may be used to find open and shorted wiring for a malfunctioning fan.

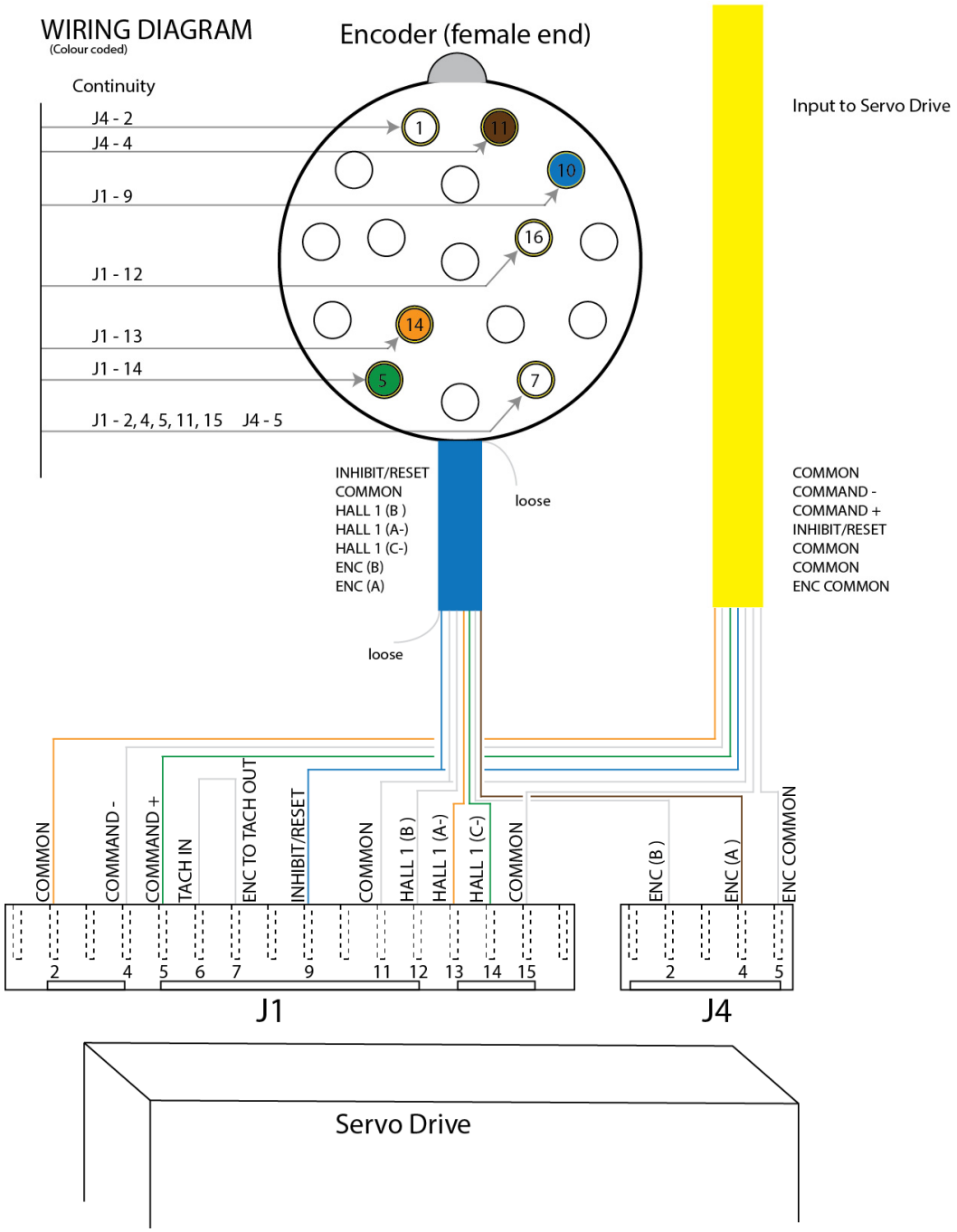


**Fig. G.1.** Servo amplifier and fan encoder wiring schematic.